frontiers | Research Topics

Technologies for prospecting, extraction, and utilization of space resources

Edited by
Paul Zabel, Philipp Reiss, Angel Abbud-Madrid, Beth Lomax, Florian Kehl, Valentin T. Bickel and Hendrik Kolvenbach

Coordinated by
Philip Arm and Gabriela Ligeza

Published in
Frontiers in Space Technologies

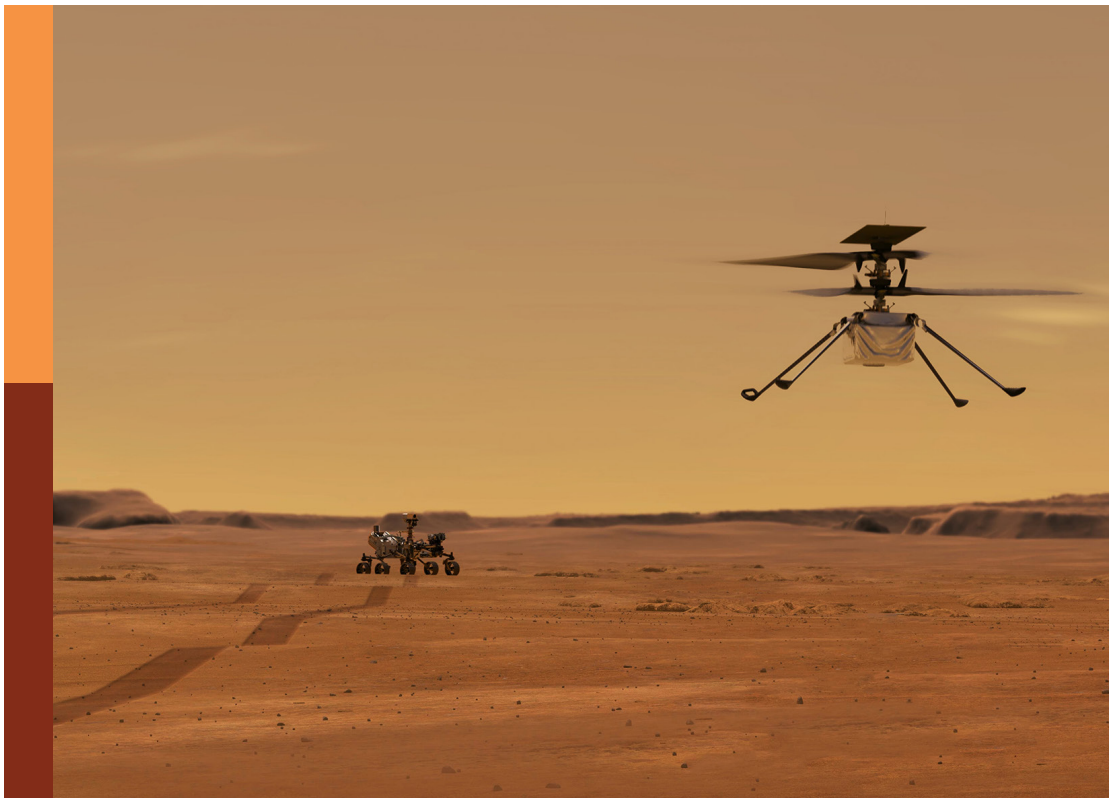

ISSN 1664-8714
ISBN 978-2-8325-5676-4
DOI 10.3389/978-2-8325-5676-4

About Frontiers

Frontiers is more than just an open access publisher of scholarly articles: it is a pioneering approach to the world of academia, radically improving the way scholarly research is managed. The grand vision of Frontiers is a world where all people have an equal opportunity to seek, share and generate knowledge. Frontiers provides immediate and permanent online open access to all its publications, but this alone is not enough to realize our grand goals.

Frontiers journal series

The Frontiers journal series is a multi-tier and interdisciplinary set of open-access, online journals, promising a paradigm shift from the current review, selection and dissemination processes in academic publishing. All Frontiers journals are driven by researchers for researchers; therefore, they constitute a service to the scholarly community. At the same time, the *Frontiers journal series* operates on a revolutionary invention, the tiered publishing system, initially addressing specific communities of scholars, and gradually climbing up to broader public understanding, thus serving the interests of the lay society, too.

Dedication to quality

Each Frontiers article is a landmark of the highest quality, thanks to genuinely collaborative interactions between authors and review editors, who include some of the world's best academicians. Research must be certified by peers before entering a stream of knowledge that may eventually reach the public - and shape society; therefore, Frontiers only applies the most rigorous and unbiased reviews. Frontiers revolutionizes research publishing by freely delivering the most outstanding research, evaluated with no bias from both the academic and social point of view. By applying the most advanced information technologies, Frontiers is catapulting scholarly publishing into a new generation.

What are Frontiers Research Topics?

Frontiers Research Topics are very popular trademarks of the *Frontiers journals series*: they are collections of at least ten articles, all centered on a particular subject. With their unique mix of varied contributions from Original Research to Review Articles, Frontiers Research Topics unify the most influential researchers, the latest key findings and historical advances in a hot research area.

Find out more on how to host your own Frontiers Research Topic or contribute to one as an author by contacting the Frontiers editorial office: frontiersin.org/about/contact

Technologies for prospecting, extraction, and utilization of space resources

Topic editors

Paul Zabel — German Aerospace Center (DLR), Germany
Philipp Reiss — Technical University of Munich, Germany
Angel Abbud-Madrid — Colorado School of Mines, United States
Beth Lomax — European Space Research and Technology Centre (ESTEC), Netherlands
Florian Kehl — University of Zurich, Switzerland
Valentin T. Bickel — Universität Bern, Switzerland
Hendrik Kolvenbach — ETH Zürich, Switzerland

Topic coordinators

Philip Arm — ETH Zürich, Switzerland
Gabriela Ligeza — University of Basel, Switzerland

Citation

Zabel, P., Reiss, P., Abbud-Madrid, A., Lomax, B., Kehl, F., Bickel, V. T., Kolvenbach, H., Arm, P., Ligeza, G., eds. (2024). *Technologies for prospecting, extraction, and utilization of space resources*. Lausanne: Frontiers Media SA.
doi: 10.3389/978-2-8325-5676-4

Table of contents

frontiers | Frontiers in Space Technologies

TYPE Editorial
PUBLISHED 31 October 2024
DOI 10.3389/frspt.2024.1493494

OPEN ACCESS

EDITED AND REVIEWED BY
Mark Sephton,
Imperial College London, United Kingdom

*CORRESPONDENCE
P. Reiss,
p.reiss@tum.de

RECEIVED 09 September 2024
ACCEPTED 23 October 2024
PUBLISHED 31 October 2024

CITATION
Reiss P, Abbud-Madrid A, Arm P, Bickel VT, Kehl F, Kolvenbach H, Ligeza G, Lomax B and Zabel P (2024) Editorial: Technologies for prospecting, extraction, and utilization of space resources.
Front. Space Technol. 5:1493494.
doi: 10.3389/frspt.2024.1493494

Editorial: Technologies for prospecting, extraction, and utilization of space resources

P. Reiss[1]*, A. Abbud-Madrid[2], P. Arm[3], V. T. Bickel[4], F. Kehl[5,6], H. Kolvenbach[3], G. Ligeza[7], B. Lomax[8] and P. Zabel[9]

[1]Department of Aerospace and Geodesy, School of Engineering and Design, Technical University of Munich, Ottobrunn, Germany, [2]Center for Space Resources, Colorado School of Mines, Golden, CO, United States, [3]Robotic Systems Lab, Department of Mechanical and Process Engineering, ETH Zürich, Zürich, Switzerland, [4]Center for Space and Habitability, University of Bern, Bern, Switzerland, [5]Space Science and Technology Group, Department of Earth and Planetary Sciences, ETH Zurich, Zurich, Switzerland, [6]Space Instruments Group, Department of Astrophysics, University of Zurich, Zurich, Switzerland, [7]Department of Environmental Sciences, University of Basel, Basel, Switzerland, [8]European Space Research and Technology Centre, European Space Agency, Noordwijk, Netherlands, [9]Institute of Space Systems, German Aerospace Center, Bremen, Germany

KEYWORDS

space exploration, space resources, technologies, instruments, moon, in situ resource utilisation

Editorial on the Research Topic
Technologies for prospecting, extraction, and utilization of space resources

Introduction

Our solar system holds an abundance of resources that can be utilized to support space exploration missions and sustain a future human presence beyond Earth. These resources include solar energy, water ice, volatiles, hydrates, minerals, metals, rare earth elements, and the regolith on various celestial bodies. The *in situ* resource utilization (ISRU) approach encompasses the production of life support consumables, such as oxygen and water, propellants, in-space manufacturing, or the construction of large structures based on these locally available materials. ISRU reduces the amount of resources needed to be supplied from Earth, thereby enabling long-term missions and permanent outposts.

The studies presented in this Research Topic showcase advancements in instrument development for the detection and characterization of space resources, as well as technologies to process feedstock and obtain valuable products such as water, oxygen, and metals. Additionally, they address the critical need for suitable terrestrial regolith analogues to support the development, testing, and validation of ISRU systems, as well as the construction of infrastructure to enable sustainable, long-term operations.

Prospecting

Various prospecting missions are currently planned to reduce uncertainties in estimated lunar resource occurrences and concentrations. The European Space Agency's PROSPECT instrument package combines the acquisition and detailed analysis of lunar samples on a lander. Trautner et al. present its design and capabilities and the recent development status.

Equipped with the ProSEED drill and ProSPA analytical laboratory, the instrument package primarily aims to extract and analyze surface and subsurface regolith samples, targeting volatile-rich areas. It also features an ISRU demonstration mode, in which regolith will be reduced with hydrogen to produce water. A multispectral imaging system allows the characterization of the surface at the landing site, and a drill-integrated permittivity sensor supports the determination of subsurface ice and the monitoring of its potential loss during sample acquisition.

Characterization of the soil properties, as well as its ice content, is essential for identifying resource-rich areas, especially for surface-bound vehicles. Gscheidle et al. present their concept of novel dielectric permittivity sensors to map water ice deposits in the lunar regolith. Such sensors could be attached to rover wheels and lander footpads and present a power- and mass-efficient instrument for exploration missions. The study discusses the sensor's functional concept and data processing techniques and demonstrates its performance in detecting ice in lunar regolith.

Laser-induced breakdown spectroscopy (LIBS) and Raman spectroscopy are emerging as powerful tools for *in situ* planetary exploration. The feasibility study by Rammelkamp et al. showcases how LIBS can effectively identify and quantify the mineral ilmenite in lunar regolith, while Raman spectroscopy can be used to monitor oxygen extraction processes. By providing real-time data on elemental composition and process efficiency, these techniques could be an important tool for future prospecting missions.

The location of feedstock, as well as its accessibility, determines the economic viability of a mining operation and subsequent resource processing. In their study, Steinert et al. investigate the influence of location selection on the viability of an in-space refueling architecture that utilizes lunar oxygen. The results suggest that the selection of oxygen production sites should prioritize resource availability and processing efficiency over transport cost variations to optimize the overall mission cost-effectiveness.

Extracting

Kulkarni et al. demonstrate a three-stage beneficiation system to enrich the feedstock concentration of the mineral ilmenite. Through sequential gravitational, magnetic, and electrostatic techniques, the ilmenite grade was increased by a factor of three, highlighting the potential of beneficiation to enable higher oxygen yields in regolith processing.

The research of Burke et al. explores the effect of reduced gravity on bubble formation and detachment in various electrolysis processes, including water electrolysis, molten salt electrolysis, and molten regolith electrolysis. The findings indicate that reduced gravity, fluid properties, electrode surface conditions, and electrode orientation significantly influence electrolytic efficiency, providing insights for designing and operating effective ISRU oxygen production systems.

Utilizing

Constructing necessary infrastructure on the Moon with locally available resources is vital for sustainable long-term missions. Walther et al. systematically investigate the autonomous construction of lunar infrastructure using unprocessed boulders. They present a promising method for building blast shields to protect lunar infrastructure from the debris of a spacecraft landing or launching. The study shows that this approach requires two orders of magnitude less energy than alternative ISRU construction methods.

One critical aspect of establishing a lunar base is ensuring a reliable supply of clean water. The study by Freer et al. addresses this challenge by characterizing the dissolution behavior of lunar regolith in water. The experiments revealed that lunar dust contamination could significantly exceed the volatile levels allowed by drinking water standards of the World Health Organization and the National Aeronautics and Space Administration, particularly in terms of pH, turbidity, and aluminum concentration. These findings underscore the importance of developing robust water purification systems to ensure the health and safety of future crew.

Terrestrial analogues

Testing ISRU systems on ground is only possible through the use of terrestrial regolith analogues, so-called simulants. Long-Fox et al. present insights into the production methods, equipment, and materials used to create planetary regolith simulants. The authors provide details on the compositional data, particle size, and applications for certain standard lunar, Martian, and asteroid simulants.

The study by Louca et al. presents a virtual model of lunar regolith that can effectively replicate regolith behavior, especially with respect to flowability. This approach offers a cost-effective, safe, and practical alternative to physical testing, particularly for large-scale applications like virtual training and teleoperation systems, and could facilitate the development of robust ISRU systems.

The articles collected on this Research Topic demonstrate the immense breadth and multi-disciplinarity of ISRU. They also highlight how fundamental and applied research complement each other to push the boundaries of space exploration and realize sustained human presence beyond low Earth orbit.

Author contributions

PR: Writing–original draft, Writing–review and editing. AA-M: Writing–review and editing. PA: Writing–review and editing. VB: Writing–review and editing. FK: Writing–review and editing. HK: Writing–review and editing. GL: Writing–review and editing. BL: Writing–review and editing. PZ: Writing–review and editing.

Funding

The author(s) declare that no financial support was received for the research, authorship, and/or publication of this article.

Conflict of interest

The author declares that the research was conducted in the absence of any commercial or financial relationships that could be construed as a potential conflict of interest.

Publisher's note

frontiers | Frontiers in Space Technologies

TYPE Original Research
PUBLISHED 27 September 2023
DOI 10.3389/frspt.2023.1255535

OPEN ACCESS

EDITED BY
Beth Lomax,
European Space Research and Technology Centre (ESTEC), Netherlands

REVIEWED BY
Aliz Zemeny,
European Space Agency (ECSAT), United Kingdom
David Karl,
Technical University of Berlin, Germany

*CORRESPONDENCE
Jared M. Long-Fox,
jared.long-fox@ucf.edu

RECEIVED 09 July 2023
ACCEPTED 14 September 2023
PUBLISHED 27 September 2023

CITATION
Long-Fox JM and Britt DT (2023), Characterization of planetary regolith simulants for the research and development of space resource technologies.
Front. Space Technol. 4:1255535.
doi: 10.3389/frspt.2023.1255535

Characterization of planetary regolith simulants for the research and development of space resource technologies

Jared M. Long-Fox* and Daniel T. Britt

Department of Physics, University of Central Florida, Orlando, FL, United States

Human planetary exploration and colonization efforts are reliant on the ability to safely interact with planetary surfaces and to leverage local regolith as a resource. The high-cost and risk-intensive nature of establishing planetary infrastructure and resource utilization facilities necessitates risk reduction through laboratory-based research and development of space resource acquisition, processing, and extraction technologies using appropriate, well-characterized, mineral-based regolith simulants. Such simulants enable the planetary exploration and resource utilization communities to test large-scale technologies and methodologies for a relatively low cost as an alternative to scarce and expensive returned samples. The fidelity of a regolith simulant for any application is, in part, determined by the mineralogical composition and particle size distribution. The importance of composition is well established for *in situ* resource utilization studies sensitive to geochemical properties but tends to be ignored in studies concerned with physical properties. Neglecting to consider mineralogy reduces the fidelity of a simulant since each mineral species has its own unique grain density, preferred grain geometry, and intergranular forces, all of which affect the physical properties of the simulant (e.g., shear strength, bearing strength, bulk density, thermal and electrical properties, magnetic properties). Traditionally, regolith simulants have been limited in quantity and availability; Exolith Lab remedies these problems by designing simulants in a constrained maximization approach to fidelity relative to cost, material availability, and safety. Exolith Lab simulants are designed to approximate the mineralogy and particle size ranges of the planetary regolith being simulated, with composition constrained by remote sensing observations and/or returned sample analyses. With facilities and equipment capable of high-volume simulant production, Exolith Lab offers standard simulants in bulk that are readily available for purchase and shipment. This work reviews the production methods, equipment, and materials used to create Exolith Lab simulants, provides compositional data, particle size data, and applications for each standard lunar, Martian, and asteroid simulant that Exolith Lab offers.

KEYWORDS

regolith simulant, mineralogy, physical properties, planetary exploration, SRU, space technology, laboratory testing

1 Introduction

Humans are turning their eyes to the sky more than ever before with an increased interest in space exploration and the resources we can obtain from planetary bodies to fuel the advancement of humanity into a space-faring species. As this interest in planetary exploration and resource utilization increases, the need to develop and test technologies ranging from in-space propellant production (Kornuta et al., 2019), mobility systems (Colaprete et al., 2019), resource acquisition (Just et al., 2020), extraction (Guerrero-Gonzalez and Zabel, 2023), transport/conveyance (Cannon et al., 2022), and infrastructure development (Thangavelauthan and Xu, 2022) systems using appropriate simulants also increases. It is not feasible to launch bulk resources and equipment to space to perform operations on the surface of the Moon, Mars, and asteroids, so local resources will need to be used, namely, planetary regolith (Sanders et al., 2022). Planetary regolith is the layer of loose rock and sediments that covers bedrock on planetary surfaces, such as the Moon and Mars (McKay et al., 1991). Since planetary regolith is composed of geologic materials (minerals, amorphous glasses, native elements, etc.), it can be used in space resource utilization (SRU) and/or *in situ* resource utilization (ISRU). NASA's Apollo missions returned both regolith and rock samples from the Moon (e.g., Schmitt et al., 1970), the NASA/ESA Mars Sample Return mission (Kminek et al., 2022) is planning on returning the first Martian samples in 2033, and asteroid sample return missions are underway (Walsh et al., 2022) with Hayabusa2 already returning to Earth (Watanabe et al., 2019; Yada et al., 2022), but none of these provide sufficient amounts of material to test and develop SRU and ISRU technologies. In this absence of abundant bulk returned regolith samples, technologies aimed for use on the surfaces of the Moon, Mars, or asteroids must be tested with terrestrially-derived simulated planetary regolith (simulants). The more closely these simulants approximate the regolith they are created to simulate, the better the quality of studies and testing. Previous simulants have generally disregarded mineralogical accuracy as a necessary design component, but this is in error since the mineralogical composition of geologic materials determine not only the geochemical properties of the simulant, but also the thermal, electrical, mechanical properties. Exolith Lab offers solutions to the planetary science and engineering communities through the bulk manufacture of mineralogically accurate lunar, Martian, and asteroid regolith simulants (Figure 1). This work details the design philosophy, design process, and manufacturing processes used to create Exolith Lab simulants as well as motivation, background, use cases, mineralogical compositions, bulk elemental compositions (in equivalent oxides) from wavelength dispersive x-ray fluorescence (XRF) data, compositional phase information from x-ray diffraction (XRD) data, and particle size distribution (PSD) at the time this work was authored. The goal of this work is to

FIGURE 1
Exolith Lab planetary regolith simulants **(A)** LHS-1, **(B)** LMS-1, **(C)** LHS-1D, **(D)** LMS-1D, **(E)** MGS-1, **(F)** MGS-1C, **(G)** MGS-1S, **(H)** JEZ-1, **(I)** CI-V2, **(J)** CM-V2, and **(K)** CR-V2.

FIGURE 2
(A) Sieves and sieve shakers used in small-batch Exolith Lab simulant production, **(B)** sieves and sieve shaker used in bulk, large-volume Exolith Lab simulant production, **(C)** hammer mill and **(D)** jaw crusher used to percussively crush rocks and minerals for use in Exolith Lab simulants, **(E)** cement mixer with steel balls added for ball milling simulants to particle sizes smaller than the Exolith Lab hammer mill and jaw crusher can produce, **(F)** cement mixers used to mix simulant and serve as ball mills when steel balls are added during mixing.

describe the philosophy and capabilities of Exolith Lab and the current main production line of lunar, Martian, and asteroid regolith simulants and establish the simulants themselves, the design philosophy, characterization methods, and the production methods as open-source standards for testing of any technology or system intended for extraterrestrial use. Forthcoming work will perform quantitative analyses on each of these simulants to compare their physical and chemical properties to the regolith they are intended to simulate, and as such, detailed comparisons are not directly provided here.

The mineralogic compositions of Exolith Lab simulants are based on returned samples and remote sensing data. Once the mineralogy of the target body or site is estimated, Exolith Lab finds terrestrial rocks and minerals with well-characterized, reliable sources to provide materials that either arrive pre-processed to specific grain size ranges or uses in-house rock crushing equipment to crush feedstock and size sort using ASTM standard sieves and sieve shakers (Figures 2A, B). To better simulate the irregular, jagged shapes of lunar and asteroid regolith grains that result from undergoing space weathering processes over billions of years, Exolith Lab strives to attain realistic grain shapes by using percussive crushing methods (hammer mill and jaw crusher, Figures 2C, D). When simulants with small (e.g., less than ~50 μm) maximum particle sizes are being produced, ball mills (Figure 2E) are used to reduce particle size to the desired range. Once each mineral or rock is prepared, the constituents are combined in the desired proportions (with <0.5 wt% difference in each production run) and mixed in cement mixers (Figure 2F).

When discussing the chemical composition of geologic materials, it is not sufficient to only describe the mineralogy since different minerals can have varying concentrations of elements and often exist on compositional continua (e.g., solid solutions). Since planetary regolith is created from different materials and in different environments from that of Earth, the relative concentrations of elements within minerals and the form those elements take (e.g., native elements, oxides, glasses, or minerals) vary widely. This means that there is a definitive need for determination of the bulk elemental composition of returned regolith and simulants to be able to accurately compare geochemical properties of simulant used for research and development of ISRU- and exploration-related technologies. The trace element profile of a regolith simulant is inherently the trace element profile of a terrestrial material since simulants are created solely from materials found on Earth, and since planetary terrestrial regolith formation processes are vastly different, a simulant should never be correlated to actual planetary regolith in trace element analyses. Here, the major and minor elemental

composition of Exolith Lab simulants is given as equivalent oxides based on XRF analysis. Comparisons to lunar, Martian, and asteroid XRF data are not provided here since this work is specifically a description of simulants, design philosophy, and characterization and production methods, but forthcoming publications should provide detailed comparisons to actual planetary regolith XRF data.

The compositional phases of planetary regolith are highly varied and impacted by weathering processes that mechanically and chemically alter the rocks and minerals on the Moon, Mars, and asteroids. Knowledge of the proportions of different mineralogic and amorphous phases present of planetary regolith provides insights into formational and evolutionary processes that affected or are still affecting the regolith in question, and this determines the processing needed to be able to use the regolith as a resource or a construction material. Even though Exolith Lab uses a mineral-based design philosophy that utilizes high-purity materials combined in specific proportions to make planetary regolith simulants, characterizations of the different compositional phases is key to the research and development of space resource technologies. Such characterizations allow comparison to planetary samples either returned or impacted onto Earth or *in situ* mineralogical/phase measurements on other planetary bodies to better understand results obtained in testing space resource technologies using a given simulant and how the simulant can be improved if new data is obtained. If simulants used in laboratory testing of space resource technologies are well characterized in terms of phases present, results from laboratory testing can provide information on the most efficient way to utilize planetary regolith and how planetary regolith weathering processes affect *in situ* regolith. As with XRF data, direct comparisons of XRD data between Exolith Lab lunar, Martian, and asteroid simulants are not given here because the intent of this paper is to formally introduce and describe the simulants presented and forthcoming publications should provide rigorous, quantitative comparisons between simulants and regolith.

The particle size range and distributions determine the physical (thermal, electromagnetic, and mechanical) and chemical properties of planetary regolith, therefore simulants should match the particle size ranges and distributions of the regolith they are intended to simulate. Since the ease and cost of space exploration, resource prospecting, mining, and processing are all so dependent on being able to operate in extreme conditions with planetary particle size ranges and distributions, technologies must be tested and validated prior to flight in appropriate testing materials with realistic compositions and particle sizes. Since particle size and PSD strongly affect the physical properties of a regolith, these properties were ranked as the top two most important properties that a regolith simulant must match (Sibille et al., 2006). Exolith Lab controls particle size range of produced simulants at the processes level with the goal to replicate the particle size range and distribution of the <1 mm size fraction of lunar and Martian regolith. Asteroid simulants are available in fine powder (<1 mm) or "cobble" (coarse aggregate) form (terminology from Britt et al., 2019), with the "cobble" form having a larger particle size range and more variable PSD with aggregates ≥10,000 μm (1 cm). Throughout this work, the geoscience standard Wentworth (1922) particle size scale and nomenclature is used for all size descriptions, and by this scheme, the "cobble" nomenclature for asteroid simulants established by Britt et al. (2019) is formally "pebbles."

2 Materials and methods

2.1 Simulant production methods

2.1.1 Design philosophy

Exolith Lab simulant design and manufacturing philosophy is a constrained maximization of fidelity relative to cost, safety, and material availability, and parameters tuned in this optimization are mineralogy and particle geometry (size and shape). Mineralogy is a cornerstone of Exolith Lab's design philosophy because mineralogy determines the geochemical and physical properties since each mineral has a unique crystal habit, cleavage planes, chemistry, and grain density. Particle size range and distribution are among the most important aspects of lunar and planetary regolith simulants (Sibille et al., 2006; Metzger et al., 2019) as they drive geomechanical properties as well as affecting material processing requirements for ISRU (e.g., melting temperatures for metal and oxygen extraction, material transport). Based on the contributions of these factors to the physical and chemical properties of planetary regolith, mineralogy and particle geometry are highly important factors that need to be considered in simulant selection for research and development efforts in mobility, dust mitigation, tool-regolith interactions, resource evaluation, resource acquisition, material transport, resource extraction and refinement, and infrastructure development.

2.1.2 Material sourcing and simulant production equipment

Exolith Lab sources bulk amounts of high purity commercially available rocks and minerals for use in simulant production. Procuring large amounts of material not only enables more simulant to be produced without downtime waiting for material to arrive, but it also provides higher product consistency. Where possible, constituents that have been or are currently being used in other commonly used simulants are being used, such as Merriam crater basalt that was used in JSC-1 (McKay et al., 1994) and Greenspar anorthosite. The use of Merriam crater basalt in Exolith Lab simulants is a recent change at the time of writing (and was used in the simulants analyzed and presented in this work), and this specific change was made to be more directly comparable to other simulants. Even though Exolith Lab aims to keep material sources and production methods consistent as possible, sometimes change is necessary due to inevitable issues such as a change in material source location (even different sites within the same mine, for example,), material supplier, or equipment upgrades. Such material changes affect the simulant by altering things such as (but not limited to) chemical composition, processing requirements that can affect particle shape and size distributions, and grain density. Exolith Lab works to keep feedstock as consistent as possible though direct connections with suppliers and changing only when material becomes unavailable or it drastically affects price and there is a suitable alternative readily available, though quantitative analysis on variation of simulant mineralogy and particle size distribution is not performed through time. Information on materials and material sources used in simulants can be requested by contacting Exolith Lab and providing information on when the simulant was purchased. For the most up-to-date information on Exolith Lab simulants, custom simulant

creation, or scientific simulant consultations, please visit the Exolith Lab website (www.exolithsimulants.com).

2.2 Data collection methods

2.2.1 XRF

XRF is an accepted method for the accurate quantification of the bulk elemental composition of geologic materials (e.g., Hooper, 1964) is widely applied to analysis of extraterrestrial material *in situ* (Adler et al., 1972a; Adler et al., 1972b; McKenzie et al., 2020), in laboratories (Rose et al., 1970), and evaluating simulant suitability for testing ISRU and exploration technologies (Isachenkov et al., 2022). Using a method similar to Johnson et al. (1999), the Hamilton Analytical Laboratory (HAL) at Hamilton College performed XRF analysis on Exolith Lab simulants to determine their bulk elemental composition and trace element abundances. These XRF data were acquired using low dilution fused bead method with graphite crucibles. Samples were ground in a tungsten carbide ring mill and the powder was then combined in a 2:1 flux:powder ratio. This mix was then blended and fused in a graphite crucible at 1,000°C. The resulting pellets were cleaned of residual carbon and then reground and refused again at 1,000°C. The surfaces of the doubly fused pellets had their surfaces finished (15 μm surface finish) and cleaned in ethanol. The prepared samples were then analyzed in the Thermo ARL Perform'X spectrometer with an accelerating voltage of 45 kV and 45 mA current. Loss on ignition (LOI) was measured for all samples by heating 15–17 h in silica crucibles at 900 °C. This temperature is chosen to allow any organic matter, carbonates, and other volatiles to be baked off while minimizing the loss of sodium, potassium, and lead, and the duration of heating is chosen to more complete oxidation of iron to a single oxidation state. The differences of the low dilution graphite fusion method include: 1) a single sample allows for major, minor, and trace elements to be analyzed, increasing efficiency without a loss of accuracy; 2) a constant voltage on an Rh target is used to achieve stability and precision for all elements; 3) the oxidation state of iron and the volatile content of the rocks and minerals being analyzed is disregarded, leaving the major element concentrations to be reported as normalized and free of volatiles with all iron expressed as FeO rather than split into Fe_2O_3 and FeO (Johnson et al., 1999). More information on the sample preparation and analysis procedure can be found in Johnson et al. (1999) and at https://www.hamilton.edu/academics/analytical-lab.

2.2.2 XRD

XRD is an analytical technique often used to identify different phases in crystalline materials (Bunaciu et al., 2015) and is hence often used to characterize the different minerals and amorphous material present in rocks and minerals, whether terrestrial or from space such as meteorites (Bland et al., 2004) or returned lunar samples (Taylor et al., 2019). The Engineering and Mining Experiment Station (EMES) at the South Dakota School of Mines and Technology used a Malvern Panalytical Empyrean x-ray diffractometer with a cobalt cathode (λ = 1.79 Å) at 40 kV accelerating voltage and 45 mA current to generate x-ray diffraction patterns for Exolith Lab lunar, Martian, and asteroid simulants. iCore and dCore automated optics using fixed slits approximately 1 cm × 1 cm footprint were normal to the beam and a PIXcel3D detector was operated as a scanning line 1D detector. The samples of simulant were crushed with a ball mill and mixed with 10%–15% corundum as an internal standard for amorphous content determination. Samples were scanned in values of 2θ from 5° to 90° at a rate of 0.3° per second with five iterative rotations and subsequent re-scans of the sample to assist in reducing texture contributions from the wide PSDs of the simulants. Phase identifications are not offered here since Exolith Lab simulants are created using specific proportions of well-documented mineral and rock components so the input mineralogy is known. XRD data presented here are available upon request to allow Exolith Lab and other simulant users to compare the phase compositions before and after working with simulants at extreme temperatures or pressures that cause phase changes such as metal and oxygen extractions. It should be noted that XRD patterns are best when the material being analyzed is of uniform particle size, but Exolith Lab simulants often have particle size ranges that span at least four orders of magnitude (and often more), which lowers overall peak intensity in XRD patterns, potentially rendering phase identification difficult, and even proper sample preparation methods may not fully resolve this. More information on XRD data collection and analysis can be found at https://www.sdsmt.edu/EMES/.

2.2.3 Particle size analysis

The PSDs of Exolith Lab simulants were measured by a CILAS 1190 volumetric particle size analyzer (0.04–2,500 μm detection range) in liquid dispersion mode using deionized (DI) water as the dispersal agent. To analyze simulant samples, the simulant was added to the vibrating dispersal cell and then was pumped to the measurement cell. In the measurement cell, lasers of 640 and 830 nm wavelengths strike incident in the suspended particles and diffract onto detectors. The CILAS 1190 uses the CILAS Size Expert software pipeline to analyze the diffraction patterns of the three independent samples of each simulant being tested, and the volumetric percentages of each size bin, or the density function (q3), and the cumulative distribution (Q3) are calculated for each of the three samples of each simulant. From these samples, the mean of both the density functions and cumulative distributions are calculated with 2σ confidence intervals. From the cumulative distribution, the D10, D30, D50, D60, and D90 particle sizes are calculated along with the span (*s*, Eq. 1) of each distribution. D10 is the particle size at which 10% of the volume of particles in the distribution are smaller than that size, and D30 is the particle size at which 30% of the volume of particles in the distribution are smaller than that particular size, D50 is the median size, D60 is the size at which 60% of the particles are volumetrically smaller, and D90 is the size at which 90% of the particles are volumetrically smaller than that size. These values are also used to calculate the coefficient of uniformity (C_u, Eq. 2) and the coefficient of curvature (C_c, Eq. 3) to serve as another standard metric to describe PSDs as described in ASTM D2487 (ASTM Standard D2487 2017).

$$s = \frac{D90 - D10}{D50} \tag{1}$$

$$C_u = \frac{D60}{D10} \tag{2}$$

$$C_C = \frac{(D30)^2}{D10 \times D60} \tag{3}$$

It should be noted that the binding agent used to produce the pebble-sized asteroid simulants from the powder simulants is soluble in water and the cobbles are relatively weak, so the asteroid simulant PSDs reported here are only representative of the loose powder forms of each asteroid simulant. Comparisons to particle size data from lunar, Martian, and asteroid regolith are not made here, for the same reasons stated before regarding XRF and XRD data: this manuscript serves only to introduce and describe the simulants with rigorous quantitative comparisons recommended for future publications describing the Exolith Lab simulants discussed here.

2.3 Lunar regolith simulants

The lunar regolith is formed from physical and chemical space weathering processes, such as impact gardening and solar irradiation, that break down the lunar bedrock (Hörz et al., 1991). The hard vacuum on the surface of the Moon is a strongly reducing environment, presenting phenomena and compositions that are not observed on Earth (Taylor et al., 2001). The lunar surface can be broken down into two main geologic provinces: the feldspathic lunar highlands which cover 80% of the lunar surface and the basaltic lunar mare (Haskin and Warren, 1991; Spudis and Pieters, 1991; Head and Wilson, 1992; Jolliff et al., 2000). Aside from the lunar highlands and mare, there are more less commonly observed geologic domains including silicic volcanic features that are similar to terrestrial rhyolitic domes (Head and McCord, 1978; Hagerty et al., 2006; Siegler et al., 2023) as well as pyroclastic deposits (Gaddis et al., 2003; Gustafson et al., 2012; Trang et al., 2017). The lunar highlands comprise the original crust formed through differentiation during the formation of the Moon and are dominantly composed of anorthosite and similar lithologies (Crites and Lucey, 2015; Taylor et al., 2019). The lunar mare formed when ancient basaltic magma originating in the lunar mantle ascended, erupted as lava, and flowed to fill topographic lows such as impact basins (Taylor et al., 1991; Head and Wilson, 1992). These two generalized geologic provinces were explored by NASA's Apollo missions which returned samples from highlands, mare, and areas near the contacts between the highlands and mare. The compositions of regolith samples from the margins between the highlands and mare show intermediate compositions that indicate mixing of the regolith from both provinces (e.g., Heiken and McKay, 1974), with material being transported as impact ejecta and subsequently impact gardened. Renewed efforts from organizations across the globe, including government space agencies, private companies, and more, aim to explore the lunar surface and establish permanent infrastructure, with the initial target being the lunar south pole. The south pole is shown to have a highlands-like composition (Lemelin et al., 2022) and contains some of the purest anorthosites (nearly 100% plagioclase) on the lunar surface (Ohtake et al., 2009). From the lunar south pole, crewed and autonomous activities will extend north and include various mare terranes, including KREEP mare basalts that are enriched in valuable and useful elements such as potassium (K), rare earth elements (REE), uranium, thorium, and phosphorus (P) (Carlson and Lugmair, 1979; Wieczorek and Phillips, 2000). With this renewed interest in sustained human and robotic presence on the lunar surface, technologies must be researched, developed, and tested using appropriate simulants on Earth to leverage the various compositions of the lunar regolith to maximize the safety and efficiency of various lunar systems.

Exolith Lab produces two main lunar regolith simulants that are designed to approximate the mineralogy and particle geometries of the lunar highlands and lunar mare regolith: LHS-1 (Figure 1A) simulates the lunar highlands, and LMS-1 (Figure 1B) simulates the lunar mare. Both of these simulants have a maximum particle size of 1,000 μm. Two "dusty" versions of each of these simulants are also offered, dubbed LHS-1D (Figure 1C) and LMS-1D (Figure 1D), and these have maximum particle sizes of ~35 μm ("clay" to "coarse silt" when classified by the Wentworth scale) and the same mineralogic composition of LHS-1 and LMS-1, respectively. The mineralogy of LHS-1 (and therefore LHS-1D) is based on the 90 to 1,000 μm portion of the particle size distribution of Apollo sample 67,461 (Simon et al., 1981), whereas LMS-1 (and therefore LMS-1D) was created based on Apollo sample 24,999 (Simon et al., 1981). As shown in Long-Fox et al. (2023), the PSD of LHS-1 and LMS-1 align well with "key" returned samples from the lunar highlands and mare, respectively, identified in the *Lunar Soils Grain Size Catalog* (Graf, 1993). LHS-1D and LMS-1D are designed to mimic the chemistry and mechanics of the finest portions of the lunar highlands and mare regolith and are manufactured by ball milling the "parent" LHS-1 and LMS-1 simulants. The clay/coarse silt-sized particles that make up LHS-1D and LMS-1D have high surface area to volume ratios, and as such, LHS-1D and LMS-1D are prone to electrostatic clumping (as seen at the base of the piles of simulant in Figures 1C, D) and other electrostatic and atmospheric effects that are not observed in LHS-1 and LMS-1 (Easter et al., 2022; Madison et al., 2022; Millwater et al., 2022).

2.4 Martian regolith simulants

The Martian regolith is produced by dynamic geologic processes, both past and present, including meteoritic impacts, eolian and fluvial processes, and volcanic activity (McCauly, 1973; Malin and Edgett, 2000; Murchie et al., 2009). Remote sensing observations indicate a global basaltic crust (McSween et al., 2009) that is processed into a globally distributed basaltic regolith (Yen et al., 2005), and three of the seven sites that have been directly sampled *in situ* by landers or rovers show similar basaltic mineralogy and bulk elemental compositions (Yen et al., 2013) with site-specific enrichments in other compositions (e.g., different volcanic and alteration products). It can be assumed that variation from this apparent global basaltic composition is driven by local geologic and environmental processes. The fine particles in the Martian regolith are lofted through various processes and entrained in atmospheric pressure systems that, just like on Earth, distribute these particles around the planet (Toon et al., 1977). The Rocknest site within Gale crater, the most well-characterized regolith on the Martian surface (Bish et al., 2013; Blake et al., 2013; Leshin et al., 2013; Achilles et al., 2017; Sutter et al., 2017), is composed of atmospherically distributed dust, and therefore can be expected to serve as a global average for the composition of the Martian regolith, despite the relative sulfur enrichment of the Curiosity landing region. The similarity of the

Rocknest regolith to the regolith of other landing sites makes it suitable to serve as the basis for mineralogically accurate Martian regolith simulants (Cannon et al., 2019).

Exolith Lab produces four Martian regolith simulants, all based on the Rocknest regolith with some supplementary contribution from remote sensing observations (e.g., Baird et al., 1976; Poulet et al., 2008). MGS-1 (Figure 1E) is the base simulant for the rest of the Martian simulants that Exolith Lab offers and was created to simulate Rocknest (Cannon et al., 2019) and hence the expected global average Martian regolith. The other Martian regolith simulants, MGS-1C (Figure 1F), MGS-1S (Figure 1G), and JEZ-1 (Figure 1H) use MGS-1 as the base component but add other mineral phases such as clay minerals and alteration products to simulate different areas of the Martian surface. MGS-1C is a modified version of MGS-1 that maintains the basaltic base component (plagioclase, olivine, and pyroxenes) but use enriched in clay minerals to simulate a clay-rich Noachian regolith. Due to the high-clay content, MGS-1C has a smaller median particle size than the rest of the Exolith Lab Martian regolith simulants. MGS-1S also maintains the root Rocknest-like composition but is amended with sulfate-rich minerals to mimic regolith found in a hydrothermally active zones on the Martian surface. Finally, JEZ-1 is the Exolith Lab simulant that approximates the expected mineralogy of Jezero crater, the site being sampled by NASA's Mars Sample Return mission that has strong mineralogical and geomorphic indications of a dynamic fluvial and lacustrine past (Horgan et al., 2020). Due to the inclusion of secondary minerals beyond the base MGS-1 composition, MGS-1C, MGS-1S, and JEZ-1 have PSDs that are multi-modal with the non-crystalline silicate phases being of larger grain size (~10–1,000 μm) and the additional, weathered/altered phases being a distinct smaller size fraction (~2–11 μm).

2.5 Asteroid regolith simulants

Asteroids, relative to other planetary bodies, are primitive objects that provide information on the nebula from which they formed, the materials that planets formed from and subsequently differentiated, cratering processes, space weathering processes (e.g., Clark et al., 2002), cratering, thermal and aqueous alteration (Keil, 2000), and general regolith formation (Housen et al., 1979; Delbo et al., 2014), and they are also of interest for developing space-based economies and resource utilization systems (Metzger et al., 2013; Mueller et al., 2016; Pohl and Britt, 2017; Mardon and Zhou, 2019; Nadoushan et al., 2020; Srivastava et al., 2023). Asteroids are too small to have atmospheres and also too small to drive internal heat generation processes after the earliest period of Solar System accretion (Housen et al., 1979) so it can be assumed that any regolith present is formed from thermal disintegration, irradiation, collisional events with impactors ranging in size from micrometeorites to other asteroids, and aqueous alteration (Housen et al., 1979; Housen and Wilkening, 1982; Clark et al., 2002; Che and Zega, 2023). A group of asteroids of great scientific and resource-based interest are the C-complex asteroids, which are thought to include some of the most primitive bodies in the Solar System and the source of the well-characterized carbonaceous chondrite meteorites (Johnson and Fanale, 1973; Rivkin, 2012). This group includes subtypes which are close in chemical composition to the Sun and the primitive solar nebula and often have water- and other volatile-enriched minerals (Brearley, 2006; King et al., 2015). The C-complex asteroids contain carbon in addition to phyllosilicates, oxides, and sulfides (Brearley, 2006), and the CI (volatile-rich), CM (moderately enriched in volatiles), and CR (lesser volatile enrichment) carbonaceous chondrites serve as the best source of information on the mineralogy of these volatile-rich asteroid materials (Britt et al., 2019). Understanding the mineralogies and volatile content that are anticipated on the surface of asteroids, and how these parameters drive spectral and physical/thermophysical properties, is key to developing asteroid focused resource and exploration technologies.

Exolith Lab produces three standardized asteroid regolith simulants, based on the mineralogy and physical properties of the carbonaceous chondrites (Britt et al., 2019): CI-V2 (Figure 1I), CM-V2 (Figure 1J), and CR-V2 (Figure 1K). The nomenclature for these simulants deviates from other Exolith Lab naming schemes so that the simulants are not implied to simulate differing degrees of aqueous alteration, such as "CM2". As outlined in Britt et al. (2019), the CI-V2 simulant is based on the mineralogy of the CI chondrite group, specifically the well-characterized Orgueil (Bland et al., 2004), CM-V2 is designed based on the Murchison meteorite (Howard et al., 2009), and CR-V2 is based on the average of five Antarctic CR chondrites (PCA 91082, LAP 02342, QUE 99177, and GRA 06100). It should be noted that the asteroid regolith simulants presented here are created using the "future update" compositions (hence the "V2" designations), rather than the "prototype" compositions given in Britt et al. (2019). Some mineralogical components of the meteorites, such as the Fe-rich serpentine cronstedtite and tochinilite are not common on Earth, so other phyllosilicates (the non-asbestiform, Mg-rich serpentines antigorite or lizardite) and sulfates are used. Each of CI-V2, CM-V2, and CR-V2 are offered, as denoted by Britt et al. (2019), as "dry powder" [≤1,000 μm; coarse sand or finer by Wentworth (1922)] or "cobble" [variable sizes; coarse pebbles or finer by Wentworth (1922)] mixes. The "dry" mixes are simply mixes of the different mineral constituents, processed to size as needed, then mixed together and packaged. These pebble-sized (Wentworth, 1922) simulants are intended to mimic the coherent strength of the pebbles on asteroid surfaces and rubble pile asteroids (Britt et al., 2019) and are produced by binding the finer (coarse sand) mix particles together. For CI-V2, a 1:4 ratio of water to dry mix (by mass) is created and air dried. The resulting solid material, bound together by the clays, loses all added water upon drying and matches strength measurements from CI chondrites (Britt et al., 2019; Metzger et al., 2019; Pohl and Britt, 2020). CM-V2 and CR-V2 have considerably lower clay content that CI-V2, so to make the relatively stronger pebbles from these two dry mixes, sodium metasilicate pentahydrate is dissolved in water, and this solution is mixed in a similar 1:4 ratio as the CI-V2 water binding process, then cured in a block-shaped mold at ~75°C. When stronger pebble-sized aggregates are desired, the concentration of sodium metasilicate can be increased. It has been shown that most of the water added is outgassed during curing and that the sodium metasilicate increases the SiO_2 and Na_2O content of the simulant

TABLE 1 Mineralogical compositions in mass percentages of Exolith Lab lunar regolith simulants LHS-1, LMS-1, LHS-1D, and LMS-1D.

Component	LHS-1 wt%	LMS-1 wt%	LHS-1D wt%	LMS-1D wt%
Anorthosite	74.4	19.8	74.4	19.8
Glass-rich basalt	24.7	32.0	24.7	32.0
Ilmenite	0.4	4.3	0.4	4.3
Olivine	0.2	11.1	0.2	11.1
Pyroxenite (bronzitite)	0.3	32.8	0.3	32.8

TABLE 2 Bulk chemistry of major and minor elements, in equivalent oxides, of the Exolith Lab lunar, Martian, and asteroid regolith simulants as measured by fused bead XRF and the measured loss on ignition (LOI) for each simulant.

Oxide	LHS-1 wt%	LMS-1 wt%	LHS-1D wt%	LMS-1D wt%	MGS-1 wt%	MGS-1C wt%	MGS-1S wt%	JEZ-1 wt%	CI-V2 wt%	CM-V2 wt%	CR-V2 wt%
SiO_2	49.12	48.22	48.67	47.42	43.90	43.83	32.60	38.57	26.44	28.19	36.54
Al_2O_3	26.29	12.40	26.23	14.02	12.84	10.42	9.59	7.87	4.31	3.64	2.43
CaO	13.52	7.65	13.41	8.26	7.91	9.13	21.39	5.39	2.61	3.14	1.89
Na_2O	2.55	1.73	2.51	1.72	1.49	1.48	1.08	0.96	0.09	1.43	1.64
FeO*	3.20	8.79	3.73	8.74	10.60	7.34	7.79	8.34	23.24	13.39	27.62
MgO	2.86	15.97	2.66	14.91	14.81	13.47	11.51	26.96	24.04	30.61	25.18
MnO	0.06	0.2	0.06	0.18	0.112	0.09	0.087	0.10	0.06	0.04	0.16
TiO_2	0.63	2.70	0.70	2.68	0.46	0.39	0.361	0.29	0.41	0.26	0.14
K_2O	0.34	0.42	0.37	0.39	0.29	1.44	0.32	0.35	0.49	0.03	0.15
P_2O_5	0.17	0.23	0.17	0.20	0.17	0.14	0.125	0.10	0.14	0.10	0.05
LOI	0.41	0.56	0.46	0.48	4.90	10.38	10.76	8.79	16.08	16.86	1.34
Total	99.15	98.87	98.97	99.00	97.48	98.11	95.61	97.73	97.90	97.69	97.14

*Cumulative FeO and Fe_2O_3. The fused bead XRF, methodology does not allow for determination of relative amounts of Fe_2O_3 and FeO so total iron content is reported as FeO.

by less than 2 wt% (Britt et al., 2019). The particle size distribution and range of the pebble-sized simulant varies from batch to batch and is able to be customized per customer needs.

3 Results and discussion

3.1 Lunar regolith simulants

3.1.1 Mineralogy and implications

Since mineralogical accuracy is a cornerstone of the Exolith Lab design philosophy, lunar simulant mineralogy (Table 1) is based on returned samples of a lunar regolith. LHS-1, a lunar highlands simulant is dominantly felsic in nature, mimicking pristine sample mineralogy around the Apollo 16 landing site in the equatorial intercrater highlands as well as around the lunar south pole, the region of interest for of NASA's Artemis program and related missions around the world. LHS-1D has the same mineralogical makeup as LHS-1 just with a reduced particle size, so it is also a mineralogically accurate lunar highlands dust simulant. LMS-1, the Exolith Lab lunar mare simulant, was developed to mimic the mineralogy of pristine and representative returned samples from the lunar mare. Likewise, LMS-1D is a mineralogically accurate lunar mare dust simulant with fidelity inherited from LMS-1.

3.1.2 XRF analysis applications and implications

Knowledge of the bulk elemental composition of lunar regolith simulants used to test technologies such as molten regolith electrolysis (MRE) and sintering in Earth-based laboratories is critical to predicting the performance of the technology on the lunar surface (Sibille et al., 2009; Humbert et al., 2022). Despite the inherent differences in the chemical properties of simulants and lunar regolith (Isachenkov et al., 2022), a mineralogically and geochemically accurate simulant is required to properly develop lunar systems. Once a quantitative understanding of a given lunar ISRU process is established in the lab, the differences in the chemistry of the simulant and actual lunar regolith will be able to be modeled and the system adapted to function more efficiently once deployed on the Moon. Considering this, the elemental abundances of major and minor element equivalent oxides detected by XRF of Exolith Lab lunar regolith simulants produced in February 2023 (and are not expected to undergo any feedstock changes in the coming years) are given in Table 2 and trace

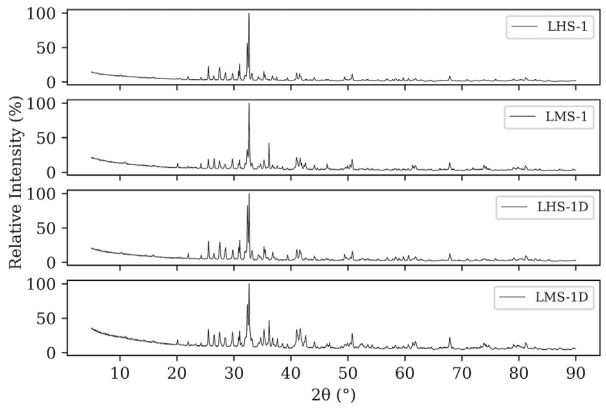

FIGURE 3
X-ray diffraction patterns of Exolith Lab lunar regolith simulants LHS-1, LMS-1, LHS-1D, and LMS-1D obtained using a cobalt cathode with a 2θ wavelength (λ) of 1.79 Å.

element concentrations for these simulants are given in Supplementary Material.

3.1.3 XRD analysis applications and implications

Mineralogy controls the physical and chemical properties of geologic materials, hence having data to characterize the phases present in lunar regolith and lunar simulants allows for better understanding of challenges and requirements for resource prospecting, acquisition, processing, and utilization as well as comparisons between data from surface operations and from in-lab testing. See Long-Fox et al. (2023) for a tabular comparison of the composition of Exolith Lab LHS-1 and LMS-1 simulant versus lunar highlands and mare regolith. The phases present in lunar regolith and lunar regolith simulants, including volcanically-derived glasses, (simulated) agglutinates, and impact melts (in the case of actual lunar regolith) will affect the mechanical strength of the regolith or simulant and how it behaves in high-temperature processes such as microwave or solar sintering and MRE. Since mineralogy underpins every interaction with lunar regolith and its simulants, characterization of the phases present is essential to developing and understanding of how to best develop technologies to leverage local resources on the lunar surface. Therefore, XRD patterns of Exolith Lab lunar regolith simulants LHS-1, LMS-1, LHS-1D, and LMS-1D are given in Figure 3 and data files (2θ angle and counts) are available upon request to the corresponding author.

3.1.4 Particle size analysis applications and implications

Particle size distributions and ranges are a major contributing factor in the geomechanical properties of lunar regolith and its simulants, so technologies developed involving lunar material transport, flow, storage, and processing need to consider particle size range and particle size distribution as a key parameter in testing. The combination of mineralogical accuracy and sample-based (Graf, 1993) particle sizes and particle size distributions of Exolith Lab's LHS-1 and LMS-1 simulants makes them appropriate for terrestrial research and development of lunar resource acquisition, transport, and processing systems (Isachenkov et al., 2022; Long-Fox et al., 2023). The particle size cumulative distribution and density function (both with 2σ confidence intervals) for these specific batches of LHS-1, LMS-1, LHS-1D, and LMS-1D produced in February 2023 are given in Figure 4 and the D10, D30, D50, D60, and D90 percentile values and corresponding distribution spans and uniformity and curvature coefficients are given in Table 3.

3.2 Martian regolith simulants

3.2.1 Mineralogy and implications

The Exolith Lab design philosophy starts with mineralogy, hence MGS-1, MGS-1C, MGS-1S, and JEZ-1 are all based on *in situ* data from Rocknest in Gale crater with some adaptations based on remote sensing data (Cannon et al., 2019). MGS-1 was created to be a global average simulant for Martian regolith in geochemical and geomechanical testing of Martian exploration and infrastructure development systems (Cannon et al., 2019), though it should be noted that the composition of MGS-1 was updated slightly from the original compositions given in Cannon et al. (2019). Since MGS-1C, MGS-1S, and JEZ-1 all use MGS-1 as the base material, remote sensing data was used to provide constraints for each of these simulant constituents beyond the base MGS-1 formula (e.g., Baird et al., 1976; Poulet et al., 2008). The basaltic mineral content (plagioclase, olivine, pyroxenes) was scaled accordingly to simulate localized alterations superimposed onto the base basaltic component. The mineralogical compositions of MGS-1, MGS-1C, MGS-1S, and JEZ-1 produced in February 2023 with no feedstock changes expected over the next few years are given in Table 4.

3.2.2 XRF analysis applications and implications

The bulk elemental composition of a Martian regolith simulant is key information to be considered when designing systems to utilize the Martian regolith for processes such as oxygen and metal extraction, agriculture systems, and other infrastructure. Just as with lunar regolith and lunar regolith simulants described in this work, there are inherent differences in the chemical properties of the Martian regolith and its simulants due to the simulant material being terrestrially derived. Given these differences, thorough investigations must be performed to understand and optimize Martian regolith resource utilization. Before this predictive analysis can happen for the research and development of Martian SRU and exploration systems, testing must first be done in the lab using appropriate simulants. Given the importance of knowing elemental abundances of a simulant for testing across a variety of disciplines, the abundances of major element equivalent oxides of Exolith Lab Martian regolith simulants MGS-1, MGS-1C, MGS-1S, and JEZ-1 detected by XRF are given in Table 2, and the trace element data are given in Supplementary Material.

3.2.3 XRD analysis applications and implications

The mineralogic composition of Martian regolith is highly complex due to the dynamic processes that have been, or are still, active on the Martian surface (Yen et al., 2005; Poulet et al., 2008; Murchie et al., 2009; Bish et al., 2013). Martian regolith simulants must reasonably match the phase compositions measured from robotic sampling operations performed on Mars

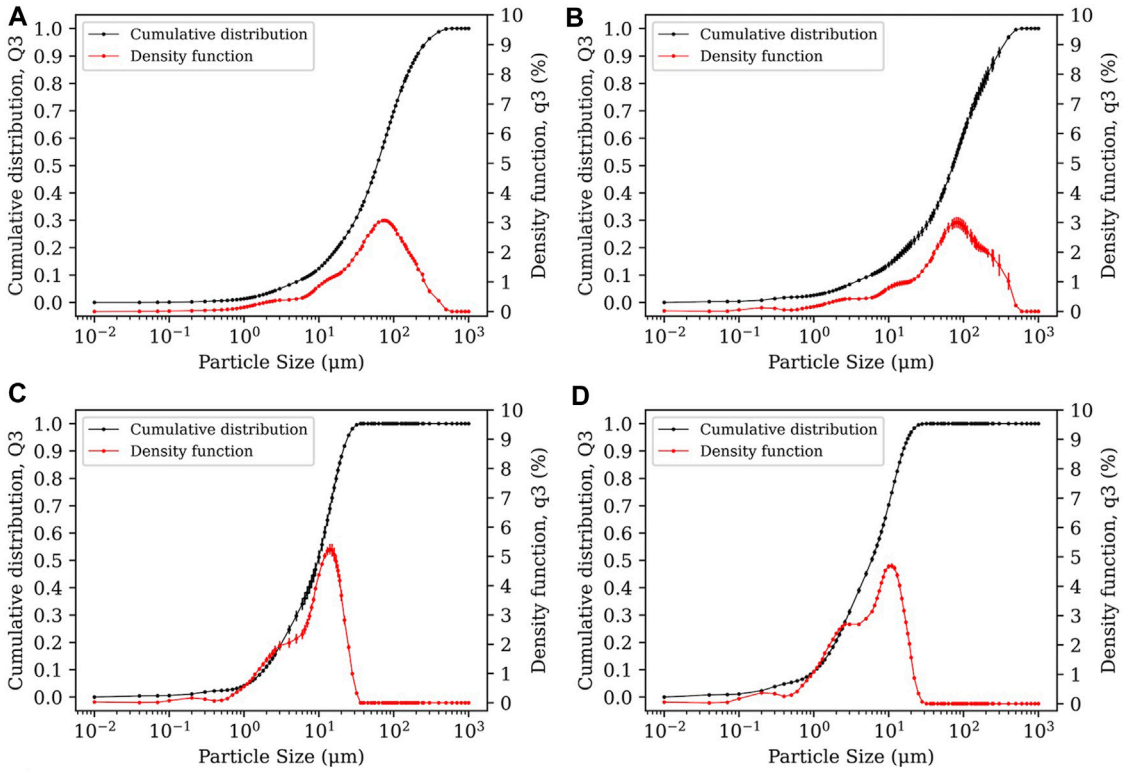

FIGURE 4
Particle size distribution plots of **(A)** LHS-1, **(B)** LMS-1, **(C)** LHS-1D, and **(D)** LMS-1D showing the mean cumulative distribution (Q3) and the density function (q3) of the samples tested with 2σ error bars.

TABLE 3 Percentile values, spans, and gradation coefficients (C_u and C_c) of the particle size distributions of LHS-1, LMS-1, LHS-1D, and LMS-1D lunar regolith simulants.

Quantity	LHS-1	LMS-1	LHS-1D	LMS-1D
D10 (μm)	7.61	5.82	1.85	1.07
D30 (μm)	30.64	35.31	5.08	2.88
D50 (μm)	59.79	72.27	9.74	5.92
D60 (μm)	77.60	95.31	11.94	7.91
D90 (μm)	202.35	282.47	21.06	15.58
Span (dimensionless)	3.26	3.83	1.97	2.45
C_u (dimensionless)	10.20	16.38	6.45	7.39
C_c (dimensionless)	1.59	2.25	1.17	0.98

(Cannon et al., 2019). The high mineralogical diversity of Mars means that there are many different rocks and minerals that can be used in construction and resource extraction for human and autonomous infrastructure development and habitation on Mars, each having a unique set of use cases. Having quantitative data for compositional phases of Martian regolith simulants used in the research and development of Martian-aimed technologies gives the ability to compare and contrast Martian ISRU process sensitivities to compositional variations and hence predict best methodologies for use in flight missions (Cannon et al., 2019). XRD patterns for Martian regolith simulants MGS-1, MGS-1C, MGS-1S, and JEZ-1 are shown in Figure 5 and the data files (2θ angle and counts) are available upon request from the corresponding author.

3.2.4 Particle size analysis applications and implications

As previously stated, the particle size distribution of planetary regolith and simulants are dominant factors that determine the geomechanical properties of the simulant and also affects chemical and thermal processing; this, of course, is also true for Martian regolith simulants. The cumulative distribution and density function (with 2σ confidence intervals) for MGS-1, MGS-1C, MGS-1S, and JEZ-1 are shown graphically in Figure 6 with, and the D10, D30, D50, D60, and D90 percentile values, spans, and coefficients of uniformity and curvature are given in Table 5.

3.3 Asteroid regolith simulants

3.3.1 Mineralogy and implications

Exolith Lab uses mineralogy as the basis of its asteroid simulants, so the mineralogy of Orgueil (Bland et al., 2004), Murchison (Bland et al., 2004), and Antarctic meteorites PCA 91082, GRA 95229, LAP 02342, QUE 99177, GRA 06100 (Howard et al., 2015) are used as reference materials for CI-V2, CM-V2, and CR-V2, respectively, with CR-V2 being based on the Antarctic CRs. As previously stated, the unique mineralogies of asteroids compared to the relatively

TABLE 4 Mineralogical compositions in mass percentages of Exolith Lab Martian regolith simulants MGS-1, MGS-1C, MGS-1S, and JEZ-1.

Component	MGS-1 wt%	MGS-1C wt%	MGS-1S wt%	JEZ-1 wt%
Anhydrite	1.7	1.0	1.0	1.0
Anorthosite	27.1	16.4	16.4	16.0
Fe-carbonate (siderite)	1.4	0.8	0.8	0.8
Ferrihydrite	3.5	2.1	2.1	2.1
Glass-rich basalt	22.9	13.7	13.7	13.5
Gypsum	0.0	0.0	40.0	0.0
Hematite	0.5	0.3	0.3	0.3
Hydrated silica	3.0	1.8	1.8	1.8
Magnetite	1.9	1.1	1.1	1.1
Mg-carbonate	0.0	0.0	0.0	11.0
Mg-sulfate (epsomite)	4.0	2.4	2.4	2.4
Olivine	13.7	8.2	8.2	32.0
Pyroxenite (bronzitite)	20.3	12.2	12.2	12.0
Smectite (montmorillonite)	0.0	40.0	0.0	6.0

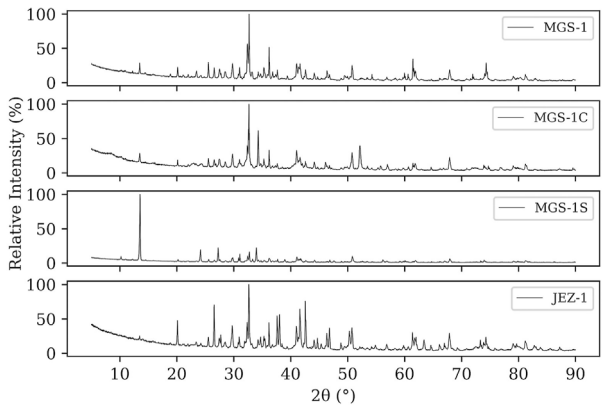

FIGURE 5
X-ray diffraction patterns of Exolith Lab Martian regolith simulants MGS-1, MGS-1C, MGS-1S, and JEZ-1 obtained using a cobalt cathode with a 2θ wavelength (λ) of 1.79 Å.

evolved and oxidized materials on Earth, are not always able to be replicated and substitutions had to be made (e.g., Mg-serpentine substituting for Fe-serpentine). These substitutions that deviate from the expected compositions of asteroidal regolith are judged to be reasonable given the trades and sacrifices of fidelity involved in using a cost-effective, open-source approach to produce large amounts of simulant (Britt et al., 2019). The formulae given in Table 6 for CI-V2, CM-V2, and CR-V2 are the "future updates" referred to in Britt et al. (2019).

3.3.2 XRF analysis applications and implications

Just as with lunar and Martian regolith simulants, the bulk elemental composition of an asteroid regolith simulant must be reasonably accurate to the regolith being simulated to serve as appropriate materials for the testing of various space resource chemical processing systems (Britt et al., 2019; Metzger et al., 2019). Since the exact composition of planetary regolith is impossible to perfectly recreate from terrestrial materials (which are generally enriched in Mg and Al with lesser amounts of Fe), any differences must be quantified and accounted for, which is recommended to be the subject of future publications. For Exolith Lab asteroid regolith simulants, one of the main differences between asteroid regolith and the simulant is the use of Mg-rich, non-asbestiform serpentines as opposed to the Fe-rich cronstedtite (not widely available) and Fe-rich tochilinite (not widely available) being substituted for other Fe-rich compounds such as iron powder. This relative depletion in Fe and enrichment in Mg, while not ideal, offers the best constrained maximization approximation of asteroidal materials while maintaining product availability, safety, and fidelity (Britt et al., 2019). The abundances of major elements in CI-V2, CM-V2, and CR-V2, detected by fused-bead XRF, are given in Table 2 and the trace element concentrations are given in Supplementary Material.

3.3.3 XRD analysis applications and implications

Asteroid regolith is mineralogically complex, and even though asteroids are some of the most primitive bodies in the Solar System and give unique views into Solar System and planetary formation, they are generally modified through radiation bombardment, impacts, and sometimes aqueous alteration. The degree and type of space weathering experienced by asteroids determines how the original mineralogy was altered, and knowledge of phases (altered and unaltered, glassy and crystalline) present in asteroid regolith can provide information on resource potential and on what is required for safe and efficient resource acquisition and extraction processes, anchoring, traversal, excavation, and processing. Such knowledge must be gained in the laboratory using appropriate simulants in research and development (Metzger et al.,

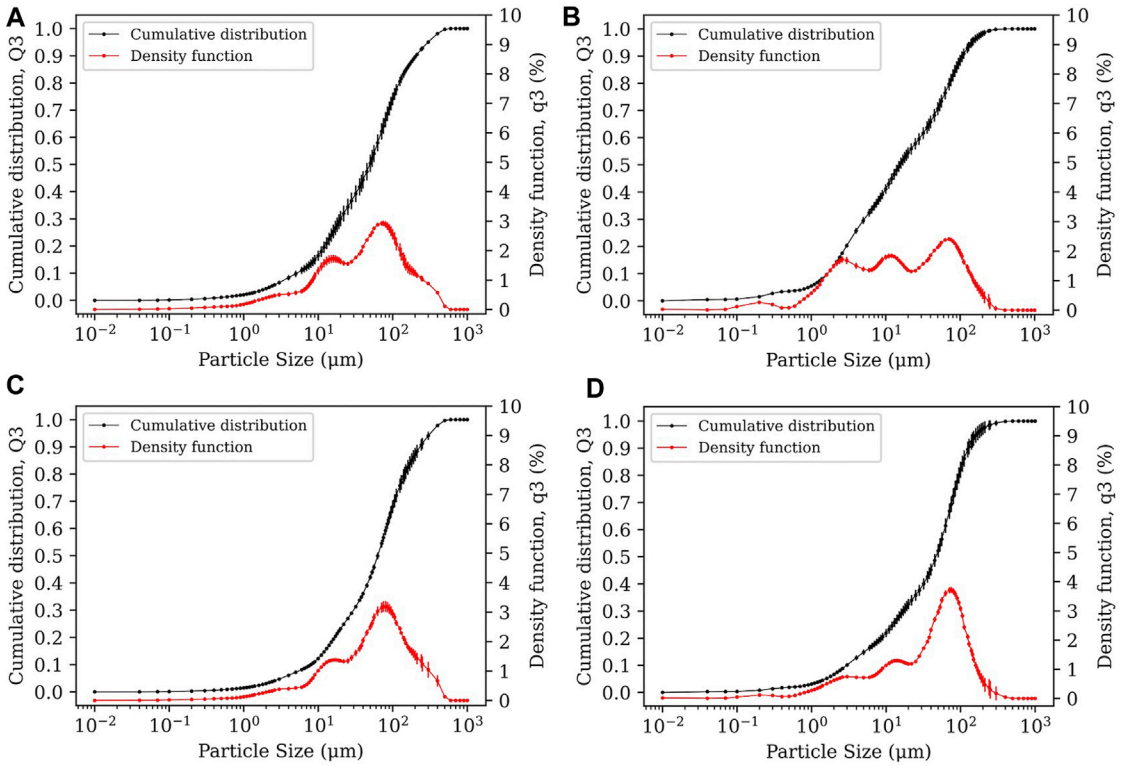

FIGURE 6
Particle size distribution plots of **(A)** MGS-1, **(B)** MGS-1C, **(C)** MGS-1S, and **(D)** JEZ-1 showing the mean cumulative distribution (Q3) and the density function (q3) of the samples tested with 2σ error bars.

TABLE 5 Percentile values, spans, and gradation coefficients (C_u and C_c) of the particle size distributions of MGS-1, MGS-1C, MGS-1S, and JEZ-1 Martian regolith simulants.

Quantity	MGS-1	MGS-1C	MGS-1S	JEZ-1
D10 (μm)	5.19	1.64	7.99	2.97
D30 (μm)	19.96	5.16	29.89	16.91
D50 (μm)	49.30	15.50	63.13	46.92
D60 (μm)	66.85	28.98	81.61	60.99
D90 (μm)	205.48	107.48	233.17	127.27
Span (dimensionless)	4.06	6.83	3.57	2.65
C_u (dimensionless)	12.88	17.67	10.21	20.53
C_c (dimensionless)	1.15	0.56	1.37	1.58

2019). Since the mineralogy is so vital to consider when designing and testing hardware and planning flight missions to interact with asteroids (Britt et al., 2019; Metzger et al., 2019), Exolith Lab asteroid regolith simulants CI-V2, CM-V2, and CR-V2 XRD patterns are given in Figure 7 with data files available upon request from the corresponding author. These data allow Exolith Lab asteroid regolith simulant users to compare results of testing resource acquisition and processing systems that involve elevated temperatures or pressures that may alter the mineralogy of the regolith to get a better understanding of process variation and efficiency.

TABLE 6 Mineralogical compositions in mass percentages of Exolith Lab asteroid regolith simulants CI-V2, CM-V2, and CR-V2.

Component	CI-V2 wt%	CM-V2 wt%	CR-V2 wt%
Amorphous silicate	0.0	0.0	9.6
Fe-carbonate (siderite)	0.0	1.0	0.0
Ferrihydrite	4.8	0.0	0.0
Fe metal powder	0.0	0.0	10.6
Magnetite	10.0	5.0	2.5
Mg-serpentine	51.3	73.8	6.8
Olivine	7.0	11.2	33.1
Palygorskite	5.3	0.0	0.0
Pyrite	7.0	3.3	5.8
Pyroxeneite (bronzitite)	0.0	2.1	29.6
Sub-bituminous coal	5.0	3.6	2.0
Vermiculite	9.6	0.0	0.0

3.3.4 Particle size analysis and implications

The particle size distribution of asteroid regolith simulants is a key property that, like any planetary regolith simulant, affects the geomechanical and thermophysical properties of the simulant.

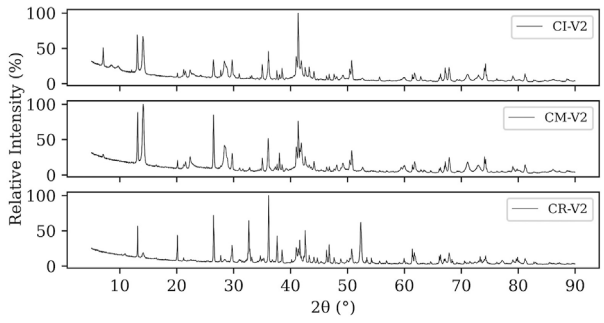

FIGURE 7
X-ray diffraction patterns of Exolith Lab asteroid regolith simulants CI-V2, CM-V2, and CR-V2 obtained using a cobalt cathode with a 2θ wavelength (λ) of 1.79 Å.

TABLE 7 Percentile values, spans, and gradation coefficients (C_u and C_c) of the particle size distributions of CI-V2, CM-V2, and CR-V2 asteroid regolith simulants.

Quantity	CI-V2	CM-V2	CR-V2
D10 (μm)	7.10	5.30	13.71
D30 (μm)	26.67	22.37	48.12
D50 (μm)	48.63	48.21	74.26
D60 (μm)	59.52	63.08	89.21
D90 (μm)	108.36	172.30	251.79
Span (dimensionless)	2.08	3.46	3.21
C_u (dimensionless)	8.38	11.90	6.51
C_c (dimensionless)	1.68	1.50	1.89

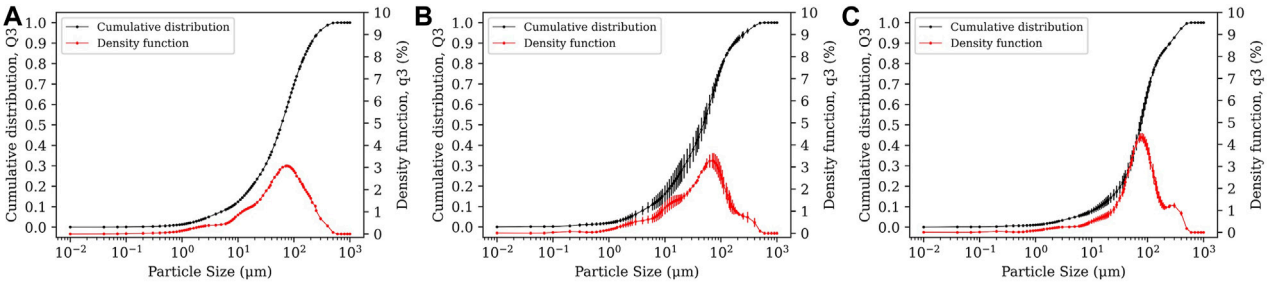

FIGURE 8
Particle size distribution plots of **(A)** CI-V2, **(B)** CM-V2, and **(C)** CR-V2 showing the mean cumulative distribution (Q3) and the density function (q3) of the samples tested with 2σ error bars.

Asteroids themselves are composed of particles from the sub-μm scale to large boulders (e.g., Burke et al., 2021), and as such, CI-V2, CM-V2, and CR-V2 are offered in both powder and a larger pebble-sized (Wentworth, 1922) form, as previously discussed here and in Britt et al. (2019). The laser-based volumetric particle size analysis performed here breaks up the pebbles, so the cumulative distribution and density functions shown in Figure 8 with 2σ confidence intervals and the D10, D30, D50, D60, and D90 percentile values, spans, and gradation coefficients given in Table 7 are only representative of the powder form of each Exolith Lab asteroid regolith simulant. Custom size orders can be placed for pebble-sized simulants if desired by contacting Exolith Lab.

4 Conclusion

Presented here are, at the time of writing, the most up-to-date data on the composition and particle size distributions of Exolith Lab lunar, Martian, and asteroid regolith simulants. Exolith Lab produces lunar, Martian, and asteroid regolith simulants in a constrained optimization of fidelity, safety, and product availability. The design philosophy used in the creation and large-scale production of all Exolith Lab simulants is to start with accurate mineralogy (based on returned samples and/or remote sensing data) and process feedstock to appropriate particle size ranges using industry standard rock and mineral handling equipment. Note that material sources, PSDs, and overall simulant compositions are subject to change due to supplier changes, source material changes, processing equipment changes, or new data that provides improved insights into lunar, Martian, or asteroid regolith. It should also be noted that the PSDs and mineralogic compositions of Exolith Lab simulants may vary from batch to batch and the data provided here are from simulants produced in February 2023. Any of the Exolith Lab simulants are able to be customized to order through free scientific consultation that can be booked at https://www.exolithsimulants.com or sending an email to exolithlab@ucf.edu. Please contact Exolith Lab (HYPERLINK "mailto:exolithlab@ucf.edu" \o "mailto:exolithlab@ucf.edu"exolithlab@ucf.edu or https://www.exolithsimulants.com) for more information on specific simulant batches for the most accurate data available for the given production run.

Data availability statement

The original contributions presented in the study are included in the article/Supplementary Material, further inquiries can be directed to the corresponding author.

Author contributions

JL-F: Conceptualization, Data curation, Formal Analysis, Methodology, Software, Visualization, Writing–original draft,

Writing–review and editing, Investigation. DB: Conceptualization, Funding acquisition, Investigation, Project administration, Resources, Supervision, Writing–review and editing.

Funding

This work was supported by the NASA Solar System Research Virtual Institute (SSERVI) Center for Lunar and Asteroid Surface Science (CLASS) through NASA Cooperative Agreement 80NSSC19M0214.

Acknowledgments

Special thanks go to Dr. Edward Duke and Dr. Jacob Petersen at the South Dakota School of Mines and Technology Engineering and Mining Experiment Station; to Dr. Zach Osborne and Dr. Brandi Langsdorf at the Hamilton College Hamilton Analytical Laboratory. The authors would also like to express our sincerest gratitude to the reviewers for offering kind and useful suggestions that greatly helped improve this manuscript.

Conflict of interest

The authors declare that the research was conducted in the absence of any commercial or financial relationships that could be construed as a potential conflict of interest.

Publisher's note

Supplementary material

The Supplementary Material for this article can be found online at: https://www.frontiersin.org/articles/10.3389/frspt.2023.1255535/full#supplementary-material

References

Achilles, C. N., Downs, R. T., Ming, D. W., Rampe, E. B., Morris, R. V., Treiman, A. H., et al. (2017). Mineralogy of an active eolian sediment from the Namib dune, Gale crater, Mars. *J. Geophys. Res.* 112, 2344–2361. doi:10.1002/2017JE005262

Adler, I., Trombka, J., Gerard, J., Scmadebeck, R., Lowman, P., Blodget, H., et al. (1972a). Apollo 15 geochemical X-ray fluorescence experiment: preliminary report. *Science* 172, 436–440. doi:10.1126/science.175.4020.436

Adler, I., Trombka, J., Gerard, J., Scmadebeck, R., Lowman, P., Blodget, H., et al. (1972b). Apollo 16 geochemical X-ray fluorescence experiment: preliminary report. *Science* 177, 256–259. doi:10.1126/science.177.4045.256

ASTM Standard D2487 (2017). *Standard practice for classification of Soils for engineering purposes (unified soil classification system)*. West Conshohocken, PA: ASTM International.

Baird, A. K., Toulmin, P., Clark, B. C., Rose, H. J., Keil, K., Christian, R. P., et al. (1976). Mineralogic and petrologic implications of viking geochemical results from Mars: interim report. *Science* 194, 1288–1293. doi:10.1126/science.194.4271.1288

Bish, D. L., Blake, D. V., Vaniman, D. T., Chipera, S. J., Morris, R. V., Ming, D. W., et al. (2013). X-ray diffraction results from Mars science laboratory: mineralogy of rocknest at Gale crater. *Science* 341, 1238932. doi:10.1126/science.1238932

Blake, D. F., Morris, R. V., Kocurek, G., Morrison, S. M., Downs, R. T., Bish, D., et al. (2013). Curiosity at Gale crater, Mars: characterization and analysis of the rocknest sand shadow. *Science* 341, 1239505. doi:10.1126/science.1239505

Bland, P. A., Cressey, G., and Menzies, O. N. (2004). Modal mineralogy of carbonaceous chondrites by X-ray diffraction and Mossbauer spectroscopy. *Meteorit. Planet. Sci.* 39, 3–16. doi:10.1111/j.1945-5100.2004.tb00046.x

Brearley, A. J. (2006). "The action of water," in *Meteorites and the early solar system II*". Editors D. S. Lauretta and H. Y. McSween (Tucson, Arizona: The University of Arizona Press), 587–624.

Britt, D. T., Cannon, K. M., Donaldson Hanna, K., Hogancamp, J., Poch, O., Beck, P., et al. (2019). Simulated asteroid materials based on carbonaceous chondrite mineralogies. *Meteorit. Planet. Sci.* 54 (9), 2067–2082. doi:10.1111/maps.13345

Bunaciu, A. A., Udristrioiu, E. g., and Aboul-Enein, H. Y. (2015). X-ray diffraction: instrumentation and applications. *Crit. Rev. Anal. Chem.* 45 (4), 289–299. doi:10.1080/10408347.2014.949616

Burke, K. N., DellaGiustina, D. N., Bennett, C. A., Walsh, K. J., Pajola, M., Bierhaus, E. B., et al. (2021). Particle size-frequency distributions of the OSIRIS-rex candidate sample sites on asteroid (101955) bennu. *Remote Sens.* 13 (7), 1315. doi:10.3390/rs13071315

Cannon, K. M., Britt, D. T., Smith, T. M., Fritsche, R. F., and Batcheldor, D. (2019). Mars global simulant MGS-1: A rocknest-based open standard for basaltic martian regolith simulants. *Icarus* 317, 470–478. doi:10.1016/j.icarus.2018.08.019

Cannon, K. M., Dreyer, C. B., Sowers, G. F., Schmitt, J., Nguyen, T., Sanny, K., et al. (2022). Working with lunar surface materials: review and analysis of dust mitigation and regolith conveyance technologies. *Acta Astronaut.* 196, 259–274. doi:10.1016/j.actaastro.2022.04.037

Carlson, R. W., and Lugmair, G. W. (1979). Sm-Nd constraints on early lunar differentiation and the evolution of KREEP. *Earth Planet. Sci. Lett.* 45 (1), 123–132. doi:10.1016/0012-821X(79)90114-6

Che, S., and Zega, T. Z. (2023). Hydrothermal fluid activity on asteroid Itokawa. *Nat. Astron.* doi:10.1038/s41550-023-02012-x

Clark, B. E., Hapke, B., Pieters, C., and Britt, D. (2002). "Asteroid space weathering and regolith evolution," in *Asteroids II*. Editors R. P. Binzel, T. Gehrels, M. S. Matthews, and A. Tucson (Tucson, Arizona, United States: University of Arizona Press).

Colaprete, A., Andrews, D., Bluethmann, W., Elphic, R. C., Bussey, B., Trimble, J., et al. (2019), "An overview of the volatiles investigating polar exploration rover (VIPER) mission," in American Geophysical Union Fall Meeting, San Francisco, CA, 11-15 December 2023 Abstract #P34B-03.

Crites, S. T., and Lucey, P. G. (2015). Revised mineral and Mg# maps of the Moon from integrating results from the Lunar Prospector neutron and gamma-ray spectrometers with Clementine spectroscopy. *Am. Mineralogist* 100, 973–982. doi:10.2138/am-2015-4874

Delbo, M., Libourel, G., Wilkerson, J., Murdoch, N., Michel, P., Ramesh, K. T., et al. (2014). Thermal fatigue as the origin of regolith on small asteroids. *Nature* 508, 233–236. doi:10.1038/nature13153

Easter, P., Long-Fox, J., Landsman, Z., Metke, A., and Britt, D. (2022). "Comparing the effects of mineralogy and particle size distribution on the angle of repose for lunar regolith simulants," in 53rd Lunar and Planetary Science Conference, Houston, TX, USA, March 7-11, 2022.

Gaddis, L. R., Staid, M. I., Tyburczy, J. A., Hawke, B. R., and Petro, N. E. (2003). Compositional analyses of lunar pyroclastic deposits. *Icarus* 161 (2), 262–280. doi:10.1016/S0019-1035(02)00036-2

Graf, J. C. (1993). Lunar soils grain size catalog. *NASA Ref. Publ.* 1265.

Guerrero-Gonzalez, F. J., and Zabel, P. (2023). System analysis of an ISRU production plant: extraction of metals and oxygen from lunar regolith. *Acta Astronaut.* 203, 187–201. doi:10.1016/j.actaastro.2022.11.050

Gustafson, J. O., Bell, J. F., Gaddis, L. R., Hawke, B. R., and Giguere, T. A. (2012). Characterization of previously unidentified lunar pyroclastic deposits using Lunar Reconnaissance Orbiter Camera data. *J. Geophys. Res. Plan.* 117 (E12). doi:10.1029/2011JE003893

Hagerty, J. J., Lawrence, D. J., Hawke, B. R., Vaniman, D. T., Elphic, R. C., and Feldman, W. C. (2006). Refined thorium abundances for lunar red spots: implications for evolved, nonmare volcanism on the Moon. *J. Geophys. Res. Plan.* 111 (E6), E06002. doi:10.1029/2005JE002592

Haskin, L., and Warren, P. (1991). Lunar chemistry, in *The lunar sourcebook: a user's guide the the moon chapter 8*. Cambridge: Cambridge University Press.

Head, J. W., and McCord, T. B. (1978). Imbrian-age highland volcanism on the Moon: the gruithuisen and mairan domes. *Science* 199 (4336), 1433–1436. doi:10.1126/science.199.4336.1433

Head, J. W., and Wilson, L. (1992). Lunar mare volcanism: stratigraphy, eruption conditions, and the evolution of secondary crusts. *Geochimica Cosmochimica Acta* 56, 2155–2175. doi:10.1016/0016-7037(92)90183-j

Heiken, G., and McKay, D. S. (1974). "Petrography of Apollo 17 soils," in Proc. 5th Lunar Sci. Conference, Houston, Tex., March 18-22, 1974, 843–860.

Hooper, P. R. (1964). Rapid analysis of rocks by X-ray fluorescence. *Anal. Chem.* 36 (7), 1271–1276. doi:10.1021/ac60213a026

Horgan, B. H. N., Anderson, R. B., Dromart, G., Amador, E. S., and Rice, M. S. (2020). The mineral diversity of Jezero crater: evidence for possible lacustrine carbonates on Mars. *Icarus* 339, 113526. doi:10.1016/j.icarus.2019.113526

Hörz, F., Grieve, R., Heiken, G., Spudis, P., and Binder, A. (1991). "Lunar surface processes," in *The lunar sourcebook: A user's guide to the moon" chapter 4* (Cambridge: Cambridge University Press).

Housen, K. R., Wilkening, L. L., Chapman, C. R., and Greenberg, R. (1979). Asteroidal regoliths. *Icarus* 39, 317–351. doi:10.1016/0019-1035(79)90145-3

Housen, K. R., and Wilkening, L. L. (1982). Regoliths on small bodies in the solar system. *Annu. Rev. Earth Planet. Sci.* 10, 355–376. doi:10.1146/annurev.ea.10.050182.002035

Howard, K. T., Alexander, C. M. O'D., Schrader, D. L., and Dyl, K. A. (2015). Classification of hydrous meteorites (CR, CM and C2 ungrouped) by phyllosilicate fraction: PSD-XRD modal mineralogy and planetesimal environments. *Geochimica Cosmochimica Acta* 149, 206–222. doi:10.1016/j.gca.2014.10.025

Howard, K. T., Benedix, G. K., Bland, P. A., and Cressey, G. (2009). Modal mineralogy of CM2 chondrites by X-ray diffraction (PSD-XRD). Part 1: total phyllosilicate abundance and the degree of aqueous alteration. *Geochimica Cosmochimica Acta* 73, 4576–4589. doi:10.1016/j.gca.2009.04.038

Humbert, M. S., Brooks, G. A., Duffy, A. R., Hargrave, C., and Akbar Rhamdhani, M. (2022). Thermophysical property evolution during molten regolith electrolysis. *Planet. Space Sci.* 219, 105527. doi:10.1016/j.pss.2022.105527

Isachenkov, M., Chugunov, S., Landsman, Z., Akhatov, I., Metke, A., Tikhonov, A., et al. (2022). Characterization of novel lunar highland and mare simulants for ISRU research applications. *Icarus* 376, 114873. doi:10.1016/j.icarus.2021.114873

Johnson, D. M., Hooper, P. R., and Conrey, R. M. (1999). XRF analysis of rocks and minerals for major and Trace elements on a single low dilution Li-tetraborate fused Bead. *Adv. X-ray Analysis* 41, 843–867.

Johnson, T. V., and Fanale, F. P. (1973). Optical properties of carbonaceous chondrites and their relationship to asteroids. *J. Geophys. Res.* 78, 8507–8518. doi:10.1029/jb078i035p08507

Jolliff, B. L., Gillis, J. J., Haskin, L. A., Korotev, R. L., and Wieczorek, M. A. (2000). Major lunar crustal terranes: surface expressions and crust-mantle origins. *J. Geophys. Res. Planets* 105 (E2), 4197–4216. doi:10.1029/1999JE001103

Just, G. H., Smith, K., Joy, K. H., and Roy, M. J. (2020). Parametric review of existing regolith excavation techniques for lunar *in Situ* Resource Utilisation (ISRU) and recommendations for future excavation experiments. *Planet. Space Sci.* 180, 104746. doi:10.1016/j.pss.2019.104746

Keil, K. (2000). Thermal alteration of asteroids: evidence from meteorites. *Planet. Space Sci.* 48, 887–903. doi:10.1016/s0032-0633(00)00054-4

King, A. J., Schofield, P. F., Howard, K. T., and Russell, S. S. (2015). Modal mineralogy of CI and CI-like chondrites by X-ray diffraction. *Geochimica Cosmochimica Acta* 165, 148–160. doi:10.1016/j.gca.2015.05.038

Kminek, G., Meyer, M. A., Beaty, D. W., Carrier, B. L., Haltigin, T., and Hays, L. E. (2022). Mars sample return (MSR): planning for returned sample science. *Astrobiology* 22, S-1–S-4. doi:10.1089/ast.2021.0198

Kornuta, D., Abbud-Madrid, A., Atkinson, J., Barr, J., Barnhard, G., Bienhoff, D., et al. (2019). Commercial lunar propellant architecture: A collaborative study of lunar propellant production. *REACH* 13, 100026. doi:10.1016/j.reach.2019.100026

Lemelin, M., Lucey, P. G., and Camon, A. (2022). Compositional maps of the lunar polar regions derived from the kaguya spectral profiler and the lunar orbiter laser altimeter data. *Planet. Sci. J.* 3 (63), 63. doi:10.3847/PSJ/ac532c

Leshin, L. A., Mahaffy, P. R., Webster, C. R., Cabane, M., Coll, P., Conrad, P. G., et al. (2013). Volatile, isotope, and organic analysis of martian fines with the Mars Curiosity rover. *Science* 341, 1238937. doi:10.1126/science.1238937

Long-Fox, J. M., Landsman, Z. A., Easter, P. B., Millwater, C. A., and Britt, D. T. (2023). Geomechanical properties of lunar regolith simulants LHS-1 and LMS-1. *Adv. Space Res.* 71, 5400–5412. doi:10.1016/j.asr.2023.02.034

Madison, A., Landsman, Z., Long-Fox, J., Metke, A., Krol, K., Easter, P., et al. (2022). "Lunar dust simulants and Their applications," in 18th Biennial American Society of Civil Engineers Earth and Space Conference, Denver, CO, USA, 25-28 April 2022.

Malin, M. C., and Edgett, K. S. (2000). Sedimentary rocks of early Mars. *Science* 290, 1927–1937. doi:10.1126/science.290.5498.1927

Mardon, A. A., and Zhou, G. (2019). "Asteroid mining and in-situ mineral resource Utilization," in 82nd Annual Meeting of The Meteoritical Society, Sapporo, held 7–12 July 2019.

McCauley, J. F. (1973). Mariner 9 evidence for wind erosion in the equatorial and midlatitude regions of Mars. *J. Geophys. Res.* 78, 4123–4137. doi:10.1029/JB078i020p04123

McKay, D. S., Carter, J. L., Boles, W. W., Allen, C. C., and Allton, J. H. (1994). JSC-1: A new lunar soil simulant. *Eng. Constr. operations space* 2, 857–866.

McKay, D. S., Heiken, G., Basu, A., Blanford, S. S., Reedy, R., French, B. M., et al. (1991). "The lunar regolith," in *The lunar sourcebook: A user's guide to the moon" chapter 7* (Cambridge: Cambridge University Press).

McKenzie, W., Taylor, G. J., Dera, P., Martel, L. M. V., Lucey, P. G., Hammer, J. E., et al. (2020). "XTRA, A combined XRD/XRF instrument for use in lunar science and resource Utilization," in 51st Lunar and Planetary Science Conference, Houston, TX, USA, March 16–20, 2020.

McSween, H. Y., Jr., Taylor, G. J., and Wyatt, M. B. (2009). Elemental composition of the martian crust. *Science* 324, 736–739. doi:10.1126/science.1165871

Metzger, P. T., Britt, D. T., Covey, S., Schultz, C., Cannon, K. M., Grossman, K. D., et al. (2019). Measuring the fidelity of asteroid regolith and cobble simulants. *Icarus* 321, 632–646. doi:10.1016/j.icarus.2018.12.019

Metzger, P. T., Muscatello, A., Mueller, R. P., and Mantovani, J. (2013). Affordable, rapid bootstrapping of the space industry and solar system civilization. *J. Aerosp. Eng.* 26, 18–29. doi:10.1061/(asce)as.1943-5525.0000236

Millwater, C., Long-Fox, J., Landsman, Z., Metke, A., and Britt, D. (2022). "Direct shear measurements of lunar regolith simulants LHS-1, LHS-1D, LMS-1, and LMS-1D," in 53rd Lunar and Planetary Science Conference, Houston, TX, USA, March 07–11, 2022.

Mueller, R. P., Howe, S., Kochmann, D., Ali, H., Andersen, C., Burgoyne, H., et al. (2016). "Automated additive construction (AAC) for Earth and space using *in-situ* resources," in Proceedings of the Fifteenth Biennial ASCE Aerospace Division International Conference on Engineering, Science, Construction, and Operations in Challenging Environments, Orlando Florida, 11-15 April 2016.

Murchie, S. L., Mustard, J., Ehlmann, B. L., Milliken, R. E., Bishop, J. L., McKeown, N. K., et al. (2009). A synthesis of Martian aqueous mineralogy after 1 Mars year of observations from the Mars Reconnaissance Orbiter. *J. Geophys. Res.* 114, E00D06. doi:10.1029/2009JE003342

Nadoushan, M. D., Ghobadi, M., and Shafaee, M. (2020). Designing reliable detumbling mission for asteroid mining. *Acta Astronaut.* 174, 270–280. doi:10.1016/j.actaastro.2020.05.025

Ohtake, M., Matsunaka, T., Haruyama, J., Yokota, Y., Morota, T., Honda, C., et al. (2009). The global distribution of pure anorthosite on the Moon. *Nature* 461, 236–240. doi:10.1038/nature08317

Pohl, L., and Britt, D. T. (2020). Strengths of meteorites – an overview and analysis of available data. *Meteorit. Planet. Sci.* 55 (4), 962–987. doi:10.1111/maps.13449

Pohl, L., and Britt, D. T. (2017). The radiation shielding potential of CI and CM chondrites. *Adv. Space Res.* 59, 1473–1485. doi:10.1016/j.asr.2016.12.028

Poulet, F., Mangold, N., Loizeau, D., Bibring, J. P., Langevin, T., Michalski, J., et al. (2008). Abundance of minerals in the phyllosilicate-rich units on Mars. *Astron. Astrophys.* 487, L41–L44. doi:10.1051/0004-6361:200810150

Rivkin, A. S. (2012). The fraction of hydrated C-complex asteroids in the asteroid belt from SDSS data. *Icarus* 221, 744–752. doi:10.1016/j.icarus.2012.08.042

Rose, H. J., Cuttitta, F., Dwornik, E. J., Carron, M. K., Christian, R. P., Lindsay, J. R., et al. (1970). Semimicro X-ray fluorescence analysis of lunar samples. *Proc. Apollo 11 Lunar Sci. Conf.* 2, 1493–1497.

Sanders, G., Kleinhenz, J., and Linne, D. (2022). *NASA plans for* in situ *resource utilization (ISRU) development, demonstration, and implementation*. Available at: https://ntrs.nasa.gov/api/citations/20220008799/downloads/NASA%20ISRU%20Plans_Sanders_COSPAR-Final.pdf.

Schmitt, H. H., Lofgren, G., Swann, G. A., and Simmons, G. (1970). "The Apollo 11 samples: introduction," in Proceedings of the Apollo 11 Lunar Science Conference, Houston, TX., held 5-8 January, 1970.

Sibille, L., Carpenter, P., Schlagheck, R., and French, R. A. (2006). *Lunar regolith simulant materials: Recommendations for standardization, production, and usage*. Washington, D.C., United States: NASA. Technical Publication TP2006214605.

Sibille, L., Sadoway, D. R., Sirk, A., Tripathy, P., Melendez, O., Standish, E., et al. (2009). "Recent advances in scale-up development of molten regolith electrolysis for oxygen production in support of a lunar Base," in 47th AIAA Aerospace Sciences Meeting Contribution, Orlando, Florida, 05 January 2009 - 08 January 2009.

Siegler, M. A., Feng, J., Lehman-Franco, K., Andrews-Hanna, J. C., Economos, R. C., St. ClairMillionHead, M. C. J. W., et al. (2023). Remote detection of a lunar granitic batholith at Compton-Belkovich. *Nature* 620, 116–121. doi:10.1038/s41586-023-06183-5

Simon, S. B., Papike, J. J., and Laul, J. C. (1981). The lunar regolith: comparative studies of the Apollo and luna sites. *Petrology soils Apollo 17, Luna 16, 20, 24" Lunar Planet. Sci. Conf. Proc.* 12, 371–388.

Spudis, P., and Pieters, C. (1991). "Global and regional data about the Moon," in *The lunar sourcebook: A user's guide to the moon" chapter 10* (Cambridge: Cambridge University Press).

Srivastava, S., Pradhan, S. S., Luitel, B., Manghaipathy, P., and Romero, M. (2023). Analysis of Technology, economic, and legislation readiness levels of asteroid mining industry: A Base for the future space resource Utilization missions. *New Space* 2023, 21–31. doi:10.1089/space.2021.0025

Sutter, B., McAdam, A. C., Mahaffy, P. R., Ming, D. W., Edgett, K. S., Rampe, E. B., et al. (2017). Evolved gas analyses of sedimentary rocks and eolian sediment in Gale crater, Mars: results of the curiosity rover's sample analysis at Mars instrument from yellowknife bay to the namib dune. *J. Geophys. Res.* 122, 2574–2609. doi:10.1002/2016JE005225

Taylor, G. J., Martel, L. M. V., Lucey, P. G., Gillis-Davis, J. J., Blake, D. F., and Sarrazin, P. (2019). Modal analyses of lunar soils by quantitative x-ray diffraction analysis. *Geochimica Cosmochimica Acta* 266, 17–28. doi:10.1016/j.gca.2019.07.046

Taylor, G. J., Warren, P., Ryder, G., Delano, J., Pieters, C., and Lofgren, G. (1991). "Lunar rocks," in *The lunar sourcebook: A user's guide to the moon" chapter 6* (Cambridge: Cambridge University Press).

Taylor, L. A., Pieters, C. M., Keller, L. P., Morris, R. V., and McKay, D. S. (2001). Lunar mare soils: space weathering and the major effects of surface-correlated nanophase Fe. *J. Geophys. Res.* 106, 27985–27999. doi:10.1029/2000je001402

Thangavelautham, J., and Xu, Y. (2022). The design of autonomous robotic Technologies for lunar launch and landing pad (LLP) preparation. *IEEE Aerosp. Conf.* doi:10.1109/AERO53065.2022.9843755

Toon, O. B., Pollack, J. B., and Sagan, C. (1977). Physical properties of the particles composing the Martian dust storm of 1971-1972. *Icarus* 30, 663–696. doi:10.1016/0019-1035(77)90088-4

Trang, D., Gillis-Davis, J. J., Lemelin, M., Cahill, J. T. S., Hawke, B. R., and Giguere, T. A. (2017). The compositional and physical properties of localized lunar pyroclastic deposits. *Icarus* 283, 232–253. doi:10.1016/j.icarus.2016.09.025

Walsh, K. J., Bierhaus, E. B., Lauretta, D. S., Nolan, M. C., Ballouz, R., Bennett, C. A., et al. (2022). Assessing the sampleability of bennu's surface for the OSIRIS-rex asteroid sample return mission. *Space Sci. Rev.* 218 (20), 20. doi:10.1007/s11214-022-00887-2

Watanabe, S., Hirabayashi, M., Hirata, N., Hirata, N., Noguchi, R., Shimaki, Y., et al. (2019). Hayabusa2 arrives at the carbonaceous asteroid 162173 ryugu—a spinning top–shaped rubble pile. *Science* 364 (6437), 268–272. doi:10.1126/science.aav8032

Wentworth, C. K. (1922). A scale of grade and class Terms for clastic sediments. *J. Geol.* 30 (5), 377–392. doi:10.1086/622910

Wieczorek, M. A., and Phillips, R. J. (2000). The 'procellarum KREEP Terrane': implications for mare volcanism and lunar evolution. *J. Geophys. Res. Plan.* 105 (E8), 20417–20430. doi:10.1029/1999JE001092

Yada, T., Abe, M., Okada, T., Nakato, A., Yogata, K., Miyazaki, A., et al. (2022). Preliminary analysis of the Hayabusa2 samples returned from C-type asteroid Ryugu. *Nat. Astron.* 6, 214–220. doi:10.1038/s41550-021-01550-6

Yen, A. S., Gellert, R., Clark, B. C., Ming, D. W., King, P. L., Schmidt, M. E., et al. (2013). "Evidence for a global martian soil composition extends to Gale Crater," in Proceedings of the Lunar and Planetary Science Conference, March 7–11, 2022.

Yen, A. S., Gellert, R., Schröder, C., Morris, R. V., Bell, J. F., III, Knudson, A. T., et al. (2005). An integrated view of the chemistry and mineralogy of martian soils. *Nature* 436, 49–54. doi:10.1038/nature03637

frontiers | Frontiers in Space Technologies

TYPE Original Research
PUBLISHED 10 January 2024
DOI 10.3389/frspt.2023.1303180

OPEN ACCESS

EDITED BY
Yosuke Yamashiki,
Kyoto University, Japan

REVIEWED BY
Noriyuki Namiki,
National Astronomical Observatory of Japan (NAOJ), Japan
Günter Kargl,
Austrian Academy of Sciences, Austria

*CORRESPONDENCE
Christian Gscheidle,
c.gscheidle@tum.de

RECEIVED 27 September 2023
ACCEPTED 18 December 2023
PUBLISHED 10 January 2024

CITATION
Gscheidle C, Witzel T, Smolka A and Reiss P (2024), Permittivity sensor development for lunar and planetary surface exploration. *Front. Space Technol.* 4:1303180. doi: 10.3389/frspt.2023.1303180

Permittivity sensor development for lunar and planetary surface exploration

Christian Gscheidle*, Thilo Witzel, Alexander Smolka and Philipp Reiss

TUM School of Engineering and Design, Professorship of Lunar and Planetary Exploration, Technical University of Munich, Ottobrunn, Germany

Permittivity sensors measure the electric permittivity (formerly known as the dielectric constant) of a sample between its electrodes and offer a reliable method to characterize the subsurface of planetary bodies *in situ*. One potential application is the identification and mapping of water ice at the poles of the Moon. In this paper, the scientific background and heritage of the permittivity sensor concept are discussed, and the implemented electronic architecture is introduced, focusing on the novel patch electrodes. The data processing approach for the measurements is based on Fourier transformation, and numerical simulation setups are used for performance predictions. The calibration of the sensor validates the functionality of the electronics, and the results from both simulations and characterization experiments show that the concept is applicable in the exploration scenario. Considering both engineering and scientific aspects, the results highlight the permittivity sensor's suitability for lunar and planetary exploration missions, albeit further points for improvement are identified.

KEYWORDS

permittivity (dielectric constant), moon, regolith, instrument development, volatiles

1 Introduction

With the renaissance of human exploration beyond low Earth orbit, *in situ* resource utilization becomes highly relevant as it enables sustainable, long-duration missions by drastically reducing their cost. Regolith and cold-trapped volatiles in permanently shadowed regions (PSRs) at the lunar poles or on other planetary objects are potential resources for human exploration; however, their nature is not well understood yet. Precise knowledge of the density, porosity, and composition of the lunar regolith, as well as the distribution, abundance, and physical state of volatiles, is crucial for planning future missions to the Moon and beyond. The data obtained from numerous remote sensing missions around the Moon have provided evidence for large reserves of water or water-equivalent hydrogen (Colaprete et al., 2010; Li and Milliken, 2017). Nevertheless, ground truth data for model verification and correlation from the lunar poles are missing (European Space Agency, 2019). Although upcoming exploration missions, such as the National Aeronautics and Space Administration's (NASA) Volatiles Investigating Polar Exploration Rover (VIPER) (Andrews, 2022) and the European Space Agency's (ESA) Package for Resource Observation and *in Situ* Prospecting for Exploration, Commercial exploitation and Transportation (PROSPECT) instrument on a commercial lander (Fisackerly et al., 2023), will hopefully improve ground truth data availability, a broader coverage and finer spatial resolution are still necessary (Lucey et al., 2021).

In this context, measuring the regolith's electric properties (conductivity and permittivity) is a relatively simple and scientifically valuable technique to quickly determine the state and abundance of water ice and characterize the geotechnical properties of the subsurface. The implementation of such a sensor considered in this work consists of an electronics unit with two electrodes between which the sample is located. The material through which the electric field propagates (a mixture including regolith and volatiles) acts as a dielectric and influences the effective capacitance between the electrodes. The sensor measures potentials and/or currents over the capacitive element in a resistive–capacitive (RC) circuit. The circuit is excited in a frequency range relevant to the specific investigation, typically ranging from a few Hz (extremely low frequency (ELF)) to several kHz. In this study, frequencies ranging from 6.25 Hz to 10 kHz were investigated. With known resistance and excitation potential, the capacitance can be inferred, and the properties of the sample can be deduced.

The physical phenomenon exploited by the proposed permittivity sensor is that water, regolith, and vacuum have distinct relative electrical permittivity ε_r (electric permittivity normalized by vacuum's electric permittivity $\varepsilon_r = \varepsilon/\varepsilon_0$ with $\varepsilon_0 = 8.854 \times 10^{-12}$ F/m), both in magnitude and in the frequency domain. At low frequencies, water has a distinct electric permittivity curve over frequency, which drops approximately from 100 to 3 at approximately 3 kHz, depending on the temperature (Lethuillier, 2016). Dry lunar regolith has a comparably low relative permittivity of 3.5 and a very low electrical conductivity (Heiken et al., 1991). Vacuum has, by definition, a relative permittivity of 1. By measuring the capacitance of a system, which is a function of the constituents' individual permittivities ($C = f(\varepsilon_r)$), and calculating the effective relative permittivity for various frequencies, the values can be fitted to previously determined (non-linear) mixing models to infer porosity and water content.

1.1 Previous missions

Several successful missions to celestial bodies have shown the usefulness of permittivity probes. The Huygens Atmospheric Structure Instrument–Permittivity and Electromagnetic Wave Analyzer (HASI-PWA) instrument on the Huygens lander of NASA's Cassini–Huygens mission monitored Titan's atmosphere using a mutual impedance probe (Grard et al., 1995; Fulchignoni et al., 2002). The Thermal and Electrical Conductivity Probe (TECP) on NASA's Phoenix lander was designed to measure temperatures and detect water at the polar caps of Mars using electrical measurements (Zent et al., 2009). The instrument "successfully measured the thermal and electrical properties of the martian regolith at the Phoenix site" (Zent et al., 2010, *p*.21). The Surface Electric Sounding and Acoustic Monitoring Experiment–Permittivity Probe (SESAME-PP) instrument on the Philae lander of ESA's Rosetta featured a mutual impedance probe (Seidensticker et al., 2007). Although the landing was not nominal, the SESAME-PP was able to return valuable scientific data using its impedance spectroscopy probe (Lethuillier et al., 2016).

ESA's upcoming PROSPECT instrument package "includes a miniaturized sensor for measuring the dielectric constant of lunar subsurface materials by means of low-frequency alternating currents injected into the regolith" (Trautner et al., 2021, p.1). The sensor electrode and its front-end electronics are integrated into the ProSEED drill element of PROSPECT. It can be inserted into the subsurface to a depth of up to 60 cm (Trautner et al., 2021) and constrain the radial distribution of volatiles in the borehole at the electrode's depth. However, due to the mission configuration using a lander, the sensor is constrained to measurements at a single location.

Other concepts for permittivity sensors have been proposed, for example, for usage on Mars by Trautner et al. (2003) or on the Moon by Nurge (2012). A permittivity probe, initially planned to be part of the Heat Flow and Physical Properties Package (HP^3) (Kargl et al., 2011), was developed and tested up to a technology readiness level 5 before the mission was terminated (Stiegler, 2011).

The novel permittivity sensor concept developed at the Technical University of Munich (TUM) and described in this paper implements an approach with the electrodes being arranged in a flat configuration, called the patch electrode, as shown in Figure 1A. This configuration enables applications in several mission scenarios and opens new design choices for flexible integration and operation.

2 Methods

The sensor concept relies on an electrode connected to a custom front-end electronics (FEE), which can be controlled by a generic back-end electronics unit. In contrast to a frequency-sweeping approach, measurements are performed in the time domain and then transformed into the frequency domain.

2.1 Sensor description

Figure 1A depicts both a patch electrode prototype and combined front-end and back-end electronics implemented onto a printed circuit board.

The electronics configuration for the sensor in this study is based on an RC circuit. In the sensor schematic, depicted in Figure 1B, measurement resistor R_1 and sample capacitance C_{reg} form the central RC circuit. Capacitors C_{P1} and C_{P2} model parasitic capacitance in the electronics and electrode, respectively. $C_{S,H}$ and $C_{P,H}$ describe capacitances of the harness between the electronics and the electrode. Operational amplifier U_3 functions as a high differential impedance buffer stage ($> 1\,G\Omega$) included to decouple the low-input-impedance read-out electronics from the measurement loop. This element is necessary, as the measurement loop would otherwise form an undesirable voltage divider. Similarly, U_4 follows the voltage at the electrode and thus mitigates the parasitic capacitive effect of the harness.

Figure 2 shows the measurement procedure in the upper part. The excitation signal V_{Exc} is generated by the controlling unit with a commercial micro-controller (Teensy 4.1). For future mission developments, however, a dedicated sensor, front-end electronics, and the central processing unit are intended to be used. Its square wave character is generated by switching an output channel on and off using the internal clock of the micro-controller. Switching the excitation voltage programmatically via software has the advantage

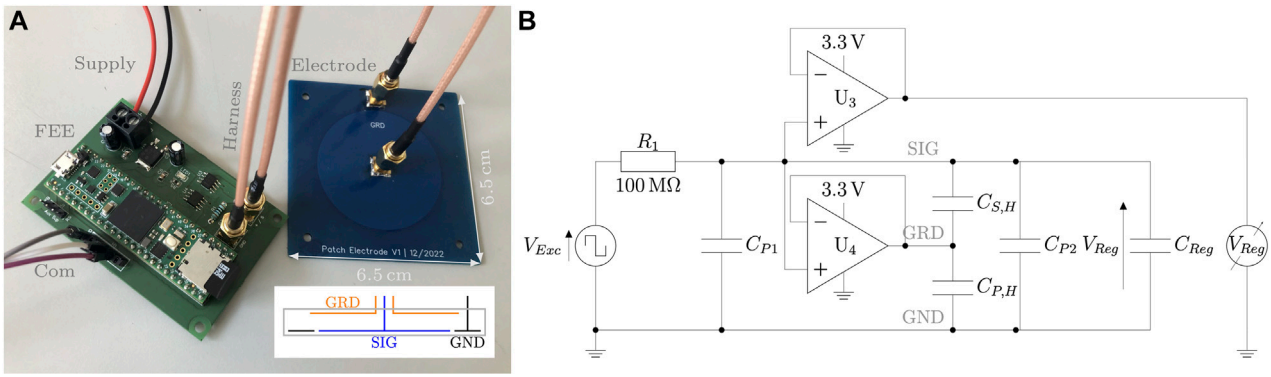

FIGURE 1
Patch electrode and electronics investigated in this study. **(A)** Picture of the patch electrode with a custom electronics board and annotations of major elements. The inset depicts the schematic cross section of the electrode. **(B)** Schematic of the sensor electronics with parasitic capacitances denoted with subscript $_P$.

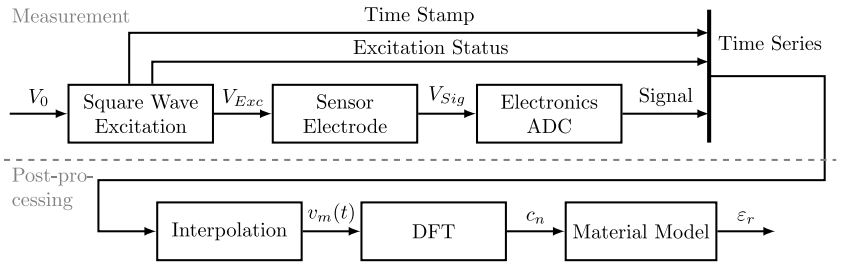

FIGURE 2
Measurement and post-processing approach: the permittivity sensor measures a time series, which is then post-processed.

of being able to adjust the sensor resolution during a mission. As switching and read-out are performed at frequencies ≤ 20 kHz and over a duration of a few seconds, these tasks could be performed by the host system's electronics or dedicated instrument electronics. Using the host system, such as a rover or lander, has the advantage of reducing the sensor's mass and complexity.

The measurement of signal voltage at the capacitive sensor is performed by the back-end electronics with an adjustable frequency, and thus $V_{Sig} = V_{Reg}$. The current baseline is 20 kHz, enabling a frequency of up to 10 kHz in the final spectrum when considering the Nyquist–Shannon criterion. The analog-to-digital converter (ADC) is set to 12-bit measurements. Along with each voltage reading, the time since the start of the measurement and the binary status of the excitation output are recorded. This setup results in 4 bytes per measurement with significant optimization and compression potential.

The prototype electrode investigated is a flat, rectangular, two-layer printed circuit board with a signal, ground, and guard electrode. The side length is 6.5 cm, and the total system weight is 18 g. Albeit the sensor needs no direct contact with the soil, it must be in close proximity, as the electric field quickly weakens with distance. Therefore, the electronics can be accommodated separately from the electrode with a shielded harness connecting these two elements, for example, in an individual electronics box or combined with the platform electronics. Qualitatively, a gap between the electrode and the soil is detrimental to the sensor's performance, for instance, if it is placed on rough surfaces. The quantitative influence still needs to be investigated. Thus, the sensor should ideally be placed in contact with a flat surface in parallel.

2.1.1 Data processing

The sensor measures a time series of capacitor voltage and excitation status. However, the concept is based on frequency-dependent information, and frequency information has to be extracted from the time series using its Fourier transform. Figure 2 shows the data processing approach in the bottom part. The coefficients for the complex Fourier transform of the square wave excitation signal V_{Exc} (with base frequency f_B) are provided in Eq. 1:

$$c_{n,Exc} = \begin{cases} \frac{V_0}{2} & \text{, if } n = 0, \\ \frac{\mathrm{i}\, V_0}{\pi\, n} & \text{, for } n \in \pm 1, \pm 3, \pm 5, \ldots, \\ 0 & \text{, for } n \in \pm 2, \pm 4, \pm 6, \ldots \end{cases} \tag{1}$$

with n being the dimensionless harmonics iterator and V_0 being the excitation voltage magnitude. Note that the coefficient's magnitude does not depend on the base frequency.

Applying Kirchhoff's circuit laws to the measurement loop (assuming no current flows through operational amplifiers and therefore negligible parasitic capacitances), the complex voltage across the capacitive element is determined as follows:

$$V_{Sig} = \frac{V_{Exc}\, Z_{Cap}}{R + Z_{Cap}} = \frac{V_{Exc}}{1 + \mathrm{i}\, 2\pi f RC} = \frac{V_{Exc}\,(1 - \mathrm{i}\, 2\pi f RC)}{1 + (2\pi f RC)^2}. \quad (2)$$

By applying the complex Fourier transform to the excitation signal, the Fourier coefficients of the ideal signal voltage can be obtained by substituting them into Eq. 2, and they are expressed in Eq. 3.

$$c_{n,Sig} = \begin{cases} \dfrac{V_0}{2} & , \text{if } n = 0, \\ \dfrac{V_0\,(\mathrm{i} + 2\pi n f_B RC)}{\pi n\left(1 + (2\pi n f_B RC)^2\right)} & , \text{for } n \in \pm 1, \pm 3, \pm 5, \ldots, \\ 0 & , \text{for } n \in \pm 2, \pm 4, \pm 6, \ldots \end{cases} \quad (3)$$

All even, non-zero coefficients disappear, and the magnitude of all odd coefficients decreases with increasing frequency. The ideal, predicted signal time series can be reconstructed by the summation of (infinitely) many Fourier coefficients. Additionally, the dependence of the capacitance on the frequency is visible in the signal's Fourier coefficients.

The measurement's (discrete) Fourier coefficients can analogously be found by applying the discrete Fourier transform (DFT) to the measured time series (Brunton and Kutz, 2022). This returns coefficients at discrete values, and a properly chosen base frequency is a multiple of the Fourier frequency, allowing for a simplified further analysis. The *FFTW*-Julia library was used to calculate the coefficients in the signal analysis (Frigo and Johnson, 2005). For noise reduction in the measured signal, especially reduced frequency jitter, the raw time series was interpolated onto a regularly spaced time vector with identical intervals compared to the sampling intervals using a linear scheme. After the transformation, the Fourier coefficients at the non-zero harmonics were selectively analyzed, equaling a Fourier filtering technique.

The capacitance values for a given frequency can then be obtained by solving Eq. 4 using the value of the complex Fourier coefficients and taking the real part of the result.

$$C(c_n, f) = \frac{1}{2\pi f R}\left(i - \frac{V_0}{\pi n c_n}\right). \quad (4)$$

Numerically, the difference between the magnitudes of coefficients was minimized with respect to the given frequency f to determine the capacitance (min $(|c_{n,measured}(f)| - |c_{n,Sig}(C, f)|)$).

Additionally, a mixing rule is necessary to model the effective electric permittivity of mixtures depending on their composition and subsequently deduce the content of water. Sihvola (2000) listed multiple approaches to describe this highly non-linear phenomenon. In this study, a power law mixing rule with coefficients of 1/3, also known as the Looyenga formula, has been used: $\varepsilon_{r,eff}^{1/3} = \sum_n \phi_n\, \varepsilon_{r,n}^{1/3}$, with ϕ being the volume fraction of the respective component n (Looyenga, 1965). A resulting dependence of the effective relative permittivity depending on the volume share of each of the mixture's three constituents is shown in Figure 3 for the static case. As an example, the case of a constant volume fraction of 0.5 for regolith is highlighted in Figure 3 with the ice-to-vacuum ratio being variable. However, as the relative permittivity of water changes significantly with both frequency and temperature (see Lethuillier, 2016), while the relative permittivity of vacuum is constant and practically constant for regolith (Heiken et al., 1991), the effective distribution exhibits differences for different frequencies mainly due to the ice content. Thus, measuring the effective relative permittivity for multiple frequencies allows the deduction of volume fractions of all three constituents.

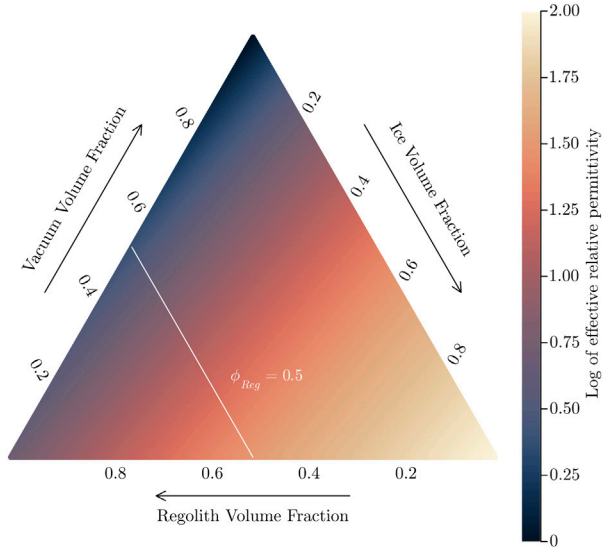

FIGURE 3
Exemplary representation of the used power law mixing rule (Log_{10}-scaling) illustrating the dependence of the relative permittivity on the volume share of the three considered components at −20°C. A constant regolith volume share of 0.5 is highlighted.

2.2 Experiments

Experiments were conducted to calibrate and characterize the sensor both with known capacitances and mixtures imitating lunar soil with various amounts of water. Generic quartz sand and lunar regolith simulant (JSC-1A) were used to mimic lunar regolith in the experiments. The electrode was placed parallel to the surface with no gap between the sample and the electrode by holding it down. The samples were large enough with a thickness of at least 10 cm to minimize boundary effects. Considering the experiments with JSC-1A, the sample was not intentionally compressed, resulting in a measured porosity of approximately 0.5. In the calibration of the electronics, generic ceramic capacitors ranging from open circuit to 220 pF with 10% uncertainty were used. The characterization experiments used the patch electrode, as shown in Figure 1.

The switching frequency was set to 12.5 Hz, with sampling occurring at 20 kHz, and the measurement duration was 2 s (note that these values were chosen based on initial tests and can be optimized). One measurement consisted of the elapsed time in µs since the measurement start, the (binary) excitation state, and the

TABLE 1 Materials used in the experiments and predictions for these setups from simulation. References refer to the relative permittivity values.

Material	Predicted capacitance (pF)	Measured capacitance (pF)	Relative permittivity (–)	Reference
Air	4.13	5.02	1.0	Haynes et al. (2016)
Polyethylene	6.12	7.42	2.5	Haynes et al. (2016)
Regolith simulant (JSC-1A)	9.34	12.70	5.0	Nurge (2012)
Granite	13.17	20.81	8.0	Haynes et al. (2016)
For reference				
Vacuum			1	By definition
Water (liquid)			3 to 100	Haynes et al. (2016)
Lunar regolith			3 to 5	Heiken et al. (1991)

signal voltage from ADC, resulting in a 570-kbyte file. The measurements were conducted under atmospheric pressure, as air and vacuum have very similar relative permittivity (Haynes et al., 2016), and no phase transition for water is expected. The temperature of the setup ranged from −40°C to 40°C. Each measurement was repeated five times to show reproducibility and for statistical evaluation.

2.3 Simulation setup

A COMSOL multi-physics model was developed to predict the electric characteristics of the sensor because no simple analytic formula exists for the proposed geometry. As the investigated patch electrode is rotational symmetric, a 2D simulation with rotational symmetry was used with zero-charge boundary conditions far away from the electrode so that the domain size did not influence the simulation. Generally, the simulation can return data on expected overall capacitances and subsurface field geometry. Both quantities are crucial for designing sufficient electronics and scaling the electrode. First, the maximum capacitance mainly influences the selection of an appropriate measurement resistor (R_1 in Figure 1B). A too small or too large resistor would make meaningful sensor readings impossible, as the circuit's time constant would be too dissimilar to the sampling period. Second, the field geometry influences the sensor's sensing depth and its scientific potential. Therefore, one major application of the simulation is the analysis of the depth to which the sensor is able to sense and characterize the subsurface. This sensing depth was taken to be the depth at which the electric potential is reduced to 10% of its maximum value directly below the center of the electrode (r = 0 mm).

Additionally, a COMSOL multi-physics model with coupled heat and mass transfer and superposed electrical field simulations is under development based on the model by Reiss (2018) and adapted to 2D domains and depth-dependent properties. This model is necessary to analyze the sensor's behavior in changing environments, as demonstrated in Gscheidle et al. (2022). Here, changes in temperature release volatiles and thus change the electric permittivity. Analysis of these changes in capacitance reveals changes in subsurface composition over time, which is especially valuable for applications on a lander as the conditions change over time and not spatially.

Furthermore, a generic Simulation Program with Integrated Circuit Emphasis (SPICE) model with a circuit, as shown in Figure 1, has been used to analyze internal electric characteristics of the sensor. The model includes realistic properties of all components supplied by the manufacturer, and the necessary input currents and internal parasitic effects of these components can be analyzed.

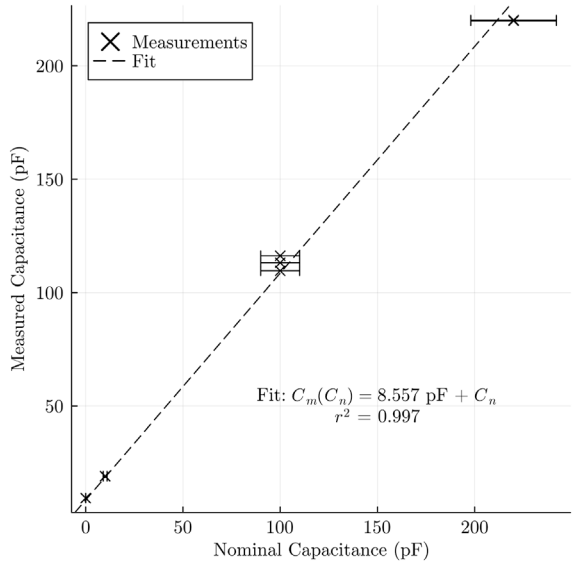

FIGURE 4
Correlation of measured over nominal capacitance for the electronics calibration.

3 Results

Materials used for the characterization of the sensor are listed in Table 1. For reference, expected values of lunar soil are also provided.

3.1 Electronics calibration

Figure 4 shows the results of the calibration experiments with capacitances of 0 pF, 10 pF, 100 pF, and 220 pF. The capacitances of test capacitors were assumed to be constant over the investigated

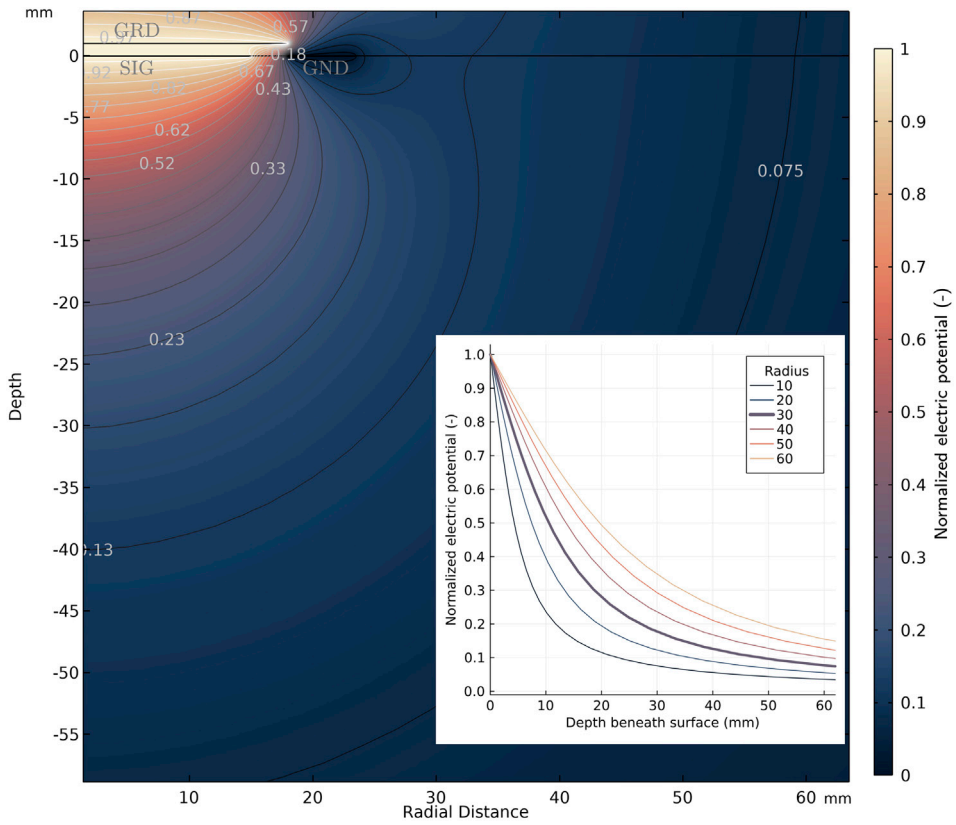

FIGURE 5
Simulated electric field normalized to its maximum excitation voltage (3.3 V) for the patch electrode (30 mm outer radius) from COMSOL simulations. The subplot shows the decline in the electric potential over depth at the central axis ($r = 0$ mm) for different electrode radii (in mm) used in the sensing depth analysis. The bold line corresponds to the depicted field.

frequency domain, and 10% nominal uncertainty is displayed. The linear fit with unity slope ($r^2 = 0.997$) returns a parasitic capacitance of 8.565 pF for the electronics board.

3.2 Simulation results

Figure 5 shows the result of the electrical simulations performed for the patch electrodes. The electric potential decreases with depth and distance from the signal electrode. Furthermore, the influence of the guard electrode is visible as the potential between the signal and guard electrode is constant, meaning that no charge is stored in this capacitance. The subplot in Figure 5 shows the decline in the electric potential with depth at the rotational axis for the evaluation of the sensing depth. The patch electrode with an electrode diameter of 60 mm has a sensing depth of 5 cm. In general, an increase in the electrode size results in an increase in sensing depth while also increasing the sensor electrode mass.

In Table 1, predicted capacitances between the signal and ground electrodes are listed based on the assumed relative permittivities of the samples. The predicted capacitances increase, and the offset for vacuum is in a reasonable range when compared to analytical models with similar characteristics, such as size and basic geometry, without the guard electrode. Predicted and measured capacitances have a correlation coefficient of 0.992.

Based on parameter studies using the simulation, the expected sensing depth increases with an increase in the electrode size, accompanied by a simultaneous increase in the expected capacitance. This correlation is in accordance with the large sensing volume of mutual impedance probes due to their spatially separated electrodes. Practically, no dependence of sensing depth on relative permittivity was observed with the current setup. However, this is expected to change once additional layers are added, for example, an air gap between regolith and electrode or an electrode protection layer.

3.3 Geotechnical properties

Figure 6 shows the results of the characterization experiments. Raw measurements are shown in Figure 6A. The curves for different materials can be clearly distinguished from one another, and the repeatability of measurements is shown. The resulting Fourier spectrum is shown in Figure 6B. Here, the characteristic peaks in the signal spectrum at $f_{peak} = (2n + 1) f_B \; \forall \; n \in \mathbb{N}_0$ (corresponding to the coefficients in Eq. 3) are clearly visible. The graph also highlights the good signal-to-noise ratio of the measurement (> 10) up to frequencies of 1 kHz with a good signal-to-noise ratio persisting over the entire frequency range (note that Figures 6B, C have been truncated in the frequency domain for better

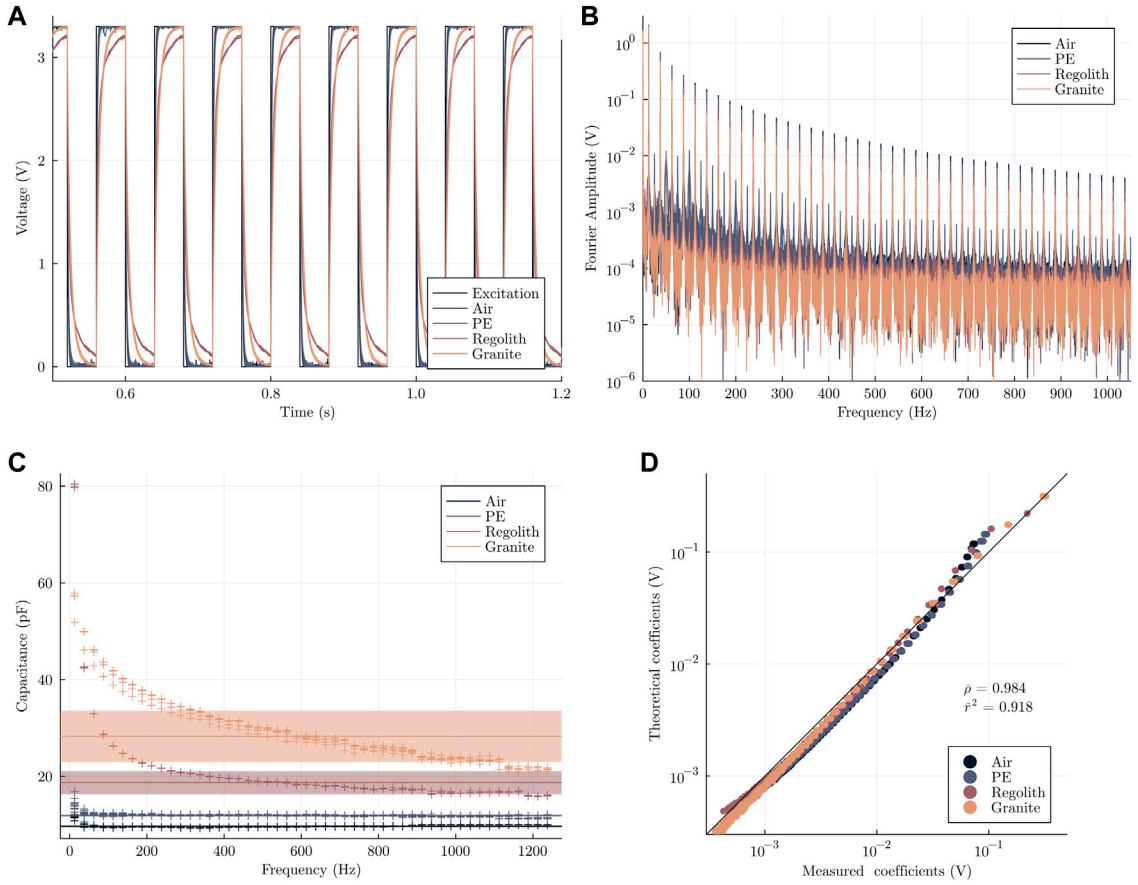

FIGURE 6
Results of the calibration with materials of known relative permittivity. **(A)** Measured time series. **(B)** Processed frequency spectrum of the time series. **(C)** Processed frequency-dependent capacitance. The ribbon shows the respective average value and one standard deviation. **(D)** Cross-plot of the measured vs predicted Fourier coefficients.

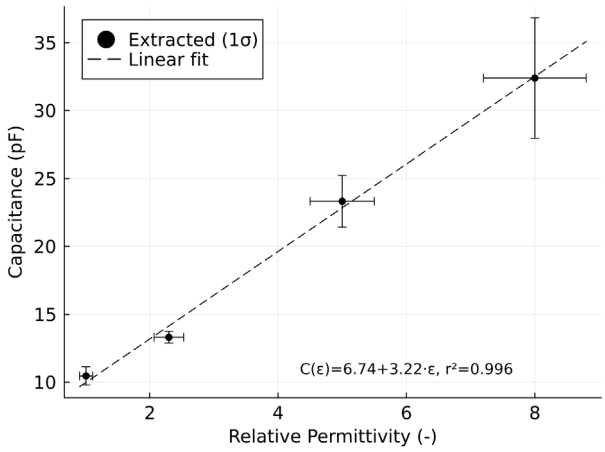

FIGURE 7
Correlation of measured capacitance over static relative permittivity. Relative permittivity error bars indicate 10% uncertainty, and capacitance error bars show 1 σ for the analysis.

visibility). Matching the measured coefficients to theoretical capacitance-dependent Fourier coefficients then yields the values illustrated in Figure 6C. Additionally, the average value and one standard deviation ribbon are plotted with the corresponding values provided in Table 1. In Figure 6D, the theoretical coefficients are plotted over the measured coefficients under the assumption of the average capacitance for each material. This returns an average correlation coefficient of $\bar{\rho} = 0.984$ and $\bar{r}^2 = 0.918$ considering all spectrums.

Figure 7 shows the resulting correlation between the relative permittivity and measured average capacitance. A linear fit to the data returns an additional parasitic capacitance of 5.948 pF and a slope of $dC_m/d\varepsilon = 2.709$ with $r^2 = 0.987$. This highlights the sensitivity of the investigated patch electrode setup with respect to changes in the sample's effective relative permittivity.

4 Discussion

The presented results show the feasibility of the novel concept of using a permittivity sensor with a patch electrode for the characterization of soil properties in the lunar exploration context. The current sensor's sensitivity is sufficient to analyze the composition and detect possible changes in the subsurface. The internal parasitic capacitance for the most recent electronics is in the same order of magnitude as the sample's capacitance.

Experiments with different samples show that the capacitance can be expressed as a function of the effective relative permittivity of the sample. The good signal-to-noise ratio in the frequency spectrum shows that unwanted noise sources can be filtered out in the data post-processing unless the noise spectrum is similar to the excitation spectrum.

Simulation and experiments show good agreement with respect to the capacitance magnitude in the low pF range and its increase with increasing relative permittivity. However, the comparison between capacitances from experiments and simulations reveals discrepancies for offset and sensitivity. The experimental data show a higher offset parasitic capacitance, which can be explained by the harness capacitance. The discrepancy in the slope can be attributed to abstractions in the numerical model, such as an omitted air gap, and to possible boundary effects in the experimental setup.

Considering the porosity values assumed for the study, these fit the mixing model to a good degree. JSC-1A in the experiments had an average porosity of approximately 0.5 and a measured capacitance between the theorized values of air and JSC-1A, which is in good agreement with the mixing rule for a stony material (such as granite) and vacuum/air. The sensor uncertainty nevertheless needs to be reduced to achieve an intended resolution of 1% for water, which will be achieved through precise sensor characterization, noise source elimination, and improved shielding.

With a maximum sensing depth of approximately 5 cm using the central depth metric, the shallow subsurface can be investigated. Albeit other sensing depth metrics could also have been used, this metric is simple to determine and interpret. Influences of non-homogeneous mixtures, such as boulders or pockets filled with ice, have not been investigated but should be detectable as the sensor measures its entire sensing domain. In these cases, a significantly different frequency response and overall porosity magnitude can be expected. Regarding the necessary sensing depth, the depth of ice stability predicted using orbital measurements and older numerical models based on these observations was greater than the sensor's sensing depth (for example, Paige et al. (2010) or Schorghofer and Aharonson (2014)). However, more recent numerical simulations exceeding the limited spatial resolution of orbital measurements, for example, by Hayne et al. (2020) or Reiss et al. (2021), predicted potential water accumulations in micro-cold traps in the shallow subsurface in lunar polar regions within the sensor's sensing depth. Therefore, the permittivity sensor has the potential to investigate the lateral distribution on these scales and confirm the existence of micro-cold traps on the Moon.

The presented sensor setup and measurement technique offer numerous advantages for lunar and planetary exploration, as their interfaces are designed with a focus on simplicity and ease of integration.

- The system has a low mass (a small backend electronics box, light electrodes on the exterior, and light harness), with the current system weighing below 100 g, including the harness.
- The electric characteristics are flexible. No specific voltage levels are required to operate the sensor as the measurements are normalized. The power required for its operation is low (currently, mostly for electronics and data processing; however, it is negligible when using an onboard computer, according to the SPICE model). The system, with its non-optimized back-end electronics, consumed an average of 1.5 W.
- Data volume is low, and handling is easily manageable as the measurements are time series data with moderate sampling frequency and duration. In addition, real-time transfer is not necessary, and compressing/optimizing the data is feasible. One uncompressed measurement has a size in the order of 500 kbyte.
- Thermal requirements are non-critical and mostly affect the electronics. Thermal tests have shown that the sensor is operational from −40°C to 60°C electronics temperature. Considering the harsh thermal conditions at the lunar poles to which sensor electrodes will be exposed (see, e.g., Paige et al., 2010), these flight models will also be tested at cryogenic temperatures to ensure mechanical and functional aptitude. Differences in the materials' coefficient of thermal expansion will be analyzed, and suitable adhesives will be used.
- With the instrument operating in ELF, noise susceptibility is low, and known sources can be filtered out during the Fourier analysis in post-processing. Additionally, the use of ELF bands reduces complexity in electronics design.
- The scientific requirement on the landing site is non-critical as the instrument can work anywhere and return data on the local subsurface. However, areas with elevated predicted surface/near-surface ice abundances are preferable for high-potential scientific return.

In comparison to the values of previous instruments given in Table 2 of Trautner et al. (2021) , the presented system's values are mostly of the same magnitude and reasonable considering the different applications. The major differences compared to the other designs are the electronics design, single electrode type, and intended accommodation. Particularly, the ability to alter the excitation frequency via software enables investigations of several frequency domains in one sample. As the signal-to-noise ratio is best close to the base frequency and gets worse with an increase in frequency, a switch of the excitation base frequency to a higher value can help characterize higher frequencies with a better signal-to-noise ratio, hence with increased confidence.

Based on the presented feasibility study, several science targets and investigation cases are conceivable. Following Biswas et al. (2020), multiple possible sites at which a mobile instrument could be used are reasonable. These include analysis around the instrument landing site to characterize the influence of the landing surface alteration and contamination, around a boulder for transient changes over a lunation, and the vicinity or interior of a permanently shadowed region for a high probability of detecting significant amounts of volatiles. These locations are also reasonable targets for a permittivity sensor system. The collected data can be used to constrain and answer the following questions:

- What is the spatial distribution of water ice on the lunar surface? Precise knowledge of the local distribution will enable better estimations of how much water ice is in the near-subsurface lunar regolith on a larger scale in correlation with remote sensing observations.
- How do the volatile distribution and state change over time? Transient analyses will allow us to further constrain and characterize the lunar water cycle and the migration of volatiles through the lunar exosphere or subsurface. Ideally,

this analysis will provide further insights into how potential cold-trapped water ice reservoirs, expected at the lunar poles, have formed and what their age might be.

- What is the density-over-depth profile of the subsurface? Data on the subsurface geotechnical properties, such as density and porosity, are not only valuable for a general understanding of the surface but also for determining its traversability and for the future applicability of *in situ* construction and *in situ* resource utilization. By measuring the bulk capacitance at various frequencies, the instrument, in principle, integrates all materials within its measurement domain. For this, the influential parameter is the relative permittivity, under the assumption that the material of the boulders is the same as the regolith (due to local scale, fragmentation, and gardening). The presence of a solid boulder within a regolith layer will effectively decrease the porosity of the sample. Furthermore, as the instrument does not penetrate the surface, boulders in the very shallow subsurface do not inhibit measurements (Bandfield et al., 2011).

Particularly, on a mobile system, the non-intrusive character of the instrument and its short duration for a single measurement are major benefits, as the path the rover takes can be closely analyzed, for example, once every wheel revolution. This can provide a very fine spatial profile of the subsurface properties for multiple conditions. In addition, as the sample is not physically disturbed by the measurement, the pristine character and transient processes can be observed in their natural state (for example, diurnal changes in volatile concentrations). Therefore, we consider rovers the preferred deployment option for the patch permittivity sensors.

Other instruments and scientific payloads can also benefit from the permittivity measurement. For ground-penetrating radars, measurement of permittivity is required to calibrate the depth information, and for sampling devices, measurement of permittivity allows us to determine or constrain the mass and density of acquired samples. Apart from its implementation as a patch electrode, the permittivity sensor concept can also be implemented in other instruments, potentially also in other bodies in the Solar System. The Lunar Volatiles Scout (LVS) is a drilling instrument with an integrated heater (Biswas et al., 2020), and the Lunar Volatiles Scout–Polar Ice Explorer (LVS-PIE) project has shown that LVS can be mounted on a small rover (Gscheidle et al., 2022). With this instrument, vertical surveys at multiple points can be performed, and the volatiles can be analyzed both in quantity and composition. Furthermore, the electrodes can be integrated into penetrators to increase the scientific return and meaningfulness of such instruments. Including additional sensors, such as thermometers and force gauges, subsurface geotechnical composition can be investigated with reasonable engineering complexity. Such sensor packages could then be used for asteroid characterization or on the icy moons of the gas giants.

5 Conclusion

Permittivity sensors are valuable additions to planetary exploration missions with few technical budget requirements. Experimental results for the novel patch electrode show sufficient sensitivity and manageable parasitic capacitance with a stable frequency response and low overall noise levels. Considering the low engineering threshold for integrating the sensors, they can be mounted even on small rovers or landers as an additional payload, providing enhanced science return. Apart from the investigated patch electrode, many different electrode geometries and configurations are possible, opening up a wide variety of mission scenarios in the planetary exploration context for which these sensors are applicable. For example, thin electrodes on penetrators, curved electrodes on wheels, or multi-pole electrodes on lander foot pads can be envisioned.

Considering these possible future flight applications, there are several fields currently under investigation for improvement: the shielding concept and noise susceptibility and the prevention of failure propagation must be further analyzed. This will enhance the general performance of the sensor and increase the concept's reliability. On the experimental side, further investigations are planned with better defined calibration materials to analyze the possibility of detecting stratification in the subsurface. The influence of the temperature range on both the measurement and instrument operation must be further analyzed. Furthermore, a heater could be included to avoid relaxation time problems. A technology readiness level of 6 is planned to be achieved within the next year.

Data availability statement

The raw data supporting the conclusion of this article will be made available by the authors without undue reservation.

Author contributions

CG: conceptualization, formal analysis, investigation, methodology, project administration, and writing–original draft. TW: formal analysis, investigation, methodology, and writing–review and editing. AS: formal analysis and writing–review and editing. PR: conceptualization, supervision, and writing–review and editing.

Funding

The author(s) declare that financial support was received for the research, authorship, and/or publication of this article. The study was performed at TUM with no additional external funding. Financial support for open access publication was provided by TUM's University Library.

Acknowledgments

The authors thank the two reviewers for their valuable comments and suggestions that led to significant improvement of this article. The authors thank the Chair of Astronautics at TUM for the internal cooperation.

Conflict of interest

The authors declare that the research was conducted in the absence of any commercial or financial relationships that could be construed as a potential conflict of interest.

Publisher's note

References

Andrews, D. (2022). "VIPER: mission design and development," in Proceedings of the 73th International Astronautical Congress (Paris, France). IAC-22,A3,2A,x67570, Baku, Azerbaijan, 2-6 October, 2023.

Bandfield, J. L., Ghent, R. R., Vasavada, A. R., Paige, D. A., Lawrence, S. J., and Robinson, M. S. (2011). Lunar surface rock abundance and regolith fines temperatures derived from LRO diviner radiometer data. *J. Geophys. Res.* 116, E00H02. doi:10.1029/2011je003866

Biswas, J., Sheridan, S., Pitcher, C., Richter, L., Reganaz, M., Barber, S. J., et al. (2020). Searching for potential ice-rich mining sites on the moon with the lunar volatiles Scout. *Planet. Space Sci.* 181, 104826. doi:10.1016/j.pss.2019.104826

Brunton, S. L., and Kutz, J. N. (2022). *Data-driven science and engineering*. second edition. Cambridge: Cambridge University Press. doi:10.1017/9781009089517

Colaprete, A., Schultz, P., Heldmann, J., Wooden, D., Shirley, M., Ennico, K., et al. (2010). Detection of water in the LCROSS ejecta plume. *Science* 330, 463–468. doi:10.1126/science.1186986

European Space Agency (2019). *ESA strategy for science on the moon, European Space Agency*. Paris: ESA. Available at: https://exploration.esa.int/web/moon/-/61371-esa-strategy-for-science-at-the-moon (Accessed 18.12.2023).

Fisackerly, R. K., Trautner, R., Heather, D., Houdou, B., Nicolae, L., Meogrossi, G., et al. (2023). "PROSPECT drilling and instrumentation package: status and next steps for flight on NASA-CLPS," in *11th European lunar symposium*.

Frigo, M., and Johnson, S. G. (2005). The design and implementation of FFTW3. *Proc. IEEE* 93, 216–231. doi:10.1109/jproc.2004.840301

Fulchignoni, M., Ferri, F., Angrilli, F., Bar-Nun, A., Barucci, M. A., Bianchini, G., et al. (2002). The characterisation of Titan's atmospheric physical properties by the Huygens atmospheric structure instrument (hasi). *Space Sci. Rev.* 104, 395–431. doi:10.1023/a:1023688607077

Grard, R., Svedhem, H., Brown, V., Falkner, P., and Hamelin, M. (1995). An experimental investigation of atmospheric electricity and lightning activity to be performed during the descent of the Huygens Probe onto Titan. *J. Atmos. Terr. Phys.* 57, 575–585. doi:10.1016/0021-9169(94)00082-y

Gscheidle, C., Biswas, J., Ivanov, D., Fernandes, D., Calzada-Diaz, A., Lamamy, J.-A., et al. (2022). Challenges of operating a drilling instrument on a small rover at the lunar poles - LVS-PIE phase A study results. *Planet. Space Sci.* 212, 105426. doi:10.1016/j.pss.2022.105426

Hayne, P. O., Aharonson, O., and Schörghofer, N. (2020). Micro cold traps on the Moon. *Nat. Astron.* 5, 169–175. doi:10.1038/s41550-020-1198-9

Haynes, W. M., Lide, D. R., and Bruno, T. J. (2016). *CRC handbook of chemistry and physics*. 97th edn. (Boca Raton, Florida, United States: CRC Press). doi:10.1201/9781315380476

Heiken, G. H., Vaniman, D. T., and French, B. M. (1991). *Lunar sourcebook: a users guide to the moon* (Cambridge England New York: Cambridge University Press).

Kargl, G., Stiegler, A., and Berghofer, G. (2011). "Measuring the permittivity on Mars: the permittivity sensor of the HP3 instrument," in *EPSC-DPS joint meeting 2011*, 1749.

Lethuillier, A. (2016). "Characterization of planetary subsurfaces with permittivity probes: analysis of the SESAME-PP/Philae and PWA-MIP/HASI/Huygens,". Ph.D. thesis (Paris: Université Paris-Saclay).

Lethuillier, A., Gall, A. L., Hamelin, M., Schmidt, W., Seidensticker, K. J., Grard, R., et al. (2016). Electrical properties and porosity of the first meter of the nucleus of 67P/Churyumov-Gerasimenko. *Astronomy Astrophysics* 591, A32. doi:10.1051/0004-6361/201628304

Li, S., and Milliken, R. E. (2017). Water on the surface of the moon as seen by the moon mineralogy mapper: distribution, abundance, and origins. *Sci. Adv.* 3, e1701471. doi:10.1126/sciadv.1701471

Looyenga, H. (1965). Dielectric constants of heterogeneous mixtures. *Physica* 31, 401–406. doi:10.1016/0031-8914(65)90045-5

Lucey, P. G., Petro, N., Hurley, D. M., Farrell, W. M., Prem, P., Costello, E. S., et al. (2021). Volatile interactions with the lunar surface. *Geochemistry* 82, 125858. doi:10.1016/j.chemer.2021.125858

Nurge, M. A. (2012). *In situ* dielectric spectroscopy for water detection on the lunar surface. *Planet. Space Sci.* 65, 76–82. doi:10.1016/j.pss.2012.01.010

Paige, D. A., Siegler, M. A., Zhang, J. A., Hayne, P. O., Foote, E. J., Bennett, K. A., et al. (2010). Diviner lunar radiometer observations of cold traps in the moon's south polar region. *Science* 330, 479–482. doi:10.1126/science.1187726

Reiss, P. (2018). A combined model of heat and mass transfer for the *in situ* extraction of volatile water from lunar regolith. *Icarus* 306, 1–15. doi:10.1016/j.icarus.2018.01.020

Reiss, P., Warren, T., Sefton-Nash, E., and Trautner, R. (2021). Dynamics of subsurface migration of water on the moon. *J. Geophys. Res. Planets* 126, 6742. doi:10.1029/2020je006742

Schorghofer, N., and Aharonson, O. (2014). The lunar thermal ice pump. *Astrophysical J.* 788, 169. doi:10.1088/0004-637x/788/2/169

Seidensticker, K. J., Möhlmann, D., Apathy, I., Schmidt, W., Thiel, K., Arnold, W., et al. (2007). Sesame – an experiment of the Rosetta lander Philae: objectives and general design. *Space Sci. Rev.* 128, 301–337. doi:10.1007/s11214-006-9118-6

Sihvola, A. (2000). Mixing rules with complex dielectric coefficients. *Subsurf. Sens. Technol. Appl.* 1, 393–415. doi:10.1023/a:1026511515005

Stiegler, A. (2011). "Mars permittivity probe calibration and instrument performance validation,". Master's thesis (Graz: Graz University of Technology).

Trautner, R., Grard, R., and Hamelin, M. (2003). Detection of subsurface ice and water deposits on Mars with a mutual impedance probe. *J. Geophys. Res.* 108, 2008. doi:10.1029/2002je002008

Trautner, R., Reiss, P., and Kargl, G. (2021). A drill-integrated miniaturized device for detecting ice in lunar regolith: the PROSPECT permittivity sensor. *Meas. Sci. Technol.* 32, 125117. doi:10.1088/1361-6501/ac261a

Zent, A. P., Hecht, M. H., Cobos, D. R., Campbell, G. S., Campbell, C. S., Cardell, G., et al. (2009). Thermal and electrical conductivity probe (TECP) for Phoenix. *J. Geophys. Res.* 114, 3052. doi:10.1029/2007je003052

Zent, A. P., Hecht, M. H., Cobos, D. R., Wood, S. E., Hudson, T. L., Milkovich, S. M., et al. (2010). Initial results from the thermal and electrical conductivity probe (TECP) on Phoenix. *J. Geophys. Res.* 115, 3420. doi:10.1029/2009je003420

frontiers | Frontiers in Space Technologies

TYPE Original Research
PUBLISHED 12 January 2024
DOI 10.3389/frspt.2023.1328341

OPEN ACCESS

EDITED BY
Antonio Mattia Grande,
Polytechnic University of Milan, Italy

REVIEWED BY
Francesco Cafaro,
Politecnico di Bari, Italy
Guang Zhang,
Chinese Academy of Sciences (CAS), China
Andrew Morse,
The Open University, United Kingdom
Ruilin Li,
China University of Mining and Technology, China

*CORRESPONDENCE
Kunal Kulkarni,
kunal.kulkarni@dlr.de

RECEIVED 26 October 2023
ACCEPTED 21 December 2023
PUBLISHED 12 January 2024

CITATION
Kulkarni K, Fabien Franke M, Jundullah Hanafi MI, Gesing TM and Zabel P (2024), Optimizing lunar regolith beneficiation for ilmenite enrichment.
Front. Space Technol. 4:1328341.
doi: 10.3389/frspt.2023.1328341

Optimizing lunar regolith beneficiation for ilmenite enrichment

Kunal Kulkarni [1]*, Michel Fabien Franke [1], Muchammad Izzuddin Jundullah Hanafi [2], Thorsten M. Gesing [2,3] and Paul Zabel [1]

[1]German Aerospace Center, Institute of Space Systems, Bremen, Germany, [2]Institute of Inorganic Chemistry and Crystallography, University of Bremen, Bremen, Germany, [3]MAPEX Center for Materials and Processes, University of Bremen, Bremen, Germany

Over the past few years, the international space industry has focused extensively on advancing technologies to enable prolonged human space exploration missions. The primary limiting factor for these endeavors is the spacecraft's capacity to transport and store essential supplies from Earth to support human life and mission equipment throughout the mission's duration. *In-situ* resource utilization (ISRU) is the preferred solution for this challenge. Previous lunar missions have identified the presence of oxygen within the lunar regolith, which is an important resource for human space exploration missions. Oxygen is present in many different minerals within the lunar regolith out of which, ilmenite provides the highest yield of oxygen per unit mass using hydrogen reduction. However, the distribution of ilmenite is neither high nor uniform throughout the lunar surface and therefore, needs beneficiation, which is an important intermediate step for ilmenite-based oxygen production. A regolith beneficiation testbed was developed at DLR Bremen which is a TRL 4 level representation of the technology. The testbed has multiple process parameters that can be adjusted to produce the desired feedstock. This work focuses on the optimization of this testbed to produce a feedstock with higher ilmenite content than the input regolith. The testbed comprises three beneficiation techniques, viz. gravitational, magnetic and electrostatic beneficiation that work sequentially to produce the desired feedstock. The optimized parameter configuration achieved up to three-fold increase in the ilmenite grade relative to the input with about 32 wt% of the total ilmenite being recovered in the enriched output. These experiments have highlighted other underlying factors that influenced the experimental research such as the design of testbed components, system residuals and limited availability for Off-the-shelf components. The observations made from these experiments have also provided insights into the further development of the technology. The work has thus produced evidence for the effectiveness of the beneficiation testbed in producing an enriched feedstock while outlining avenues for future improvements.

KEYWORDS

ISRU, beneficiation, Moon, lunar regolith, simulants, ilmenite, oxygen extraction

1 Introduction

The choice of the Moon as the destination for upcoming space missions is primarily due to its greater accessibility compared to other celestial bodies, the *in situ* experience gained during the Apollo missions and the resources present in the lunar regolith that can be extracted and used for space exploration activities. The Apollo missions by NASA and the LUNA missions by ROSCOSMOS, being the initial participants for lunar exploration, were followed by international missions such as SMART-1 by ESA, SELENE by JAXA, CHANG'E by CNSA as well as the CHANDRAYAAN missions by ISRO (Sundararajan 2006; Colaprete et al., 2012); (Foing et al., 2005); (Ouyang et al., 2010). Upon analysis of all the mission data, it is clear that the lunar regolith contains essential minerals that can be utilized for future space missions. This led to the motivation of going back to the Moon with an intention of establishing a long-term human presence in space.

The utilization of space resources is the primary solution for enabling this vision and realizing this, the global space industry has taken major steps towards the development of ISRU technologies. The lunar regolith is the most abundant natural resource on the Moon which makes it a prime candidate of raw material for future ISRU missions. The minerals in lunar regolith contain high amounts of oxygen bonded in various forms such as silicates and oxides Click or tap here to enter text (Heiken et al., 1991). The capability of producing oxygen *in situ* is not only important for supporting human life but also to produce rocket fuel for further exploration. Out of all the available minerals, ilmenite (FeTiO3) provides the highest efficiency for extraction of oxygen per unit mass with hydrogen reduction (Gibson and Knudsen 1985). However, ilmenite is predominantly only found in the lunar mare regions with very scarce deposits in the lunar highlands making it difficult to make use of its higher yield (Heiken et al., 1991). Therefore, the excavated regolith will require additional processing for producing a feedstock with high ilmenite content that can be used for producing oxygen with improved process efficiency. This additional process is called beneficiation which involves the preparation of a consistent feedstock that is rich in the target mineral and is otherwise suited for the subsequent extraction process. The higher efficiency also translates to a lower energy demand for the same amount of oxygen produced.

Ilmenite-based production of oxygen is one of the most widely studied oxygen production techniques for ISRU technologies (Bunch et al., 1979; Gibson and Knudsen, 1985). Upon successful beneficiation, the ilmenite-rich feedstock will be further reduced by using molecular hydrogen producing iron, titanium oxide and water. Hydrogen and oxygen can then be produced by subsequent electrolysis of the produced water. The chemical reactions for both processes are shown in Eqs 1.1, 1.2 respectively.

$$FeTiO_3 + H_2 \rightarrow Fe + TiO_2 + H_2O \quad (1.1)$$

$$2H_2O \rightarrow 2H_2 + O_2 \quad (1.2)$$

Some early studies of lunar regolith beneficiation were done right after the Apollo and LUNA missions. In one such study a test bed was developed to examine the separation of metallic minerals using magnetic beneficiation (Agosto, 1981; Oder, 1991). The research provided a comprehensive feasibility analysis of the magnetic beneficiation system for lunar regolith along with the necessary resources for its implementation in future space missions. The results from another study on regolith beneficiation for ilmenite enrichment show an average eleven-fold increase in the concentrations of ilmenite going from 7.9 wt% to 90 wt% after a single pass in a nitrogen environment with a reduced enrichment in vacuum conditions (Agosto, 1985). More recently, a concept called the Lunar Soil Particle Separator (LSPS) was proposed for beneficiation of lunar regolith (Berggren et al., 2011). It comprises different stages starting with a particle size separator followed by magnetic and electrostatic separation stages which is similar to the testbed used for experiments presented in this work. The experimental results from LSPS show an increase in the recovery and grade of target minerals such as iron oxides and ilmenite using the multi-stage sequential approach. In summary, prior research provides robust evidence for the efficacy of beneficiation techniques in concentrating specific lunar regolith materials, serving as benchmarks for this study, aiming to beneficiate the lunar regolith for producing a feedstock enriched with ilmenite.

2 Materials and methods

2.1 Experimental setup

The testbed used for the beneficiation experiments discussed within this research was developed at the DLR, Institute of Space Systems in Bremen (Franke, 2019). Figure 1 illustrates the fully assembled testbed highlighting the relevant components. The components are arranged vertically so that the gravitational force

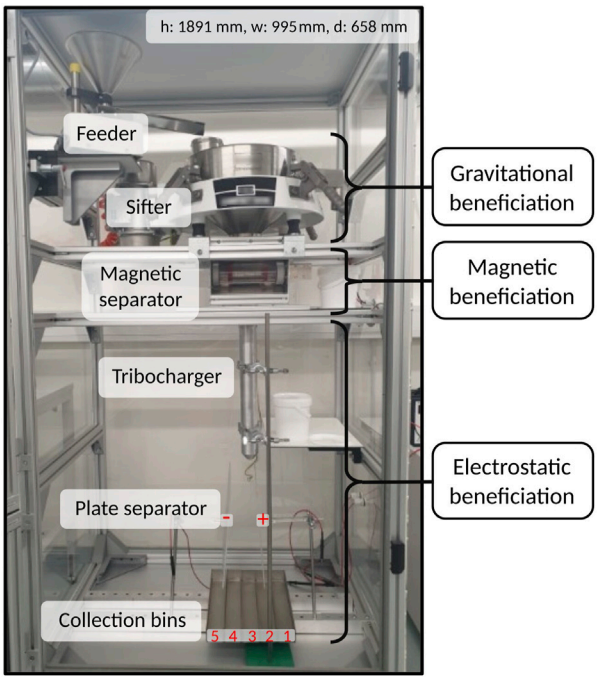

FIGURE 1
Lunar regolith beneficiation testbed.

is the primary mode of conveyance. The testbed has a height of 1891 mm, a width of 995 mm, and a depth of 658 mm. The entire setup is encapsulated in an assembly of aluminum profiles, plates, and various fixation elements.

Laborette 24, a vibratory feeder produced by *Fritsch GmBH* is the inlet for the testbed. This allows for a constant and controlled flow of regolith into the system. The feed rate can be adjusted manually using its control panel. The output of the feeder is a V-shaped channel that is connected to the further stages of beneficiation. The testbed comprises three beneficiation strategies: gravitational, magnetic, and electrostatic beneficiation respectively.

The first stage is gravitational beneficiation, which consists of the *Russel Compact Sieve*, a horizontal vibratory sifter used for the segregation of particles based on their size All particles with a diameter greater than 200 µm are removed at this stage. It is known from the Apollo samples that the ilmenite grain size ranges from 45–500 µm with highest concentrations in the 45–75 µm range (Heiken et al., 1991). Therefore the sifter indirectly increases the ilmenite grade while also achieving the correct feedstock size for subsequent processes.

The finer particles that are smaller than this threshold are transferred to the second stage of magnetic beneficiation. This stage uses a permanent magnet drum separator, developed at DLR Bremen, to segregate minerals based on their respective magnetic susceptibilities. It consists of an outer cylinder made from polycarbonate, which rotates at a user-defined rotational speed, and a stationary inner cylinder that holds permanent, arc-shaped neodymium-iron-boron (NdFeB) magnets. The fine particles from the sieve are fed into the magnetic separator from above, directly onto the rotating cylinder. As a result, the weakly magnetic particles fall off the drum sooner than the magnetic ones which remain adhered to the drum until they reach the last of the magnets and then get brushed off into a separate outlet. The goal of this stage is to remove the ferromagnetic agglutinates and metallic dust particles from the regolith leaving behind para- and diamagnetic minerals such as ilmenite, olivine, and other tailings.

These para- and dia-magnetic minerals are further transferred to the third stage of electrostatic beneficiation. The subprocess that is employed in the testbed's electrostatic separator is called tribocharging with plate separation. The tribocharger consists of a metallic spiral, which is used as an electrode to impart charge on the regolith particles via the triboelectric effect. This effect is directly related to the molecular content of the minerals. According to theory, the poorly chargeable ilmenite should retain little to no charge (due to its relatively high conductivity), while olivine and other tailings are expected to gain a net negative charge. A detailed analysis for the behavior of different regolith particles with tribocharging can be found in the testbed design document (Franke, 2019). The charged particles are then passed through a parallel plate separator that creates a homogeneous, high-voltage electrostatic field. Prior studies indicate a broad spectrum of field voltages that could be beneficial for ilmenite enrichment and are taken into consideration for the optimization experiments (Li et al., 1999; Trigwell et al., 2006; Trigwell et al. 2009; Trigwell et al. 2013). Due to the differences in developed charges, the particles are directed on different, distinguishable trajectories, which allows their collection in an array of bins with defined positions from the center of the tribocharger outlet. For more details on the internal assembly design of the magnetic and electrostatic separators please refer the Supplementary Material document.

TABLE 1 List of adjustable process parameters of the beneficiation testbed.

Beneficiation stage	Process parameter	Unit	Range
Gravitational beneficiation	Feed rate	$kg*h^{-1}$	0–28.82
	Sieve size	µm	200[a]
Magnetic beneficiation	Motor rotational speed	rpm	0–1324
Electrostatic beneficiation	Electrostatic field voltage	kV	0–25
	Plate separation distance	mm	200[b]

[a]A different sieve size can be used but the current configuration remains fixed at 200 µm.
[b]The plate separation distance can be changed at regular intervals of 100 mm.

2.2 Beneficiation process parameters

The beneficiation testbed features a range of process parameters, as outlined in Table 1, which allow for adjustments to enhance the system's beneficiation performance. This study concentrates on optimizing three critical parameters: feed rate (f), motor rotational speed (ω_m), and electrostatic field voltage (V). To maintain consistency and minimize experimental variables during the initial optimization phase, the other parameters remain fixed.

2.3 Beneficiation performance quantification

The testbed's beneficiation performance is quantified through the utilization of parameters outlined in Table 2.

The yield and recovery together represent the material processing efficiency of the system while the grade and enrichment ratio indicate the degree of separation for ilmenite achieved with the beneficiation methods. An optimized system should exhibit good performance across both categories.

2.4 Lunar regolith simulants for experimental analysis

Analysis of samples from the Apollo missions indicates that the lunar mare regions generally contain a higher average ilmenite content in the regolith compared to the lunar highlands (Heiken et al., 1991). Hence, the LMS-1 simulant from *Exolith Lab* and the TUBS-M-based modular regolith from the *Technische Universität Berlin*, both representing the lunar mare regions, were consequently selected for the optimization experiments (Exolith Lab, 2014; Linke et al., 2020). The custom version of the TUBS-M-based modular regolith simulant used in this work is labeled as TMIA4 indicating the presence of TUBS-M base simulant, 4 wt% ilmenite, and agglutinates. Table 3 presents a comparative analysis of both simulants.

TABLE 2 Beneficiation parameters used for quantification of system performance Click or tap here to enter text (Hadler et al., 2020).

Parameter	Unit	Formula	Description
Yield	wt%	$\frac{M_{tm,o}}{M_i}$	The total mass of ilmenite in the output per unit mass of input material
Recovery	wt%	$\frac{M_{tm,o}}{M_{tm,i}}$	The mass of ilmenite in the output per unit mass of ilmenite in the input material
Grade	wt%	$\frac{M_{tm,o}}{M_o}$	The mass of ilmenite in the output per unit mass of output material
Enrichment ratio	-	$\frac{G_o}{G_i}$	Ratio of grade of ilmenite in the output material to the grade of ilmenite in the input material

TABLE 3 LMS-1 and TUBS-M based modular regolith simulant comparative analysis (Exolith Lab, 2014; Linke et al., 2020).

Parameter	LMS-1	TMIA4
Grain density [g/cm^3]	2.92	2.96
Angle of repose [°]	38.3	41.9–45.8
Ilmenite content [wt%]	4.03	4.00
Mean particle size [μm]	91	87
Particle size distribution [μm]	0.04–1000	0–2000

2.5 Characterization of experimental samples

2.5.1 X-ray powder diffraction analysis

Ilmenite rock, two lunar regolith simulants (LMS-1 and TUBS-M), and several samples from various input parameter configurations were ground for phase analysis by X-ray powder diffraction (XRPD). The data collection was carried out on a Bruker D8 DISCOVER X-ray diffractometer equipped with CuK$_{\alpha1,2}$ radiations ($\lambda_{K\alpha1}$ = 154.05929 (5) pm, $\lambda_{K\alpha2}$ = 154.4414 (2) pm) in Bragg–Brentano geometry. The data were collected at ambient conditions from 5° to 85° 2θ with a step width of 0.0149° 2θ and a measurement time of 0.42 s per step using an energy-discriminating LynxEye-XET multi-strip detector. Ilmenite rock sample was measured for longer time (7.7 s per step) to obtain better intensity to noise ratio. The Rietveld refinements of the XRPD data were performed using the available software suite (TOPAS V6.0, Bruker AXS). Rietveld refinement of ilmenite rock was used as a reference for phase quantification of the simulants and the experiment samples.

2.5.2 Microscopy

An additional elemental analysis was employed on the ilmenite sample by scanning electron microscopy/energy dispersive X-ray (SEM/EDX) spectroscopy. SEM was carried out using a JMS-6510 (JEOL) equipped with an X-Flash 410-M detector (Bruker) for EDX spectroscopy. A small amount of ilmenite was taken on conducting carbon tabs and sputtered with gold for 20 s with a JFC-1200 coater (JEOL) followed by inserting it into the SEM chamber.

2.6 Experimental approach

2.6.1 Systematic approach to planning and conducting experiments

A multi-phase optimization strategy is implemented to efficiently optimize the beneficiation testbed. Initially, all experiments are conducted with the LMS-1 simulant. In total, the experiments are categorized into four phases *viz.* phase 0, A, B, C, and D respectively. Phase 0 encompasses preliminary experiments and primarily validating the operational aspects of all testbed components. The insights gained from these experiments inform subsequent optimization efforts.

In phase A, the optimization of magnetic and gravitational beneficiation stages is achieved by conducting experiments across varying feed rates and rotational speeds of the magnetic separator while analyzing the beneficiation performance. This phase also aims to validate the magnetic separator's operational design.

Phases B and C concentrate on optimizing electrostatic beneficiation. Phase B investigates the output from the electrostatic plate separator across the entire range of possible field voltages. Phase C investigates the system output further across a field voltage range of ±2 kV relative to the optimum voltage from Phase B, determining the optimized process parameters for producing the desired feedstock.

Phase D is dedicated to validating system repeatability and reliability post-optimization. The optimized parameter configuration is applied to the TMIA4 simulant system, and the resulting beneficiation output is compared to phase C results. Any disparities in outcomes are examined to analyze the simulant-specific behavior of the beneficiation testbed, ultimately determining its applicability across diverse lunar regions.

Every experiment is conducted with a 300 g input sample. In order to compensate for experimental deviations, every configuration of process parameters is tested three times and the average of all the trials is considered for further analysis.

2.6.2 Experiment procedure

A standardized experimental procedure is adopted for the optimization to mitigate experimental variations thereby achieving reliable results. The procedure for this study is divided into multiple steps, each crucial for obtaining reliable and meaningful results.

The first step is sample preparation, which involves drying the simulant samples at 80°C for a duration of 48 h. Once dried, they are stored in airtight containers to prevent moisture absorption. For each experiment, a consistent amount of 300 g of dried sample is then dispensed.

The second step, experiment machine setup, is essential to ensure accurate and controlled conditions. During this step, the machine parameters are configured according to the predefined process parameter settings for the specific experiment. Subsequently, the dried sample is loaded into the feeder, which marks the readiness for the experimental run.

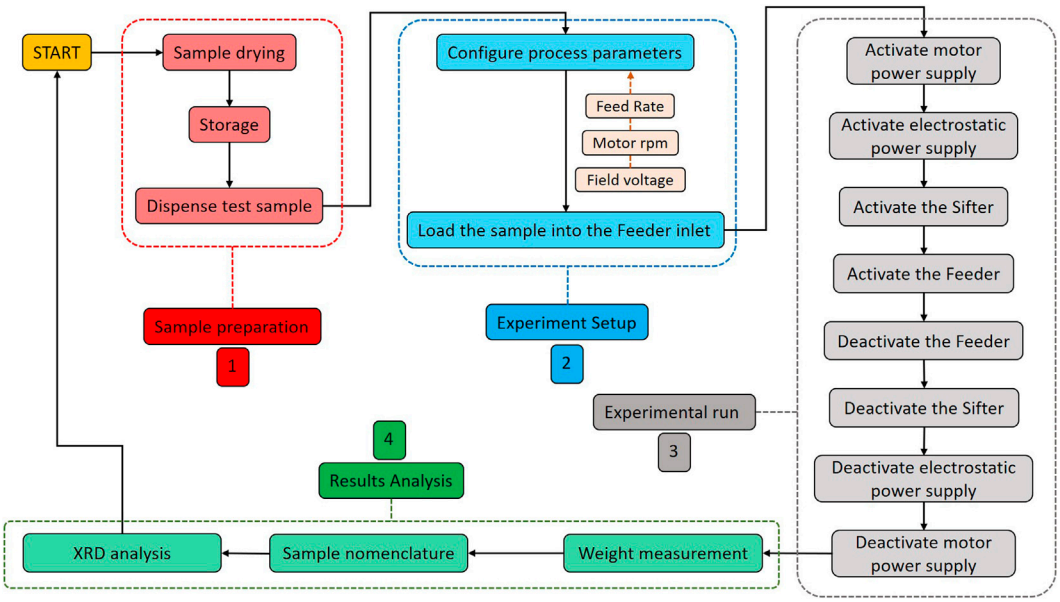

FIGURE 2
Experimental procedure for optimization of beneficiation testbed.

The third step, the experimental run, is the core of the procedure. This is where the actual experiment is conducted based on the set parameters. It involves activating different stages of beneficiation in a predefined sequence to process the sample thoroughly.

The final step, results analysis, is critical for interpreting and understanding the outcomes. Firstly, all system outlets are carefully weighed. The collected samples undergo XRPD analysis, which provides insights into the mineral composition and phase characteristics of the samples. The diffraction intensities are directly related to crystal structure and the amounts of each phase, hence a precise quantitative analysis with detection limit of 1.3 wt% is yielded from the well-known Rietveld method (Bish and Chipera, 1994; Reid and Hendry, 2006; Bish and Plötze, 2010; Xie et al., 2017). The XRPD results are used for analyzing system beneficiation performance using the performance parameters discussed in Section 3.3. Figure 2 gives an overview of the experimental procedure.

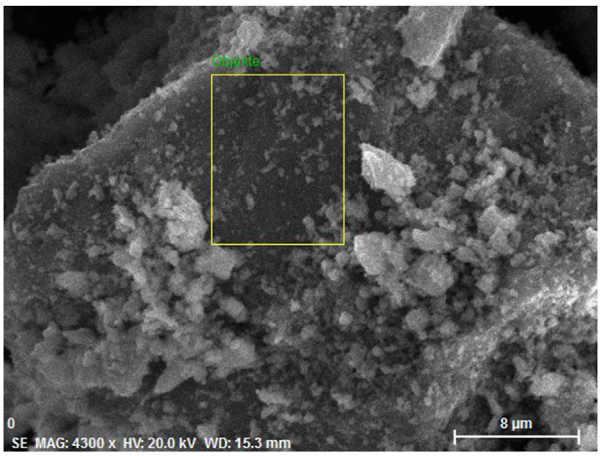

FIGURE 3
Representative scanning electron micrographs of ilmenite sample.

3 Results

3.1 Ilmenite characterization

In order to identify the elements, present in an ilmenite sample, a SEM/EDX analysis was conducted. Selected electron micrographs of ilmenite powder are provided in Figure 3. EDX spectra were analyzed for concentration of different elements contained in ilmenite. It can be inferred that there is a dominance of titanium and iron (69 and 28 wt%, respectively) in the tested samples.

X-ray powder data Rietveld refinement were employed to have a precise phase quantification of the sample. This characterization method confirms that ilmenite rock comprises of 12 phases. Among them, rutile (TiO_2), moganite (SiO_2), iron titanium oxide ($(FeTiO_3)_{0.8}(Fe_2O_3)_{0.2}$) and hematite ($Fe_2O_3$) can be considered as major phase (>10 wt%). These four major ilmenite-associated phases were summed as reference and designated as grade (see Section 2.3) to quantify the Lunar simulants and output testbed samples. XRPD Rietveld refinement plot of the tested ilmenite sample is given in Figure 4.

3.2 Lunar simulants characterization

Lunar simulants of TMIA4 and LMS-1 were subjected to XRPD characterization to examine the presence of four major ilmenite-associated phases. XRPD Rietveld plots of both simulants are depicted in Figures 5, 6. Several phases such as enstatite ferroan,

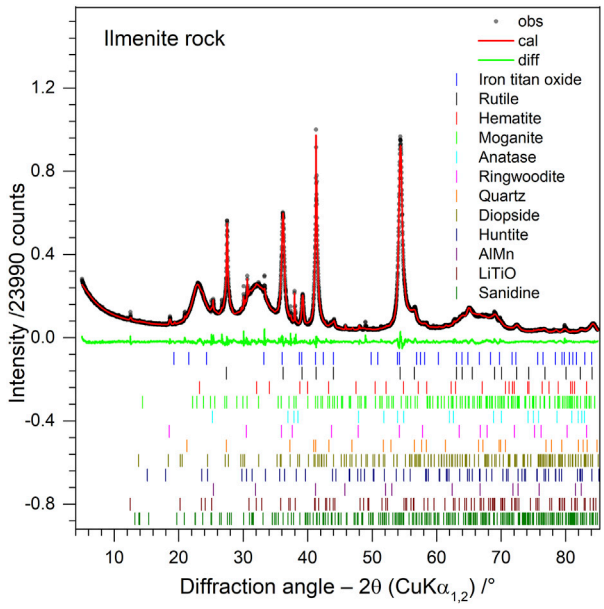

FIGURE 4
X-ray powder data Rietveld plot of ilmenite.

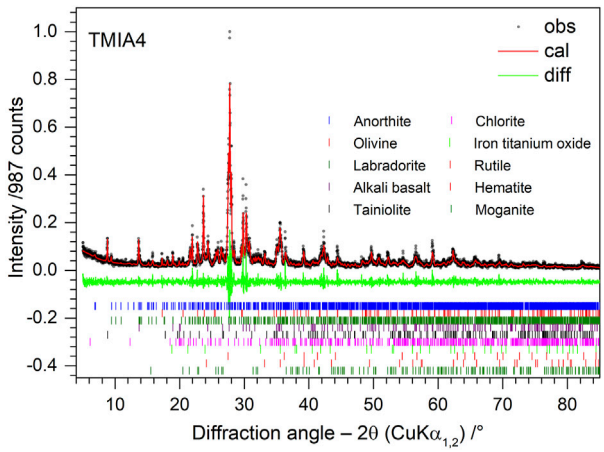

FIGURE 5
X-ray powder data Rietveld plots of TMIA4.

quartz, chabazite, and amphibole were only found in LMS-1. Among the main interests, all four major ilmenite-associated phases were identified in TMIA4, whereas LMS-1 does not contain any hematite. The phase quantifications give approximately 2.8 (4) and 1.6 (2) wt% grade of ilmenite in TMIA4 and LMS-1, respectively. The numbers in brackets are the calculated estimated standard deviations of the obtained values in the last digit.

3.3 Phase 0: preliminary experiments

The primary aim of the preliminary experiments was to test the operational designs of the testbed components and ensure their

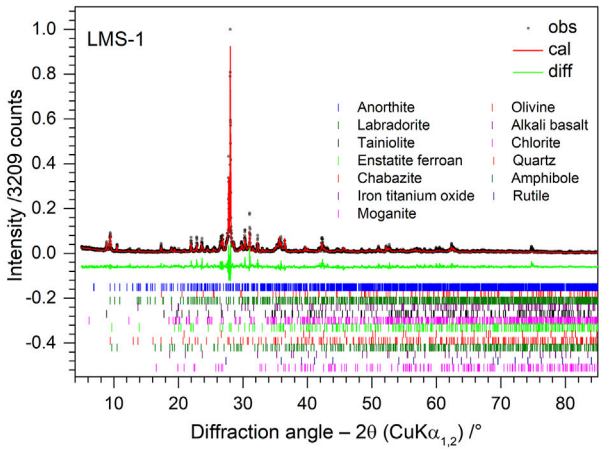

FIGURE 6
X-ray powder data Rietveld plots of LMS-1.

functionality. It was observed that at feed rates lower than 6.14 kg*h^{-1}, the dust build-up on the feeder output rail is significant and reduces the effective feed rate. This corresponds to a higher maintenance frequency for cleaning the output rail and retaining the processing speed. Moreover, a major challenge was observed with magnetic beneficiation. The selected motor configuration did not possess the requisite torque, limiting the adjustment of rotational speeds. Consequently, the optimization experiments were confined to a fixed rotational speed of 794 rpm for the magnetic separator.

3.4 Phase A: optimization of gravitational and magnetic beneficiation

The primary aim of this phase is to study the effects of changing feed rate and rotational speeds on the beneficiation outcome. As the preliminary experiments concluded, the magnetic separator's rotational speed remains fixed at 794 rpm due to design limitations. Therefore, experiments are performed at different feed rates. The samples from the magnetic and non-magnetic outputs are analyzed for beneficiation performance. Figure 7 shows the average grade of ilmenite at different feed rates for the magnetic and non-magnetic output samples. It can be seen that the average grade of ilmenite for the non-magnetic output is in the range of 2.23–2.85 wt% while that in the magnetic output is in the range of 0.37–0.77 wt%. This validates the ability of the magnetic beneficiation stage to remove ferromagnetic agglutinates from the regolith leaving behind most of the ilmenite in the non-magnetic output.

Figure 8 illustrates the ilmenite grade within the non-magnetic output samples at different feed rates. Across the entire range of tested feed rates, the average grade of ilmenite varies only by 0.62 wt% with a minimum of 2.23 wt% and a maximum of 2.85 wt%. This indicates that variation in feed rate has less impact on the average ilmenite grade. Consequently, these findings lead to the conclusion that, within the testbed, the feed rate exerts minimal influence on the magnetic separator's

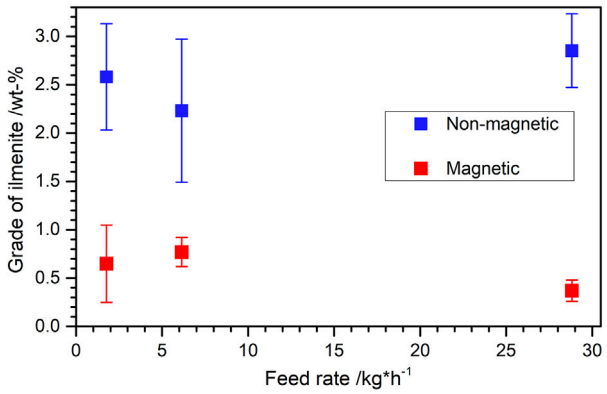

FIGURE 7
Average grade of ilmenite at varying feed rates (Phase A).

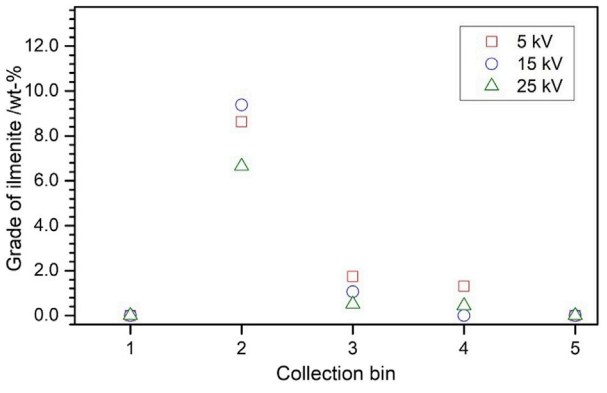

FIGURE 9
Distribution of ilmenite grade across the collection bins (Phase B).

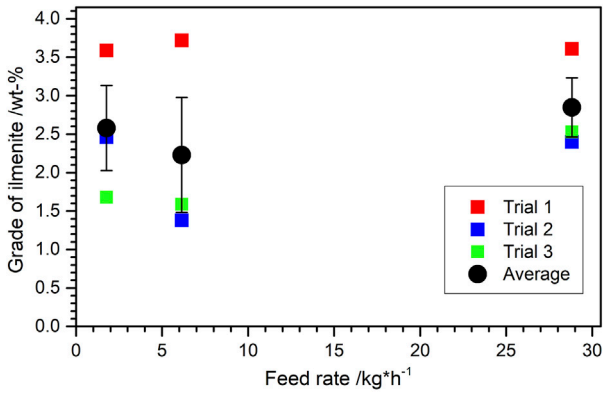

FIGURE 8
Grade of ilmenite across feed rate for all non-magnetic output samples (Phase A).

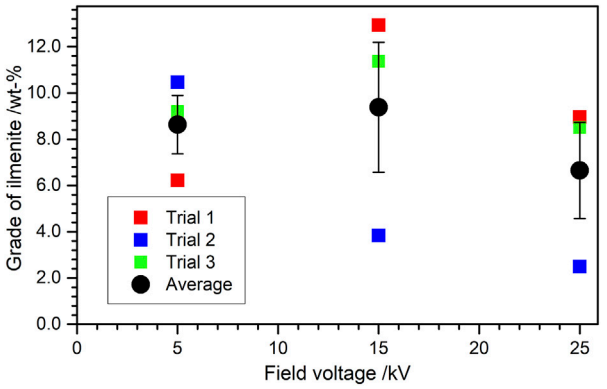

FIGURE 10
Grade of ilmenite for samples from collection bin 2 at different field voltages (Phase B).

beneficiation performance. Considering the increased maintenance frequency observed at lower feed rates during the preliminary experiments as well as the material processing capacity for the magnetic separator which cannot process high amount of regolith at the same time due to its smaller dimensions, the value of 6.14 kg*h^{-1} is chosen with the rotational speed of 794 rpm for further optimization.

3.5 Phase B: optimization of electrostatic beneficiation (first iteration)

This phase of optimization focuses on the electrostatic beneficiation stage, specifically the voltage of the electrostatic parallel plate separator. It was decided to test the beneficiation performance across all available field voltages from 0–25 kV and analyze the results. This is split into two stages. The first iteration (Phase B) involves experiments at larger intervals to encompass the entire available range. The next iteration (Phase C) will then choose a narrower range depending on the results from this phase of experiments.

An important aspect of understanding the effectiveness of electrostatic beneficiation is to determine the distribution of ilmenite across the five collection bins. This examination aims to identify the bin with the highest ilmenite concentration, thereby yielding the desired enriched feedstock. As shown in Figure 9, it is observed that the grade of ilmenite in bin 2 lies in the range of 6.65–9.38 wt% across all tested field voltages. In contrast to this, the grade of ilmenite in bins 3 and 4 lies in the range 0.44–1.74 wt% which is much lower compared to the samples from bin 2. Moreover, the bins 1 and 5 collect no sample material in any of the experimental configurations. Therefore, collection bin 2 is considered as the desired output with ilmenite-enriched feedstock. As a result, further analyses are performed with samples from the collection bin 2.

Figure 10 shows the grade of ilmenite for samples from collection bin 2 at varying field voltages. The plotted average data points exhibit a consistent rise in grade from 8.63 wt% to 9.38 wt% when increasing the field voltage from 5 to 15 kV, followed by a decrease to 6.65 wt% at 25 kV. Based on this analysis, it is concluded that field voltages near 15 kV are more likely to produce the desired

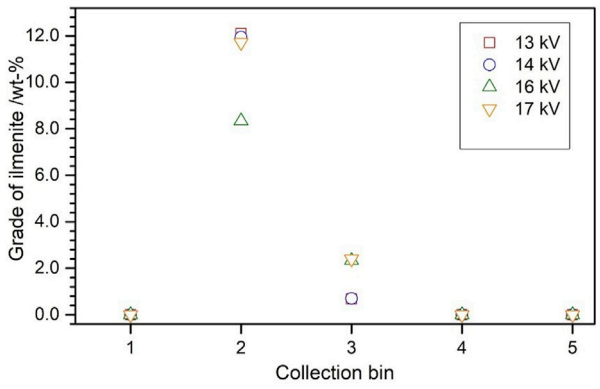

FIGURE 11
Distribution of ilmenite grade across the collection bins (Phase C).

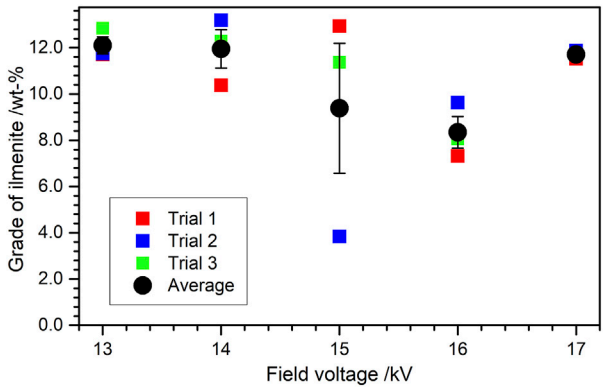

FIGURE 12
Grade of ilmenite for samples from collection bin 2 at different field voltages (Phase C).

results. Consequently, 15 kV is chosen as the reference for the next iteration of optimization.

3.6 Phase C: optimization of electrostatic beneficiation (second iteration)

The phase C experiments follow a similar procedure as in phase B, focusing on a narrower range of field voltages. Given the favorable beneficiation outcomes achieved at 15 kV, it serves as the reference point. Consequently, a range spanning from 13 kV to 17 kV is chosen, with a testing interval of 1 kV. The objective is to assess the testbed's beneficiation performance within this smaller voltage range and determine the optimized field voltage value.

An analysis of the ilmenite grade across all collection bins is conducted to reaffirm the earlier findings. As depicted in Figure 11, the results align closely with the previous analysis with an ilmenite grade between 11.71–12.10 wt% in bin 2 while only about 0.68–2.33 wt% in bin 3 with no material collected in bins 1, 4 and 5. As the collection bin 2 consistently exhibits a higher average ilmenite grade, only the samples from bin 2 are considered for subsequent analyses.

Figure 12 illustrates the grade of ilmenite across the narrower range of field voltages (13–17 kV). The grade of ilmenite does not follow a consistent trend in this narrow range and therefore, it is not independently conclusive about the most optimum configuration of process parameters for producing the desired feedstock.

Therefore, a trade-off between the four beneficiation parameters is conducted for all samples collected in bin 2 at the field voltages used in this phase. The results of experiments performed at 15 kV from the previous phase are also considered for reference. Table 4 shows the beneficiation parameters at different field voltages. It is observed that at 13 kV, the system produces the highest concentration of ilmenite indicated by the grade of 12.10 wt% and enrichment ratio of 3.00. This shows a higher degree of separation for ilmenite achieved at 13 kV. In contrast to this, at 17 kV, the yield and recovery are the highest at 1.33 wt% and 33.00 wt%, respectively, indicating a higher material processing efficiency. However, this also translates to the recovery of more unwanted material which is indicated by the reduced grade and enrichment ratio of 11.71 wt% and 2.90, respectively.

An optimized solution, considering all the relevant factors, is evident at 14 kV. This configuration yields an ilmenite yield of 1.29 wt%, a recovery of 31.93 wt%, a grade of 11.95 wt%, and an enrichment ratio of 2.96, representing the second-highest values across all the beneficiation performance parameters. Therefore, the final optimized configuration of parameters derived from the experiments in phases A, B, and C is established as follows: f = 6.14 kg*h^{-1}, ω_m = 794 rpm, and V = 14 kV.

3.7 Phase D: validation of optimized configuration with TMIA4 simulant

The phase D experiments are focused on the validation of the optimized performance of the beneficiation testbed on a different simulant. The aim is to test the repeatability and reliability of results generated in the previous experiments. The experiments in this phase are performed with the TMIA4 simulant using the optimized parameter configuration from the phase C results.

The first step of this validation is to study the distribution of ilmenite across the collection bins and compare it to the previous results. As shown in Figure 13, similarly to previous results the collection bin 2 has a higher average ilmenite grade varying between 7.97–9.07 wt% across all the trials. However, the grade of ilmenite in bin 3 is higher than that in the previous experiments. The average grade of ilmenite in bin 3 is 5.64 wt% at 14 kV which is eight times more than that as seen with LMS-1. This indicates a potential for further optimization of the process with TMIA4.

A comparative analysis of the beneficiation parameters for ilmenite with the optimized parameter configuration from phase D with TMIA4 simulant and phase C with LMS-1 simulant is illustrated in Table 5. The LMS-1 simulant demonstrates a higher degree of separation of ilmenite evidenced by the grade of 11.95 wt% and enrichment ratio of 2.96 which are both higher than that of TMIA4. However, TMIA4 exhibits a higher efficiency of material processing which is evidenced by the higher yield of 1.49 wt% and recovery of 37.02 wt% in the produced feedstock. One of the factors

TABLE 4 Beneficiation parameters for ilmenite at different field voltages with standard error in brackets (Phase C).

Field Voltage/kV	Yield/wt%	Recovery/wt%	Grade/wt%	Enrichment ratio
13	0.84 (0.12)	20.78 (2.96)	12.10 (0.37)	3.00 (0.09)
14	1.29 (0.27)	31.93 (6.69)	11.95 (0.82)	2.96 (0.20)
15	1.28 (0.79)	31.76 (19.59)	9.38 (2.8)	2.33 (0.69)
16	1.10 (0.26)	27.22 (6.46)	8.34 (0.68)	2.07 (0.16)
17	1.33 (0.55)	33.00 (13.55)	11.71 (0.10)	2.90 (0.02)

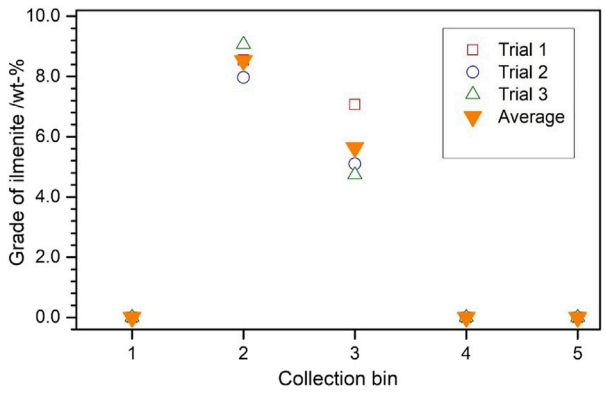

FIGURE 13
Distribution of ilmenite grade across the collection bins (Phase D).

TABLE 5 Comparison of beneficiation results with LMS-1 and TMIA4 with standard error in brackets.

Beneficiation parameter	LMS-1	TMIA4
Yield/wt%	1.29 (0.27)	1.49 (0.58)
Recovery/wt%	31.93 (6.69)	37.02 (14.46)
Grade/wt%	11.95 (0.82)	8.53 (0.31)
Enrichment Ratio	2.96 (0.20)	2.11 (0.07)

for this discrepancy is the higher aspect ratio of particles in the TMIA4 simulant compared to that of the LMS-1 (Exolith Lab, 2014; Linke et al., 2020). However, further experiments with TMIA4 are indeed necessary for making more reliable claims about the simulant-dependent behavior of the beneficiation testbed. These results reveal a comparable beneficiation performance of the system across both the simulant systems.

4 Discussion

The experiments encountered specific limitations that prevented the complete optimization of the system. One major challenge was experienced with the selected motor configuration for the magnetic separator. The selection primarily revolved around the necessary rotational speed, but the final assembly revealed a lack of torque provided by the motor. Consequently, the rotational speed of the magnetic separator remained fixed, and optimization of this stage could not be undertaken within the scope of this study. Another limitation of this research was regarding the smaller sample size of three trials for every parameter configuration. This is reflected in the deviations seen from the experimental results. The experimental deviations can also be attributed to the in-homogeneity of the regolith simulants which could not be verified within the scope of this research. These limitations should be taken into consideration while evaluating future beneficiation experiments.

A peculiar observation was made during the optimization experiments regarding the system residuals. Despite ensuring a clean setup for each new parameter configuration to prevent sample contamination, it was consistently observed that the amount of residuals decreased and eventually stabilized at a constant level with each experimental run. This phenomenon suggests that the system residuals can reach a saturation point over time, maintaining a steady state during continuous operation. Consequently, this observation hints at the possibility of improving the system's material processing efficiency, potentially resulting in more consistent system performance.

This work also underscores the influence of constraints associated with the availability of off-the-shelf equipment for the particle sizing stage of the testbed, which initially led to high residuals. During the testbed development phase, the majority of available commercial vibratory sifters had high processing capacities, and therefore the choice was made with the lowest possible alternative. However, this led to substantial residuals when used with smaller batches as discussed in this work, which negatively impacted material processing efficiency, a concern that would otherwise be neglected with larger batches. Therefore, future developments in ISRU technologies, particularly those dealing with processing planetary regoliths, will need additional alternatives to address the disparity between equipment demand and supply.

In regards to the future implementation of a beneficiation system on the lunar surface, multiple variables need to be considered. First of all, the reduced gravity on the lunar surface will affect such a system to high degrees. Specifically, the processing speed of the setup will likely decrease due to reduced gravitational acceleration. However, the reduced speed will benefit the electrostatic beneficiation stage as the particles will travel longer through the electrostatic fields, providing more time for the field forces to deflect their trajectories further apart from each other. Moreover, the vacuum environment is claimed to improve the

beneficiation performance further according to previous research (Agosto, 1985). However, in orderto support the oxygen production infrastructure of an entire lunar base, the feedstock requirements are expected to be in the order of tons every day (Cilliers et al., 2020; Colozza, 2020; Cilliers et al., 2020). The current design has limitations to its scalability to support such infrastructures and would need to be considered for future developments of the system. Upon successful scaling up of the design, the expected outcomes are expected to show similar or even better results as the relative quantity of residual material reduce with increased overall processing quantity.

It should be noted that while this research focuses on ilmenite as the target mineral, the underlying principles of beneficiation can be extended to the processing of other minerals present in lunar or even martian regoliths too whichopens up more avenues for future research and development in the field.

5 Conclusion and outlook

The experimental analysis of the lunar regolith beneficiation testbed has yielded promising results and the optimization process was successful in identifying the optimal configuration of process parameters for producing an ilmenite-rich feedstock. It is evident from this analysis that the improvement in beneficiation parameters of the produced feedstock takes place gradually with every optimization phase. The grade of ilmenite in the output went from 2.55 wt% in phase A to 9.00 wt% in phase B and further to 12.00 wt% in phase C. A similar increase of enrichment ratio from 0.71 in phase A, to 2.33 in phase B and 2.96 in phase C is observed. This demonstrates the effectiveness of the developed strategy in optimizing the beneficiation performance of the testbed. The final results show that up to 32 wt% of the total ilmenite from the input regolith simulant is recovered in the produced feedstock with the optimized parameter configuration.

The total time for processing 300 g of regolith simulant is about 30 min resulting in an average energy consumption of about 61 Wh for the entire testbed. The discovery of the peculiar crystal structure of ilmenite used in the regolith simulants was also accomplished during the XRPD measurements. This analysis will further enable the development of processing techniques for lunar as well as other planetary regoliths.

In summary, this work has successfully demonstrated the feasibility as well as optimization capabilities of a small-scale, TRL 4 lunar regolith beneficiation testbed. Through a systematic approach, the process parameters of the system have been investigated and refined to achieve improved beneficiation outcomes. The optimization experiments have demonstrated the effectiveness of the testbed in producing ilmenite-rich feedstock, with measurable improvements observed in the grade, recovery, and enrichment ratio of ilmenite. The comparative analysis of different simulant systems highlights the adaptability and repeatability of the implemented beneficiation processes. In summary, the authors anticipate that this study will enhance comprehension of the optimization of lunar regolith beneficiation processes and offer insights into prospective research directions and practical applications in the realm of space exploration and resource utilization.

Data availability statement

The raw data supporting the conclusions of this article will be made available by the authors, without undue reservation.

Author contributions

KK: Formal Analysis, Investigation, Methodology, Writing–original draft, Writing–review and editing. MF: Writing–original draft. MJ: Writing–original draft. TG: Writing–review and editing. PZ: Writing–review and editing.

Funding

The author(s) declare financial support was received for the research, authorship, and/or publication of this article. The development of the beneficiation testbed and all related expenses were funded by the DLR internal funding sources. Contributions of MJ and TG is financially supported through the APF project “Materials on Demand” within the “Humans on Mars” Initiative funded by the Federal State of Bremen and the University of Bremen.

Acknowledgments

The first author would like to thank Prof. Dr.-Ing. Enrico Stoll and Joel Patzwald from the *Technische Universität Berlin*, for providing the TUBS-M simulants as well as the laboratory facilities for producing the TMIA4 simulant mixture used in the experiments presented here.

Conflict of interest

The authors declare that the research was conducted in the absence of any commercial or financial relationships that could be construed as a potential conflict of interest.

Publisher’s note

Supplementary material

The Supplementary Material for this article can be found online at: https://www.frontiersin.org/articles/10.3389/frspt.2023.1328341/full#supplementary-material

References

Agosto, W. N. (1981). "Beneficiation and powder metallurgical processing of lunar soil metal," in 4th Space manufacturing; Proceedings of the Fifth Conference, Princeton, NJ, USA, May, 1981.

Agosto, W. N. (1985). Electrostatic concentration of lunar minerals. Available online at https://ui.adsabs.harvard.edu/abs/1985lbsa.conf.453A/abstract.

American Institute of Aeronautics and Astronautics (1981). "Space manufacturing 4," in 4th Space manufacturing; Proceedings of the Fifth Conference, Princeton, NJ, USA, May, 1981.

American Institute of Aeronautics and Astronautics (2011). "Aerospace Sciences meetings," in 49th AIAA Aerospace Sciences Meeting including the New Horizons Forum and Aerospace Exposition, Orlando, Florida, USA, January, 2011.

Berggren, M., Zubrin, R., Jonscher, P., and Kilgore, J. (2011). "Lunar soil particle separator," in 49th AIAA Aerospace Sciences Meeting including the New Horizons Forum and Aerospace Exposition, Orlando, Florida, USA, January, 2011.

Bish, D. L., and Chipera, S. J. (1994). Accuracy in quantitative X-ray powder diffraction analyses. *Adv. x-ray Anal.* 38, 47–57. doi:10.1154/S0376030800017638

Bish, D. L., and Plötze, M. (2010). "X-Ray powder diffraction with emphasis on qualitative and quantitative analysis in industrial mineralogy," in *Giovanni ferraris*. Editor G. E. Christidis (European Mineralogical Union and the Mineralogical Society of Great Britain & Ireland), 35–76. doi:10.1180/EMU-notes.9.3

Bunch, T. E., Williams, R. J. P., Mckay, D. S., and Giles, D. (1979). Mining and beneficiation of lunar ores. Available online at https://ui.adsabs.harvard.edu/abs/1979srss.rept.275B/abstract.

Captain, J. G., Arens, E. E., Quinn, J. W., and Calle, C. I. (2009). The use of tribocharging in the electrostatic beneficiation of lunar simulant. *IEEE Trans. Ind. Appl.* 45 (3), 1060–1067. doi:10.1109/TIA.2009.2018976

Cilliers, J. J., Rasera, J. N., and Hadler, K. (2020). Estimating the scale of Space Resource Utilisation (SRU) operations to satisfy lunar oxygen demand. *Planet. Space Sci.* 180, 104749. doi:10.1016/j.pss.2019.104749

Colaprete, A., Elphic, R. C., Heldmann, J., and Ennico, K. (2012). An overview of the lunar crater observation and sensing satellite (LCROSS). *Space Sci. Rev.* 167 (1-4), 3–22. doi:10.1007/s11214-012-9880-6

Colozza, J. A. (2020). Small lunar base camp and *in situ* resource utilization oxygen production facility power system Comparison. Available online at https://ntrs.nasa.gov/citations/20200001622.

Exolith Lab (2014). "LMS-1 lunar mare simulant: fact sheet," in *Dictionary geotechnical engineering/wörterbuch GeoTechnik*. Editors Herrmann H. and Herbert B. (Berlin, Heidelberg: Springer Berlin Heidelberg), 603.

Franke, M. (2019). Development of a testbed for the beneficiation of lunar regolith. Available online at https://elib.dlr.de/185548/1/MA_SpaceEngineering_Franke_3218889_Digital2.pdf.

Gibson, M. A., and Knudsen, C. W. (1985). Lunar oxygen production from ilmenite. Available online at https://adsabs.harvard.edu/full/1985lbsa.conf.543G.

Hadler, K., Martin, D. J. P., Carpenter, J., Cilliers, J. J., Morse, A., Starr, S., et al. (2020). A universal framework for space resource utilisation (SRU). *Planet. Space Sci.* 182, 104811. doi:10.1016/j.pss.2019.104811

Heiken, G. H., Vaniman, D. T., and French, B. M. (1991). Lunar sourcebook: a user's guide to the Moon. Available online at https://www.lpi.usra.edu/publications/books/lunar_sourcebook/pdf/LunarSourceBook.pdf.

Herrmann, H., and Bucksch, H. (2014). *Dictionary geotechnical engineering/wörterbuch GeoTechnik*. Berlin, Germany: Springer Berlin Heidelberg.

Li, T. X., Ban, H., Hower, J. C., Stencel, J. M., and Saito, K. (1999). Dry triboelectrostatic separation of mineral particles: a potential application in space exploration. *J. Electrost.* 47 (3), 133–142. doi:10.1016/S0304-3886(99)00033-9

Linke, S., Windisch, L., Kueter, N., Wanvik, J. E., Voss, A., Stoll, E., et al. (2020). TUBS-M and TUBS-T based modular Regolith Simulant System for the support of lunar ISRU activities. *Planet. Space Sci.* 180, 104747. doi:10.1016/j.pss.2019.104747

Oder, R. R. (1991). Magnetic separation of lunar soils. *IEEE Trans. Magn.* 27 (6), 5367–5370. doi:10.1109/20.278841

Reid, J. W., and Hendry, J. A. (2006). Rapid, accurate phase quantification of multiphase calcium phosphate materials using Rietveld refinement. *J. Appl. Crystallogr.* 39 (4), 536–543. doi:10.1107/S0021889806020395

Space, (2006). *Space*. Reston, Virigina: American Institute of Aeronautics and Astronautics.

Sundararajan, V. (2006). "International missions to the Moon: space exploration goals, programs and economics," in *Space 2006*, Reston, Virigina: American Institute of Aeronautics and Astronautics.

Trigwell, S., Captain, J., Captain, J., Ellen, A., Quinn, J., and Calle, C. I. (2006). Electrostatic beneficiation of lunar simulant. Available online at https://ntrs.nasa.gov/citations/20130011155.

Trigwell, S., Captain, J., Weis, K., and Quinn, J. (2013): Electrostatic beneficiation of lunar regolith: applications in *in situ* resource utilization. In *J. Aerosp. Eng.* 26 (1), pp. 30–36. doi:10.1061/(ASCE)AS.1943-5525.0000226

Xie, R., Li, Y., Liu, H., and Zhang, X. (2017). Insights into the structural, microstructural and physical properties of multiphase powder mixtures. *J. Alloys Compd.* 691, 378–387. doi:10.1016/j.jallcom.2016.08.266

10.3389/frspt.2023.1328341

Nomenclature

DLR	Deutsches Zentrum für Luft- und Raumfahrt
ISRU	In-Situ Resource Utilization
ESA	European Space Agency
JAXA	Japanese Aerospace Exploration Agency
NASA	National Aeronautics and Space Administration
ISRO	Indian Space Research Organisation
CNSA	China National Space Administration
XRPD	X-Ray Powder Diffraction
SEM/ EDX	Scanning electron microscopy with Energy dispersive X-ray spectroscopy
M_i	Total mass of unprocessed raw material at the input
M_o	Total mass of processed material at the output
$M_{tm,i}$	Mass of target mineral in input
$M_{tm,o}$	Mass of target mineral in output
G_i	Grade of target mineral in input
G_o	Grade of target mineral in output

frontiers | Frontiers in Space Technologies

TYPE Original Research
PUBLISHED 22 February 2024
DOI 10.3389/frspt.2024.1303964

OPEN ACCESS

EDITED BY
Florian Kehl,
University of Zurich, Switzerland

REVIEWED BY
Andrea Colagrossi,
Polytechnic University of Milan, Italy
James A. Nabity,
University of Colorado Boulder, United States

*CORRESPONDENCE
Joe Louca,
joe.louca@bristol.ac.uk

RECEIVED 28 September 2023
ACCEPTED 19 January 2024
PUBLISHED 22 February 2024

CITATION
Louca J, Vrublevskis J, Eder K and Tzemanaki A (2024), Verification of a virtual lunar regolith simulant.
Front. Space Technol. 5:1303964.
doi: 10.3389/frspt.2024.1303964

Verification of a virtual lunar regolith simulant

Joe Louca[1,2]*, John Vrublevskis[3], Kerstin Eder[4] and Antonia Tzemanaki[1,2]

[1]School of Engineering Mathematics and Technology, University of Bristol, Bristol, United Kingdom, [2]Bristol Robotics Laboratory, Bristol, United Kingdom, [3]Advanced Concepts Team, Thales Alenia Space (UK), Bristol, United Kingdom, [4]Trustworthy Systems Laboratory, University of Bristol, Bristol, United Kingdom

Introduction: Physical regolith simulants are valuable tools for developing *In-Situ* Resource Utilisation hardware. However, using virtual models of regolith instead can reduce costs, limit exposure to hazardous materials, and offer a practical method of testing the effects of reduced gravity.

Methods: We verify a virtual model of regolith as macroparticles against physical tests. Using space partitioning techniques to identify neighbouring particles, we present a scalable model of regolith, in which the computation time increases roughly proportionally with the number of particles. We evaluated the performance of this virtual simulant vs. a physical simulant (Exolith LMS-1) by comparing the flow rate through funnels of various diameters, and the resultant angle of repose of material on both large (500 g) and small (16 g) scale tests.

Results: For large scale tests, the flow rates were within the predicted range for macroparticles with radii 3–7 mm, with the greatest accuracy achieved for radii 4–5 mm. However, the macroparticles blocked the simulated funnels more easily than in the physical trials, due to their high cohesion. The angle of repose was not accurately represented by this model for either of the tests.

Discussion: The high efficiency of this model makes it best suited for applications which require large scale approximations of regolith with real-time execution, such as virtual training for robot operators or providing visual and haptic feedback in model-mediated teleoperation systems. The results of this model in reduced gravity could be further verified against data from upcoming lunar missions in future work.

KEYWORDS

***in-situ* resource utilisation (ISRU), lunar regolith simulant, model-mediated teleoperation (MMT), verification and validation (V & V), teleoperation, virtual training**

1 Introduction

The high financial and environmental costs of space launches means that it is unfeasible to transport all of the resources required for the developing space industry from the Earth's surface (Bennett et al., 2020). Instead, extracting key materials from resources readily available outside the Earth's gravitational influence could enable humans to expand our presence in space in a sustainable and sustained manner (Austin et al., 2020). *In-situ* resource utilisation (ISRU) of lunar regolith to extract oxygen, water, or construction materials, in particular, would provide many of the key components for habitats, spacecraft fuel and human life support (Corrias et al., 2012; Crawford, 2015; Schlüter and Cowley, 2020), reducing the tonnes of material that would otherwise have been needed to be

launched from Earth. Recent advancements in ISRU technology include terrestrial demonstrators of the carbothermal reduction process for extraction of water (Prinetto et al., 2023) and oxygen (White et al., 2023), and additive manufacture of glassy lunar regolith simulant products using laser powder bed fusion (Wang et al., 2023). To carry out these processes, regolith must first be collected from the lunar surface.

Lunar regolith is a difficult material to work with: having been exposed to harsh solar radiation and meteoroid bombardment for billions of years, without the usual weathering processes encountered on Earth, the dust on the Moon's surface is fine-grained, electro-statically charged, and irregularly shaped (Heiken et al., 1991). This results in highly cohesive and abrasive particles which can stick to tools and themselves. These properties affect the flow characteristics of regolith, which can lead to clogging, for example, of funnels (Reiss et al., 2014). It is important to consider these characteristics when developing collection and processing equipment, as a blockage could impact the success of the mission (Otto et al., 2018). This has led to the development of novel methods of sorting and transporting regolith using electrodynamic traveling waves to avoid any reliance on mechanical systems (Kawamoto et al., 2022; Olson, 2022). The reduced gravity on the lunar surface adds further challenges for regolith handling, but this can be difficult to replicate on Earth. Therefore, it is important, but non-trivial, to provide astronauts, robot operators, or component designers with a suitably realistic practice environment on which they can familiarise themselves with the related tasks.

Currently, lunar hardware components are tested and developed using artificial lunar regolith, i.e., lunar regolith simulants (Long-Fox et al., 2023). While these are certainly an important development tool, they can be costly and involve safety considerations as, due to their fine particulate size, they can be hazardous to humans if inhaled (Ludivig et al., 2020). Large scale indoor testing arenas, such as the University of Luxembourg's 'LunaLab' or the European Space Agency (ESA) and the German Aerospace Center's (DLR) 'Luna' facilities, the 'Lunar Lab and Regolith Testbeds' at NASA Ames Lab (NASA AMES Research Center, 2023) and provide large quantities of basalt or regolith simulant on which robots and teams can be tested, developed and trained (Ludivig et al., 2020). Although these installations provide largely realistic representations of the lunar environment, there are still aspects which are practically difficult to replicate, such as the behaviour of regolith under reduced gravity or in a vacuum. Additionally, access to these facilities is limited and have a geographical constraint (Casini et al., 2020) and, hence, they could be more suited for testing in the later stages of development.

A less resource-demanding testing environment would reduce these constraints (Otto et al., 2018) and encourage earlier testing of components. With this in mind, virtual models of lunar regolith are being developed, based on a combination of Discrete Element Method (DEM) and Computational Fluid Dynamics (CFD), and have resulted in accurate representations of physical regolith behaviours (Kuang et al., 2013; Otto et al., 2018). By using a virtual regolith, it is easy to adjust the strength of gravity, which would otherwise have been practically challenging. However, due to the small particle size, and the subsequently high number of particles (N) to be computed, these models have a high computational cost. For example, a 0.6 s duration simulation of 5 g lunar regolith (N = 1 million), carried out on a 128-processor (2,100 GHz/processor) machine, took 9 days 10 h to complete (Otto et al., 2018). While the high fidelity of these simulations will be valuable for fine-tuning hardware designs, there are many applications such as early stage prototyping and robot operator training which would benefit from a less resource intensive virtual representation of regolith.

Pereira and Schmidt (2021) presented an efficient model of lunar regolith which can compute haptic interactions of particles with a tool in real time, refreshing at rates > 1 kHz. This was achieved using DEM with Smoothed-Particle Hydrodynamics (Cirio et al., 2011) and representing regolith as a collection of individual macroparticles (Hoffmann, 2006). Using this approach, they were able to represent key properties of the material: density, internal friction and cohesion.

Their model can be summarised as follows. Inter-particle forces are modelled as an attractive force at the macroparticle edge. Eq. 1 computes the magnitude of these forces, $F(a)$, as a non-linear function of the distance between the two macroparticle, a. When a is greater than the minimum separation distance required for attraction, R_{attr} (set to 1.1 R in the original work, where R is the macroparticle radius), there is no interaction force between the two macroparticles. a_{thr} is the separation distance below which the particles act as a linear spring, with the spring constant, k. $a_{thr} = a_{min} + \sqrt{\frac{\gamma}{k}}$, where $a_{\min}$ is the theoretical minimum distance between particles given the maximum density of the material and the packing structure of the particles. γ is a cohesion parameter given as an input to the model. Inter-particle forces are damped to maintain stability using (2), where p is the number of macroparticles contacting the macroparticle, Δt is the timestep of the simulation loop, and $\dot{\boldsymbol{x}}$ is the macroparticle velocity.

$$\|F(a)\| = \begin{cases} 0 & a \geq 2R_{attr} \\ \dfrac{\gamma}{a - a_{min}} - \dfrac{\gamma}{2R - a_{min}} & a_{thr} \leq a \leq 2R_{attr} \\ ka_{thr} + F(a_{thr}) - ka & a < a_{thr} \end{cases} \tag{1}$$

$$F_{damp} = -\frac{pk\Delta t}{2}\dot{\boldsymbol{x}} \tag{2}$$

Friction and cohesion forces on a macroparticle are modelled using (3). The original work set $\lambda = 0.8$, to avoid the slow creep of particles. $\hat{\mu}$ is the model's friction parameter based on the internal friction of the material, μ, (4). $\|F_{contact}\|$ is the sum of the magnitudes of the inter-particle contact forces, obtained with (1).

$$\|F_{fr,c}\| \begin{cases} \leq \hat{\mu}\Sigma\|F_{contact}\| & \|\dot{\boldsymbol{x}}\| = 0 \\ = \lambda\hat{\mu}\Sigma\|F_{contact}\| & \|\dot{\boldsymbol{x}}\| > 0 \end{cases} \tag{3}$$

$$\hat{\mu} = \sqrt{6}\mu \tag{4}$$

Collisions between macroparticles and the tool are represented using a viscoelastic model (5), where z is the penetration of the macroparticle with the tool, and $\dot{z}$ is their relative velocity. The tool stiffness and cohesion parameters are calculated as: k_{tool} = 500 N/m, and $c_{tool} = 1.4\frac{\Delta t k_{tool}}{2}$.

$$\|F(z,\dot{z})\| = \begin{cases} 0 & z \leq -0.002R \\ k_{tool}z + c_{tool}\dot{z} & z > -0.002R \end{cases} \tag{5}$$

While faster than the high fidelity simulations mentioned above, this model still calculates interactions of all combinations of particle

pairs. Therefore, computation time increases proportionally to N^2, where N is the number of particles. This severely limits the scalability of the model. The intention of this work was to generate a "convincing haptic feel" of lunar regolith, and, as such, was validated by users for the subjective "feel" of the haptic feedback. In our work, we examine the feasibility of Pereira and Schmidt (2021)'s model in simulating the behaviour of regolith, by verifying it against a physical system.

In the following sections, we present an updated algorithm to virtually model lunar regolith, followed by an experimental verification of the model vs. a physical regolith simulant. We aim to build on Pereira and Schmidt (2021)'s previous work and attempt to answer the following questions:

- Q1: Can the scalability of Pereira and Schmidt's model be improved?
- Q2: Are virtual macroparticles a valid representation of fine grained particles?
- Q3: Is the cohesion and friction in the model a valid representation of physical samples?

Q1 is addressed in Section 2.1, where we utilise a space partitioning approach to reduce the number of inter-particle collision pairs, and compare how the number of particles affects computation time of this updated algorithm against that of the original. Using this updated algorithm, we then experimentally verify the virtual model against a physical equivalent, using two granular materials: sand and a lunar regolith simulant. To assess the validity of representing these materials as virtual macroparticles (Q2), we measure how changing the macroparticle size impacts the accuracy of the model. Finally, we virtually replicate flow rate and angle of repose tests using two materials to assess the model's representation of friction and cohesion (Q3). The results of these verification tests are described in Sections 3.1 and 3.2.

2 Methods

Our work is separated into two sections: improving the scalability of the model, and experimentally verifying the model. In this section, first, we give details of the steps taken to improve the scalability of the model, and demonstrate how it compares with the original algorithm. Next, we set out the procedure for experimentally verifying the model through three tests: two assessing the flow rate of the material, and another to assess the angle of repose. We also describe our methods for varying the macroparticle size (to explore Q2 from the previous section). Finally, we report the two sample materials used in these validations, selected to address Q3.

2.1 Improving the scalability of the model

The main issue with the scalability of the model is that it relies on checking each particle-particle pair for collisions (Pereira and Schmidt, 2021). This results in N^2 calculations, where N is the number of particles, for each simulation frame. Here, we improve the efficiency of the algorithm by, instead, only checking for collisions with nearby particles. To achieve this, first, the virtual environment is divided into a 3D grid of cubic cells, where the length of each cell side is $2R_{attr}$, the distance at which particles begin to exert an attractive force towards each other (Figure 1). Each of these cells is assigned an ID number based on its position in the grid, starting with '0' at the origin, and ascending sequentially along the x, then y, then z directions. These cells are represented in the software as a 1-dimensional array, 'cell world', and the ID number of a cell is its index number in the array. For each cell in the grid, the ID numbers of the 26 neighbouring cells (those with a contacting face, edge, or corner) are subsequently identified and stored in an index. This is achieved by, firstly, using (6) to computes the 'cell space' co-ordinates in the x, y and z direction (a, b and c, respectively). These values are then used in (7) to compute the IDs of the cells in neighbouring rows, columns and layers. ID is the index number of the cell; x, y and z are the Cartesian positions; L is the length of the side of each cell, and A and B are the number of rows of cells in the virtual environment in the x and y directions, respectively.

$$\begin{aligned} c &= \left\lfloor \frac{ID}{AB} \right\rfloor \\ b &= \left\lfloor \frac{ID - cAB}{A} \right\rfloor \\ a &= ID - cAB - bA \end{aligned} \tag{6}$$

$$ID_{\text{neighbour}}(a,b,c) = a + bA + cAB \qquad \begin{aligned} a &= [a-1\,..\,a+1] \\ b &= [b-1\,..\,b+1] \\ c &= [c-1\,..\,c+1] \end{aligned} \tag{7}$$

To set up the simulation, the Cartesian start position of each particle is converted to 'cell space' using (8), to identify the IDs of the cells in which they lie. Using these cell IDs, the particles are stored in the relevant element of the 'cell world' array, to represent that particle being in that cell.

$$ID = \left\lfloor \frac{x}{L} \right\rfloor + \left\lfloor \frac{y}{L} \right\rfloor A + \left\lfloor \frac{z}{L} \right\rfloor AB \tag{8}$$

In the main simulation loop, inter-particle interaction forces are computed. For each particle, the cell ID is calculated based on its current position. This ID is used to identify the 26 IDs of all the neighbouring cells from the neighbouring cells index. Elements of the 'cell world' array are accessed using each of these neighbouring cell IDs, to check for particles in neighbouring cells. Collision checking is only carried out on these particles; particles outside of the neighbouring cells are ignored. When N is large, this vastly reduces the number of collisions to compute compared with the original algorithm.

To evaluate the impact of this change on computation time and scalability, both algorithms were run using the C++ library, Chai3D (Conti et al., 2003), on an Intel i7-10850H CPU 2.70 GHz, 16 GB RAM machine. The number of simulated particles was increased from 1 to 10,000, recording the mean time taken to compute the inter-particle interactions for each frame. In the original algorithm, computation time increased exponentially with N, whereas, in our modified neighbour-based algorithm, this increased linearly with N (Figure 2).

2.2 Experimental verification of the model

To verify the accuracy of the model, the behaviour of the virtual material was compared against that of its physical equivalent.

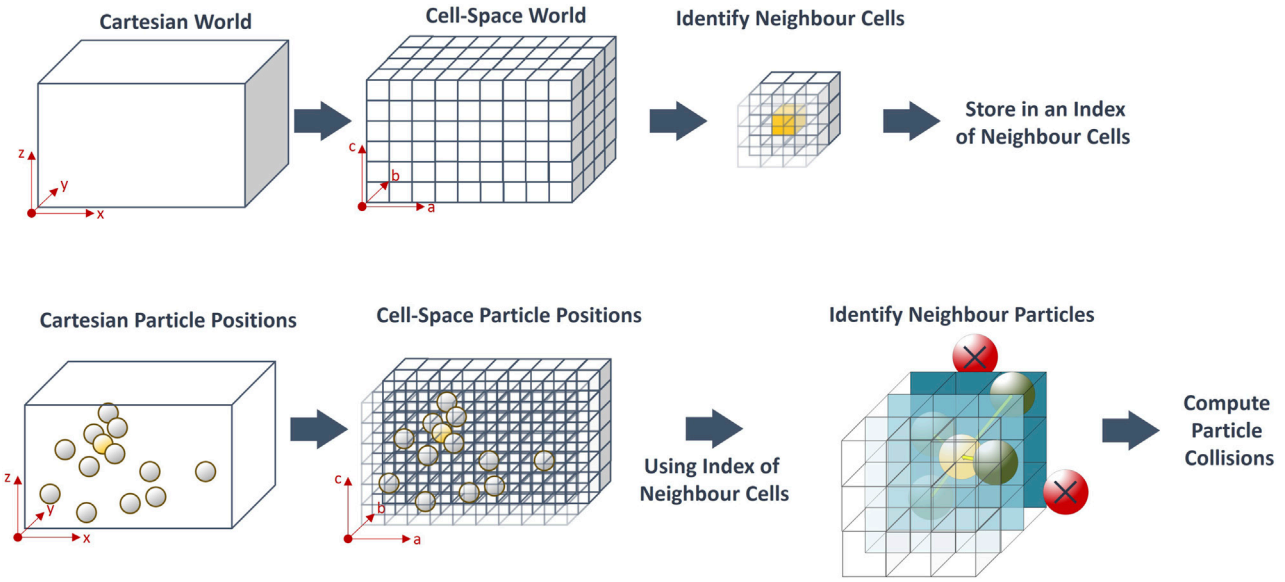

FIGURE 1
Identification of nearby particles in neighbouring cells. The world is divided into cubic cells. For a given particle (yellow), neighbouring particles (green) are identified as those in cells that share a face, edge, or corner, with the original particle. These neighbouring particles are checked for collisions, whereas particles in cells outside of this range (red) are ignored.

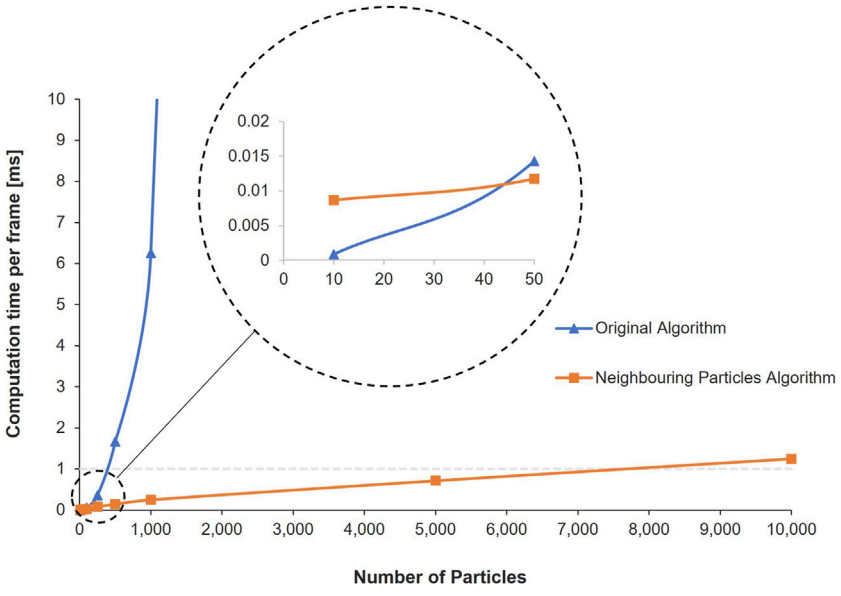

FIGURE 2
Effect of number of particles on computation times of the original algorithm Pereira and Schmidt (2021) and the neighbouring particles algorithm used in this paper. Dashed grey line represents the maximum computation time that would achieve 1 kHz refresh rate required for haptic feedback.

Identical physical and virtual test setups were constructed for three scenarios: the flow rate tests and the angle of repose tests described by Long-Fox et al. (2023), and a similar flow rate test using a smaller sample. Funnel tests have been previously used to examine the behaviour of lunar regolith, as its mechanical properties affect its ability to flow, which can lead to blocking funnels (Reiss et al., 2014; Otto et al., 2018). It is likely that any practical method for the collection and processing of lunar regolith would involve transferring the material from one container to another, and, hence, it is important to understand its flow properties.

2.2.1 Experimental tests

2.2.1.1 Large-scale flow rate tests

Firstly, to assess large-scale behaviours of the material, the flow rate experiment used to characterise the properties of LMS-1 by Long-Fox et al. (2023) was replicated in simulation. In Long-Fox

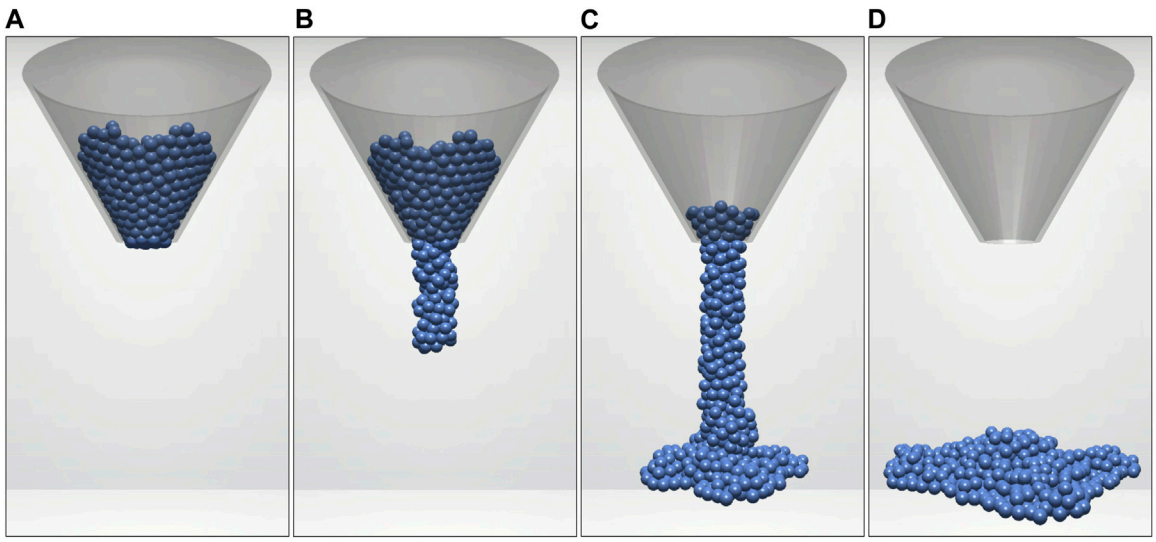

FIGURE 3
Virtual experimental setup for large funnel tests with 5 cm hole diameter and 4 mm macroparticle radius. Starting with a blocked funnel **(A)**, the virtual sample was allowed to flow **(B–C)** through a 30° funnel with a variable hole diameter to land on a flat surface **(D)**, imitating the setup described by Long-Fox et al. (2023).

et al. (2023)'s procedure, 500 g of LMS-1 were gently placed into polycarbonate funnels with a slope angle of 30°, initially with the hole blocked. In order to prevent cohesive arches forming and blocking the funnel, four 3 V DC coin-style vibration motors were fixed to the outside of the funnel to mechanically agitate the material during these physical experiments. Once the material was stationary and it was confirmed that the funnel was level, the vibration motors were activated, the stopper blocking the hole was removed, and the rate of material flowing through the funnel was recorded using an Intelligent Weighing Technology PBW-A 3200 laboratory balance. They repeated this process for funnel hole diameters 2.5–5.0 cm, at 0.5 cm intervals. From these experimental data, they produced a best-fit curve of flow rate through varying hole diameters, based on five repeated trials. We replicated this procedure, in simulation, to compare their curve against the flow rate results of the model (Section 3.1.1). As the virtual macroparticles blocked the flow through the smaller funnels, we extrapolated the best-fit curve from Long-Fox et al. (2023)'s physical trials, in order to compare the flow rates for additional, larger funnel diameters: 5–9 cm, at 1 cm intervals. The experimental setup for the virtual large funnel tests can be seen in Figure 3. Full details and images of the experimental setup used by Long-Fox et al. (2023) are provided in their original paper.

2.2.1.2 Small-scale flow rate tests

Secondly, to verify the performance of the simulation for a smaller-scale task, we set up a comparable funnel experiment. 16 g of simulant were placed onto one side of a rectangular funnel, 50 mm across, with a 45°slope, and a 20 mm deep spout with varying hole widths (5 mm, 10 mm, 15 mm, Open). The funnel was 3D printed using polylactic acid (PLA), and the surface roughness parameters of the components were: Ra = 0.400 μm, Rq = 0.511 μm, Rsk = −0.503. The open condition represents a funnel hole so wide that it could be considered infinite for the volume of sample material. A 45°slope was chosen as it is greater than the angle of repose of LMS-1 (35°), to ensure that the material would flow through the funnel without the need for vibration. Once stationary, the material was released to flow through the funnel. In the physical setup, this was done via a release flap operated using a 28BYJ-48 stepper motor to reduce variability between test runs. After releasing the material, we measured the flow rate in g s^{-1}. In the physical setup, flow rate was measured using a 6-axis force-torque sensor (ATI Axia80-M8, United States) which recorded the mass of material over time. In the virtual setup, the flow rate was calculated by measuring the number of particles below the bottom of the funnel at each timestep. Here, we report flow rates as the mean flow rate over the time period between the first and last particle falling through the funnel. The experimental setup for the small funnel tests can be seen in Figure 4, with a comparison of physical and virtual flow tests depicted in Figure 5.

Each of the trials for the physical conditions were repeated five times, as was the case in the work by Long-Fox et al. (2023). These tests were then repeated using the same volume of dry sand to compare the results against a cohesion-less material of comparable internal friction.

2.2.1.3 Angle of repose tests

In addition, we replicated in simulation the angle of repose tests described by Long-Fox et al. (2023). For these tests, 500 g of material were poured through a funnel of 3 cm hole diameter onto a 30°chute, which then allowed the sample material to gently fall against a vertical wall. The angle of repose of the resultant pile was then recorded, and compared against the results of Long-Fox et al. (2023). Full details and images of the experimental setup used by Long-Fox et al. (2023) are provided in their original paper.

2.2.2 Particle size

In both virtual models, there is a trade-off of the computational demand vs. the number of particles (N) and, subsequently, the particle

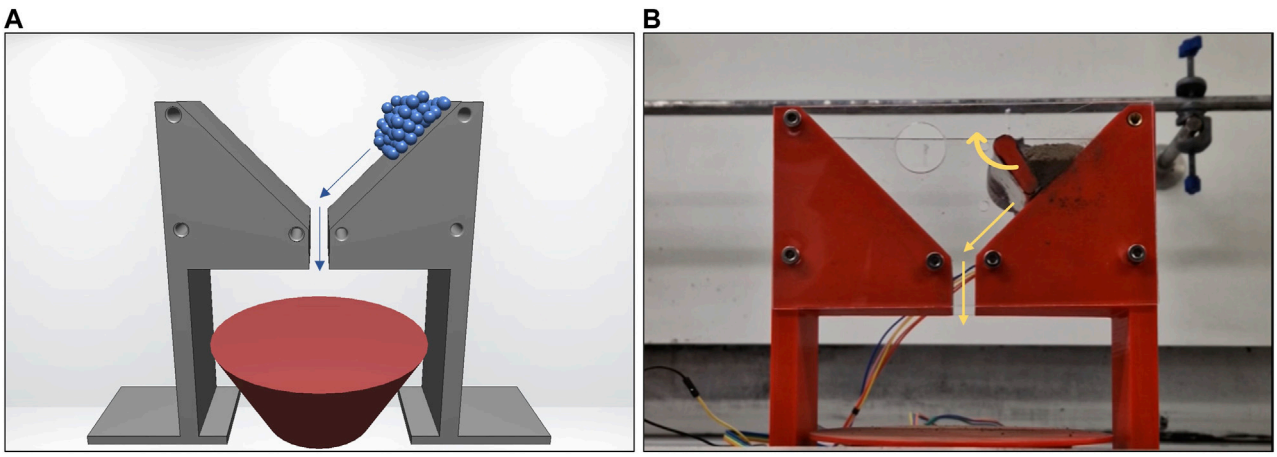

FIGURE 4
Virtual **(A)** and physical **(B)** experimental setup for small funnel tests. The sample was released from the top right-hand side, allowing it to fall down a 45° slope through holes of variable widths.

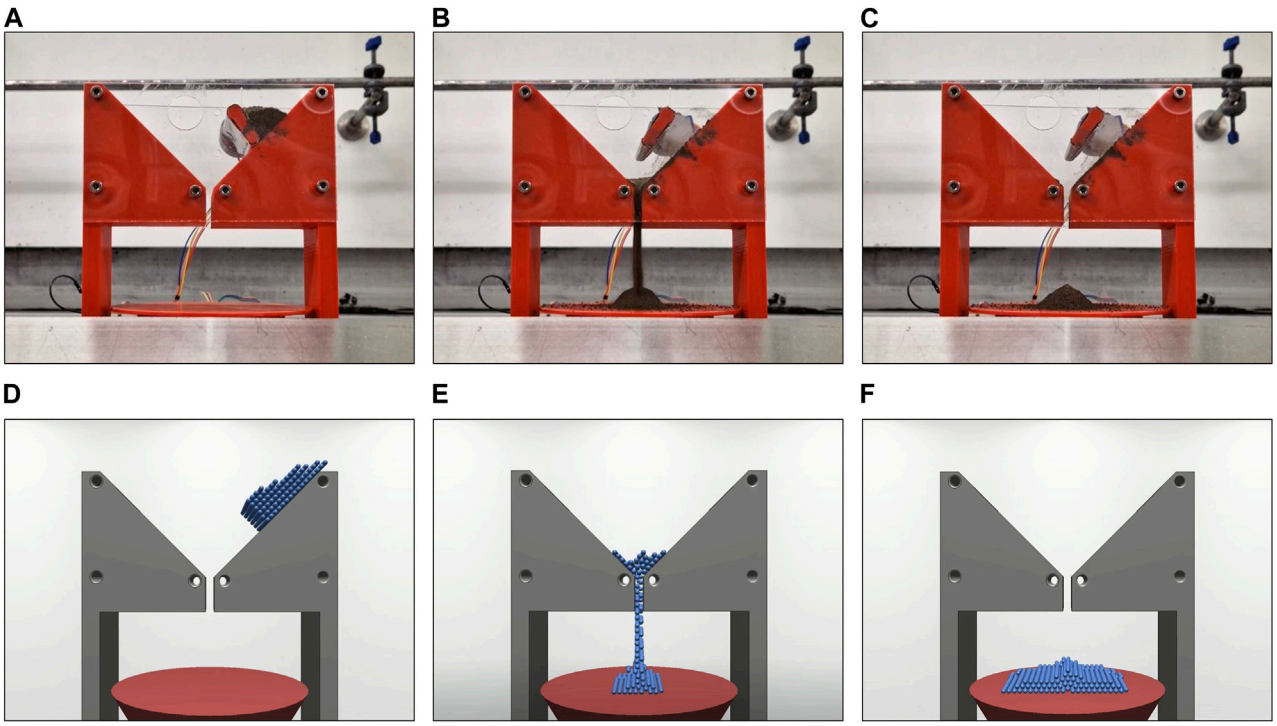

FIGURE 5
From left to right, flow of material during the physical **(A–C)** and virtual **(D–F)** small funnel tests.

radius (R). Setting N = 128, Pereira and Schmidt (2021) were able to achieve simulation refresh rates required for haptic feedback (≥1,000 Hz), their size (R = 7 mm) was much larger than in physical regolith (R = 0.030–0.045 mm) (McKay et al., 1972). This may lead to an inaccurate representation of regolith. Therefore, to address question Q2 (Section 1), we repeated each of the virtual flow rate and angle of repose trials with varying particle radii (R = 2–7 mm) to compare with the results of the physical trials. The smallest particle radius was 2 mm because, beyond this, N would become too large to render graphically.

2.2.3 Materials

Two materials were used to verify the performance of this model: Lunar Mare Simulant 1 (LMS-1) (Exolith Lab) and dry sand (40–100 mesh, CAS: 14808–60–7, Fischer Scientific). LMS-1 is a readily available lunar regolith simulant which is commonly used in research (Stupar et al., 2021; Isachenkov et al., 2022; Meurisse et al., 2022). It was chosen for this work due to its well documented physical properties (Long-Fox et al., 2023), including the density, cohesion and friction parameters required for this model. Sand was

TABLE 1 Physical properties of test materials.

Material	∅/mm	ρ/kg m^{-3}	μ	C/kPa
Sand	0.15–0.40	1,360	0.284	0.000
LMS-1	0.091	1,470	0.284	0.393

Particle diameter, ∅; Density, ρ; Friction coefficient, μ; and Cohesion, C.

selected as a comparison material, as it has a similar grain size and internal friction to LMS-1 (Carter and Bentley, 1991), but can be assumed to be a cohesionless material (US Navy, 1982). The particle size distributions of the two materials are as follows: Sand—Mean particle diameter = 301.1 µm (SD = 128.4 µm), median = 256.7 µm (Young and Ball, 1997); LMS-1—Mean particle diameter = 85.65 µm (SD = 27.68 µm), median = 62.48 µm (Long-Fox et al., 2023). Table 1 summarises the physical properties of the two test materials used in this study. By comparing the differences between LMS-1 and sand in physical trials, we can identify the impact of cohesion. If a similar change is observed in virtual trials, we can then determine whether the model's representation of cohesion between macroparticles is valid.

3 Results

In this section, we report the results of the three experimental verification tests described in Section 2. First, we describe the results of virtual large funnel LMS-1 flow rate experiments and compare these against the data from the equivalent physical experiment reported by Long-Fox et al. (2023). Next, we describe the results of the virtual and physical small funnel flow rate experiments conducted as part of this study, using LMS-1 and sand. Finally, we report the results of the virtual angle of repose tests conducted in this study and compare these against the equivalent physical tests.

3.1 Flow rate tests

3.1.1 Large funnels

Figure 6 shows the average flow rate of LMS-1 through large funnels of different hole widths for our virtual trials and the physical trials by Long-Fox et al. (2023). The changes in flow rate of each virtual condition, compared with the best-fit curve of the physical test results from Long-Fox et al. (2023), are shown in Table 2 for LMS-1. For funnel diameters ≤3 cm the virtual macroparticles blocked flow through the funnel. For funnel diameter = 3.5 cm, for all particle radii blocked the funnel except for 5 mm where the flow of virtual LMS-1 was heavily restricted, causing the flow to stop and start. For funnel diameters ≥5 cm, the virtual model overestimated the flow rate for larger macroparticles, but underestimated the flow rate for smaller macroparticles, when compared with the physical results. Macroparticles with 4 mm or 5 mm radii produced results most similar to the physical trials. Flow rates were within the upper and lower bounds of the results (and extrapolated results) of the physical trials, with the exception of the conditions which were blocked, and those which were close to being blocked (5 mm particles through 3.5 cm funnel, 4 mm particles through 4 cm funnel, and 3 mm particles through 5 cm funnel). In those trials where flow was heavily reduced but not blocked, an intermittent flow behaviour was observed. This was similar, although less pronounced, to the cohesive arch formation and collapse of LMS-1 reported by (Reiss et al., 2014).

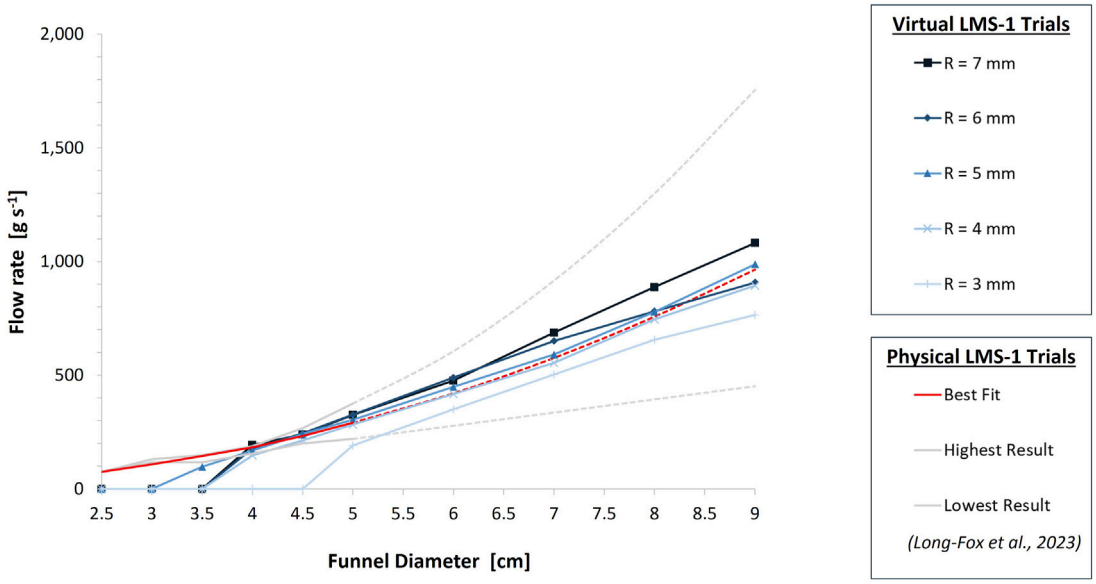

FIGURE 6
Comparison of flow rates of virtual LMS-1 (blue) of different macroparticle sizes against physical LMS-1 (red) during the large funnel tests. Physical trial data comes from Long-Fox et al. (2023), virtual trial data comes from the simulations conducted in this work. The solid red line represents the best-fit curve of their results and the solid grey lines represent the upper and lower limits of their individual physical trials, up to 5 cm funnel diameter. The dashed red and grey lines are extrapolations of their best-fit and physical data for funnel diameters > 5 cm.

TABLE 2 Change in flow rate of virtual LMS-1 through large funnels of varying hole width, compared with physical trials.

Funnel hole diameter	Particle radius				
	3 mm	4 mm	5 mm	6 mm	7 mm
2.5 cm	−100%	−100%	−100%	−100%	−100%
3.0 cm	−100%	−100%	−100%	−100%	−100%
3.5 cm	−100%	−100%	−32%	−100%	−100%
4.0 cm	−100%	−21%	−9%	−4%	+4%
4.5 cm	−100%	−9%	+3%	+4%	+2%
5.0 cm	−34%	−2%	+5%	+12%	+12%
6.0 cm	−17%	−1%	+7%	+16%	+13%
7.0 cm	−13%	−4%	+3%	+13%	+19%
8.0 cm	−13%	−2%	+3%	+3%	+17%
9.0 cm	−21%	−7%	+3%	−6%	+12%

Red cells indicate where the funnel was blocked by the virtual macroparticles.

3.1.2 Small funnels

Figures 7, 8 show the average flow rate of sand and LMS-1, respectively, through small funnels of different widths for virtual and physical trials. The changes in flow rate of each virtual condition, compared with the mean physical test result, are shown in Tables 3, 4 for sand and LMS-1, respectively.

The physical tests showed an increasing flow rate as funnel width was increased, reaching a plateau at 15 mm. The results (Figure 7) showed reducing the funnel width had little effect on reducing the flow of virtual sand for R = 3–7 mm, except for when the macroparticles were too large to fit through the hole. This was due to the lack of cohesive forces between particles causing the sample pile to collapse and flow through the funnel as a single layer. Therefore, if the particle diameter was smaller than the funnel width, there was no interaction with the opposite side of the funnel, and, as such, the virtual sand behaved similarly to in the open condition. However, when R = 2 mm, the larger number of layers (as illustrated in Figure 9) in the sample meant that it had not fully collapsed by the time it reached the funnel hole (Figure 10) and, hence, the flow rate was reduced through the smallest funnels for the smallest particles. Table 3 shows that the virtual sand tended to have a slower flow rate than the physical tests for the open and 15 mm funnels. This decrease was 6%–19% for R = 2–6 mm, whereas for the largest macroparticle size (R = 7 mm), there was a larger decrease (30%–31%). Funnels only became blocked when the particle size was greater than the funnel width.

As for sand, the physical tests using LMS-1 showed that the flow rate increased with the funnel width. However, this continued to increase beyond 15 mm and did not plateau. The results (Figure 8) showed a decrease in flow rate for macroparticles with R ≤ 5 mm, as funnel width decreased, and also did not plateau. Unlike virtual sand, the virtual LMS-1 tended to have a faster flow rate through the funnels compared to the physical tests for macroparticles with R ≥ 5 mm (Table 4).

The cohesive properties of LMS-1 were demonstrated in these virtual tests. Unlike the sand trials, funnels became blocked with virtual LMS-1 when the particle size was greater than the funnel width, or for smaller particles. Although the particles were smaller and should, therefore, flow more easily, there were a greater number of inter-particle cohesive forces, which led the material to coalesce and block the funnel. For R = 2 mm, for example, flow was completely blocked in all but the open funnels.

The density of LMS-1 is approximately 7.6% greater than that of sand and, as such, one might expect its flow rate to increase proportionally to this. The physical trials, however, show that LMS-1 flows more slowly than sand, by 12%–35% (Table 5). Of the virtual tests in which the funnels were not blocked, a similar decrease was seen in the virtual tests for: R = 5 mm in the 15 mm funnel, R = 4 mm in the open and 15 mm funnels, and R = 3 mm in the open funnel. For larger particles (R ≥ 6 mm), the reduced number of particles in the sample resulted in fewer cohesive interparticle forces, causing virtual LMS-1 to flow faster than virtual sand. Consequently, the greater gravitational forces applied to LMS-1 particles due to their greater density became the predominant difference between these tests. Conversely, for R = 2 mm, virtual LMS-1 flowed 61% slower than virtual sand as the stronger cohesive interparticle forces of LMS-1 counteracted the forces resulting from their increased density.

3.2 Angle of repose tests

The original method for measuring the angle of repose involved pouring regolith from a funnel with a hole diameter of 3 cm. However, as demonstrated in Section 3.1.1, the virtual regolith blocked funnels of this size, meaning that the original method would be unsuitable in this case. We, therefore, measured the angle of repose of material resulting from the small funnel tests, instead. The experimentally obtained angle of repose resulting from pouring the physical samples through the small funnels was 21.58° for sand and 35.58° for LMS-1. This result for LMS-1 was comparable to that of the larger scale (500 g) tests by Long-Fox et al. (2023) (37.5° ± 3.4°). These results were not successfully replicated in the virtual models because, although the internal

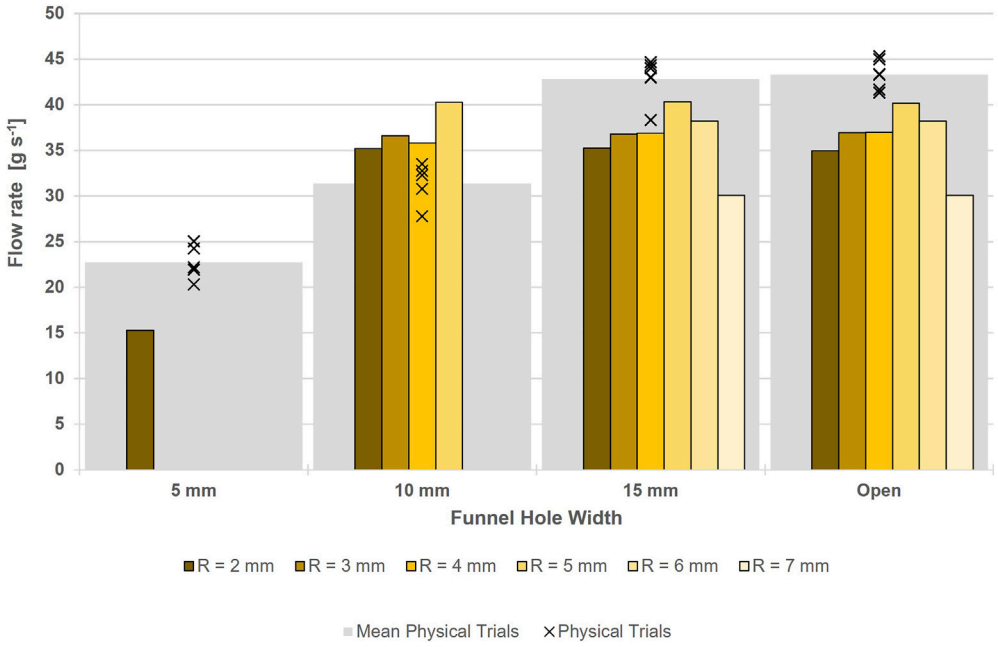

FIGURE 7
Comparison of flow rates of virtual (yellow) sand of different macroparticle sizes against physical sand (grey) in the small funnel tests.

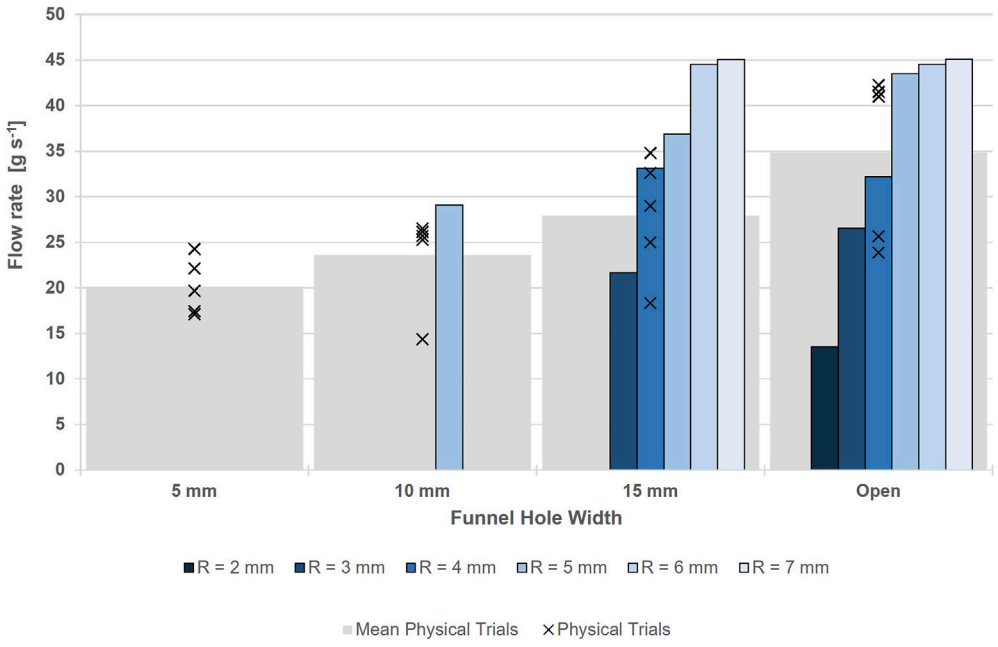

FIGURE 8
Comparison of flow rates of virtual LMS-1 (blue) of different macroparticle sizes and physical LMS-1 (grey) in the small funnel tests.

friction was calculated based on the physical properties of regolith, this was simplified to reduce computation time by calculating the friction force based on the total sum of contacting forces on that particle (3), as opposed to a sum of multiple friction forces from multiple particles (Pereira and Schmidt, 2021). Friction against the tool objects was also simplified using an arbitrary cohesion parameter (5). These simplifications meant that because the total friction forces were insufficient to hold the particles in place, they eventually slipped down to a single layer in all conditions, resulting in an angle of repose of 0°. Long-Fox et al. (2023) identified that

TABLE 3 Change in flow rate of virtual sand through small funnels of varying hole width, compared with physical trials.

Funnel hole width	Particle radius					
	2 mm	3 mm	4 mm	5 mm	6 mm	7 mm
5 mm	−33%					
10 mm	+12%	+17%	+14%	+28%		
15 mm	−18%	−14%	−14%	−6%	−11%	−30%
Open	−19%	−15%	−15%	−7%	−12%	−31%

Grey cells indicate where the virtual macroparticle size is greater than the funnel size, so zero flow can occur.

TABLE 4 Change in flow rate of LMS-1 through small funnels of varying hole width, compared with that of sand.

Funnel hole width	Particle radius						
	2 mm	3 mm	4 mm	5 mm	6 mm	7 mm	Physical
5 mm	−100%						−12%
10 mm	−100%	−100%	−100%	−28%			−25%
15 mm	−100%	−41%	−10%	−8%	+17%	+50%	−35%
Open	−61%	−28%	−13%	+8%	+17%	+50%	−20%

Red cells indicate where the funnel was blocked by the virtual macroparticles. Grey cells indicate where the virtual macroparticle size is greater than the funnel size, so zero flow can occur.

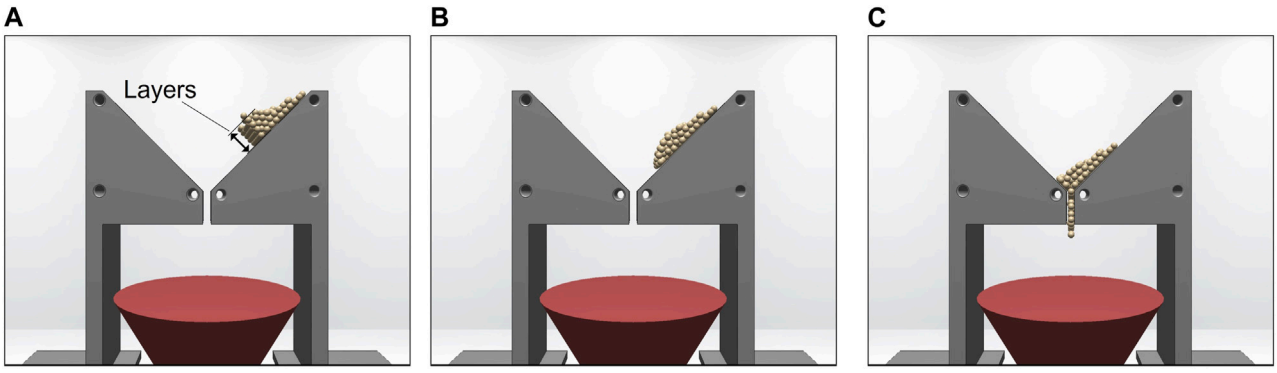

FIGURE 9
Virtual sand falling through the 5 mm small funnel **(A–C)** for macroparticles of R = 2 mm. To start, the particles are stacked in layers four particles deep. As the particles reach the funnel, the sample is still stacked in several layers, slowing the flow material when compared with the open funnel condition.

adjusting $\lambda = 1.0$ to $\lambda = 0.8$ in (3) led to improved friction behaviour by eliminating the "slow creep" of particles. However, this proved to be insufficient in our trials. This was, perhaps, because the original simulation held the particles in a virtual box, which provided some support to the particles, whereas our task was carried out in a more 'open' world, where the particles could spread more easily.

4 Discussion

This section discusses the results of the tests presented above, with respect to the three questions, outlined in Section 1, along with the implications for practical applications and further research.

4.1 Model scalability

The neighbouring particles algorithm described in Section 2.1 was an effective way of preventing computation time from increasing exponentially with the number of particles, N. As demonstrated in Figure 2, the computation time per frame using neighbouring particles algorithm increases approximately linearly with N. This resulted in a faster computation time per frame, providing N was not very small, i.e., $N > 45$.

However, a consequence of increasing N for a given sample volume is that the macroparticle size must decrease. The reduced size of the particles means that their movements in each frame of the simulation are larger, relative to their size. This can cause

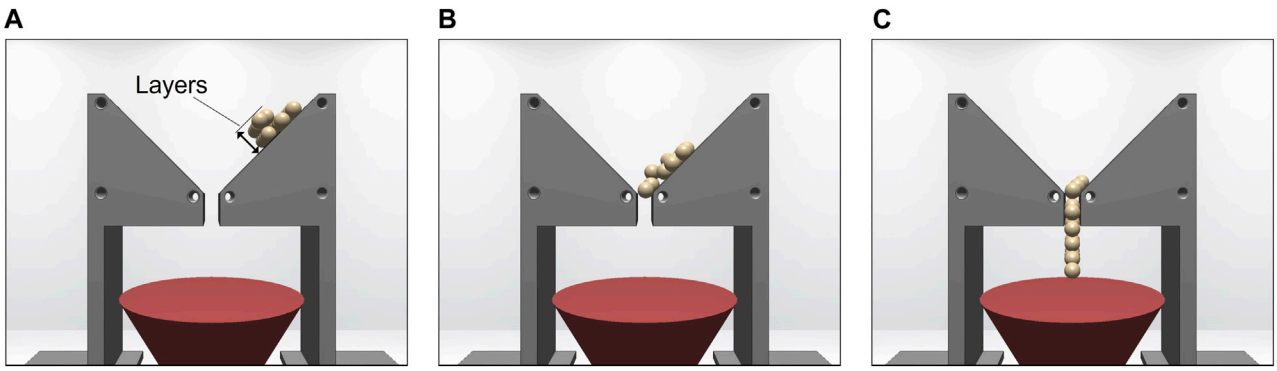

FIGURE 10
Virtual sand falling through the 10 mm small funnel **(A–C)** for macroparticles of R = 5 mm. To start, the particles are stacked in layers two particles deep, which collapse by the time the particles reach the funnel. This results in a similar flow rate the open funnel condition.

TABLE 5 Change in flow rate of virtual LMS-1 through small funnels of varying hole width, compared with physical trials.

Funnel hole width	Particle radius					
	2 mm	3 mm	4 mm	5 mm	6 mm	7 mm
5 mm	−100%					
10 mm	−100%	−100%	−100%	+23%		
15 mm	−100%	−23%	+19%	+32%	+59%	+61%
Open	−61%	−24%	−8%	+25%	+28%	+29%

Red cells indicate where the funnel was blocked by the virtual macroparticles. Grey cells indicate where the virtual macroparticle size is greater than the funnel size, so zero flow can occur.

instabilities in the model because, between each discrete frame, particles will move greater distances relative to their size. This can result in them moving to positions where their sphere boundary has a large overlap with a neighbouring particle, which would subsequently apply a large repulsive force to separate the two particles, and cause the particles to jitter even while undisturbed. The way to mitigate this is to calculate interactions at smaller time steps; for example, instead of refreshing at 1 kHz for particle with R = 7 mm, the model requires a refresh rate of 100 kHz when R = 1 mm. The model must, therefore, compute 100 times more frames per second of simulation time for the smaller particles.

If the required refresh rate to ensure stability is less than that which is achievable computationally, the simulation can run in real-time. However, if the refresh rate for stability increases above the computational limit, the simulation will run at a fraction of real-time. This has implications for model-mediated teleoperation, as real-time control would be required. If haptic feedback is required, the refresh rate must be ≥1 kHz (Pereira and Schmidt, 2021). To achieve the 1 kHz frame-rate required for haptic feedback on the hardware used in our work, this algorithm could simulate 7,500 particles, a 15-fold increase compared to the original algorithm. For design testing, however, the simulation could run at a fraction of real-time. For very large sample volumes, this is not an issue as R can remain large enough for a practical simulation refresh rate, whilst also having a large number of particles. For small samples, however, increasing N can decrease R so much that the required refresh rate for stability is not feasible, computationally. Although the neighbouring particles algorithm significantly improved the scalability of the simulation, further improvements to the model are needed to ensure stability when using small macroparticles.

4.2 Macroparticles

The size of macroparticles affected the flow rate in both the large and small funnel tests. In the large funnel tests which were not blocked (funnel diameter ≥3 cm) and in the small funnel tests, flow rate decreased as the particle size decreased. This occurred because the granular material was discretised into macroparticles. Larger macroparticles, therefore, recorded a more sudden, step-wise increase of mass through the funnel. Compounding this, the samples of smaller particles would have a greater number of layers (Figure 9). These layers collapsed as the sample flowed down the funnel slope, spreading out the sample. The first particles of the sample would therefore exit the funnel sooner and the final particles would exit later, resulting in a longer total flow time and, subsequently, a reduced flow rate.

The most obvious issue with using this macroparticle representation was that funnels became blocked far more easily than in the physical systems. This would be particularly problematic for virtual design testing applications. Furthermore, although we saw slight indications of cohesive arch formation, we did not observe any of the more complex behaviours mentioned in the literature,

such as "ratholing" or "dust fountains" (Reiss et al., 2014; Schulze, 2021).

The accuracy of the virtual macroparticle representations varied with particle size, when compared with the physical test data. In the large funnel tests, the model overestimated or underestimated the flow rate for larger and smaller macroparticles, respectively. The most accurate results were obtained using macroparticles with R = 4 mm, although flow rates were within the range of projected results from Long-Fox et al. (2023) for nearly all trials where the funnel was not completely blocked. Conversely, in the small funnel tests, as particle size decreased, the flow rate rapidly declined and became less accurate. In wider funnels, as R increased, the flow rate plateaued at values greater than the physical tests. This suggests that the macroparticle representations are more accurate on a large scale rather than at small scales where the behaviour is not realistic.

One major assumption of this model is that regolith can be represented as a collection of uniform spheres, which is contrary to a realistic regolith sample which would contain a range of particle sizes. Adding some variation in particle sizes may create more realistic behaviour, for instance, by disrupting the ordered layering seen in the small funnel tests (Figure 9). However, the original model parameters were derived by analysing the hexagonal close-packing structure of equal macroparticle spheres (Pereira and Schmidt, 2021). Therefore, as well as increasing the computational demand due to increased complexity, introducing a particle size distribution may introduce further inaccuracies without significant revisions to the model. For example, additional smaller particles would occupy interstitial spaces in the virtual regolith, leading to more numerous inter-particle contacts, which we predict would result in an overestimation of cohesive forces. Another challenge is that the true particle size distribution of regolith covers several orders of magnitude (McKay et al., 1972), which would be computationally demanding to model and visualise. One method of efficiently representing a range of particle sizes could be to revise the model parameters based on a more complex binary or ternary sphere packing structure.

4.3 Cohesion and friction

In the small funnel tests, the reduced flow rate effect of smaller macroparticles was seen more strongly in the virtual LMS-1, compared with the virtual sand, due to the addition of a cohesive interparticle force. Smaller macroparticles mean that there is a greater number of macroparticles in a sample of a given volume. This will increase the number of inter-particle contacts, and, therefore, increase the total cohesive force of the sample. Even in the open funnel condition, these cohesive forces in virtual LMS-1 slowed the flow by 32% compared with virtual sand, for R = 2 mm.

In the large funnel tests, unexpectedly, the smallest macroparticles (R = 3 mm) blocked the largest diameter funnels (≤4.5 mm). This was due to the cohesive forces between many macroparticles across the funnel hole forming a plug which could resist the pull of gravity and the mass of particles in the funnel, above. As particle size decreases, and the number of particles increases, the number of interparticle contacts, and subsequently, the cohesive force increases. The cohesion in this model appears to be overstated, particularly as particle size decreases.

The results in Section 3.2 demonstrate that friction is not accurately represented in the simulation due to insufficient modelling of the inter-particle friction, and the friction between the macroparticles and the funnel, wall or floor objects. In particular, this appears to be an issue with the dynamic friction. Adjusting λ in (3) may be one method of addressing this qualitatively, although this may impact other aspects of the model. To build a more accurate model, the different friction properties of specific tool materials need to be included.

4.4 Practical implications

This model may be suitable for rough virtual demonstrations of regolith moving through a system, but it lacks the accuracy to carry out fine design testing. Other virtual models of regolith have been developed which achieve greater accuracy, albeit at the cost of longer computation times (Otto et al., 2018). Although the neighbouring particles algorithm allows us to scale up the number of simulated particles, the remaining limitations with respect to particle size mean that this system would be best suited towards larger volume simulations.

As suggested by Pereira and Schmidt (2021), this model would be of benefit for time-adjusted, model-mediated teleoperation system (Hulin et al., 2021), where a more general approximation of regolith would be acceptable. It could also be used to train operators using virtual robots in a low-risk scenario, which we have previously identified as a key requirement for developing trust in teleoperated systems (Louca et al., 2023). When compared with using physical simulants, conducting early training using a simulation such as this would likely be cheaper and safer. Furthermore, it offers a reusable solution where experiments could be set up quickly by avoiding the need for hardware, and, crucially, it allows a practical method of interacting with regolith in reduced gravity.

4.5 Limitations and future work

The model is largely based on data from the Apollo missions (McKay et al., 1972; Mitchell et al., 1972; Houston et al., 1974; Heiken et al., 1991). It is known that regolith cohesion and friction forces are stronger in a vacuum and under lunar gravity (Heiken et al., 1991; Chang and Hicher, 2009), whereas the physical tests of this work were conducted under Earth's gravity in ambient pressure. The assumptions of the model take this into account and may be the root of some of the inaccuracies when compared against physical tests. Future work which compares the results of this model against a physical reduced gravity test would be required before using this for teleoperation tasks. This could be carried out during a parabolic flight, as a dedicated test during spaceflight, or by virtually replicating example tasks from upcoming rover missions (Potter, 2023).

Although this work uses just one example of a lunar regolith simulant, several others have been developed that represent the chemical and physical properties of regolith, to varying degrees of accuracy (Toklu and Akpinar, 2022). The assumptions in the model used here, evidently, do not lead to a perfect representation of LMS-1 behaviour. Further comparisons of these results against other simulants, considering their physical properties, could lead to the

identification of other parameters which could be included in to improve the accuracy of the model.

Furthermore, the properties and composition of regolith vary across different lunar regional areas (Papike et al., 1982). One limitation of this work is that the simulant used is representative only of mare regions. Highland regions will also be relevant for upcoming lunar missions, for example, Artemis III which is targeting the south pole of the Moon (Smith et al., 2020), based in the southern highlands (Spudis et al., 2007). Similar verification tests using lunar highland simulants are, therefore, recommended area for future work.

The model used in this work represents regolith as a collection of homogenous macroparticles. Although this simplification helps to reduce the computational demand of the model, this is not representative of a physical sample which would have a wider particle size distribution. Further work is required to assess whether using a range of macroparticle sizes to represent the particle size distribution of the sample would improve the performance of the model, whilst also considering the impact of this change on the computation time. Inclusion of smaller macroparticles, as a result, may necessitate a faster simulation refresh rate to ensure stability, as discussed in Section 4.1, which should also be taken into account.

4.6 Summary

In this work, we have presented an updated algorithm which improves the scalability of Pereira and Schmidt (2021)'s model of lunar regolith, and have reported the results of three experiments comparing the virtual model against physical equivalents. This method of modelling granular material as a collection of macroparticles provides a computationally efficient representation of regolith behaviour on a large scale, but is not suitable for smaller scale, high resolution tests. The inter-particle cohesion appears to be overstated in this model, and the friction is understated, when compared against one physical simulant (LMS-1). Additional testing against other examples of simulants would confirm this.

Other simulations are available which offer greater accuracy and resolution (Otto et al., 2018), albeit at the cost of lengthy computation times. The main advantage of this model over using other virtual representations, however, is that it is lightweight enough to run in real-time. In addition, this model offers a cheap, safe, and reusable method of examining regolith behaviour, with the possibility of easily adjusting key parameters such as cohesion, density and gravity, which is practically challenging if using physical simulants. The minimal hardware requirements of this simulation reduce the barrier of entry for those interested in testing ISRU systems.

5 Conclusion

The model of lunar regolith presented by Pereira and Schmidt (2021) predicted flow rate of a physical system with reasonable accuracy when used on a large scale (500 g sample through funnels of 4–9 cm diameter). When macroparticle radius = 5 mm, for example, the virtual flow rate through funnels of these diameters was on average 2% greater than the extrapolated mean experimental result reported by Long-Fox et al. (2023) Although the macroparticles tended to block small funnels more readily than in physical experiments, when the material flowed consitently, the flow rate was within the extrapolated range of upper and lower-bound results for nearly all the conditions tested. However, for smaller scale, finer tests (16 g sample through funnels of 5–15 mm width), the model did not accurately replicate the physical system.

The neighbouring particles algorithm presented in this paper is a computationally efficient method of simulating greater numbers of particles. However, as small particles require a faster frame-rate to ensure stability, this means that this can simulate larger volumes of material, rather than the same volumes in higher fidelity. This points towards the model being useful as an approximation of regolith behaviour on a large scale (100 s of grams), rather than for detailed design testing. It would be particularly useful for applications such as training robot operators in unfamiliar environments, such as reduced gravity, or in model-mediated teleoperation of robots for delayed Earth-Moon systems.

Data availability statement

The datasets presented in this study can be found in online repositories. Data are available at the University of Bristol data repository, data.bris, at https://doi.org/10.5523/bris.2qq66srmernh62kzpqbfdtojwa.

Author contributions

JL: Conceptualization, Data curation, Methodology, Software, Writing–original draft. JV: Conceptualization, Funding acquisition, Writing–review and editing. KE: Conceptualization, Writing–review and editing. AT: Conceptualization, Funding acquisition, Writing–review and editing.

Funding

The author(s) declare financial support was received for the research, authorship, and/or publication of this article. This research was funded by EPSRC (Grant no. EP/V519650/1) and Thales Alenia Space (United Kingdom). Thales Alenia Space was not involved in the study design, analysis, interpretation of data, the writing of this article or the decision to submit it for publication.

Conflict of interest

Author JV was employed by company Thales Alenia Space in the UK.

The remaining authors declare that the research was conducted in the absence of any commercial or financial relationships that could be construed as a potential conflict of interest.

Publisher's note

References

Austin, A., Sherwood, B., Elliott, J., Colaprete, A., Zacny, K., Metzger, P., et al. (2020). Robotic lunar surface operations 2. *Acta Astronaut.* 176, 424–437. doi:10.1016/j.actaastro.2020.06.038

Bennett, N. J., Ellender, D., and Dempster, A. G. (2020). Commercial viability of lunar *in-situ* resource utilization (ISRU). *Planet. Space Sci.* 182, 104842. doi:10.1016/j.pss.2020.104842

Carter, M., and Bentley, S. P. (1991). *Correlations of soil properties*. London: Pentech Press Publishers.

Casini, A. E., Mittler, P., Cowley, A., Schlüter, L., Faber, M., Fischer, B., et al. (2020). Lunar analogue facilities development at EAC: the LUNA project. *J. Space Saf. Eng.* 7, 510–518. doi:10.1016/j.jsse.2020.05.002

Chang, C. S., and Hicher, P.-Y. (2009). Model for granular materials with surface energy forces. *J. Aerosp. Eng.* 22, 43–52. doi:10.1061/(asce)0893-1321(2009)22:1(43)

Cirio, G., Marchal, M., Hillaire, S., and Lécuyer, A. (2011). Six degrees-of-freedom haptic interaction with fluids. *IEEE Trans. Vis. Comput. Graph.* 17, 1714–1727. doi:10.1109/TVCG.2010.271

Conti, F., Barbagli, F., Balaniuk, R., Halg, M., Lu, C., Morris, D., et al. (2003). The CHAI libraries. *Proc. Eurohaptics* 2003, 496–500. Dublin, Ireland.

Corrias, G., Licheri, R., Orrù, R., and Cao, G. (2012). Optimization of the self-propagating high-temperature process for the fabrication *in situ* of Lunar construction materials. *Chem. Eng. J.* 193-194, 410–421. doi:10.1016/j.cej.2012.04.032

Crawford, I. A. (2015). Lunar resources: a review. *Prog. Phys. Geogr.* 39, 137–167. doi:10.1177/0309133314567585

Heiken, G. H., Vaniman, D. T., and French, B. M. (1991). *Lunar sourcebook: a user's guide to the Moon*. Cambridge University Press, 285–356. chap. The Lunar.

Hoffmann, R. (2006). DEM simulations of toner particles with an O (N log N) hierarchical tree code algorithm. *Granul. Matter* 8, 151–157. doi:10.1007/s10035-006-0002-6

Houston, W. N., Mitchell, J. K., and Carrier, W. D., III (1974). "Lunar soil density and porosity" In Proceedings Lunar Science Conference, 5th, Houston, Tex., March 18-22, 1974, Vol. 3.(*A75-39540 19-91*) New York, Pergamon Press, Inc. 2361–2364.

Hulin, T., Panzirsch, M., Singh, H., Coelho, A., Balachandran, R., Pereira, A., et al. (2021). Model-augmented haptic telemanipulation: concept, retrospective overview, and current use cases. *Front. Robotics AI* 8, 611251–611322. doi:10.3389/frobt.2021.611251

Isachenkov, M., Chugunov, S., Smirnov, A., Kholodkova, A., Akhatov, I., and Shishkovsky, I. (2022). The effect of particle size of highland and mare lunar regolith simulants on their printability in vat polymerisation additive manufacturing. *Ceram. Int.* 48, 34713–34719. doi:10.1016/j.ceramint.2022.08.060

Kawamoto, H., Morooka, H., and Nozaki, H. (2022). Improved electrodynamic particle-size sorting system for lunar regolith. *J. Aerosp. Eng.* 35. doi:10.1061/(asce)as.1943-5525.0001371

Kuang, S. B., LaMarche, C. Q., Curtis, J. S., and Yu, A. B. (2013). Discrete particle simulation of jet-induced cratering of a granular bed. *Powder Technol.* 239, 319–336. doi:10.1016/j.powtec.2013.02.017

Long-Fox, J. M., Landsman, Z. A., Easter, P. B., Millwater, C. A., and Britt, D. T. (2023). Geomechanical properties of lunar regolith simulants LHS-1 and LMS-1. *Adv. Space Res.* 71, 5400–5412. doi:10.1016/j.asr.2023.02.034

Louca, J., Vrublevskis, J., Eder, K., and Tzemanaki, A. (2023). Elicitation of trustworthiness requirements for highly dexterous teleoperation systems with signal latency. *Front. Neurorobotics* 17, 1187264. doi:10.3389/fnbot.2023.1187264

Ludivig, P., Calzada-Diaz, A., Mendez, M. O., Voos, H., and Lamamy, J. (2020). "Building a piece of the moon: construction of two indoor lunar analogue environments," in Proceedings of the International Astronautical Congress, IAC 2020-Octob, 12–14.

McKay, D. S., Heiken, G. H., Taylor, R. M., Clanton, U. S., Morrison, D. A., and Ladle, G. H. (1972). "Apollo 14 soils: size distribution and particle types," in Proceedings of the Lunar Science Conference, Houston, Texas (Cambridge, MA: MIT Press), 983.

Meurisse, A., Lomax, B., Selmeci, Ã., Conti, M., Lindner, R., Makaya, A., et al. (2022). Lower temperature electrochemical reduction of lunar regolith simulants in molten salts. *Planet. space Sci.* 211, 105408. doi:10.1016/j.pss.2021.105408

Mitchell, J. K., Houston, W. N., Scott, R. F., Costes, N. C., Carrier, W. D., III, and Bromwell, L. G. (1972). Mechanical properties of lunar soil: density, porosity, cohesion and angle of internal friction. *Proc. Lunar Sci. Conf.* 3, 3235.

NASA AMES Research Center (2023). *Regolith Testbeds*.

Olson, A. D. (2022). "Design and testing of a prototype electrodynamic regolith conveyor for lunar ISRU," in Proceedings of the International Astronautical Congress, IAC 2022-Septe, 18–22.

Otto, H., Kerst, K., Roloff, C., Janiga, G., and Katterfeld, A. (2018). CFD–DEM simulation and experimental investigation of the flow behavior of lunar regolith JSC-1A. *Particuology* 40, 34–43. doi:10.1016/j.partic.2017.12.003

Papike, J. J., Simon, S. B., and Laul, J. C. (1982). The lunar regolith: chemistry, mineralogy, and petrology. *Rev. Geophys.* 20, 761–826. doi:10.1029/RG020i004p00761

Pereira, A., and Schmidt, A. (2021). "Efficient haptic rendering of regolith," in 2021 IEEE International Conference on Robotics and Automation (ICRA) (IEEE), 13975–13981.

Potter, N. (2023). *The many planned Moon landings of 2023*. IEEE Spectrum.

Prinetto, J., Colagrossi, A., Dottori, A., Troisi, I., and Lavagna, M. R. (2023). Terrestrial demonstrator for a low-temperature carbothermal reduction process on lunar regolith simulant: design and AIV activities. *Planet. Space Sci.* 225, 105618. doi:10.1016/j.pss.2022.105618

Reiss, P., Hager, P., Hoehn, A., Rott, M., and Walter, U. (2014). Flowability of lunar regolith simulants under reduced gravity and vacuum in hopper-based conveying devices. *J. Terramechanics* 55, 61–72. doi:10.1016/j.jterra.2014.04.005

Schlüter, L., and Cowley, A. (2020). Review of techniques for *In-Situ* oxygen extraction on the moon. *Planet. Space Sci.* 181, 104753. doi:10.1016/j.pss.2019.104753

Schulze, D. (2021). *Powders and bulk solids*. Berlin, Heidelberg: Springer.

Smith, M., Craig, D., Herrmann, N., Mahoney, E., Krezel, J., McIntyre, N., et al. (2020). The Artemis program: an overview of NASA's activities to return humans to the moon. *IEEE Aerosp. Conf. Proc.* 1–10. doi:10.1109/AERO47225.2020.9172323

Spudis, D., Plescia, J., Bussey, B., Josset, J.-L., Beauvivre, S., and Team, t. A. (2007). "The geology of the south Pole of the moon and age of shackleton crater," in 39th Annual Lunar and Planetary Science Conference, League City, Texas, 1626. doi:10.1029/2007GL029954

Stupar, D., Chabrol, G., Razak, A., Lecler, S., Tessier, A., Cutard, T., et al. (2021). "Feasibility of additive manufacturing processes for lunar soil simulants," in MMA 2021-14th International scientific conference MMA 2021-Flexible technologies, 223–227.

Toklu, Y. C., and Akpinar, P. (2022). Lunar soils, simulants and lunar construction materials: an overview. *Adv. Space Res.* 70, 762–779. doi:10.1016/j.asr.2022.05.017

US Navy (1982). *Foundations and earth structures*. Alexandria, Virginia: Tech. rep.

Wang, R., Qiao, G., and Song, G. (2023). Additive manufacturing by laser powder bed fusion and thermal post-treatment of the lunar-regolith-based glass-ceramics for *in-situ* resource utilization. *Constr. Build. Mater.* 392, 132051. doi:10.1016/j.conbuildmat.2023.132051

White, B. C., Haggerty, N. P., and Space, S. (2023). Carbothermal reduction system overview and developments in support of the Artemis program and a commercial lunar economy

Young, D. F., and Ball, W. P. (1997). Injection mode effects on tracer experiments in columns. *J. Hydrologic Eng.* 2, 113–119. doi:10.1061/(asce)1084-0699(19972:3(113)

frontiers | Frontiers in Space Technologies

TYPE Original Research
PUBLISHED 01 March 2024
DOI 10.3389/frspt.2024.1336548

OPEN ACCESS

EDITED BY
Marek Tulej,
University of Bern, Switzerland

REVIEWED BY
Rico Georgio Fausch,
University Hospital of Bern, Switzerland
Pavel Pořízka,
Brno University of Technology, Czechia

*CORRESPONDENCE
Kristin Rammelkamp,
kristin.rammelkamp@dlr.de
Susanne Schröder,
susanne.schroeder@dlr.de

RECEIVED 10 November 2023
ACCEPTED 19 February 2024
PUBLISHED 01 March 2024

CITATION
Rammelkamp K, Schröder S, Lomax BA, Clavé E and Hübers H-W (2024), LIBS for prospecting and Raman spectroscopy for monitoring: two feasibility studies for supporting *in-situ* resource utilization.
Front. Space Technol. 5:1336548.
doi: 10.3389/frspt.2024.1336548

LIBS for prospecting and Raman spectroscopy for monitoring: two feasibility studies for supporting *in-situ* resource utilization

Kristin Rammelkamp[1]*, Susanne Schröder[1]*, Bethany A. Lomax[2], Elise Clavé[1] and Heinz-Wilhelm Hübers[1,3]

[1]Institute of Optical Sensor Systems, German Aerospace Center (DLR), Berlin, Germany, [2]European Space Research and Technology Centre (ESA-ESTEC), European Space Agency, Noordwijk, Netherlands, [3]Department of Physics, Humboldt-Universität zu Berlin, Berlin, Germany

Laser-induced breakdown spectroscopy (LIBS) and Raman spectroscopy are still rather new techniques for *in-situ* exploration of extraterrestrial planetary surfaces but have shown their suitability and great potential in several successful robotic missions already. Next to serving primary scientific applications, both methods can also be used in the context of *in-situ* resource utilization (ISRU) such as scouting for wanted substances and the surveillance of extraction processes. Here, we present two laboratory studies conducted in the context of ISRU with a focus on the chain from prospecting to extracting oxygen from lunar regolith. For LIBS, with optimized data processing and combined with state-of-the-art multivariate data analysis approaches, we show the potential of the technique for identifying samples with increased ilmenite content and for elemental quantification. The measurements were done using lunar regolith simulant and low pressures simulating vacuum on atmosphereless bodies such as the Moon. With Raman spectroscopy, we analyzed lunar regolith simulant samples that underwent electrochemical alteration for oxygen extraction and production of metal alloys demonstrating the potential of Raman spectroscopy for ISRU process monitoring. We also discuss the results in a broader context, evaluating the potential of both methods for other aspects of ISRU support.

KEYWORDS

ISRU, LIBS, Raman, spectroscopy, *in-situ*, Moon

1 Introduction

In recent years, there has been a resurgence of interest and ambition surrounding humanity's return to the Moon (Crawford et al., 2012), driven by a collaborative effort between organizations from both the public and private sectors. Enabling scientific research and exploration while also establishing a long-term and cost-effective robotic and human presence on the Moon will lay the groundwork for future human missions to Mars and beyond. For this, the implementation and optimization of utilizing local resources becomes absolutely necessary. *In-situ* resource utilization (ISRU) will reduce costs, mass, and even risks of the missions and activities by extracting and processing indigenous resources including water, minerals, and gases, for a variety of applications such as life support, construction materials, and propellants for spacecrafts (Anand et al., 2012; Crawford, 2015). Specifically, the most important products from ISRU on the Moon are thought to include

O_2 and H_2O for life support, H_2 and O_2 for fuel and propellant, and other elements and substances for metallurgic and chemical production processes (Anand et al., 2012). The lunar regolith covering most of the Moon's surface with a thickness of several meters presents a likely primary feed stock for ISRU (McKay et al., 1991; Anand et al., 2012). The lunar regolith contains 45 wt% oxygen (Schlüter and Cowley, 2020). One particularly interesting mineral candidate for ISRU and oxygen extraction is the titanium-iron oxide ilmenite ($FeTiO_3$), as the iron oxide it contains can be reduced with hydrogen at a lower temperature compared to other processes. While reliance on ilmenite limits the oxygen yield and the locations on the lunar surface where the process is relevant, hydrogen reduction is one of the most studied ISRU processes (Anand et al. (2012) and references therein). More recently, molten salt electrolysis has been shown to extract almost all of the oxygen from lunar regolith using process temperatures similar to ilmenite reduction, which would allow for the simultaneous extraction of oxygen and metals from lunar regolith at any location (Lomax et al., 2020).

Furthermore, in the context of the increasing demand for technology metals, platinum group elements and rare earth elements (REE) are becoming an interesting target. Their extraction is not only of interest in a lunar context, but also extends to other bodies in the Solar System such as asteroids (Andrews et al., 2015).

The first step in ISRU is the scouting for and identification of wanted and suitable substances and could be done autonomously by robots with appropriate sensors and instruments. As an example, the composition of the lunar regolith is known to be very localized due to only minor lateral mixing processes (Anand et al., 2012) and areas with best suited materials have to be identified. Next, in the realm of ISRU applications, the necessity of process surveillance and control emerges as a critical aspect in ensuring the efficiency, reliability, and safety of resource extraction and utilization processes. The complex nature of the extraction and processing steps, coupled with the inherent challenges of operating in extraterrestrial environments, necessitates meticulous monitoring and control to optimize resource utilization, mitigate risks, and maximize mission success.

Two laser-based methods with high potential for various aspects in the context of ISRU from prospecting to surveying different processing steps are LIBS (laser-induced breakdown spectroscopy) and Raman spectroscopy. Both methods are increasingly used to study geomaterials with laboratory and portable instrumentation, e.g., (Senesi, 2014; Harmon et al., 2017; Jehlička and Culka, 2022; Senesi et al., 2021), and have entered the field of space exploration within the last decade being successfully applied in mobile robotic missions for *in-situ* analysis on other bodies of the Solar System such as on Mars, see below for more information and references. LIBS and Raman spectroscopy can both be applied with optical access only and without the necessity of sample preparation. Moreover, both methods are widely used for process surveillance and control in terrestrial applications across various industries facilitating real-time monitoring and optimization of different processes, e.g., Noll et al., 2014; Pedarnig et al., 2021.

Raman spectroscopy is a vibrational spectroscopy method that provides fingerprint information about molecular or lattice structure, allowing the identification of compounds and the analysis of crystallographic properties. Raman spectroscopy can be used to analyse minerals, detect impurities, and monitor the progress of chemical reactions or mineral transformations during extraction processes. Raman spectroscopy analyses the small fraction of laser light that is inelastically scattered by the sample and therefore undergoes an energy change, providing information about structure and bonding. Raman spectroscopy had its debut in space exploration with the ultraviolet Raman spectrometer SHERLOC (Bhartia et al., 2021) and the time-resolved Raman spectrometer as part of the SuperCam instrument suite (Wiens et al., 2021; Maurice et al., 2021) both on the Perseverance rover of NASA's Mars2020 mission. The Raman spectrometer called RAX (Hagelschuer et al., 2022; Schröder et al., 2023) for the small rover for JAXA's Martian Moons eXploration (MMX) mission (Michel et al., 2022; Ulamec et al., 2023) that will explore the surface of Mars' moon Phobos, will only be the third Raman spectrometer for extraterrestrial applications, scheduled to launch in 2026. RAX is a particularly compact, low-mass Raman instrument with a volume of only approximately 1 dm^3 and a mass of 1.5 kg. Another Raman spectrometer called RLS was developed for ESA's ExoMars rover (Rull et al., 2017).

LIBS is a technique that allows rapid *in-situ* multi-elemental analysis with no sample preparation and only optical access, making it particularly suitable for exploration tasks. LIBS is particularly sensitive to various metals, including light elements such as hydrogen, and a measurement can be made in seconds. LIBS uses a pulsed, focused laser to ablate a small amount of sample material and create a luminescent microplasma. The plasma emission has characteristic emission lines from which the qualitative and quantitative elemental composition of the sample can be deduced. LIBS is particularly well suited for geomaterial analysis and is increasingly used for both terrestrial, e.g., Rammelkamp et al., 2021; Müller et al., 2021, and extraterrestrial applications. LIBS is being used for *in-situ* geochemical analysis on Mars by NASA's two active rovers: The first LIBS instrument in space exploration is the ChemCam instrument on Curiosity, which has been collecting LIBS data from Gale Crater since the rover's landing in 2012 (Maurice et al., 2012; Wiens et al., 2012; Maurice et al., 2016). With the SuperCam instrument suite on Perseverance, the second LIBS for extraterrestrial purposes has been active in Jezero Crater since landing in 2021 (Wiens et al., 2021; Maurice et al., 2021). One third LIBS instrument on a Mars rover was developed by the Chinese space agency CNSA with MarSCoDe (Xu et al., 2021; Wan et al., 2021) and collected data between late 2021 and 2022. A LIBS instrument was also developed as a payload for the small lunar surface exploration rover of the Indian Chandrayaan-2 mission (Laxmiprasad et al., 2013). While Chandrayaan-2 was not successful due to the lander failing to make a soft landing in 2019, India's follow-up mission succeeded in reaching the Moon. The Chandrayaan LIBS instrument is particularly light-weight with less than 1.2 kg, has no focusing system and measures the lunar regolith beneath the rover's chassis at a constant distance of 0.2 m. For Mars, a high-performant LIBS instrument is currently being developed for space aiming for a mass below 2 kg (Rapin et al., 2023). More LIBS instruments for the Moon were proposed and developed such as the VOILA (Volatiles Identification by Laser Analysis instrument) instrument for the LUVMI-X (Lunar Volatiles Mobile Instrumention - Extended) rover which was - as the

names suggest - specifically designed for volatile analysis with a focus on hydrogen detection (Losekamm et al., 2022; Vogt et al., 2022a). LIBS instruments such as ChemCam and SuperCam are comparatively large (≈20 L) and heavy (≈10 kg), but are very flexible with their telescopic systems and can measure samples at a wide range of distances of up to 7 m (Maurice et al., 2012; 2021; Wiens et al., 2012; 2021). LIBS instruments for ISRU may be smaller, which may require compromises with regard to their performance and versatility, e.g., in tuning them to specific use cases while reducing their utility to others. The size, mass, and energy consumption of LIBS instruments are dependent on whole mission concepts, on the objectives, the hosting platforms, working distances, *etc.*, and cannot be specified in general terms. As an example, power consumption of the existing space LIBS instruments ranges from less than 5 W (Chandrayaan) to several tens of watts. It is important to note that the characteristics of the laser-induced plasma strongly depend on ambient conditions, such as pressure (Effenberger and Scott, 2010). For laboratory studies, these have to be simulated experimentally in vacuum chambers. It was found that while Martian atmospheric conditions are close to ideal, also in lower pressures such as on the Moon and other bodies without an atmosphere, suitable LIBS data can be obtained (Lasue et al., 2012; Kubitza et al., 2020; Vogt et al., 2022a).

While in a previous study, we have focused on hydrogen detection and its quantification in a lunar context (Vogt et al., 2022a), the focus of this work is on two aspects of the oxygen extraction chain and how LIBS and Raman spectroscopy could support ISRU activities. We optimize data processing and analysis of the LIBS data obtained in vacuum with state-of-the-art multivariate data analysis approaches and show the capability of LIBS for identifying and potentially quantifying enrichments of ilmenite in lunar regolith simulant. Moreover, we demonstrate the capability to survey the progression of oxygen extraction and metal alloy production with Raman spectroscopy, using samples of lunar regolith simulant reduced by molten salt electrolysis. The results are discussed in a broader context of the potential for ISRU supporting applications of both methods comparing to the state-of-the art.

2 LIBS

2.1 Experimental setup: LIBS breadboard model VOILA

LIBS data were measured with a breadboard model of an instrument called Volatiles Identification by Laser Analysis instrument (VOILA) which was developed as payload for a lightweight rover for *in-situ* exploration of the lunar south pole. The initial design and development of this rover and its payload was part of the Lunar Volatiles Mobile Instrumention - Extended (LUVMI-X) project (Losekamm et al., 2022; Vogt et al., 2022a) describe the VOILA breadboard model in detail and the choices made in its design. We would like to refer to this work for more details on the VOILA instrument and provide only the most relevant information below.

The samples are placed in a vacuum chamber which can be evacuated to pressures lower than 10 mPa to simulate the low pressure on the surface of the Moon. In this pressure range, the mean free path is large enough for the LIBS plasma to expand freely without being confined by the surrounding atmosphere. Going to even lower pressures such as on the surface of the Moon (Heiken et al., 1991) is expected to not change the behaviour of the laser-induced plasma so that experiments simulating the vacuum of atmosphereless bodies are typically done in the range of 10–100 mPa (Knight et al., 2000; Lasue et al., 2012; Kubitza et al., 2020). The laser was developed by the Laser Zentrum Hannover e.V. (LZH) in the framework of the LUVMI-X project. The active medium is a Yb:YAG crystal emitting at a wavelength of 1,030 nm with a pulse duration of 7.8 ns. The energy per pulse is adjustable up to a maximum of 25 mJ. The optical head where the laser beam is expanded was built of commercial off-the-shelf components (COTS). The expanded beam is then focused inside the simulation chamber onto the sample at a working distance of 400 mm. The emitted radiation by the plasma is collected by the same optics which is used for the focusing of the laser beam. Within the optical head, a dichroic mirror separates the two light paths and the collected plasma radiation is guided to a fiber-coupled compact spectrometer (Avantes, model AvaSpec-Mini). With a spectral resolution of about 0.4 nm, the spectrometer covers a spectral range of 340–900 nm, from which we use only the range 390–800 nm as before 390 nm and beyond 800 nm the transmission of the optical head is limited. As previously noted, the instrument design decisions are discussed in Vogt et al. (2022a) and are not part of this study. However, we want to comment on the smaller spectral range compared to instruments such as ChemCam and SuperCam. These instruments were designed for different purposes and missions. VOILA has to be much smaller and lighter, which limits the choice of spectral range, in which we ensured that the chosen range includes emission lines from the majority of oxides in lunar material (Si, Al, Ti, Fe, Mg, and Ca), as well as from alkali elements (Na, Li, and K) and H and O.

2.2 LIBS samples and sample preparation

For the study on the potential of detection and quantification of ilmenite enrichments in lunar regolith with LIBS, two commercially available lunar regolith simulants were mixed with concentrated ilmenite which was provided by the Museum für Naturkunde Berlin (MfN). The lunar regolith simulants representing the Lunar mare composition (LMS-1) and the Lunar highland composition (LHS-1), respectively, are both from Exolith. The mineral and oxide composition is given in Table 1. In their pure form, LHS-1 contains 0.4 wt% and LMS-1 4.3 wt% of ilmenite. All three components are available in form of fine to coarse grained powders and were mixed and further crushed with mortar and pestle. The resulting mixtures with varying ilmenite concentrations were pressed into pellets of about 1 g and 14 mm diameter at a pressure of 5 t for about 10 min. We produced 15 and 14 samples per simulant, respectively, one pure sample of both simulants and one pure ilmenite sample, giving a total of 32 samples, an overview of which is given in Table 2.

TABLE 1 Overview of both mineralogical and elemental oxide composition of the two lunar regolith simulants LMS-1 and LHS-1 used in the LIBS experiments. The LMS-1 is also the starting material of electrolysis samples measured with Raman spectroscopy. Trace elements such as Cl, Cr_2O_3, NiO, SO_3, and SrO are not shown.

Mineral component	wt% LMS-1	wt% LHS-1	Oxide	wt% LMS-1	wt% LHS-1
Pyroxene	32.8	0.3	SiO_2	40.2	48.1
Glass-rich basalt	32.0	24.7	TiO_2	7.3	1.1
Anorthosite	19.8	75.4	Al_2O_3	14.0	25.8
Olivine	11.1	0.2	FeO	13.9	3.7
Ilmenite	4.3	0.4	MnO	0.3	0.1
			MgO	12.0	0.3
			CaO	9.8	18.4
			K_2O	0.6	0.7

TABLE 2 Overview of samples measured with LIBS.

Component	# of samples	Pure ilmenite [wt%]	Range of ilmenite concentrations [wt%]
LMS-1	15	4.3	4.3–52.0
LHS-1	16	0.4	0.4–39.5
Ilmenite	1	100	-

2.3 LIBS measurements

All mixtures of lunar regolith simulants with ilmenite were measured with the VOILA setup described in Section 2.1. The pressure in the vacuum chamber was reduced to below 10 mPa. Each sample was measured at ten different locations by moving the sample holder. The laser was started with a repetition rate of 10 Hz together with the spectrometer with an exposure time of 3 s, i.e., the emission of 30 successively laser-induced plasmas was accumulated for one spectrum at one position. A dark spectrum was measured with the same exposure time for each sample and used for all ten spectra. The laser pulse energy was adjusted to 17 mJ.

2.4 LIBS data preprocessing and analysis

Before the analysis, several preprocessing steps were applied. For all ten measurements on one sample, one dark spectrum was measured which is subtracted from the LIBS active data first. Then, all spectra are corrected for the response function of the spectrometer and the transmittance of the optical head. The mostly undiagnostic continuum emission of the laser-induced plasma that is superimposing the emission lines of the atoms and ions was removed computationally by performing background subtraction. This was carried out iteratively by first smoothing the spectrum and subsequently masking all un-smoothed spectrum values that are larger than the smoothed ones. When repeating this procedure multiple times, a satisfactory fit of the background can be achieved without affecting the emission line intensities. A more detailed description of the baseline correction can be found in the Supplementary Material.

As part of our initial exploration of the data, we used the multivariate technique principal component analysis (PCA) on all of the spectra. PCA is a matrix decomposition technique in which the data is rotated into a new space where the majority of the variation in the initial data can be represented by a reduced number of dimensions, termed as components (Lever et al., 2017). Applied to LIBS data, it is in particular useful to group similar spectra together, investigate correlations, and to check for outliers (Pořízka et al., 2018). In our study, it was seen that the amount of explained variance increases at a slow rate as additional components are added. The initial four components account for 61% of the variance, however, subsequent components result in only marginal increments. This trend implies the presence of uncorrelated noise among the spectra and gave rise to the approach of using the first four components to denoise the spectra, which is a common approach in spectral data processing, e.g., Stephan et al. (2008). We then applied this method, taking into account four components, and obtained eigenvalues, also called scores, for each spectrum. Finally, we used the model to back-transform these eigenvalues, resulting in notably cleaner spectra. An example is shown in Figure 1, which shows the original spectrum, the reconstructed spectrum and, in the lower plot, the residuals. The residuals show no spectral characteristics, indicating the successful removal of noise in the back-transformation.

2.5 LIBS ilmenite detection

For a better understanding of the measured LIBS data, we first looked at the spectra of pure LMS-1, LHS-1 and ilmenite. The average spectra of the ten measurements were taken and are shown in Figure 2. The top row shows two zooms to spectral regions with

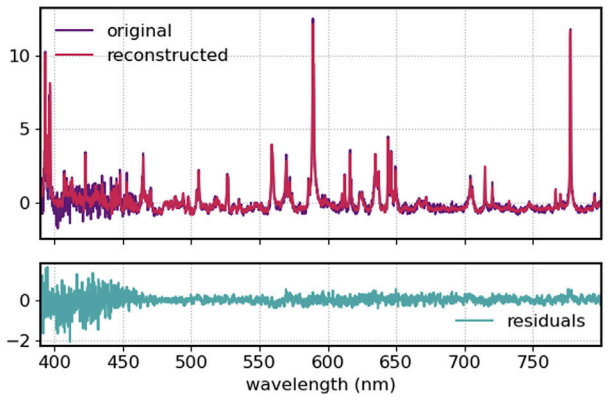

FIGURE 1
Example spectrum of an LHS-1 sample, original spectrum and back-transformed using a four-dimensional PCA model. The bottom plot shows the residuals between the original and reconstructed spectrum. The reconstructed spectrum is reduced in noise but not in spectral information, as can be seen from the residuals.

strong Ti emission lines. Fe emission lines can also be observed in the ilmenite spectrum, but they are weaker than the Ti lines. The LMS-1 spectrum shows very weak Ti emission lines even though it contains 4.3 wt% ilmenite. In general, both spectra of LMS-1 and LHS-1 have a few weak features in the regions with strong Ti emission lines, 452–458 nm and 497–504 nm. However, they are difficult to interpret because they cannot be clearly distinguished from noise. The main difference between the two lunar regolith simulants lies in the strength of the Mg and Ca emission lines: The LMS-1 spectrum has stronger Mg emission lines, whereas the LHS-1 spectrum has stronger Ca emission lines, consistent with their compositions, compare Table 1.

Two approaches to the identification and prospective quantification of ilmenite enrichments were investigated. In the first, all counts in the spectral range 496.5–503.0 nm were summed, as most of the intensities there are expected to be from Ti. Although ilmenite also contains Fe, we decided to focus on Ti because Ti emission lines are more prominent in the instrument's spectral range than those of Fe, see Figure 2. From a geological perspective, Ti is a better indicator of the presence of ilmenite than Fe, since Fe is a major constituent in most geological materials. For this approach, the calibrated spectra were used but no standardization or data normalization was applied.

The second approach is based on the matrix decomposition technique non-negative matrix factorization (NMF), which was applied to the entire data set with the aim of extracting a factor that can be assigned to ilmenite. NMF belongs to the family of source separation techniques and assumes nonnegativity in the data set which makes it in particular useful for data with a physical interpretation (Pauca et al., 2006). An NMF model with four factors can reconstruct the data with a reconstruction error of 6.7%. We also tested models with more factors, but this resulted in only a small reduction in the reconstruction error, while the factors modelled more noise. We also applied NMF to the data that had not undergone PCA denoising. This also showed that clear

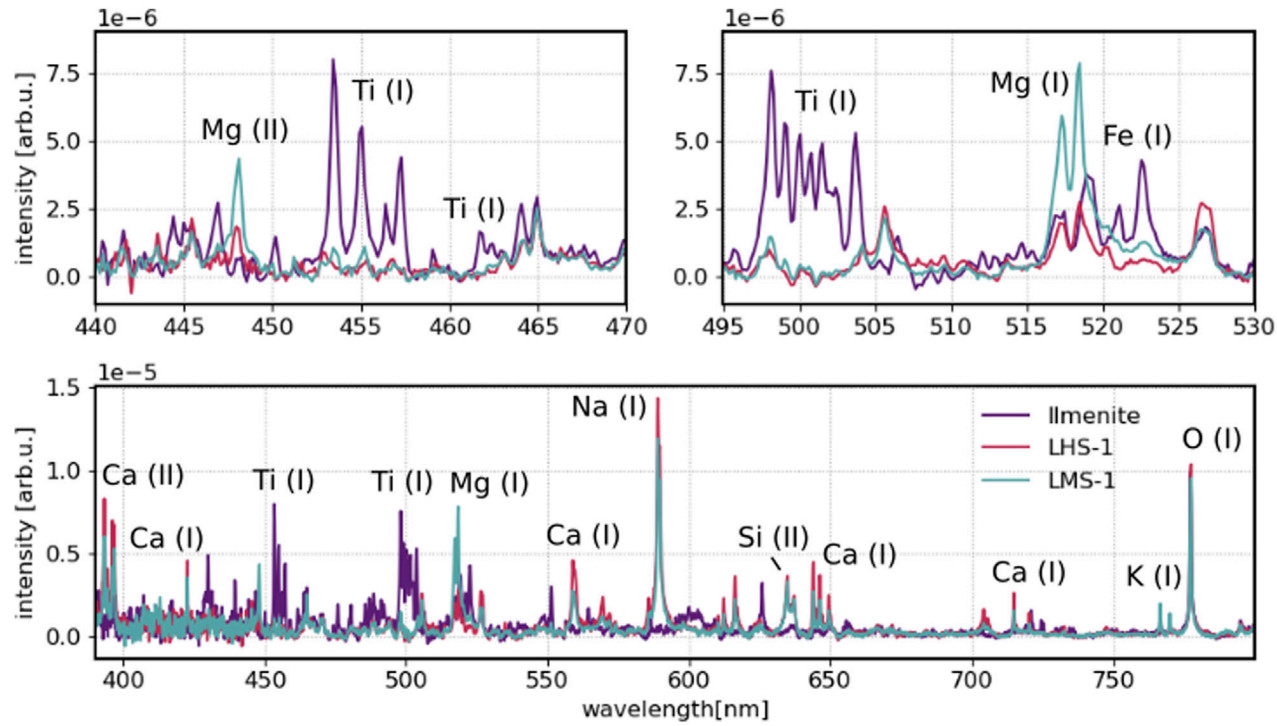

FIGURE 2
Mean LIBS spectra of pure LMS-1, LHS-1 and ilmenite samples. The lower plot shows the full spectral range used in this study. The most prominent emission lines are annotated. Major differences between the three samples are observed for the Ca, Mg and Ti emission lines. The plots in the top row zoom in on the spectral regions with the strongest Ti emission lines indicative of ilmenite.

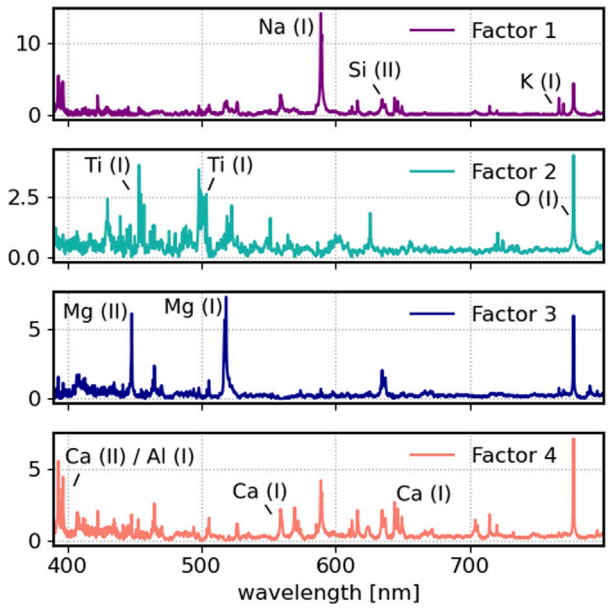

FIGURE 3
All four factors of the NMF model with annotations of the most prominent emission lines on each factor. Factor 2 can be interpreted as the ilmenite component showing dominant Ti emission lines while factor 3 and factor 4 represents LMS-1 and LHS-1 components, respectively.

factors were difficult to identify as they were characterized by noise variations. Finally, we decided on the four-factor model whose extracted factors are shown in Figure 3. The first NMF factor primarily represents the alkalis Na and K, and Si, which are present in comparable quantities in both lunar regolith simulants. Thus, this factor may be interpreted as a shared baseline. The NMF factor 2 can be assigned to ilmenite mainly on the basis of strong Ti emission lines. Factor 3 represents the LMS-1 component with strong Mg lines, while dominant Ca emission lines on factor 4 indicate a correspondence with the LHS-1 component. This is confirmed by the fact that the majority of LHS-1 samples have the highest scores on factor 4 and the same can be observed for LMS-1 samples and factor 3.

In Figure 4, for each sample except the pure ilmenite sample, the summed Ti intensities and the scores on NMF factor 2 are plotted versus their known ilmenite concentration. Both values are shown as box plots, where each box corresponds to one sample and contains the values of all ten measurements. For both approaches, an overall increase of the ilmenite measure is observable with increasing ilmenite concentrations. However, the values show in both cases a large scatter and also a few targets which do not follow the overall increase. Since the scatter is observable for both approaches, the reason is likely related to the samples and the measured data and not to the data analysis approach. Also worth mentioning is that no clear trends were observed when looking at the two lunar regolith simulants separately from each other.

Although the components were crushed and mixed with mortar and pestle, the samples are not homogeneous on the scale of the ablation zone, i.e., the laser spot size. To investigate this, images of the samples were taken using a digital microscope, a selection of which are shown in Figure 5. For both simulants, the pure sample, a sample with medium and a sample with high ilmenite enrichment are shown. The ilmenite grains can be recognised by the fact that they are black and reflective. As expected, the density of the ilmenite grains increases with increasing concentration. Their distribution is not homogeneous and the grains also differ in size. In a recent study, regolith simulants from Exolith Lab including the two lunar simulants used for the LIBS samples LMS-1 and LHS-1 were extensively investigated and their production process described in detail (Long-Fox and Britt, 2023). Besides the mineralogical composition, the physical properties of the simulants including the grain size distribution were designed to match Apollo samples. The grain size in both samples vary in a range of < 0.04 μm–1,000 μm. To compare this to our LIBS investigated spot sizes, we also investigated the craters that are left after a LIBS measurement (not shown). These craters generally vary somewhat in size with smaller or larger grains removed from the crater edges and have an average diameter of 500 μm and a typical depth of 200–500 μm when formed by 30 consecutive laser shots and the subsequent plasma.

With the observed heterogeneity of the samples, it is therefore not surprising that with increasing concentration of ilmenite, the scatter of the points increases. At a higher density, the probability is higher that several of the ten points measured on a sample mainly hit ilmenite grains. Accordingly, we have introduced a measure for both approaches that is closer to the reality of heterogeneous geological samples: we count how many points of all points measured on a sample have a clear signature of ilmenite. The definition of a clear signature in our case is empirical for which the definition of the limit of detection was followed, but adapted to the measurement data. Instead of a true blank sample, samples with an ilmenite concentration of less than 5 wt% were considered as samples without a clear signal. This included 4 samples with a total of 40 measurements. The threshold for a clear signature was then calculated by taking the mean value plus 3 times the standard deviation of these 40 measurements for both summed Ti intensities and NMF 2 scores. For the summed Ti intensity, we obtained a value of 2.0×10^{-5} as the limit, see purple dashed line in Figure 4 upper plot. For the NMF Factor 2 score, the limit is at 0.1, indicated by the turquoise dashed line in the lower plot of Figure 4. All measurement points that have a value above these limits are counted as ilmenite detections. The plots in Figure 6 display the rate of ilmenite detections for each approach as ilmenite concentrations increase. Both approaches show an increase in ilmenite detections, with the highest rates occurring predominantly in samples with a concentration greater than 30 wt% ilmenite. Furthermore, the NMF factor 2 approach begins to detect a significant number of occurrences at approximately 10 wt% ilmenite. The summed Ti intensity is less responsive to increments in ilmenite concentration as there is still one sample with zero ilmenite detections while these samples have ilmenite concentrations greater than 10 wt%. Although this dataset exhibits heterogeneity that precludes reliable quantification of ilmenite abundances, the approach based on the extracted NMF factor can be inferred as a type of lower detection limit for ilmenite enrichments. Two or more detections of ilmenite within a raster containing ten points may indicate that this target or area possesses an average ilmenite enrichment greater than 10 wt%.

Overall, both approaches have their advantages and disadvantages for the detection of ilmenite with LIBS. While the summation of Ti intensities is relatively easy to implement, it is not guaranteed that lines from other elements found in the same spectral range do not influence the results. The lines do not even have to be

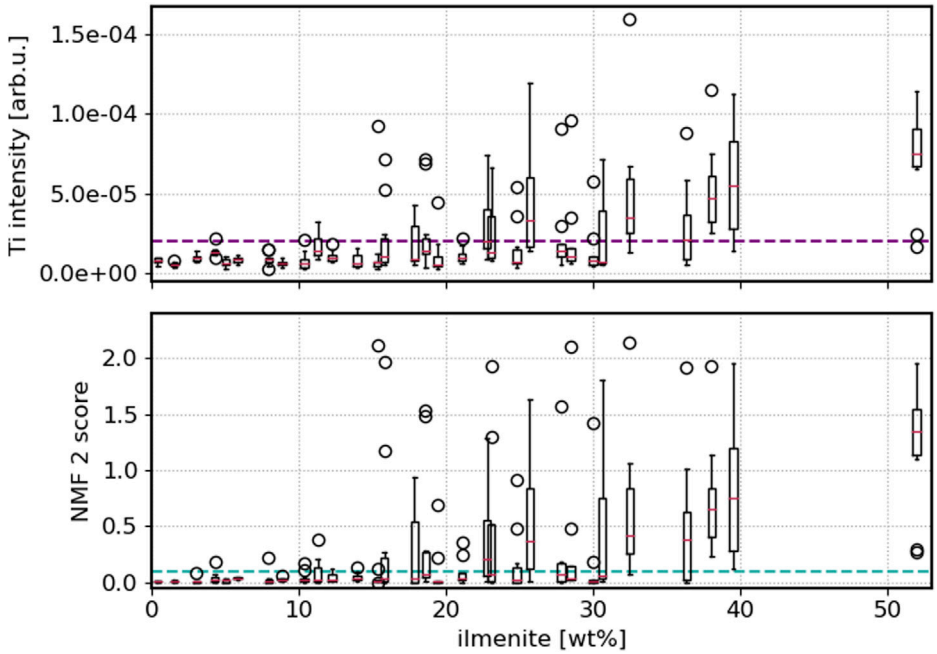

FIGURE 4
For both approaches, the summation of Ti intensity and NMF factor 2 values, are shown as a function of ilmenite concentration in the samples. For each sample a box is shown, as known from conventional box plots, containing all 10 measurements from one sample. The dashed lines correspond to the thresholds defined to discriminate between ilmenite not being detected and ilmenite detected. In both cases there is a general increase with increasing ilmenite concentration, but what increases more is the scatter between the 10 measurements on a sample.

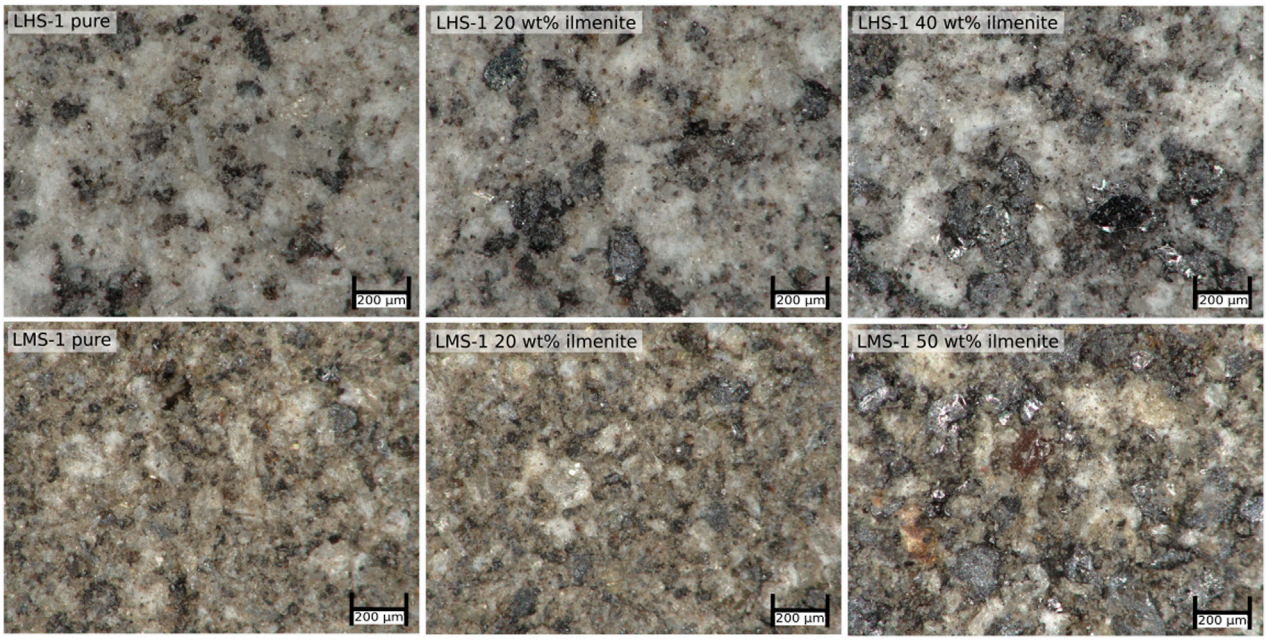

FIGURE 5
Images of selected samples taken with a digital microscope. For each lunar regolith simulant, the pure samples, a sample with a moderate addition of ilmenite, and the sample with the largest amount of ilmenite added are shown. In general, it can be seen that the samples are heterogeneous. In addition, the shiny metallic grains that are ilmenite are not evenly distributed and it is very likely that the laser is not hitting ilmenite grains in each measurement, although the overall ilmenite abundance may be high.

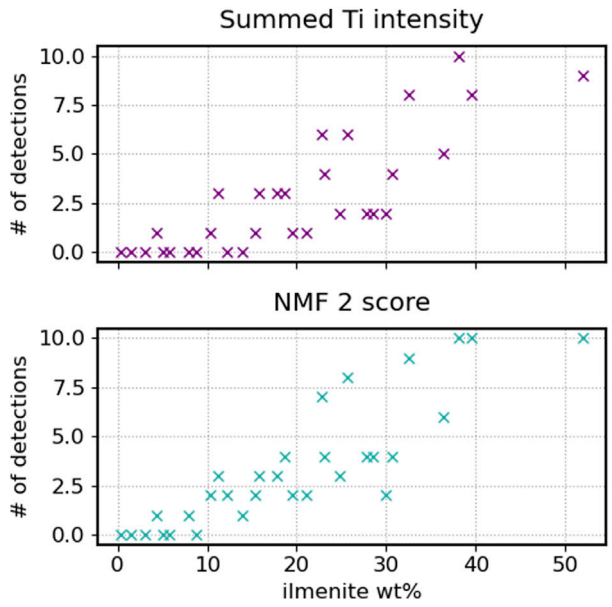

FIGURE 6
Number of ilmenite detections per sample and therefore per ilmenite concentration for both approaches. Starting with samples with more than 10 wt% of ilmenite, the number of ilmenite detections increases with increasing ilmenite concentration. However, the increase is not continuous and some samples have less detections than samples with lower ilmenite abundances.

particularly strong and directly recognisable to influence the results. On the other hand, extracting a suitable component with methods like NMF that can mainly be assigned to ilmenite minimizes the risk of taking into account influences from other elements. How this approach can be applied to a more comprehensive and realistic data set with enhanced mineral diversity of the samples and in particular the effects of variations in iron content needs further investigation. LIBS detects elements rather than minerals, which means that other Ti-bearing minerals may also contribute to the detection, potentially biasing the ilmenite result. However, previous analyses of the lunar surface have shown that Ti is mainly present in the mineral ilmenite, and less frequently in Si-Ti phases such as silcate glasses (Lucey et al., 1998; Anand et al., 2012). Additionally, as previously mentioned, the NMF approach is less influenced by other elements. To achieve a high score on NMF factor 2, all Ti lines must be present. and lines that are not part of the factor, such as Si (see Figure 3), do not count. In closing, this study yielded promising results that LIBS is indeed suitable for *in-situ* detection and quantification of ilmenite enhancements in lunar regolith with dedicated data processing and state-of-the-art multivariate data analysis.

3 Raman

3.1 Experimental setup: Confocal Raman microscope

The experiments were performed with a commercial confocal and continuous-wave (cw) Raman microscope (WITec alpha300 R system) at DLR Berlin, Germany. A frequency-doubled cw Nd:YAG laser with an excitation wavelength of 532 nm was used. The laser radiation was focused to a spot of approximately 1.5 μ m diameter on the sample surface using a Nikon ×10 objective. An edge filter which opens around 70 cm^{-1} suppresses the detection of Rayleigh scattered photons. The spectrometer covers a spectral range up to 3,800 cm^{-1} and has a spectral resolution of about 4 cm^{-1}.

3.2 Raman samples and sample preparation

To demonstrate one use case for Raman spectroscopy in the context of ISRU, a sample set that was chemically altered in an electrochemical FFC (Fray, Farthing, Chen) process (Chen and Fray, 2020; Schlüter and Cowley, 2020) for oxygen extraction was chosen. In recent studies by Lomax et al. (2020) and Meurisse et al. (2022), the FFC process was demonstrated for the direct electro-deoxidation of solid-state lunar regolith simulant. Besides the process, also the development of inert anodes is an important research area (Hu et al., 2016; Du et al., 2021) to ensure that there are deployable models in space when the process is ready for use on the Moon. For our study, samples that had undergone the FCC process using the experimental set up described in Meurisse et al. (2022) were measured with Raman spectroscopy. This set of samples contained lunar regolith simulant at different stages throughout the process, with successively less oxygen and more metals.

The starting material for all samples was the lunar regolith simulant LMS-1 (Exolith Lunar Mare Simulant, procured in 2019), of which the composition can be seen in Table 1. The untreated LMS-1 starting material was used as a reference and contains approximately 42 wt% oxygen. Five samples that spent different lengths of time in the electrolysis process were analysed. The samples are therefore labelled: 00, 05, 10, 13, 16, 24 h. Following 24 h of processing, approximately 80% of the oxygen had been removed from the LMS-1 material. Similar to the LIBS samples (Section 2.2), the samples were pressed into pellets.

3.3 Raman measurements

All measurements were carried out with the same measurement parameters. We made single measurements on the samples but also line scans where mostly eight points were measured on a line previously drawn in the microscope image of the samples. For both the single measurements and the line scans, the Raman signal was integrated for 5 seconds and no further accumulations were made. The laser power was set to 7 mW for all measurements. The number of measurements per sample varied, but a minimum of 33 spectra per sample were acquired from all. A detailed list is given in Table 3.

3.4 Raman data preprocessing

Not all measured spectra show Raman signatures and also varying contributions of luminescence were observed. The observed luminescence was deemed undiagnostic for this study and the broad superimposing emission was therefore removed in

a first data preprocessing step with a baseline subtraction. For this, we employed the asymmetrically reweighted penalized least squares algorithm which is based on the Whittaker smoother (Baek et al., 2015). The subtraction of the baseline is not crucial for the subsequent evaluation, however, for more information on the methods used see the Supplementary Material. To filter out spectra without relevant Raman signatures, a criterion based on signal-to-noise ratio was used. The maximum signal value in the spectrum was picked and the ratio of its height to the standard deviation of a nearby peak-free area in the spectrum was taken. After analyzing the ratio and examining the spectra, we decided that a ratio of eight was a reasonable threshold, so that spectra with a ratio greater than eight were kept for further analysis. The final numbers of spectra per sample are also listed in Table 3.

3.5 Raman results

The analysis of the Raman spectra is mainly based on qualitative observations, i.e., the identification of minerals and components in each sample. We first present examples of spectra and corresponding mineral identification in the starting and end materials (00-h and 24-h samples). We then observe the evolution of the identified Raman signatures throughout the series, to monitor the changes happening in the sample during the process.

Note that the material analyzed in the current study is not the most ideal material for Raman spectroscopy. Lomax et al. (2020) showed that the final material consists predominantly of metal alloys that are weak Raman scatterers. Consequently, several Raman spectra of the treated samples expectedly do not exhibit any detectable Raman signal, see Table 3. In spite of this we have observed several spectra with significant Raman signatures.

Starting with the Raman spectra of the untreated sample, it was possible to identify Raman spectra of minerals that match the known mineralogical composition of the starting material. The upper part of Figure 7 shows an image of the sample taken with the microscope together with the course of a line scan and Raman spectra of three highlighted positions. At position 1, a plagioclase spectrum was measured, at position 2 an olivine spectrum and at position 3 a pyroxene spectrum. These minerals are consistent with the mineralogical composition of the starting material (Table 1). The sample that was in the electrolysis for the longest time, 24 h, shows very different signatures. The lower part of Figure 7 shows a picture and also three selected Raman spectra of this final sample. Looking at the microscope image alone, it is noticeable that the parts of the sample are more reflective and look more metallic overall compared to the untreated sample. The spectrum of position 1 shows spectra of three components: silicon, carbonate, and graphite. Raman modes of these materials also occur at position 2 with both silicon and graphite modes, and at position 3 with the modes of graphite alone.

The comparison of the initial and final samples demonstrates that Raman spectroscopy has the potential to assist in controlling the results of the oxygen extraction process. Moreover, Raman may also be applicable *in-situ* for real-time monitoring of the process. In this instance, it would be possible to measure several tens of spectra and use the statistics of these spectra to monitor the evolution of the sample. Based on our investigation of the starting and end material, we identified the occurrences and characteristics of different signatures in the series.

First, we track the minerals identified in the starting material: olivine, pyroxene and plagioclase. Considering these minerals as characteristic of the starting material, their presence was monitored in the treated samples and the results are displayed in the last column of Table 3. Keeping in mind that all samples are mixtures and heterogeneous on the scale of the Raman laser spot size, and that it is always possible that we have not measured relevant phases, it can still be observed that the number of starting material mineral detections decreases significantly for the 5-h sample. Only two additional olivine spectra were measured for the later samples. This suggests that despite incomplete oxygen extraction for these samples, the starting material has already been altered to a considerable degree after 5 h of electrolysis.

Secondly, the Si mode around 500 cm^{-1} is visible in numerous spectra of the treated samples and will be discussed in more detail in the following. The Si mode appears mainly around 500 cm^{-1}, for example, also in the spectrum measured at position 2 (lower part of Figure 7). For crystalline silicon one would expect a sharp peak around 520 cm^{-1} associated to a transversal optical phonon. The mode that we observe in our study is shifted towards lower Raman shifts and broadened which could indicate that the silicon is in a more amorphous than crystalline phase (Zwick and Carles, 1993). For the samples which spent 5, 13 and 24 h, respectively in the electrolysis process, the Si mode is shown in the upper part of Figure 8. The gray lines belong to spectra of each of the samples which exhibits a clear Si mode whereas the pink line is the mode of crystalline Si measured on a Si wafer with the same experimental set-up. All spectra were normalized to their maximum intensity for better comparison. The comparison clearly shows that the Si Raman modes of the reduced lunar regolith simulant samples are broadened and also shifted to lower Raman shifts. To investigate whether the magnitude of the shift and the line width is related to the time the samples spent in electrolysis, we fitted the modes with Voigt profiles and checked their line center as well as their width via the full width at half maximum (FWHM). The lower part of Figure 8 shows the results as violin plots for all spectra having the Si mode. The violin plots display the distributions of both fit parameters for each sample where the middle horizontal line represents the median. There is no distinct trend observable with regard to the duration, nevertheless some differences appear. Regarding the peak positions (shown in the lower left of Figure 8), the 5 and 10-h samples with the shortest duration have mainly peak positions larger than 510 cm^{-1} and smaller than 520 cm^{-1}. A larger spread of center positions can be observed for the 13 and 16-h samples, reaching from 490 cm^{-1} up to 520 cm^{-1}. The 24-h samples with the longest duration in the electrolysis feature center positions that are again less scattered but are mainly at a lower Raman shift close to 500 cm^{-1}. The Si mode widths (shown in the lower right of Figure 8) for samples electrolysed for 5 and 10-h are on average narrower than those for longer duration samples. The 13 and 16-h samples exhibit wider distributions, while the Si mode widths for the 24-h sample are less dispersed, but larger than those for the 5 and 10-h samples. The observed variations in center position and width suggest that a Si phase with varying degrees of crystallinity could have emerged during electrolysis. Amorphous silicon has a broad peak

TABLE 3 Overview of Raman spectroscopy measurements on the different treated samples including the starting material. Not all spectra exhibit identifiable Raman modes; therefore, not all spectra were kept for further analysis as described in the text. The rate shown is for the remaining spectra. The last column gives the number of measured spectra which could be assigned to primary minerals characteristic of the starting material, i.e., to pyroxene, plagioclase or olivine.

Sample	# of measurement points	# of proofed spectra	Rate [%]	# of primary minerals spectra
00 h	34	12	35	10
05 h	33	27	82	7
10 h	41	29	71	0
13 h	34	23	68	1
16 h	49	42	86	1
24 h	50	38	76	0

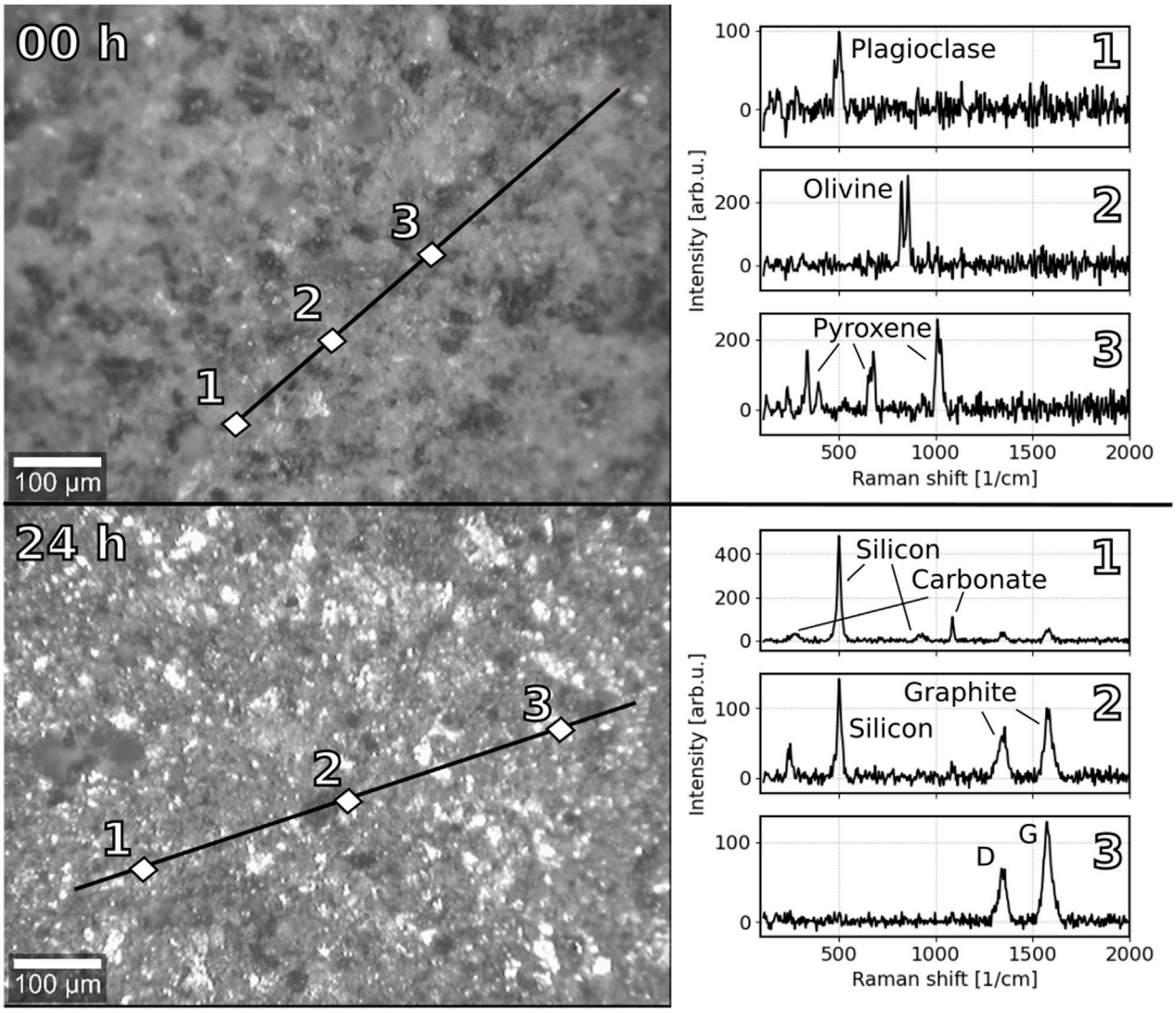

FIGURE 7
Examples of the untreated (top) and the 24-h sample (bottom) viewed through the Raman microscope. The 24-h sample reveals an increased presence of reflective sections, typically observed in metallic substances. In both images, the black line marks the course of a linescan with three positions highlighted. The corresponding Raman spectra from these positions are displayed on the right. While the untreated sample displays spectra of minerals belonging to the initial material, the 24-h sample spectra may be interpreted as results of the electrolysis process.

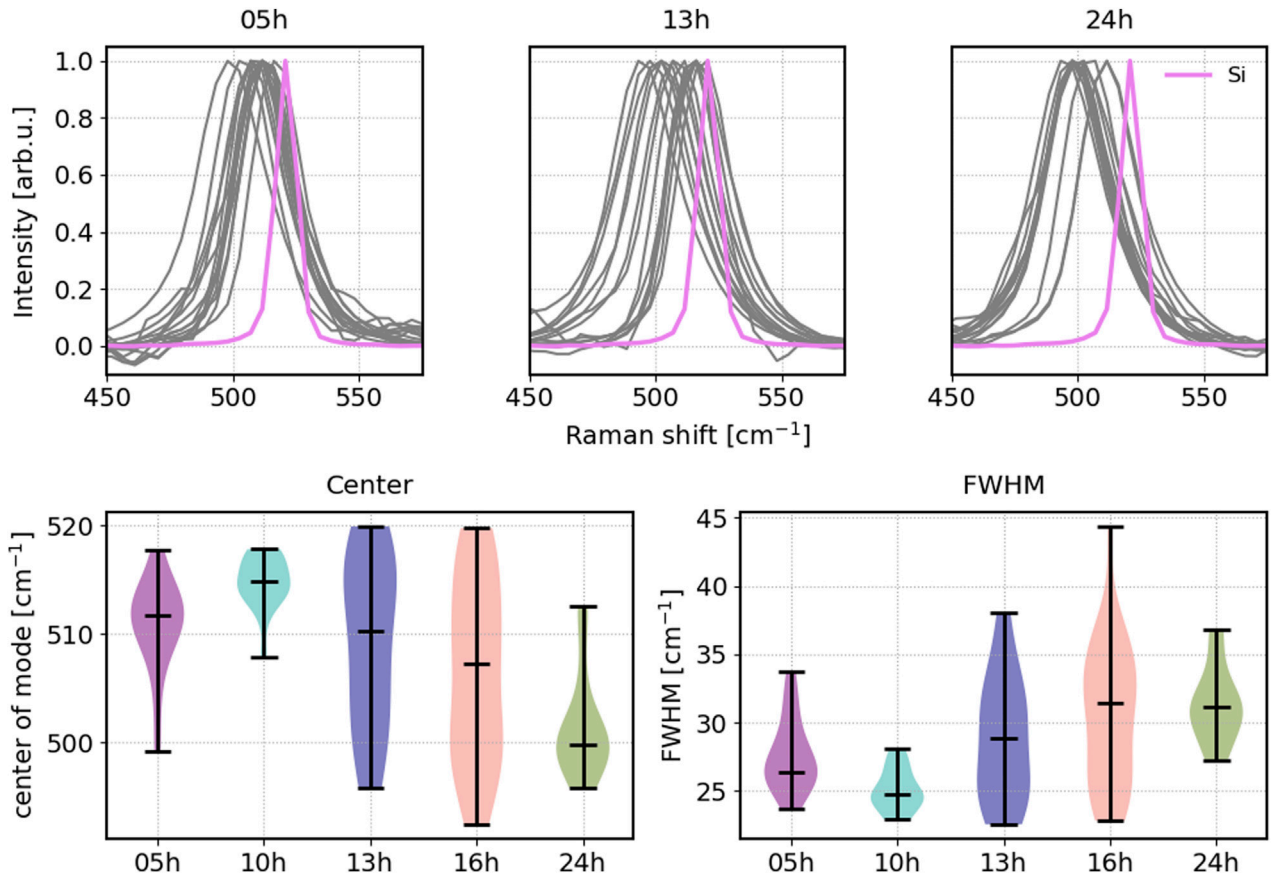

FIGURE 8
Investigation of Si Raman mode at 520 cm^{-1}. *Top row*: Zoom for spectra measured on the 5, 13 and 24-h samples (gray lines), only spectra with a clear Si mode are shown. For comparison, the Si mode measured on a Si wafer with the same set-up is shown in pink. All spectra were normalized to their maximum intensity. *Bottom row*: Mode fitting results as violin plots where the middle horizontal line represents the median. *Left*: The center is at higher wavenumbers on average for the 5 and 10-h samples than for the 24-h sample, while a wider distribution for the 13 and 16-h samples than for the others is observable. *Right*: Also, the broadening indicates variations among the samples: there is again a more extensive spread observed for the 13 and 16-h samples, whereas the Si modes of the shorter duration samples are narrower when compared to those of the 24-h sample.

around 480 cm^{-1} and depending on the crystalline fraction, it overlaps more or less with the crystalline Si mode at 520 cm $^{-1}$ resulting in shifts to lower Raman shifts (Kimura and Katoda, 1997; Islam and Kumar 2001). Several studies have investigated the impact of strain and stress on both crystalline and amorphous silicon, and have explored how these influences affect the Raman Si modes (Ureña et al., 2013; Strubbe et al., 2015). However, in order to make conclusive interpretations from our samples and to potentially link the Si mode to the amount of extracted oxygen, further research would be necessary that specifically targets the Si phases.

Finally, we observed the appearance of carbon-related features. Carbonate is identified by the A_{1g} mode of the CO_3 polyhedra at 1,085 cm^{-1} (Dufresne et al., 2018). Graphite is observable in all of the three selected spectra of the 24-h sample shown in Figure 7 by means of the so called D and G modes at 1,370 cm^{-1} and 1,580 cm^{-1}, respectively. The G mode is the typical E_{2g} mode of sp^2 carbon systems due to stretching of C-C bonds while the D mode was named for disorder-induced-mode (Reich and Thomsen, 2004). Graphite is formed as a result of degradation of the graphite anode utilized in the electrolysis process. In the spectrum of the 10-h sample, graphite modes can be observed for the first time, while no graphite spectrum was measured from the 13-h sample. The modes appear quite regularly for the 16 and 24-h samples as expected because of the anode's gradual degradation over time. The electrolysis focused on the reduction processes and end products obtained from the regolith, rather than on the anodic processes. In real ISRU scenarios, an inert anode will be employed to produce oxygen directly and prevent carbon contamination.

In summary, future studies may need to further investigate the different phases formed during electrolysis, but this study has shown that it is possible to use Raman spectroscopy to detect changes in the samples related to the duration of electrolysis and therefore the amount of oxygen extracted.

4 Conclusion

The two separately presented studies show that LIBS and Raman spectroscopy are promising techniques to support ISRU activities. With LIBS we could show the suitability for the detection of enrichments of ilmenite and the potential for elemental

quantification. This was possible despite the fact that the used VOILA breadboard model was optimized for the detection of H and O and therefore not including the UV wavelength range where intense Ti and Fe emission can be detected, and furthermore with only limited sensitivity below 450 nm resulting there in noisy data. With an instrument optimized for the UV and lower visible spectral range even better results are expected. On the other hand, with Raman spectroscopy, we could show that a chemical alteration process can be monitored and changes in the sample can be seen. Here, however, the sample set was not ideal to demonstrate the potential of Raman spectroscopy for process surveillance since the metals and metaloxides forming from the lunar regolith simulant are weak Raman scatterers. In this particular use case, Raman spectroscopy seems most useful for the tracking of the primary raw material that enters the oxygen extraction process. Other use cases, where processes observing the extraction of hydrogen and water are monitored, could yield even better results with Raman spectroscopy. In another study (Vogt et al., 2022b), the same samples were measured with the VOILA LIBS setup and promising results for the monitoring of the LIBS O signal are reported. Thus, combining LIBS and Raman spectrocopy can result in a powerful approach for the *in-situ* characterisation of the lunar regolith and for the online monitoring of the extraction process.

Both studies share the conclusion that it is important to measure multiple positions per sample on the very fine grained and locally heterogeneous lunar regolith. At this point, it is relevant to note that the samples used in this study were prepared as pressed pellets with an even surface. Although geological samples may deviate from this, it should not be an issue if LIBS and Raman instruments have a focusing mechanism to ensure that each measuring point is in the optimal focus, regardless of the possible unevenness of samples. The anticipated sample heterogeneity has already been discussed for the LIBS study, which is why we recommend taking several measurements per sample. The acquisition of multiple measurements allows that statistical approaches can be included in the data analysis chain which are needed for more robust quantitative results. For LIBS we propose rasters with a minimum of 10 points and 20–50 shots per position to obtain also information from some depth. With LIBS, small craters of some mm depth can be obtained in the lunar regolith that could allow the detection of ice in the most shallow subsurface. For Raman analysis and a holistic assessment of the composition of samples, an even bigger raster is suggested in order to allow quantitative estimates from the distribution and number of detections of the measured minerals. In closing, both methods proved useful in their respective applied studies for ISRU applications, showing their potential to contribute to the efforts of achieving sustainable and scientifically fruitful lunar and eventually Martian missions.

Next steps would be the development of setups and breadboards dedicated to specific use cases in the framework of ISRU applications for more detailed investigations and feasibility studies, to include the analysis of space-related effects and to increase the technological readiness level (TRL) of prototypes.

Data availability statement

The raw data supporting the conclusion of this article will be made available by the authors upon request, without undue reservation.

Author contributions

KR: Conceptualization, Data curation, Formal Analysis, Investigation, Writing–original draft, Writing–review and editing, Methodology. SS: Conceptualization, Methodology, Supervision, Writing–original draft, Writing–review and editing. BL: Resources, Writing–review and editing, Methodology. EC: Methodology, Writing–review and editing, Conceptualization. H-WH: Funding acquisition, Writing–review and editing.

Funding

The author(s) declare financial support was received for the research, authorship, and/or publication of this article. This research was funded by DLR. Reduced simulant sample preparation was funded by ESA.

Acknowledgments

The authors would like to thank the Museum für Naturkunde Berlin for providing the ilmenite used for this study and Olivier Beyssac for fruitful discussions.

Conflict of interest

The authors declare that the research was conducted in the absence of any commercial or financial relationships that could be construed as a potential conflict of interest.

Publisher's note

Supplementary material

The Supplementary Material for this article can be found online at: https://www.frontiersin.org/articles/10.3389/frspt.2024.1336548/full#supplementary-material

References

Anand, M., Crawford, I. A., Balat-Pichelin, M., Abanades, S., Van Westrenen, W., Péraudeau, G., et al. (2012). A brief review of chemical and mineralogical resources on the Moon and likely initial *in situ* resource utilization (ISRU) applications. *Planet. Space Sci.* 74, 42–48. doi:10.1016/j.pss.2012.08.012

Andrews, D. G., Bonner, K., Butterworth, A., Calvert, H., Dagang, B., Dimond, K., et al. (2015). Defining a successful commercial asteroid mining program. *Acta Astronaut.* 108, 106–118. doi:10.1016/j.actaastro.2014.10.034

Baek, S.-J., Park, A., Ahn, Y.-J., and Choo, J. (2015). Baseline correction using asymmetrically reweighted penalized least squares smoothing. *Analyst* 140, 250–257. doi:10.1039/C4AN01061B

Bhartia, R., Beegle, L. W., DeFlores, L., Abbey, W., Razzell Hollis, J., Uckert, K., et al. (2021). Perseverance's scanning habitable environments with Raman and luminescence for organics and chemicals (SHERLOC) investigation. *Space Sci. Rev.* 217, 58. doi:10.1007/s11214-021-00812-z

Chen, G. Z., and Fray, D. J. (2020). "Invention and fundamentals of the FFC cambridge process," in *Extractive metallurgy of titanium* (Elsevier), 227–286. doi:10.1016/B978-0-12-817200-1.00011-9

Crawford, I., Anand, M., Cockell, C., Falcke, H., Green, D., Jaumann, R., et al. (2012). Back to the Moon: the scientific rationale for resuming lunar surface exploration. *Planet. Space Sci.* 74, 3–14. doi:10.1016/j.pss.2012.06.002

Crawford, I. A. (2015). Lunar resources: a review. *Prog. Phys. Geogr.* 39, 137–167. doi:10.1177/0309133314567585

Du, Y., Kou, M., Tu, J., Wang, M., and Jiao, S. (2021). An investigation into the anodic behavior of TiB2 in a CaCl2-based molten salt. *Corros. Sci.* 178, 109089. doi:10.1016/j.corsci.2020.109089

Dufresne, W. J., Rufledt, C. J., and Marshall, C. P. (2018). Raman spectroscopy of the eight natural carbonate minerals of calcite structure. *J. Raman Spectrosc.* 49, 1999–2007. doi:10.1002/jrs.5481

Effenberger, A. J., and Scott, J. R. (2010). Effect of atmospheric conditions on LIBS spectra. *Sensors* 10, 4907–4925. doi:10.3390/s100504907

Hagelschuer, T., Böttger, U., Buder, M., Bunduki, Y., Cho, Y., Dietz, E., et al. (2022). "Rax: the Raman spectrometer for the mmx phobos rover," in *73rd international astronautical congress*.

Harmon, R. S., Hark, R. R., Throckmorton, C. S., Rankey, E. C., Wise, M. A., Somers, A. M., et al. (2017). Geochemical fingerprinting by handheld laser-induced breakdown spectroscopy. *Geostand. Geoanalytical Res.* 41, 563–584. doi:10.1111/ggr.12175

Heiken, G., Vaniman, D., and French, B. M. (1991). *Lunar sourcebook: a user's guide to the Moon*, 1259. Cambridge University Press. Available at: https://www.lpi.usra.edu/publications/books/lunar_sourcebook/.

Hu, L., Song, Y., Ge, J., Jiao, S., and Cheng, J. (2016). Electrochemical metallurgy in $CaCl_2$-CaO melts on the basis of TiO_2·RuO_2Inert anode. *J. Electrochem. Soc.* 163, E33–E38. doi:10.1149/2.0131603jes

Islam, M. N., and Kumar, S. (2001). Influence of crystallite size distribution on the micro-Raman analysis of porous Si. *Appl. Phys. Lett.* 78, 715–717. doi:10.1063/1.1343494

Jehlička, J., and Culka, A. (2022). Critical evaluation of portable Raman spectrometers: from rock outcrops and planetary analogs to cultural heritage – a review. *Anal. Chim. Acta* 1209, 339027. doi:10.1016/j.aca.2021.339027

Kimura, Y., and Katoda, T. (1997). Effects of strain on crystallization of amorphous silicon characterized by laser Raman spectroscopy. *Appl. Surf. Sci.* 117-118, 790–793. doi:10.1016/S0169-4332(97)80184-5

Knight, A. K., Scherbarth, N. L., Cremers, D. A., and Ferris, M. J. (2000). Characterization of laser-induced breakdown spectroscopy (LIBS) for application to space exploration. *Appl. Spectrosc.* 54, 331–340. doi:10.1366/0003702001949591

Kubitza, S., Schröder, S., Dietz, E., Frohmann, S., Hansen, P. B., Rammelkamp, K., et al. (2020). Detecting sulfur on the Moon: the potential of vacuum ultraviolet laser-induced breakdown spectroscopy. *Spectrochim. Acta Part B At. Spectrosc.* 174, 105990. doi:10.1016/j.sab.2020.105990

Lasue, J., Wiens, R. C., Clegg, S. M., Vaniman, D. T., Joy, K. H., Humphries, S., et al. (2012). Remote laser-induced breakdown spectroscopy (LIBS) for lunar exploration. *J. Geophys. Res. E Planets* 117, 1–18. doi:10.1029/2011JE003898

Laxmiprasad, A. S., Sridhar Raja, V. L., Menon, S., Goswami, A., Rao, M. V., and Lohar, K. A. (2013). An *in situ* laser induced breakdown spectroscope (LIBS) for Chandrayaan-2 rover: ablation kinetics and emissivity estimations. *Adv. Space Res.* 52, 332–341. doi:10.1016/j.asr.2013.03.021

Lever, J., Krzywinski, M., and Altman, N. (2017). Principal component analysis. *Nat. Methods* 14, 641–642. doi:10.1038/nmeth.4346

Lomax, B. A., Conti, M., Khan, N., Bennett, N. S., Ganin, A. Y., and Symes, M. D. (2020). Proving the viability of an electrochemical process for the simultaneous extraction of oxygen and production of metal alloys from lunar regolith. *Planet. Space Sci.* 180, 104748. doi:10.1016/j.pss.2019.104748

Long-Fox, J. M., and Britt, D. T. (2023). Characterization of planetary regolith simulants for the research and development of space resource technologies. *Front. Space Technol.* 4, 1–16. doi:10.3389/frspt.2023.1255535

Losekamm, M. J., Biswas, J., Chupin, T., Deiml, M., Deremetz, M., Evagora, A. M., et al. (2022). Assessing the distribution of water ice and other volatiles at the lunar southsouth Pole with LUVMI-X: a mission concept. *Planet. Sci. J.* 3, 229. doi:10.3847/PSJ/ac8cfd

Lucey, P. G., Blewett, D. T., and Hawke, B. R. (1998). Mapping the FeO and TiO 2 content of the lunar surface with multispectral imagery. *J. Geophys. Res. Planets* 103, 3679–3699. doi:10.1029/97JE03019

Maurice, S., Clegg, S. M., Wiens, R. C., Gasnault, O., Rapin, W., Forni, O., et al. (2016). ChemCam activities and discoveries during the nominal mission of the mars science laboratory in Gale Crater, mars. *J. Anal. Atomic Spectrom.* 31, 863–889. doi:10.1039/c5ja00417a

Maurice, S., Wiens, R. C., Bernardi, P., Caïs, P., Robinson, S., Nelson, T., et al. (2021). The SuperCam instrument suite on the mars 2020 rover: science objectives and mast-unit description, 217. *Author*. doi:10.1007/s11214-021-00807-w

Maurice, S., Wiens, R. C., Saccoccio, M., Barraclough, B., Gasnault, O., Forni, O., et al. (2012). The ChemCam instrument suite on the Mars Science Laboratory (MSL) rover: science objectives and mast unit description. *Space Sci. Rev.* 170, 95–166. doi:10.1007/s11214-012-9912-2

McKay, D. S., Heiken, G., Basu, A., Blanford, G., Simon, S., Reedy, R., et al. (1991). "The lunar regolith," in *Lunar sourcebook, A user's guide to the moon*. Editors G. H. Heiken, D. T. Vaniman, and B. M. French, 285–356.

Meurisse, A., Lomax, B., Selmeci, Á., Conti, M., Lindner, R., Makaya, A., et al. (2022). Lower temperature electrochemical reduction of lunar regolith simulants in molten salts. *Planet. Space Sci.* 211, 105408. doi:10.1016/j.pss.2021.105408

Michel, P., Ulamec, S., Böttger, U., Grott, M., Murdoch, N., Vernazza, P., et al. (2022). The MMX rover: performing *in situ* surface investigations on Phobos. *Earth, Planets Space* 74, 2. doi:10.1186/s40623-021-01464-7

Müller, S., Meima, J. A., and Rammlmair, D. (2021). Detecting REE-rich areas in heterogeneous drill cores from Storkwitz using LIBS and a combination of k-means clustering and spatial raster analysis. *J. Geochem. Explor.* 221, 106697. doi:10.1016/j.gexplo.2020.106697

Noll, R., Fricke-Begemann, C., Brunk, M., Connemann, S., Meinhardt, C., Scharun, M., et al. (2014). Laser-induced breakdown spectroscopy expands into industrial applications. *Spectrochim. Acta Part B At. Spectrosc.* 93, 41–51. doi:10.1016/j.sab.2014.02.001

Pauca, V. P., Piper, J., and Plemmons, R. J. (2006). Nonnegative matrix factorization for spectral data analysis. *Linear Algebra its Appl.* 416, 29–47. doi:10.1016/j.laa.2005.06.025

Pedarnig, J. D., Trautner, S., Grünberger, S., Giannakaris, N., Eschlböck-Fuchs, S., and Hofstadler, J. (2021). Review of element analysis of industrial materials by in-line laser—induced breakdown spectroscopy (LIBS). *Appl. Sci.* 11, 9274. doi:10.3390/app11199274

Pořízka, P., Klus, J., Képeš, E., Prochazka, D., Hahn, D. W., and Kaiser, J. (2018). On the utilization of principal component analysis in laser-induced breakdown spectroscopy data analysis, a review. *Spectrochim. Acta Part B At. Spectrosc.* 148, 65–82. doi:10.1016/j.sab.2018.05.030

Rammelkamp, K., Schröder, S., Ortenzi, G., Pisello, A., Stephan, K., Baqué, M., et al. (2021). Field investigation of volcanic deposits on Vulcano, Italy using a handheld laser-induced breakdown spectroscopy instrument. *Spectrochim. Acta - Part B At. Spectrosc.* 177, 106067. doi:10.1016/j.sab.2021.106067

Rapin, W., Maurice, S., Ollila, A., Wiens, R. C., Dubois, B., Nelson, T., et al. (2023). "μlibs: a micro-scale elemenal analyser for lightweight *in situ* exploration," in *54th lunar and planetary science conference* (Houston: Lunar and Planetary Institute). Abstract #1942.

Reich, S., and Thomsen, C. (2004). Raman spectroscopy of graphite. *Philosophical Trans. R. Soc. Lond. Ser. A Math. Phys. Eng. Sci.* 362, 2271–2288. doi:10.1098/rsta.2004.1454

Rull, F., Maurice, S., Hutchinson, I., Moral, A., Perez, C., Diaz, C., et al. (2017). The Raman laser spectrometer for the ExoMars rover mission to mars. *Astrobiology* 17, 627–654. doi:10.1089/ast.2016.1567

Schlüter, L., and Cowley, A. (2020). Review of techniques for *In-Situ* oxygen extraction on the moon. *Planet. Space Sci.* 181, 104753. doi:10.1016/j.pss.2019.104753

Schröder, S., Böttger, U., Buder, M., Bunduki, Y., Cho, Y., Dietz, E., et al. (2023). "Rax: the Raman spectrometer on the mmx rover for *in-situ* surface analysis on phobos," in *54th lunar and planetary science conference* (Houston: Lunar and Planetary Institute). Abstract #2549.

Senesi, G. S. (2014). Laser-Induced Breakdown Spectroscopy (LIBS) applied to terrestrial and extraterrestrial analogue geomaterials with emphasis to minerals and rocks. *Earth-Science Rev.* 139, 231–267. doi:10.1016/j.earscirev.2014.09.008

Senesi, G. S., Harmon, R. S., and Hark, R. R. (2021). Field-portable and handheld laser-induced breakdown spectroscopy: historical review, current status and future prospects. *Spectrochim. Acta - Part B At. Spectrosc.* 175, 106013. doi:10.1016/j.sab.2020.106013

Stephan, K., Hibbitts, C., Hoffmann, H., and Jaumann, R. (2008). Reduction of instrument-dependent noise in hyperspectral image data using the principal component analysis: applications to galileo nims data. *Planet. Space Sci.* 56, 406–419. doi:10.1016/j.pss.2007.11.021

Strubbe, D. A., Johlin, E. C., Kirkpatrick, T. R., Buonassisi, T., and Grossman, J. C. (2015). Stress effects on the Raman spectrum of an amorphous material: theory and experiment on a-Si:H. *Phys. Rev. B* 92, 241202. doi:10.1103/PhysRevB.92.241202

Ulamec, S., Michel, P., Grott, M., Böttger, U., Schröder, S., Hübers, H. W., et al. (2023). Science objectives of the MMX rover. *Acta Astronaut.* 210, 95–101. doi:10.1016/j.actaastro.2023.05.012

Ureña, F., Olsen, S. H., and Raskin, J.-P. (2013). Raman measurements of uniaxial strain in silicon nanostructures. *J. Appl. Phys.* 114. doi:10.1063/1.4824291

Vogt, D. S., Schröder, S., Richter, L., Deiml, M., Weßels, P., Neumann, J., et al. (2022a). VOILA on the LUVMI-X rover: laser-induced breakdown spectroscopy for the detection of volatiles at the lunar southsouth Pole. *Sensors* 22, 9518. doi:10.3390/s22239518

Vogt, D. S., Schröder, S., Sandig, N., Gensch, M., Hübers, H.-W., Lomax, B., et al. (2022b). "Laser-induced breakdown spectroscopy for the support of *in-situ* resource utilization (isru) on the moon," in *53rd lunar and planetary science conference* (Houston: Lunar and Planetary Institute). Abstract #1872.

Wan, X., Li, C., Wang, H., Xu, W., Jia, J., Xin, Y., et al. (2021). Design, function, and implementation of China's first libs instrument (Marscode) on the zhurong mars rover. *At. Spectrosc.* 42, 294–298. doi:10.46770/AS.2021.608

Wiens, R. C., Maurice, S., Barraclough, B., Saccoccio, M., Barkley, W. C., Bell, J. F., et al. (2012). The ChemCam instrument suite on the Mars Science Laboratory (MSL) rover: body unit and combined system tests. *Space Sci. Rev.* 170, 167–227. doi:10.1007/s11214-012-9902-4

Wiens, R. C., Maurice, S., Robinson, S. H., Nelson, A. E., Cais, P., Bernardi, P., et al. (2021). *The SuperCam instrument suite on the NASA Mars 2020 rover: body unit and combined system tests*, 217. Space Science Reviews. Available at: https://link.springer.com/article/10.1007/s11214-020-00777-5.

Xu, W., Liu, X., Yan, Z., Li, L., Zhang, Z., Kuang, Y., et al. (2021). *The MarSCoDe instrument suite on the Mars rover of China's tianwen-1 mission*, 217. Springer Nature B.V. The Author(s), under exclusive licence to. doi:10.1007/s11214-021-00836-5

Zwick, A., and Carles, R. (1993). Multiple-order Raman scattering in crystalline and amorphous silicon. *Phys. Rev. B* 48, 6024–6032. doi:10.1103/PhysRevB.48.6024

frontiers | Frontiers in Space Technologies

TYPE Original Research
PUBLISHED 02 April 2024
DOI 10.3389/frspt.2024.1304579

OPEN ACCESS

EDITED BY
Philipp Reiss,
Technical University of Munich, Germany

REVIEWED BY
Philippe Mandin,
Université Bretagne Sud, France
Shrihari Sankarasubramanian,
University of Texas at San Antonio, United States

*CORRESPONDENCE
Paul A. Burke,
paul.burke@jhuapl.edu

RECEIVED 29 September 2023
ACCEPTED 12 February 2024
PUBLISHED 02 April 2024

CITATION
Burke PA, Nord ME, Hibbitts CA and Berdis JR (2024), Modeling electrolysis in reduced gravity: producing oxygen from *in-situ* resources at the moon and beyond.
Front. Space Technol. 5:1304579.
doi: 10.3389/frspt.2024.1304579

Modeling electrolysis in reduced gravity: producing oxygen from *in-situ* resources at the moon and beyond

Paul A. Burke[1]*, Michael E. Nord[2], Charles A. Hibbitts[1] and Jodi R. Berdis[2]

[1]Johns Hopkins University Applied Physics Laboratory, Space Exploration Sector, Space Science and Instrumentation Branch, Laurel, MD, United States, [2]Johns Hopkins University Applied Physics Laboratory, Space Exploration Sector, Space Systems and Analysis Branch, Laurel, MD, United States

Molten Regolith Electrolysis, as an *in situ* resource utilization (ISRU) technology, has the potential to enable the production of oxygen and metallic alloys on the Lunar surface; opening new doors in Cis-Lunar, and eventually Martian space exploration. This research studies the fundamental physics which govern the formation, growth, detachment, and rise of electrolytic bubbles. To this end, computational fluid dynamic (CFD) models were developed and run, to simulate water electrolysis, molten salt electrolysis (MSE), and molten Lunar regolith (MRE) electrolysis across multiple reduced gravity levels. The results demonstrate that reduced gravity, electrode surface roughness (possibly due to surface degradation), fluid properties, and electrode orientation can all affect electrolytic efficiency and possibly even stall electrolysis by delaying bubble detachment. The findings of this research must be considered when designing and operating electrolysis systems at reduced gravity levels.

KEYWORDS

ISRU, reduced gravity, electrolysis, molten regolith electrolysis, CFD, molten salt electrolysis, lunar regolith, oxygen production

1 Introduction and importance of work

In the current decade, the National Aeronautics and Space Administration (NASA), other national space agencies, and private companies plan to establish a sustained presence on the Lunar surface. While the exploration plans include crewed missions, a strategic focus in the coming years of Lunar exploration will be on uncrewed missions and operations. These uncrewed mission plans include rovers, autonomous habitats, robotic landers, power-generation stations, and *in situ* resource utilization (ISRU) systems. In the context of continued robotic missions to Mars and possible crewed missions to Mars, multiphase fluid systems are set to play a pivotal role in the future of spaceflight operations, both on the Lunar and Martian surfaces. A wide range of critical systems are expected to be developed for exploration of the Moon and Mars, including cryogenic fuel management, heat exchangers, microfluidics, phase separators, *in situ* sample collection and analysis tools, environmental control and life-support systems (ECLSS), and ISRU systems. One area of particular interest to this work is electrolysis systems. Whether it is a basic water electrolysis system or more complex reactions like molten regolith electrolysis (MRE) or molten salt electrolysis (MSE) at high temperatures, many of the fundamental physics and unanswered questions remain. These questions often fall within the broader field of reduced-gravity fluid

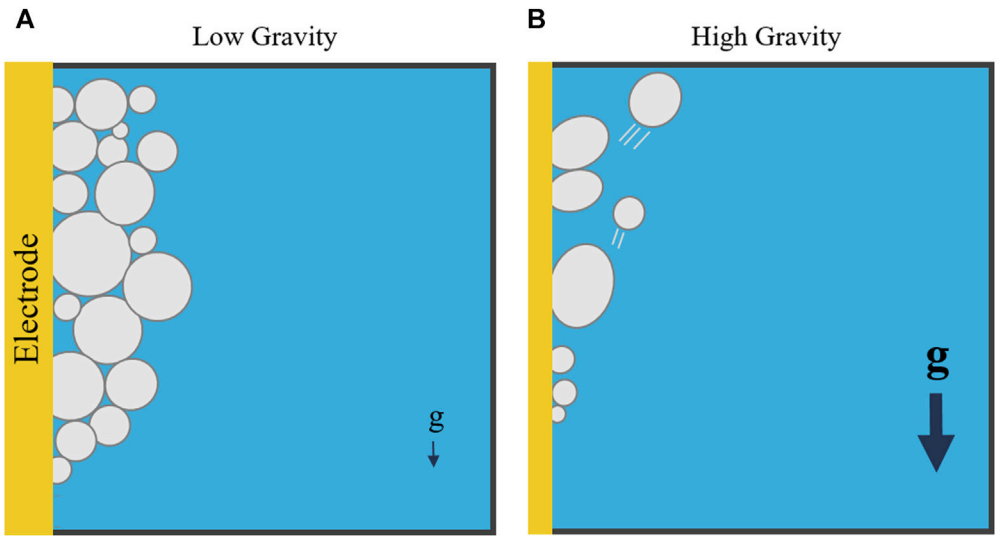

FIGURE 1
Bubbles forming on an electrode in low gravity **(A)** and high gravity **(B)**. In low gravity regimes, bubbles may not detach and could stall electrolysis by covering the electrode's surface. Based on image by Lomax et al. (Lomax et al., 2022), licensed CC-BY-4.0.

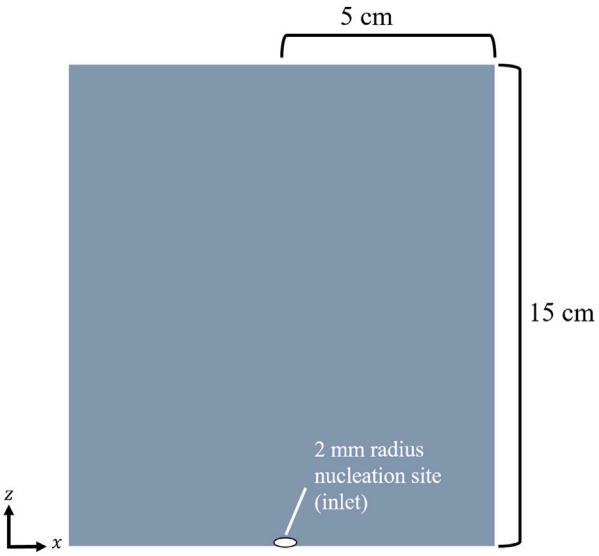

FIGURE 2
Diagram detailing the dimensions and geometry of the fluid chamber.

physics, covering phenomena like bubble growth and detachment, convective heat transfer, or surface-tension driven flows. Reduced gravity fluid physics continues to be an active area of research.

Extensive research has been conducted to study fluid dynamics in microgravity environments; however, our understanding of fluid behavior under the influence of partial gravity, such as the Moon's 1/6th g or Mars' 3/8th g, remains limited and poorly characterized. In the familiar 1 g environment on Earth, multiphase fluid behavior is primarily influenced by buoyancy. However, in microgravity, surface tension dominates fluid flows. Thus, understanding the fundamental physics underlying both surface tension and buoyancy is paramount, particularly when it comes to studying fluid systems operating within partial gravity, *between* microgravity and 1 g. This partial gravity regime includes both the Lunar and Martian gravity levels.

Since nearly the start of the space race, fluid systems operating in reduced gravity have encountered unanticipated problems, sometimes leading to system failures (Kamotani et al., 1996; 1995; 1994a; 1994b; Burgess, 2016). Experiments conducted aboard the International Space Station (ISS) have revealed unexpected issues related to bubble nucleation and transport (Qiu et al., 2000). These issues have manifested as the destruction of microfluidic biological samples, decreased heat transfer in heat exchangers, reduced flow rates in heat pipes, and the formation of bubbles in intravenous medical systems (Chiaramonte and Joshi, 2004; Dhir et al., 2007; Herman, 2013; Burke, 2021). To this day, problems encountered by the ISS ECLSS systems are unable to be replicated in terrestrial laboratories, operating under 1 g conditions (Hurlbert et al., 2004; Burke, 2021).

Reduced gravity fluid behavior has been modeled and experimentally studied by several researchers. Using reduced gravity environments produced by parabolic flights, Kim found that there exists a nonlinear and discontinuous relationship between gravity-level and heat flux of a water-submerged boiling heat exchanger (Kim et al., 2002; Kim and Raj, 2014). Lomax similarly used parabolic flights to conduct a study on water electrolysis at Lunar gravity levels (Lomax et al., 2022). It was found that oxygen-generating water electrolysis is 11% less efficient in Lunar gravity than on Earth (Lomax et al., 2022). Through the development of Computational Fluid Dynamic (CFD) models, Burke identified a power-law relationship between gravity level and bubble volume generated by a submerged orifice (Burke and Dunbar, 2021). Considering the scarcity of experimental platforms capable of simulating partial gravity and the recent expansion of CFD investigations, several unanswered questions

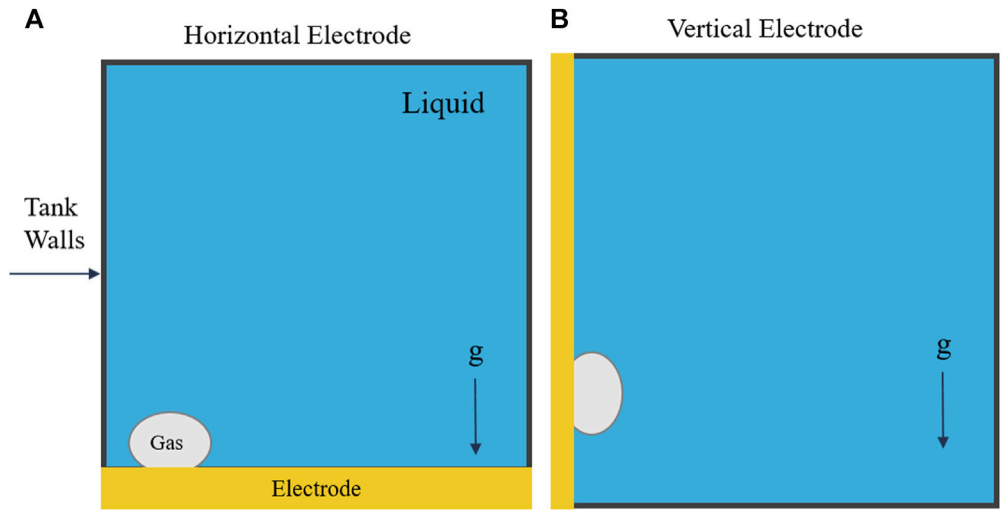

FIGURE 3
The two electrode orientations which were tested: horizontal **(A)** and vertical **(B)**.

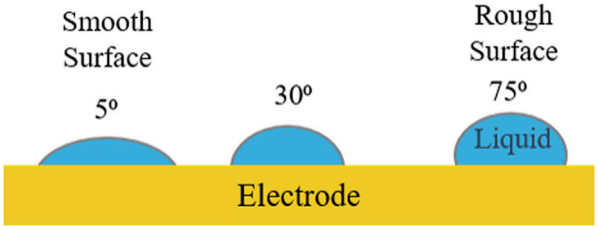

FIGURE 4
The three different electrode surface roughness values which were tested. The surface roughness was modeled via a Sessile drop contact angle boundary condition.

remain with respect to partial gravity fluid physics (Pamperin and Rath, 1995; Tsuge et al., 1997; Welch, 1998).

Electrolysis, specifically, has been studied experimentally under variable gravity environments as well. Using parabolic flights and drop towers, water electrolysis in microgravity has been studied by multiple researchers (Mandin et al., 2008; Brinkert and Mandin, 2022). Using experimental parabolic flights, it was found that current density decreases and resistance increases under microgravity, due to the layer of gas bubbles on the electrode (Derhoumi et al., 2013; Lomax et al., 2022). Mandin and others also convey that systems and processes which rely on electrochemical techniques, such as purification or electrodeposition, must consider the effects gravity has on fluid behavior (Mandin et al., 2007; Akay et al., 2022; Brinkert and Mandin, 2022). Past experimental studies have stressed the importance of improved modeling techniques, which can capture the unique fluid transport mechanisms which are prevalent in microgravity (Derhoumi et al., 2013; Brinkert and Mandin, 2022).

Molten regolith electrolysis (MRE) has emerged as a technology of significant interest within the *in situ* resource utilization (ISRU) community. Its ability to generate oxygen and metallic alloys holds immense importance for Lunar exploration efforts and has even been identified by space agencies and companies as a potential part of the future Cis-Lunar economy (Sibille et al., 2009). While molten salt electrolysis (MSE), an Earth-based MRE analog, has produced viable amount of oxygen, questions of MRE viability remain.

MRE's viability could be affected by several factors. Not only will these systems typically be expected to operate autonomously for long periods of time, they will also operate in extreme and non-Earth-like environments. With reduced gravity (on the Moon or Mars), comes reduced buoyancy. A reduction in buoyancy leads to lower bubble detachment rates, which could possibly stall electrolysis or reduce its efficiency (Figure 1). In their partial gravity water electrolysis experiments, Lomax observed a larger bubble froth layer on the electrode surface, caused by reduced bubble detachment rates (Lomax et al., 2022). This froth layer increased ohmic resistance and decreased efficiency of the overall system. Derhoumi et al. found similar results in microgravity using parabolic flights (Derhoumi et al., 2013). Unlike water electrolysis, MRE systems have never been tested in reduced gravity environments, due to safety concerns on board parabolic flights. As modeling is still in its infancy, the lack of empirical data in partial gravity represents a critical gap in our understanding of MRE's performance in the unique Lunar environment. Most researchers are relying solely on Earth-based experiments (operating in 1 g) to determine the efficacy and design of MRE systems, which will eventually be operating in Lunar gravity.

The research presented in this work aims to apply several well-established CFD methodologies, such as volume of fluid interface tracking and fluid property/material property variation, in new and novel ways. Modeling a single bubble, in order to study the detailed, fundamental growth and detachment mechanisms has been performed by a limited number of fluid physicists (Fritz and Ende, 1936; Chesters, 1978; Kim et al., 2002; Kulkarni and Joshi, 2005; Burke, 2021; Iwata et al., 2021). After an extensive literature review and prior experience, the authors believe this is the most expansive parameter space, related to the

TABLE 1 Physical Properties used as inputs to the CFD model. Major differences are in green.

Physical Property	Water Value	Regolith Value (Humbert et al., 2022)	Molten Salt ($CaCl_2$) Value (Janz et al., 1975)
Acceleration due to gravity on Earth	9.81 m/s^2	9.81 m/s^2	9.81 m/s^2
Acceleration due to gravity on Mars	3.68 m/s^2	3.68 m/s^2	3.68 m/s^2
Acceleration due to gravity on the Moon	1.625 m/s^2	1.625 m/s^2	1.625 m/s^2
Working Temperature	25°C	1800°C	1170°C
Surface Tension between liquid and gas	0.0720 N/m	475 N/m	0.14254 N/m
Gas Density	1.184 kg/m^3	1.184 kg/m^3	1.184 kg/m^3
Liquid density	997 kg/m^3	2600 kg/m^3	2010 kg/m^3
Kinematic viscosity of Gas	15.62 * 10^{-6} m^2/s	15.62 * 10^{-6} m^2/s	15.62 * 10^{-6} m^2/s
Kinematic viscosity of Liquid	8.93 * 10^{-7} m^2/s	1.923 * 10^{-4} m^2/s	1.258 * 10^{-7} m^2/s

TABLE 2 Water electrolysis results across three gravity levels, two electrode orientations, and three electrode surface roughness values. The larger the contact angle value, the rougher the electrode surface.

Gravity level	Orientation of electrode	Electrode contact angle (deg)	Time to first bubble detachment (s)	Volume of bubble at detachment (mL)
1 g	Horizontal	5	0.125	0.0895
Martian	Horizontal	5	0.25	0.1791
Lunar	Horizontal	5	0.475	0.3402
1 g	Vertical	5	0.175	0.1254
Martian	Vertical	5	0.325	0.2328
Lunar	Vertical	5	0.575	0.4119
1 g	Horizontal	30	0.125	0.0895
Martian	Horizontal	30	0.25	0.1791
Lunar	Horizontal	30	0.475	0.3402
1 g	Vertical	30	0.15	0.1074
Martian	Vertical	30	0.3	0.2149
Lunar	Vertical	30	0.625	0.4477
1 g	Horizontal	75	0.125	0.0895
Martian	Horizontal	75	0.25	0.1791
Lunar	Horizontal	75	0.75	0.5372
1 g	Vertical	75	0.1	0.0716
Martian	Vertical	75	0.225	0.1612
Lunar	Vertical	75	0.4	0.2865

modeling of molten regolith and salt electrolysis. The work presented includes several variations in gravity level, electrolyte, electrode surface roughness, and electrode orientation, with all combinations of parameters being modeled. Finally, due to a lack of experimental platforms in partial gravity, it is common to only model fluid processes in Earth's gravity (1 g) and microgravity. This work is one of a small collection of studies which present model or experimental results at multiple reduced gravity levels, enabling analysis into the scaling of fluid behavior across gravity levels (Tsuge et al., 1997; Qiu et al., 2000; Di Bari et al., 2013; Kim and Raj, 2014; Burke et al., 2023).

TABLE 3 Molten regolith electrolysis results across three gravity levels, two electrode orientations, and three electrode surface roughness values. The larger the contact angle value, the rougher the electrode surface.

Gravity level	Orientation of electrode	Electrode contact angle (deg)	Time to first bubble detachment (s)	Volume of bubble at detachment (mL)
1 g	Horizontal	5	7.525	10.7800
Martian	Horizontal	5	8.175	11.7112
Lunar	Horizontal	5	19.5	27.9350
1 g	Vertical	5	30.4	43.5500
Martian	Vertical	5	30	42.9770
Lunar	Vertical	5	38.45	55.0822
1 g	Horizontal	30	7.075	10.135
Martian	Horizontal	30	10.2	14.612
Lunar	Horizontal	30	20.75	29.725
1 g	Vertical	30	26.4	37.819
Martian	Vertical	30	23.7	33.952
Lunar	Vertical	30	35.3	50.569
1 g	Horizontal	75	32+ Seconds (computationally limited)	
Martian	Horizontal	75	32+ Seconds (computationally limited)	
Lunar	Horizontal	75	32+ Seconds (computationally limited)	
1 g	Vertical	75	41+ Seconds (computationally limited)	
Martian	Vertical	75	88+ Seconds (computationally limited)	
Lunar	Vertical	75	88+ Seconds (computationally limited)	

2 Methodology

2.1 Scope of computational fluid dynamic (CFD) models

The experimental and computational study of bubbles is far from simple. Exhaustive studies remain difficult, complex, and dependent upon factors which cannot typically be controlled. Bubbles which detach from a solid surface are highly sensitive to several interdependent forces and factors. These include: electrode surface properties (including any imperfections or inclusions), bubble-to-bubble interactions, chamber wall effects, and fluid composition (including any contaminants). Empirical and computational bubble studies are also limited by the very small time and length scales over which bubbles form, grow, and detach (Di Bari et al., 2013; Burke, 2021).

When studying bubble behavior and related phenomena (such as electrolysis), a common approach is to simplify and isolate individual bubble parameters and behaviors to model and analyze. In order to understand the fundamental physics affecting bubbles formed via electrolysis and with consideration to limited computational resources, the modeling effort described in this research follows the aforementioned approach.

Therefore, the research presented herein examines the formation, growth, detachment, and rise of oxygen gas bubbles formed via water electrolysis, MRE, and MSE across various gravity levels. To this end, a simplified electrolysis process was modeled. The model includes an individual bubble forming at a single, isolated nucleation site on an electrode. Modeling single bubble growth is a common assumption when studying phenomena such as boiling, electrolysis, and submerged orifices (Cooper, 1982; Di Bari et al., 2013). Although not realistic for an operational electrolysis system, a single bubble nucleation site allows for the careful study of bubble behavior throughout the entire process of bubble formation, growth, necking, detachment, and rise.

2.2 CFD solver

All CFD models developed and presented in this research use OpenFOAM, an open-source CFD toolbox (Greenshields, 2023). Specifically, the interFoam solver, a two-phase, isothermal, incompressible, transient, immiscible, volume of fluid (VOF) solver, was used to develop and run all models. The solver is a VOF, Euler-Euler solver. The VOF method is an efficient free surface modeling method used to track the fluid's free surface using the concept of volume fraction and immiscible fluids (Hirt and Nichols, 1981; Hamdan et al., 2020). An independent solver then computationally solves the Navier-Stokes equations (Hirt and Nichols, 1981; Heyns and Oxtoby, 2014). All other assumptions of this solver (two-phase, isothermal, incompressible, etc.) are reasonable assumptions for a gas bubble forming and rising in a homogeneous melt.

The interFoam solver uses the below constant-density continuity equation.

TABLE 4 Molten salt ($CaCl_2$) electrolysis results across three gravity levels, two electrode orientations, and three electrode surface roughness values. The larger the contact angle value, the rougher the electrode surface.

Gravity level	Orientation of electrode	Electrode contact angle (deg)	Time to first bubble detachment (s)	Volume of bubble at detachment (mL)
1 g	Horizontal	5	0.125	0.0895
Martian	Horizontal	5	0.25	0.1791
Lunar	Horizontal	5	0.475	0.3402
1 g	Vertical	5	0.175	0.1253
Martian	Vertical	5	0.35	0.2507
Lunar	Vertical	5	0.575	0.4118
1 g	Horizontal	30	0.125	0.0895
Martian	Horizontal	30	0.25	0.1791
Lunar	Horizontal	30	0.475	0.3402
1 g	Vertical	30	0.15	0.1074
Martian	Vertical	30	0.3	0.2148
Lunar	Vertical	30	0.6	0.4297
1 g	Horizontal	75	0.125	0.0895
Martian	Horizontal	75	0.25	0.1791
Lunar	Horizontal	75	0.75	0.5372
1 g	Vertical	75	0.1	0.0716
Martian	Vertical	75	0.225	0.1612
Lunar	Vertical	75	0.425	0.3044

$$\frac{\partial u_j}{\partial x_j} = 0$$

The momentum equation is represented by the interFoam solver by the below equation, where density, surface tension, and curvature are defined in the subsequent equations (Brackbill et al., 1992; Heyns and Oxtoby, 2014).

$$\frac{\partial(\rho u_i)}{\partial t} + \frac{\partial}{\partial x_j}(\rho u_j u_i) = -\frac{\partial p}{\partial x_i} + \frac{\partial}{\partial x_j}\left(\tau_{ij} + \tau_{t_{ij}}\right) + \rho g_i + f_{\sigma i}$$

$$\rho = \alpha\rho_1 + (1-\alpha)\rho_2$$

$$f_{\sigma i} = \sigma K \frac{\partial \alpha}{\partial x_i}$$

$$K = -\frac{\partial n_i}{\partial x_i} = -\frac{\partial}{\partial x_i}\left(\frac{\partial \alpha / \partial x_i}{|\partial \alpha / \partial x_i|}\right)$$

Finally, the VOF solver tracks the phase interface using the interphase equation below.

$$\frac{\partial \alpha}{\partial t} + \frac{\partial(\alpha u_j)}{\partial x_j} = 0$$

2.3 Model geometry and meshing

Gmsh was used to develop the model's geometry and mesh. Gmsh is an open source 3-dimensional and 2-dimensional finite-element geometry and mesh generator. The model contained a structured mesh. The geometry primarily includes a fluid chamber (Figure 2). The chamber consists of an electrode (containing the single 2-mm radius bubble nucleation site) on one of the chamber walls and an outlet on the top of the chamber. The chamber dimensions are 15 cm tall by 10 cm by 10 cm. The width of the chamber walls was chosen to be wide enough as to mitigate any wall effects on the bubble's shape or size during bubble formation and growth (Albadawi et al., 2013).

To ensure a satisfactory level of mesh refinement, a simple mesh refinement study was performed (Prakash and Ethier, 2000). The model's mesh was gradually refined from coarse mesh to highly refined mesh. A standard case was run across all meshes and the bubble volume was measured for each case. The mesh was considered to be sufficiently refined when the bubble volume remained constant, even with increasing mesh refinement. This mesh refinement study is critical to ensuring consistent results, while maintaining computational efficiency (Prakash and Ethier, 2000; Contreras et al., 2002).

2.4 Computational resources

All models were run in parallel across six cores. The runs were conducted using OpenFOAM version 9 on high-performance computing resources at the Johns Hopkins University Applied Physics Laboratory.

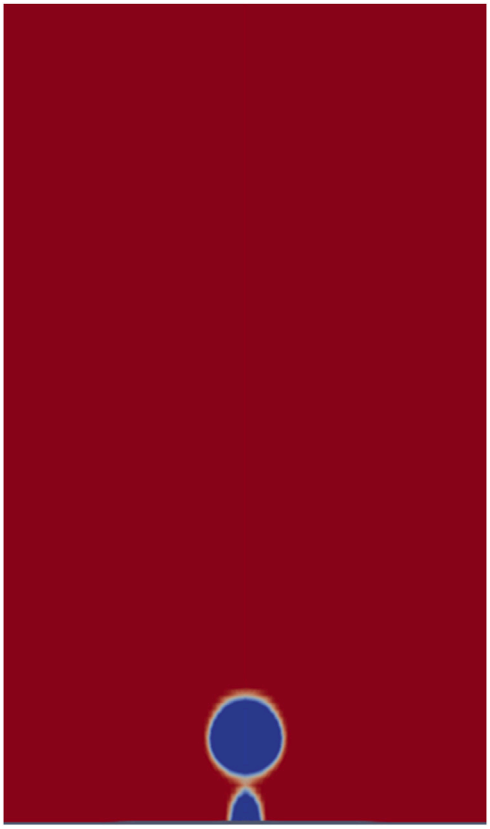

FIGURE 5
Visual CFD model results for water electrolysis in Lunar gravity using a horizontal electrode.

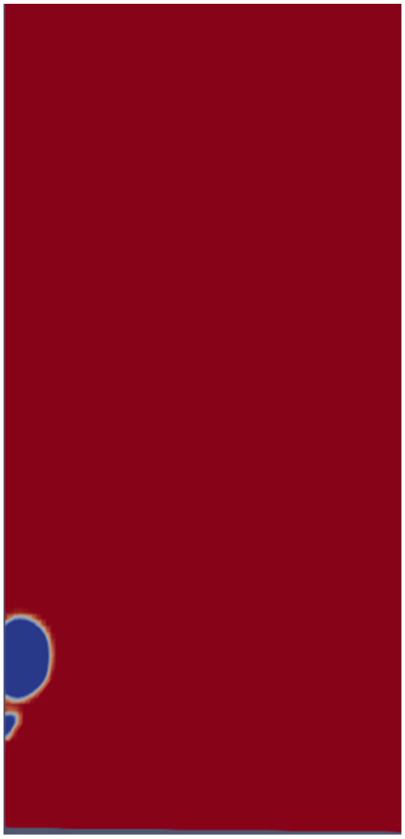

FIGURE 6
Visual CFD model results for water electrolysis in Lunar gravity using a vertical electrode.

2.5 Variables tested

The primary aim of this research was to explore the influence common design choices and environmental factors could have on oxygen gas bubbles formed via electrolysis. Four primary variables were tested by the models: choice of fluid, electrode orientation (Figure 3), electrode surface roughness, and gravity level. Models were developed and run for water, molten Lunar regolith, and molten salt ($CaCl_2$). All liquids were run in 1 g, Martian gravity, and Lunar gravity. The electrode orientation and surface properties were varied across all liquids. Models for water, MRE, and MSE were run with both horizontal (perpendicular to the gravity vector) and vertical (parallel to the gravity vector) electrode orientations. Three electrode surface roughness values were tested: smooth, medium, and rough. Specific values for all variables will be detailed in subsequent sections.

2.6 Boundary conditions

Standard boundary conditions were used in the model. Wall boundary conditions were used for all chamber walls and the electrode. The wall boundary condition includes conditions of fixed flux pressure and no slip. Using the zero-gradient pressure condition, the outlet was modeled as a fluid open to ambient atmosphere. This ensures that no pressure ever builds up in the chamber as gas bubbles are produced. All parts of the model include an isothermal boundary condition, as well.

The bubble nucleation site was modeled as a gas inlet with a constant and uniform velocity profile. For the horizontal electrode configuration, the inlet is directed vertically into the fluid chamber and is located on the electrode in the center of the chamber. For the vertical electrode orientation, the inlet is located on a vertical electrode and directed horizontally into the fluid chamber. A very low volumetric flow rate ($7.16*10^{-7}$ m^3/s) was chosen for the inlet, to emulate quasi-steady bubble growth.

As mentioned above, the electrode's surface roughness was varied during this modeling effort. To account for this, an apparent Sessile drop contact angle boundary condition was used on the electrode's surface. The Wenzel equation below relates the intrinsic contact angle (on a theoretically smooth surface) to the apparent contact angle (on a rough surface) (Wenzel, 1936). As described by the Wenzel relation, the apparent contact angle increases with rougher electrode surfaces (Wenzel, 1936). This is due to the fact that rougher surfaces provide more liquid-solid interfacial area per unit length than a smooth surface (Wolansky and Marmur, 1999; Li et al., 2021). Figure 4 illustrates that liquids are most likely to spread on smooth electrode surfaces. Using contact angle boundary conditions allows for the generalization of electrode material

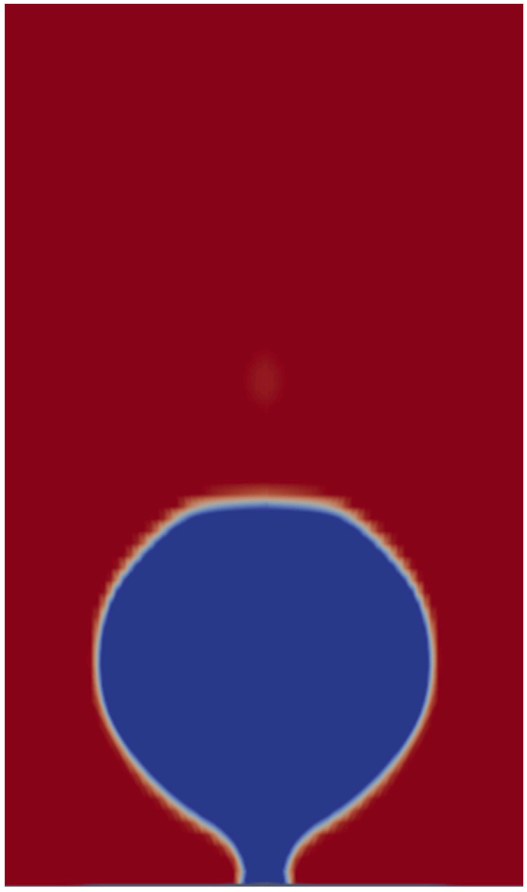

FIGURE 7
Visual CFD model results for MRE in 1 g using a horizontal electrode.

selection, since no material properties are needed as inputs into the model. Using real-world fluid and electrode material properties, actual surface roughness values could be calculated from these contact angle boundary conditions. Although the bubbles never come in contact with the fluid chamber walls, it is important to note that the surface roughness of the fluid chamber walls remained constant at a 40° contact angle.

$$\cos(\theta_{rough}) = roughness\,factor * \cos(\theta_{instrinsic})$$

2.7 Physical properties of fluids tested

The physical properties which were used as inputs into the model (either as initial conditions or boundary conditions) were collected from tabulated references. All physical properties used are displayed in Table 1. While it is a limitation of the current model implementation, in order to study the effects of only the variables of keen interest (electrolyte selection, gravity level, and surface roughness), gaseous fluid properties were kept constant for all runs.

2.8 Post-analysis methodology

All post-processing and model analysis was conducted using ParaView version 5.6. ParaView is an open-source data analysis and visualization software. The primary uses of ParaView in this research included mesh visualization and data collection via visualization and bubble volume measurements.

2.9 Model limitations and assumptions

Multiple simplifying assumptions were made in this model. First, the developed model is a computational fluid dynamic model, not a multiphysics simulation. As opposed to multiphysics models, this CFD model is not able to model the spontaneous nucleation of gas bubbles across several points on the electrode's surface. Instead, the model was designed to study the formation, growth, spreading, detachment, and rise of a single oxygen bubble from a carefully-placed nucleation site on the electrode. Concentrating on a single gas bubble's formation, growth, and detachment allows for measurements and physical analysis which would not be possible if dozens to hundreds of bubbles were nucleating and growing at the same time. The lack of multiphysics modeling also means that the precipitation of any metals during MRE is also not able to be modeled.

Beyond the above assumptions, the model assumes uniform temperature fields, thus the model does not resolve the temperature field. The model also assumes homogeneous melts for water electrolysis, MRE, and MSE.

Lastly, the model assumes a constant contact angle boundary condition on the electrode. The constant contact angle boundary condition limits the model in two ways. First, it does not account for any degradation of the electrode, which is likely to occur with time,

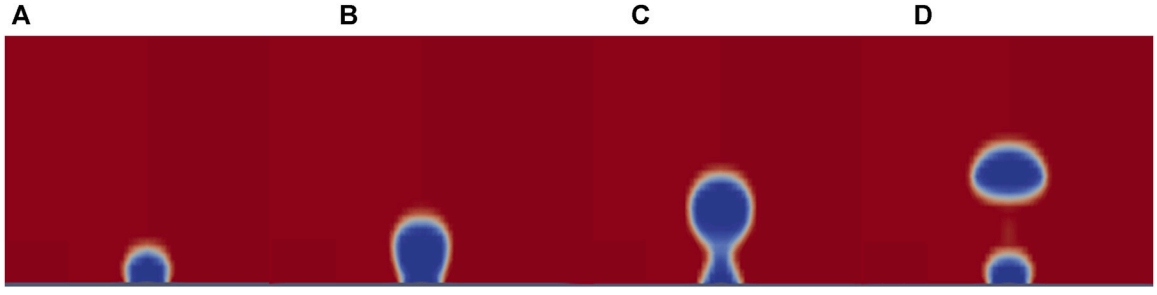

FIGURE 8
Visual CFD model results for MSE in Martian gravity using a horizontal electrode at times: **(A)** 0.05 s, **(B)** 0.15 s, **(C)** 0.225 s, and **(D)** 0.25 s.

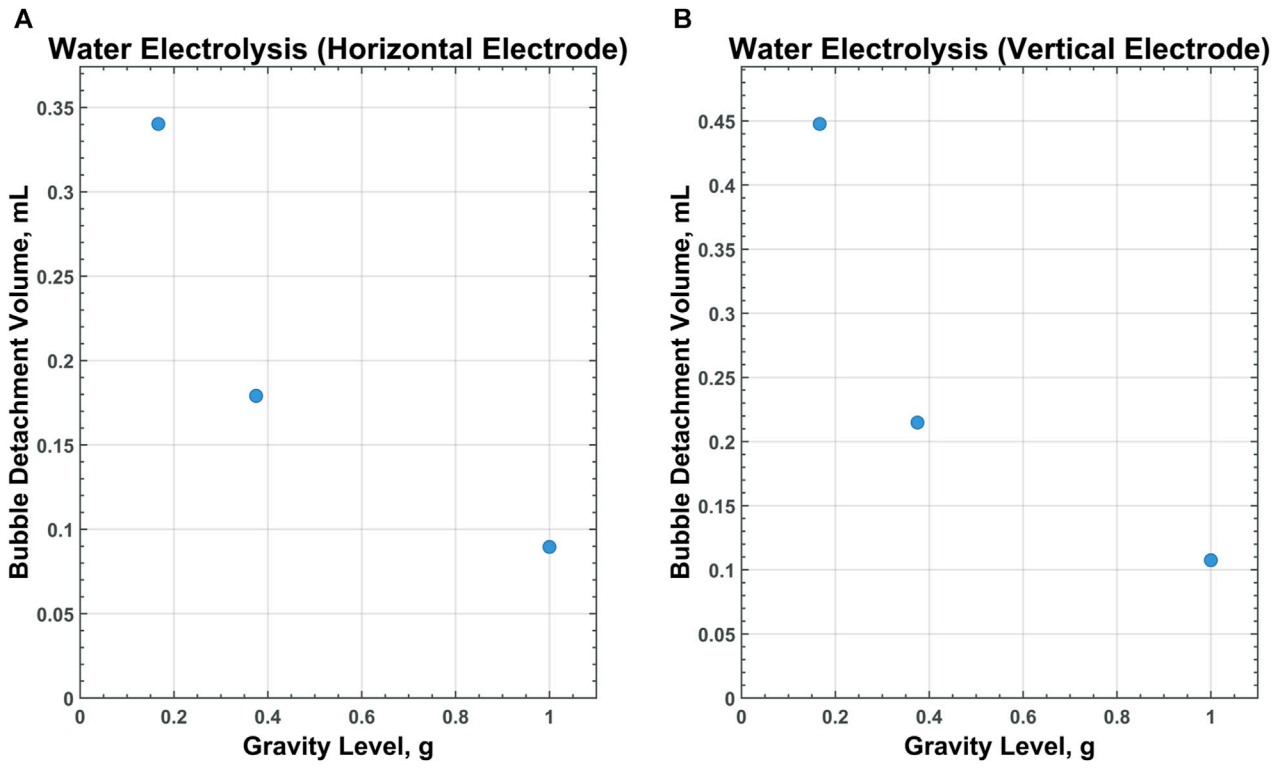

FIGURE 9
CFD data for water electrolysis on a horizontal **(A)** and vertical **(B)** electrode with medium-surface roughness across all gravity levels tested.

especially at high temperatures. However, the timescales over which electrode degradation are likely to occur are orders of magnitude longer than the growth and detachment of a single bubble. Thus, this is a fair assumption when using the model to study a single bubble's growth and detachment. Secondly, the constant contact angle boundary condition limits the model by not modeling the change in contact angle which would result from the applied potential. When a potential is applied to an electrolyte, its surface tension and contact angle with the electrode both decrease. This was first described by Lippmann (Lippmann, 1875). If the electrolytic system was potentiostatic, then the voltage would remain constant and the electrolyte's surface tension and contact angles would not change with time. However, if the system used a galvanostatic technique, applying a constant current, the potential would increase/decrease as the electrode's resistance increased/decreased (with changing amounts of bubble coverage). With a changing potential, the electrolyte's contact angle with the electrode would become time-dependent, affecting the time to detachment and bubble volume at detachment. The model presented in this research assumes a constant contact angle, and thus a potentiostatic electrolytic reaction.

3 Results

3.1 Water electrolysis

Results have been obtained for water electrolysis at 1 g, Martian gravity, and Lunar gravity. The results also include variation in electrode orientation and surface roughness. The results are presented in Table 2.

3.2 Molten regolith electrolysis (MRE)

Results have been obtained for molten Lunar regolith electrolysis at 1 g, Martian gravity, and Lunar gravity. The results also include variation in electrode orientation and surface roughness. The results are presented in Table 3. It is important to note that due to limited computational resources, bubbles forming in MRE on very rough electrodes were not observed to detach after dozens of seconds. With longer computational runs, it is expected that the bubbles will eventually detach from the rough electrodes.

3.3 Molten salt electrolysis (MSE)

Results have been obtained for molten salt ($CaCl_2$) electrolysis at 1 g, Martian gravity, and Lunar gravity. The results also include variation in electrode orientation and surface roughness. The results are presented in Table 4.

3.4 Visualization of results

Sample visual representations of the bubble growth, detachment, and rise are displayed in Figures 5–8.

Videos of molten salt electrolysis models at various gravity levels and electrode orientations are available as Supplementary Material.

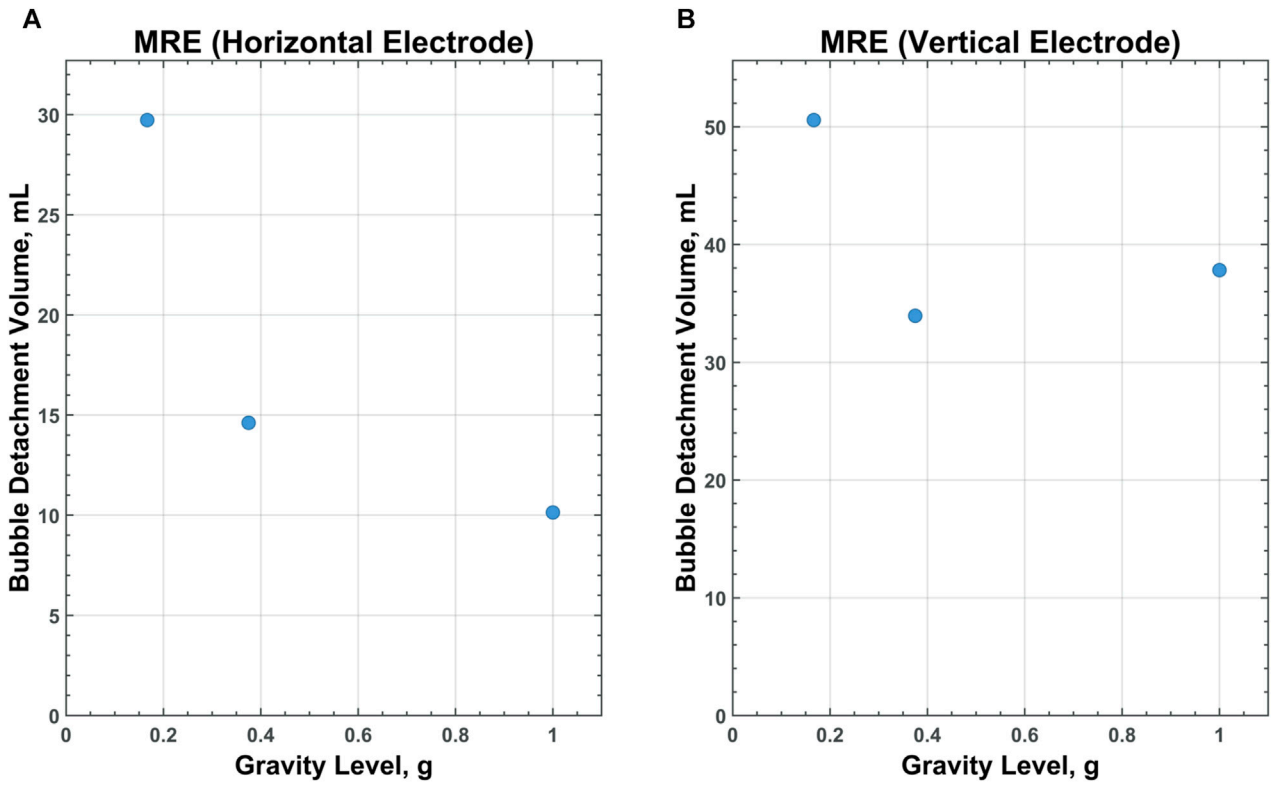

FIGURE 10
CFD data for MRE on a horizontal **(A)** and vertical **(B)** electrode with medium-surface roughness across all gravity levels tested.

4 Discussion

4.1 Effects of reduced gravity

For all liquids and electrode properties tested, it was observed that a decrease in gravitational acceleration results in delayed bubble detachment and thus, larger bubble volumes at detachment. A decrease in gravitational acceleration causes a decrease in bubble buoyancy, according to the below equation.

$$F_b = -\rho g V$$

A reduced buoyancy force decreases bubble detachment forces. With lowered bubble detachment forces, bubbles stay attached to the electrode and continue to grow larger in volume for longer periods of time.

The modeling data suggests that bubbles forming in MRE are less dependent upon gravity levels than bubbles forming in MSE or water electrolysis. For the case of the horizontal electrode with medium surface roughness, bubbles detaching in water or molten salt are 3.8 times larger in Lunar gravity than they are in 1 g. For bubbles rising in molten Lunar regolith, however, the detachment volumes are only 2.9 times larger in Lunar gravity than in 1 g.

Of particular interest is the relationship between scaling gravity levels and bubble detachment time/volume. A nonlinear, power-law trend is observed when bubble detachment volume is scaled from 1 g to Lunar gravity. Figures 9–11 display plots, exhibiting the relationship between bubble detachment volume and gravity level for horizontal and vertical electrodes with medium surface roughness. The nonlinear trend exhibited by the models agree well with other research conducted on scaling bubble behavior across variable gravity levels, including submerged orifice bubble growth, boiling, and water electrolysis (Burke and Dunbar, 2021; Lomax et al., 2022).

4.2 Effects of fluid properties

Fluid properties can affect the rate at which bubbles grow and detach from an electrode. As mentioned previously, the physical properties used as inputs into the model are summarized in Table 1. Despite large differences in working temperatures and densities, water and molten salt have relatively similar surface tensions and viscosities. Potentially due to these similar fluid properties, water electrolysis and MSE exhibited bubble detachment volumes and time to detachments in the same order of magnitude.

Molten regolith electrolysis, however, saw bubble volumes and time to detachments at least two orders of magnitude larger than water electrolysis and MSE. The largest differences in fluid properties between these liquids are molten regolith's very high viscosity, density, and surface tension. With high viscosity and surface tension, bubbles neck, detach, and rise at lower rates.

4.3 Effects of electrode orientation

The orientation of the electrode was observed to effect bubble detachment volume and time to detachment. For all liquids and

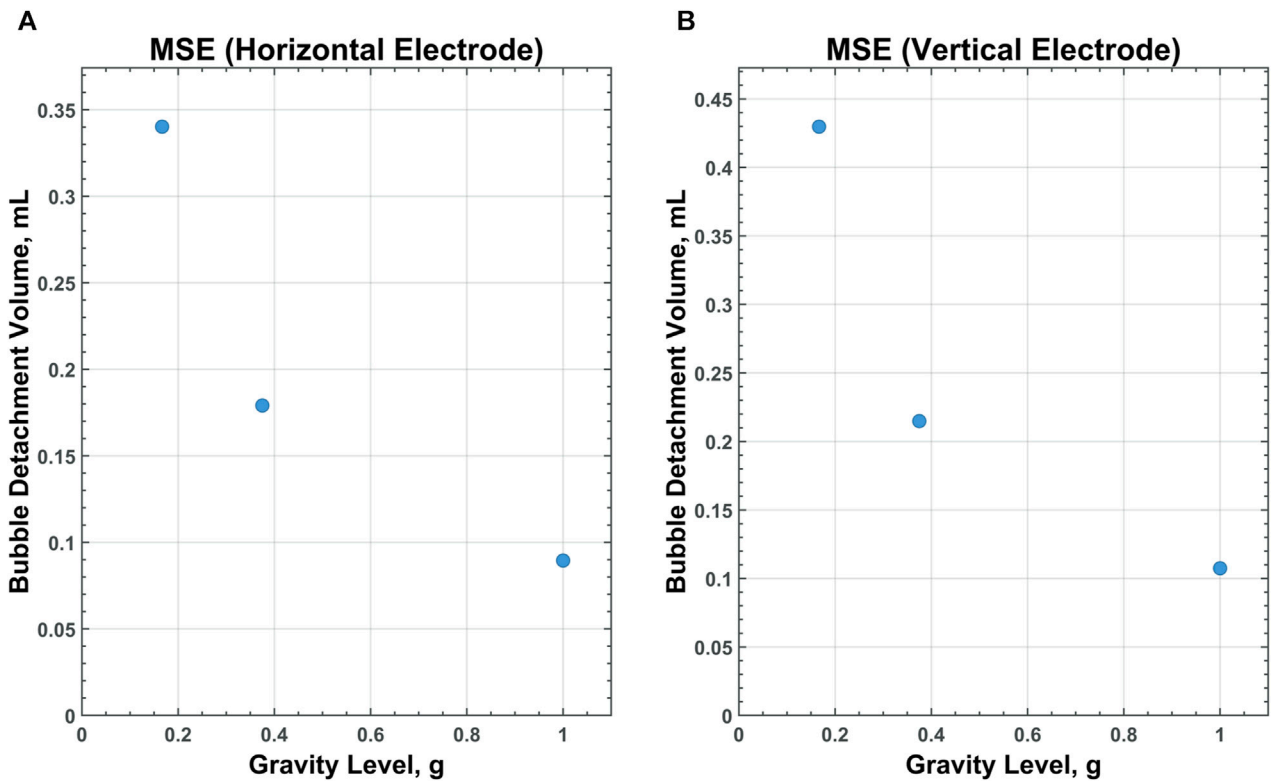

FIGURE 11
CFD data for MSE on a horizontal **(A)** and vertical **(B)** electrode with medium-surface roughness across all gravity levels tested.

nearly all electrode surface roughness values, bubbles forming and detaching from vertical electrodes were found to be larger in volume and detach later, compared to horizontal electrodes. At vertical electrode orientations, bubbles appear to spread vertically along the electrode's surface, due to the upward buoyancy force (Figure 6). As the bubble spreads along the electrode's surface, its contact area with the surface increases. Surface tension is directly related to bubble contact area (see below equation) and is an attachment force, opposing bubble detachment. Thus, increasing the bubble contact area via spreading would increase the surface tension force (increasing attachment forces between the bubble and electrode) and delay bubble detachment. It must be noted, however, that when several bubbles form on an electrode, instead of single bubble, rising bubbles and bubble-to-bubble interactions are expected to induce early detachment of other surrounding bubbles.

$$F_\sigma = -\pi\sigma d_c$$

4.4 Effects of electrode surface properties

Surface roughness of the electrode was also observed to effect bubble detachment volume and time to detachment. At high surface roughness values, bubbles were observed to grow larger in volume and detach at lower rates. This is especially true for MRE. In molten regolith, bubbles remain attached to the electrode for extended amounts of time.

Similar to electrode orientation, this trend is hypothesized to be caused by varying amounts of bubble spreading along the electrode surface. At high values of surface roughness, the liquid melt does not spread across the electrode's surface. The *bubble*, instead, spreads along the electrode. It has been shown that increased bubble spreading increases the surface tension forces between the bubble and the electrode, delaying bubble detachment (Burke and Dunbar, 2021).

Some surface roughness will always be present on an electrode. A manufactured electrode for instance, no matter how precise the manufacturing process, will have some degree of surface roughness. Surface defects, such as impurities, can also be expected to contribute to surface roughness. Surface roughness does not only come from manufacturing processes, however. When an electrode is used for extended amounts of time in extreme conditions, such as high-temperature molten regolith, its surface typically degrades. This surface degradation could unpredictably cause an increase in surface roughness.

No matter how surface roughness is introduced, a highly rough electrode will allow electrolytic bubbles to spread and remain attached, potentially stalling electrolysis completely. Even if the electrolytic process is not stalled, its efficiency could be negatively affected. As discussed in prior assumptions, if the model is used to predict the electrolytic production of oxygen over long timescales, modifications would have to be made to account for the slow, but significant degradation of the electrode's surface. A time-variant contact angle boundary condition would most likely be chosen.

4.5 Future work

The results suggest a few gaps which should be investigated by further research and modeling. The model should be improved to a more realistic, operational design. This could include multiple nucleation sites and a larger fluid chamber/electrode. The variable parameter space could also be expanded to include more types molten regolith or other electrode orientations (possibly a 45° angle). Lastly, mitigation techniques could be studied, if determined to be necessary. While electrolysis in Lunar gravity may be a viable form of oxygen production, it is possible that the reduced gravity and other effects discussed above detrimentally limit the efficiency of electrolysis in Lunar gravity. If that is the case, it would be advantageous to study various mitigation techniques. These could possibly include: induced cross flow over the electrode, vibrations, or electrode surface coatings to encourage bubble detachment.

5 Conclusion

The results presented by this research convey important insights into electrolysis in reduced gravity. Gravity level affects bubble detachment volume and time to detachment. At reduced gravity levels, bubble detachment is delayed and bubbles continue to grow larger. The relationship between bubble volume and gravity level follows a non-linear power-law trend. This trend emphasizes the importance of considering gravity level when designing and testing systems which rely on multiphase fluid flows. If the system is designed and tested in Earth's gravity, one cannot expect similar, or even linearly scalable, results in Lunar gravity.

When bubbles spread along an electrode, bubble detachment is delayed. This is due to the fact that when bubbles spread along the electrode, the surface tension force (keeping the bubble attached to the electrode) increases. Bubble spreading can be caused by various factors. Vertical electrodes cause bubbles to spread (due to vertical buoyancy force) more than horizontal electrodes. Rough electrodes also cause increased bubble spreading, due to liquid-solid wetting properties. MRE in particular, is very dependent upon electrode surface properties, particularly surface roughness.

This research provides important insights into the feasibility of electrolytic processes (water, molten regolith, and molten salt) in reduced gravity environments, such as those of the Lunar or Martian surfaces. Molten regolith's unique physical properties, especially high surface tension and viscosity, causes MRE to produce very large gas bubbles. These bubbles can remain attached and grow on the electrode for so long that electrolysis could possibly be stalled or decrease in efficiency, especially at reduced gravity levels.

This study has identified some characteristics which are important to control and consider, when designing or operating an electrolysis system in reduced gravity. First, the influence of electrode orientation should be taken into account when designing any future electrolysis system. The electrode's surface properties, most importantly surface roughness, should also be considered. Smoother electrodes will best allow for the release of bubbles. Finally, when designing electrolysis systems, or any multiphase fluid system, expected to operate in reduced gravity, the nonlinear scaling relationship between fluid behavior and gravity level must not be overlooked. Success on Earth does not equate to success on the Moon or Mars.

Data availability statement

The original contributions presented in the study are included in the article/Supplementary Material, further inquiries can be directed to the corresponding author.

Author contributions

PB: Conceptualization, Formal Analysis, Investigation, Methodology, Resources, Software, Validation, Visualization, Writing–original draft, Writing–review and editing. MN: Conceptualization, Resources, Supervision, Writing–review and editing. CH: Conceptualization, Funding acquisition, Project administration, Supervision, Writing–review and editing. JB: Project administration, Supervision, Writing–review and editing.

Funding

The author(s) declare financial support was received for the research, authorship, and/or publication of this article. This research was supported and paid for by NASA's Space Technology Mission Directorate (STMD) via the Lunar Surface Innovation Initiative (LSII) task within Johns Hopkins University Applied Physics Laboratory. The LSII contract number is: 80MSFC20D0004.

Acknowledgments

The authors would like to acknowledge the Lunar Surface Innovation Consortium (LSIC) *in-situ* Resource Utilization (ISRU) Focus Group for expert inputs and insight on Molten Regolith Electrolysis.

Conflict of interest

The authors declare that the research was conducted in the absence of any commercial or financial relationships that could be construed as a potential conflict of interest.

Publisher's note

Supplementary material

The Supplementary Material for this article can be found online at: https://www.frontiersin.org/articles/10.3389/frspt.2024.1304579/full#supplementary-material

SUPPLEMENTARY VIDEO S1
Model of bubbles forming, detaching, and rising via molten salt electrolysis in 1 g on a horizontal electrode with medium surface roughness.

SUPPLEMENTARY VIDEO S2
Model of bubbles forming, detaching, and rising via molten salt electrolysis in 1 g on a vertical electrode with medium surface roughness.

SUPPLEMENTARY VIDEO S3
Model of bubbles forming, detaching, and rising via molten salt electrolysis in Martian gravity on a horizontal electrode with medium surface roughness.

SUPPLEMENTARY VIDEO S4
Model of bubbles forming, detaching, and rising via molten salt electrolysis in Martian gravity on a vertical electrode with medium surface roughness.

SUPPLEMENTARY VIDEO S5
Model of bubbles forming, detaching, and rising via molten salt electrolysis in Lunar gravity on a horizontal electrode with medium surface roughness.

SUPPLEMENTARY VIDEO S6
Model of bubbles forming, detaching, and rising via molten salt electrolysis in Lunar gravity on a vertical electrode with medium surface roughness.

References

Akay, Ö., Poon, J., Robertson, C., Abdi, F. F., Cuenya, B. R., Giersig, M., et al. (2022). Releasing the bubbles: nanotopographical electrocatalyst design for efficient photoelectrochemical hydrogen production in microgravity environment. *Adv. Sci.* 9, 2105380. doi:10.1002/advs.202105380

Albadawi, A., Donoghue, D. B., Robinson, A. J., Murray, D. B., and Delauré, Y. M. C. (2013). On the analysis of bubble growth and detachment at low Capillary and Bond numbers using Volume of Fluid and Level Set methods. *Chem. Eng. Sci.* 90, 77–91. doi:10.1016/j.ces.2012.12.004

Brackbill, J. U., Kothe, D. B., and Zemach, C. (1992). A continuum method for modeling surface tension. *J. Comput. Phys.* 100, 335–354. doi:10.1016/0021-9991(92)90240-Y

Brinkert, K., and Mandin, P. (2022). Fundamentals and future applications of electrochemical energy conversion in space. *Npj Microgravity* 8, 52–59. doi:10.1038/s41526-022-00242-3

Burgess, C. (2016). *Aurora 7: the mercury SPaceflight of M. Scott carpenter*. Bangor, NSW, Australia: Springer.

Burke, P. (2021). *Computational fluid dynamic (CFD) modeling and experimental study of the formation and buoyancy-driven detachment of bubbles in variable gravity environments (PhD)*. College Station, TX, USA: Texas A&M University.

Burke, P. A., and Dunbar, B. J. (2021). "Development of computational fluid dynamic (CFD) models of the formation and buoyancy-driven detachment of bubbles in variable gravity environments," in *AIAA scitech 2021 forum, AIAA SciTech forum* (American Institute of Aeronautics and Astronautics). ,Reston, VI, USA doi:10.2514/6.2021-1838

Burke, P. A., Nord, M. E., Berdis, J., and Hibbitts, C. (2023). "Oxygen production on the lunar surface: modeling molten regolith electrolysis and water electrolysis at reduced gravity levels," in *Ascend 2023* (American Institute of Aeronautics and Astronautics). Reston, VI, USA, doi:10.2514/6.2023-4793

Chesters, A. K. (1978). Modes of bubble growth in the slow-formation regime of nucleate pool boiling. *Int. J. Multiph. Flow.* 4, 279–302. doi:10.1016/0301-9322(78)90003-4

Chiaramonte, F., and Joshi, J. (2004). *Workshop on critical issues in microgravity fluids, transport, and reaction processes in advanced human support technology*. Washington, DC: National Aeronautics and Space Administration.

Contreras, J., Corral, R., Fernández Castañeda, J., Pastor, G., and Vasco, C. (2002). *Semi-unstructured grid methods for turbomachinery applications*. Amsterdam, Netherlands: ASME. doi:10.1115/GT2002-30572

Cooper, M. G. (1982). Growth and departure of individual bubbles at a wall. *Appl. Sci. Res.* 38, 77–84. doi:10.1007/BF00385939

Derhoumi, Z., Mandin, P., Roustan, H., and Wüthrich, R. (2013). Experimental investigation of two-phase electrolysis processes: comparison with or without gravity. *J. Appl. Electrochem.* 43, 1145–1161. doi:10.1007/s10800-013-0598-2

Dhir, V. K., Abarajith, H. S., and Li, D. (2007). Bubble dynamics and heat transfer during pool and flow boiling. *Heat. Transf. Eng.* 28, 608–624. doi:10.1080/01457630701266421

Di Bari, S., Lakehal, D., and Robinson, A. J. (2013). A numerical study of quasi-static gas injected bubble growth: some aspects of gravity. *Int. J. Heat. Mass Transf.* 64, 468–482. doi:10.1016/j.ijheatmasstransfer.2013.04.002

Fritz, W., and Ende, W. (1936). Über den Verdampfungsvorgang nach kinematographischen Aufnahmen an Dampfblasen. *Phys. Z* 37, 391–401.

Greenshields, C., 2023. OpenFOAM v11 user guide [WWW document]. CFD Direct. URL https://doc.cfd.direct/openfoam/user-guide-v11/index (Accessed 9.23).

Hamdan, M., Sebastia-Saez, D., Hamdan, M., and Arellano-Garcia, H. (2020). "CFD analysis of the use of desert sand as thermal energy storage medium in a solar powered fluidised bed harvesting unit," in *Computer aided chemical engineering, 30 European symposium on computer aided process engineering*. Editors S. Pierucci, F. Manenti, G. L. Bozzano, and D. Manca (Elsevier), Amsterdam, Netherlands, 349–354. doi:10.1016/B978-0-12-823377-1.50059-8

Herman, C. (2013). Bubble Formation and coalescence under the influence of electric fields. *Heat Transf. Therm. Eng.* 8C, IMECE2013. doi:10.1115/IMECE2013-64991Volume

Heyns, J. A., and Oxtoby, O. F. (2014). *Modelling surface tension dominated multiphase flows using the VOF approach*. Barcelona, Spain: World Congress on Computational Mechanics.

Hirt, C. W., and Nichols, B. D. (1981). Volume of fluid (VOF) method for the dynamics of free boundaries. *J. Comput. Phys.* 39, 201–225. doi:10.1016/0021-9991(81)90145-5

Humbert, M. S., Brooks, G. A., Duffy, A. R., Hargrave, C., and Rhamdhani, M. A. (2022). Thermophysical property evolution during molten regolith electrolysis. *Planet. Space Sci.* 219, 105527. doi:10.1016/j.pss.2022.105527

Hurlbert, K. M., Witte, L. C., Best, F. R., and Kurwitz, C. (2004). Scaling two-phase flows to Mars and Moon gravity conditions. *Int. J. Multiph. Flow.* 30, 351–368. doi:10.1016/j.ijmultiphaseflow.2004.01.004

Iwata, R., Zhang, L., Wilke, K. L., Gong, S., He, M., Gallant, B. M., et al. (2021). Bubble growth and departure modes on wettable/non-wettable porous foams in alkaline water splitting. *Joule* 5, 887–900. doi:10.1016/j.joule.2021.02.015

Janz, G. J., Tomkins, R. P. T., Allen, C. B., Downey, J. R., Jr., Garner, G. L., Krebs, U., et al. (1975). Molten salts: volume 4, part 2, chlorides and mixtures—electrical conductance, density, viscosity, and surface tension data. *J. Phys. Chem. Ref. Data* 4, 871–1178. doi:10.1063/1.555527

Kamotani, Y., Chang, A., and Ostrach, S. (1996). Effects of heating mode on steady axisymmetric thermocapillary flows in microgravity. *J. Heat. Transf.* 118, 191–197. doi:10.1115/1.2824034

Kamotani, Y., Ostrach, S., and Pline, A. (1994a). Analysis of velocity data taken in surface tension driven convection experiment in microgravity. *Phys. Fluids* 6, 3601–3609. doi:10.1063/1.868432

Kamotani, Y., Ostrach, S., and Pline, A. (1994b). "Some results from the surface tension driven convection experiment aboard USML-1 spacelab," in *32nd aerospace sciences meeting and exhibit, aerospace sciences meetings* (American Institute of Aeronautics and Astronautics). Reston, VI, USA, doi:10.2514/6.1994-238

Kamotani, Y., Ostrach, S., and Pline, A. (1995). A thermocapillary convection experiment in microgravity. *J. Heat. Transf.* 117, 611–618. doi:10.1115/1.2822621

Kim, J., Benton, J. F., and Wisniewski, D. (2002). Pool boiling heat transfer on small heaters: effect of gravity and subcooling. *Int. J. Heat. Mass Transf.* 45, 3919–3932. doi:10.1016/S0017-9310(02)00108-4

Kim, J., and Raj, R. (2014). *Gravity and heater size effects on pool boiling heat transfer*. Cleveland, OH: National Aeronautics and Space Administration Glenn Research Center.

Kulkarni, A. A., and Joshi, J. B. (2005). Bubble Formation and bubble rise velocity in Gas–Liquid systems: a review. *Ind. Eng. Chem. Res.* 44, 5873–5931. doi:10.1021/ie049131p

Li, C., Zhang, J., Han, J., and Yao, B. (2021). A numerical solution to the effects of surface roughness on water–coal contact angle. *Sci. Rep.* 11, 459. doi:10.1038/s41598-020-80729-9

Lippmann, G. (1875). Relation entre les phénomènes électriques et capillaires. *Ann. Chim. Phys.* 5.

Lomax, B. A., Just, G. H., McHugh, P. J., Broadley, P. K., Hutchings, G. C., Burke, P. A., et al. (2022). Predicting the efficiency of oxygen-evolving electrolysis on the Moon and Mars. *Nat. Commun.* 13, 583. doi:10.1038/s41467-022-28147-5

Mandin, Ph., Cense, J. M., Georges, B., Favre, V., Pauporté, Th., Fukunaka, Y., et al. (2007). "Prediction of the electrodeposition process behavior with the gravity or acceleration value at continuous and discrete scale," in Electrochimica Acta, ELECTROCHEMICAL PROCESSING OF TAILORED MATERIALS Selection of papers from the 4th International Symposium (EPTM 2005), Kyoto, Japan, 233–244. doi:10.1016/j.electacta.2007.01.044Electrochim. Acta3-5 October 200553

Mandin, P., Matsushima, H., Fukunaka, Y., Wüthrich, R., Calderon, E. H., and Lincot, D. (2008). *One to two-phase electrolysis processes behavior under spatial conditions*. Sayama, Japan: The Japan Society of Microgravity Application.

Pamperin, O., and Rath, H.-J. (1995). Influence of buoyancy on bubble formation at submerged orifices. *Chem. Eng. Sci.* 50, 3009–3024. doi:10.1016/0009-2509(95)00140-Z

Prakash, S., and Ethier, C. R. (2000). Requirements for mesh resolution in 3D computational hemodynamics. *J. Biomech. Eng.* 123, 134–144. doi:10.1115/1.1351807

Qiu, D., Dhir, V. K., Hasan, Md.M., Chao, D., Neumann, E., Yee, G., et al. (2000). Dynamics of bubble growth on a heated surface under low gravity conditions. *AIP Conf. Proc.* 504. doi:10.2514/6.2000-852

Sibille, L., Sadoway, D., Sirk, A., Tripathy, P., Melendez, O., Standish, E., et al. (2009). "Recent advances in scale-up development of molten regolith electrolysis for oxygen production in support of a lunar base," in 47th AIAA Aerospace Sciences Meeting Including The New Horizons Forum and Aerospace Exposition, Aerospace Sciences Meetings, Orlando, Florida (American Institute of Aeronautics and Astronautics). doi:10.2514/6.2009-659

Tsuge, H., Terasaka, K., Koshida, W., and Matsue, H. (1997). Bubble formation at submerged nozzles for small gas flow rate under low gravity. *Chem. Eng. Sci.* 52, 3415–3420. doi:10.1016/S0009-2509(97)00159-0

Welch, S. W. J. (1998). Direct simulation of vapor bubble growth. *Int. J. Heat. Mass Transf.* 41, 1655–1666. doi:10.1016/S0017-9310(97)00285-8

Wenzel, R. N. (1936). RESISTANCE OF SOLID SURFACES TO WETTING BY WATER. *Ind. Eng. Chem.* 28, 988–994. doi:10.1021/ie50320a024

Wolansky, G., and Marmur, A. (1999). Apparent contact angles on rough surfaces: the Wenzel equation revisited. *Colloids Surf. Physicochem. Eng. Asp.* 156, 381–388. doi:10.1016/S0927-7757(99)00098-9

10.3389/frspt.2024.1304579

Nomenclature

F_b	Force of buoyancy
F_σ	Force due to surface tension
ρ	Density
g	Gravitational acceleration
V	Volume (of displaced fluid)
σ	Surface tension of liquid
d_c	Contact diameter
u	Velocity
p	Pressure
τ_{ij}	Viscose stress
$\tau_{t_{ij}}$	Turbulent stress
$f_{\sigma i}$	Surface tension
α	Interphase fraction
σ	Surface tension constant
K	Curvature

frontiers | Frontiers in Space Technologies

TYPE Original Research
PUBLISHED 03 April 2024
DOI 10.3389/frspt.2024.1331828

OPEN ACCESS

EDITED BY
Joseph N. Pelton,
International Space University, United States

REVIEWED BY
Jerry Stone,
Spaceflight UK, United Kingdom
Zhiping He,
Chinese Academy of Sciences (CAS), China

*CORRESPONDENCE
R. Trautner,
Roland.Trautner@esa.int

RECEIVED 01 November 2023
ACCEPTED 19 February 2024
PUBLISHED 03 April 2024

CITATION
Trautner R, Barber SJ, Fisackerly R, Heather D, Houdou B, Howe C, Iacobellis S, Leese M, Mariani A, Meogrossi G, Murray N, Panza C, Reiss P, Rusconi A, Abernethy F, Cann N, Chinnery H, Gscheidle C, Landsberg P, Lindner R, Morse AD, Mortimer J, Nicolae L, Picchi P, Sheridan S and Verchovsky A (2024), PROSPECT: A comprehensive sample acquisition and analysis package for lunar science and exploration.
Front. Space Technol. 5:1331828.
doi: 10.3389/frspt.2024.1331828

PROSPECT: A comprehensive sample acquisition and analysis package for lunar science and exploration

R. Trautner[1]*, S. J. Barber[2], R. Fisackerly[1], D. Heather[1], B. Houdou[1], C. Howe[3], S. Iacobellis[1], M. Leese[2], A. Mariani[4], G. Meogrossi[5], N. Murray[6], C. Panza[5], P. Reiss[7], A. Rusconi[5], F. Abernethy[2], N. Cann[1], H. Chinnery[2], C. Gscheidle[7], P. Landsberg[2], R. Lindner[1], A. D. Morse[2], J. Mortimer[2], L. Nicolae[1], P. Picchi[4], S. Sheridan[2] and A. Verchovsky[2]

[1]European Space Agency, ESA/ESTEC, Noordwijk, Netherlands, [2]School of Physical Sciences, The Open University, Milton Keynes, United Kingdom, [3]RAL Space / STFC, Fermi Ave, Harwell, Didcot, United Kingdom, [4]Kayser Italia S.r.L., Livorno, Italy, [5]Leonardo S.p.A., Airborne & Space Systems Division, Nerviano, Italy, [6]Dynamic Imaging Analytics Ltd, Foxhunter Drive, Milton Keynes, United Kingdom, [7]Technical University of Munich, Ottobrunn, Germany

PROSPECT is a comprehensive payload package developed by the European Space Agency which will support the extraction and analysis of lunar surface and subsurface samples as well as the acquisition of data from additional environmental sensors. The key elements of PROSPECT are the ProSEED drill and the ProSPA analytical laboratory. ProSEED will support the acquisition of cryogenic samples from depths up to 1 m and deliver them to the ProSPA instrument. ProSPA will receive and seal samples in miniaturized ovens, heat them, physically and chemically process the released volatiles, and analyze the obtained constituents via mass spectrometry using two types of spectrometers. Contextual information will be provided by cameras which will generate multi-spectral images of the drill working area and of acquired samples, and via temperature sensors and a permittivity sensor that are integrated in the drill rod. The package is designed for minimizing volatile loss from the sample between acquisition and analysis. Initially developed for a flight on the Russian Luna-27 mission, the payload package design was adapted for a more generic lander accommodation and will be flown on a lunar polar lander mission developed within the NASA Commercial Lunar Payload Services (CLPS) program. PROSPECT targets science and exploration in lunar areas that might harbor deposits of volatiles, and also supports the demonstration of *In-Situ* Resource Utilization (ISRU) techniques in the lunar environment. PROSPECT operations are designed to be automated to a significant degree but rely on operator monitoring during critical phases. Here, we report the PROSPECT flight design that will be built, tested, and qualified according to European space technology engineering standards before delivery to the lander provider for

spacecraft integration. The package is currently in the hardware manufacturing and integration phase with a target delivery to the NASA-selected CLPS lander provider in 2025.

KEYWORDS

prospect, lunar drill, lunar volatiles, sample analysis, mass spectrometry, multispectral imaging, permittivity sensor

1 Introduction

The renewed international interest in lunar science and lunar resources is generating numerous opportunities for performing scientific experiments and testing *in-situ* resource utilization (ISRU) technologies on the lunar surface. Water and other volatiles are of particular interest, with the potential for significant abundance of water ice near the lunar south pole suggested by the M3 instrument on Chandrayaan-1 (Pieters, 2009) and confirmed by NASA's LCROSS mission, which impacted an empty rocket stage into a crater on the lunar surface and identified ice in the ejected plume (Colaprete, 2010). These results, in combination with thermal modeling showing the potential stability of water ice at depth across large portions of the lunar south pole in particular (e.g., Paige and Pieters, 2010; King et al., 2020), have suggested that these regions may be host to a far more significant amount of water than was previously thought. The exact distribution, form, quantity, and origins of any water or hydroxyl are still untested, requiring direct sampling and surface analyses, and these are some of the questions that PROSPECT aims to address.

The PROSPECT package provides a comprehensive set of sample acquisition and handling functionalities as well as multiple types of instrumentation to address science and exploration goals. PROSPECT was initially developed to a preliminary design stage for a flight on the Russian Luna-27 lunar lander (Trautner et al., 2018), and has since then been re-designed, refined and matured to become a more generic payload package suitable for accommodation on different lunar lander platforms. With a strong focus on acquisition of samples containing lunar volatiles that are expected to be found predominantly in lunar polar areas, PROSPECT is designed for flight opportunities to high latitude landing sites. The first flight opportunity is on a mission of NASA's CLPS program, designated as CP-22, for a landing in 2026. PROSPECT will acquire samples for analysis from the surface down to a maximum sampling depth of 1 m and compile a comprehensive inventory of lunar polar volatiles found in the exosphere, surface regolith, and the subsurface at the landing site. This investigation will be supported by several secondary instruments and sensors that will provide additional data on landing site context and sample characteristics.

2 PROSPECT overview

The PROSPECT package consists of two key subassemblies: the ProSEED drill, which supports the acquisition of samples from the lunar surface and subsurface up to a depth of ~1 m, and the ProSPA instrument, which allows the analysis of acquired samples by means of volatile extraction, gas processing and mass spectrometry techniques. The electrical interface to the lander is provided by the ProSEED Control Electronics Unit (CEU), which connects to the spacecraft's payload control unit via two power links and a serial data link. ProSEED provides a Positioner Rotation Joint (PRJ) that allows the selection of a drilling site within the constraints of its working area and includes an imaging system and a permittivity sensor for supporting science and to achieve engineering-related objectives like the assessment of operational risks. The drill provides two different sampling mechanisms for acquiring samples of different sizes; the smaller sample type is suitable for the ProSPA instrument. ProSPA consists of two separate subassemblies, the Solids Inlet System (SIS) and the Analytical Package (AP). Samples acquired by the drill are delivered to the SIS, where they are imaged and sealed in miniature ovens before analysis. The SIS functionality is managed by the electronics in the Local Electronics System (LES) in the AP. The ProSPA instrument draws power from the ProSEED CEU and connects to it via a SpaceWire (SpW) link. ProSPA includes two mass spectrometers and a flexible set of functionalities for processing the acquired samples and the released volatiles. High-level control of the PROSPECT package functions, such as data exchange with the host platform and management of command sequences, is provided by the ProSEED CEU, while ProSPA functions are controlled at AP level. The unified interface to the lander simplifies the integration with the platform and allows the synchronization of ProSPA and ProSEED operations without lander interaction, which reduces the complexity of PROSPECT operations and system testing.

PROSPECT is expected to be accommodated on the side of the lander that is facing poleward after landing. This minimizes solar irradiation during drilling and allows keeping acquired samples at minimum temperatures during sample acquisition and sample transfer. A typical configuration for accommodation on a lander is depicted in Figure 1. The relative positioning of the PROSPECT units is governed by some specific constraints that are explained in subsequent chapters.

2.1 Industrial/academic consortium

The PROSPECT package is developed under a contract from the European Space Agency (ESA). The industrial consortium is led by Leonardo S.p.A. (Italy) who are also developing the ProSEED drill in collaboration with lower-level subcontractors Beyond Gravity (Switzerland, PRJ mechanism), Maxon (Switzerland, actuators), Sener (Spain, DTJ mechanisms), Kayser Italia S.r.L. (Italy, imaging system and EGSE), 3DPLUS/Lambda-X (France/

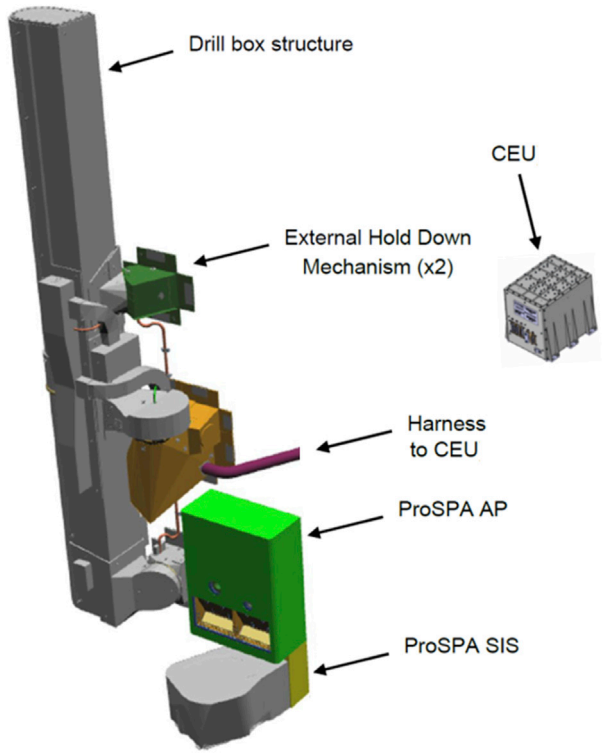

FIGURE 1
The elements of the PROSPECT package, schematically depicted in a typical accommodation configuration. Left: ProSEED drill box with External Hold Down Mechanisms (EHDMs) and positioner base tower/rotation joint; center: ProSPA Analytical Package with SIS installed below; right: PROSPECT CEU. The harness connection from CEU to ProSEED drill box and AP is not shown in detail.

Belgium, camera head), and Astronika (Poland, mechanisms). The ProSPA instrument is provided by key subcontractor The Open University (United Kingdom) in collaboration with lower-level subcontractors Airbus Defence and Space (United Kingdom, thermal design), RAL Space (United Kingdom, electronics and software), Technical University of Munich (Germany, SIS/ISRU technology and permittivity sensor), Max-Planck Institute for Solar System Research (Germany, SIS mechanisms), DIAL (United Kingdom, sample imager) and Leonardo S.p.A. (Utaly, mechanisms) (Italy, mechanisms).

In parallel to the industrial/academic project consortium, PROSPECT science investigations are actively supported and accompanied by a dedicated PROSPECT Science Team, which comprises researchers from several European industrial and academic institutions alongside some US participants.

2.2 Key science objectives and volatile preservation

The key science objective for PROSPECT is the detection and characterization of lunar polar volatiles in surface and subsurface samples. In this context, the preservation of volatiles in acquired samples up to the analysis stage is among the main challenges for PROSPECT.

When a volatile-bearing sample is acquired, the mechanical acquisition by the ProSEED sampling tool implies a first potential loss of volatiles due to thermal interaction with the temperature-controlled hardware. During extraction of the sample from the subsurface and up to delivery to the ProSPA instrument an additional volatile loss occurs. Another potential volatile loss is expected during the period from receiving the sample in the SIS up to sealing the sample in the oven. Finally, the leakage of oven seals and valves up to and during the gas analysis in the AP also imply a potential loss of volatiles. It is possible and necessary (but non-trivial) to model the losses for these operational steps in order to reduce the overall measurement error on volatile quantity in the sample; related work to investigate this in more detail is supported by separate ESA contracts.

The effect of volatile loss is illustrated in Figure 2. The upper solid line (black) leading from pristine sample (left side) to the point of sample analysis (right side) indicates the loss of volatiles from the sample during the acquisition, transfer, sealing and analysis stages. The blue line leading back from measurement result to derived sample volatile content makes use of volatile loss models. The dashed blue lines depict the error bars for the derived volatile content resulting from Mass Spectrometer (MS) measurement error and volatile loss modeling errors.

The quality of volatile loss modeling is also important for the instrument's volatile detection limits, as the detection limit of the spectrometers (determined by noise and background levels) is amplified by the volatile loss that is incurred up to the point of measurement. This is depicted in the lower curve in Figure 2. The sensitivity limit for volatile detection can be derived from the MS noise level and the reconstruction of the incurred volatile loss. The resulting error for the detection limit is derived from the combined modeling errors for the individual volatile loss stages.

Key requirements for reducing volatile loss include keeping the sample temperature as low as possible and minimizing the time spent from sample acquisition to sample sealing. These constraints are influenced by multiple factors including achievable mechanism speed, drill-regolith interaction (friction, conductive heat transfer), shadowing of drilling site, drill rod and SIS, thermal interface and accommodation aspects, and related operational approaches. The volatile loss varies for different molecular species, as their isotopic fractionation is also temperature dependent; as a result the volatile loss needs to be limited to ensure accurate measurements (Mortimer et al., 2018). These factors need to be taken into account for volatile loss modeling.

For PROSPECT, volatile loss can be minimized by several means. First, allowing the drill tool to cool down after drilling and before sample acquisition limits the drill tip temperature and related desorption of volatile content in the sample. Second, it is beneficial to design (on lander level) for a sufficiently low SIS interface temperature, ideally around −50 °C and not exceeding 0 °C during surface operations. Third, choosing an appropriate SIS cooldown period before a sample is delivered will allow the ovens to reach an appropriate temperature for sample reception. Furthermore, the time between sample transfer to the oven and

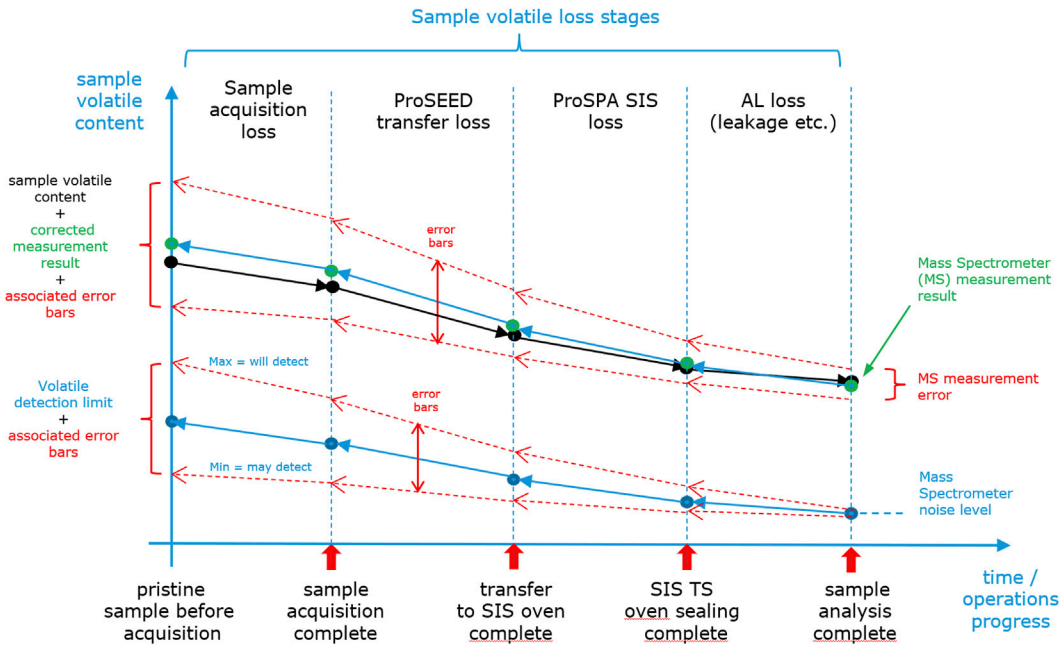

FIGURE 2
Qualitative depiction of the impact of sample volatile loss on measurement accuracy and volatile detection limits.

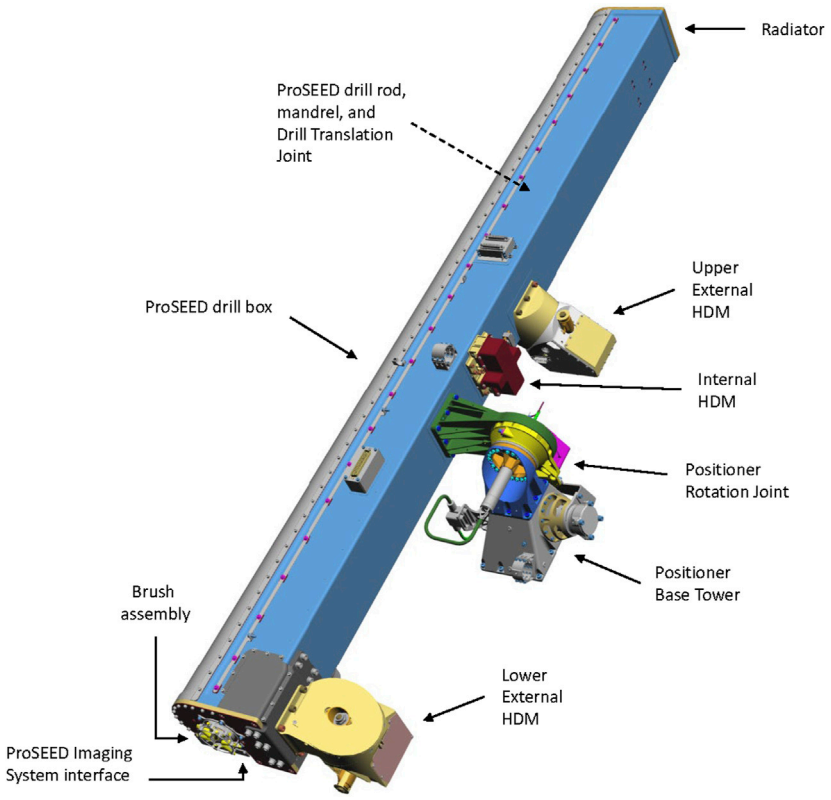

FIGURE 3
ProSEED drill box and main subassemblies. MLI is not shown in this depiction.

sample sealing is affected by the choice of the oven on the carousel; some ovens imply a shorter or longer transfer time depending on their relative positions on the rotary mechanism. Finally, the acquisition of accurate temperature information for the hardware elements involved in the sample handling and transfer will support volatile loss modeling. As a result,

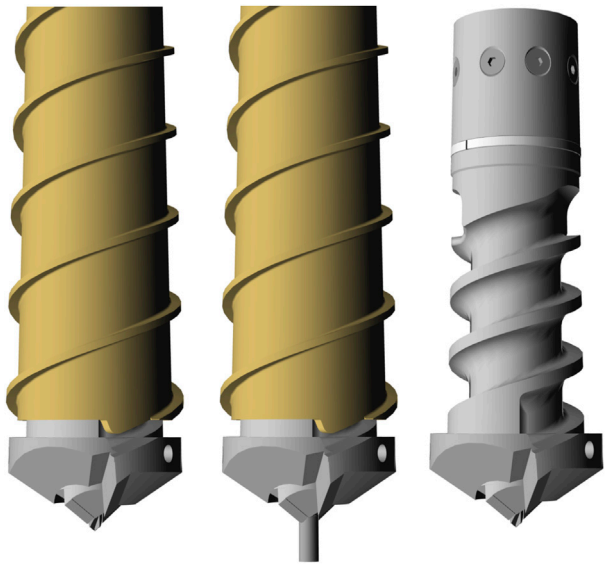

FIGURE 4
ProSEED sampling tool design. The sampling device used for acquisition of ProSPA samples is a push tube (left: retracted, middle: deployed). An additional sampling mechanism is provided for higher volume samples (right side, shown without drill rod tube) which allows acquisition of larger volumes of loose sample material. Both sample types are acquired while drilling; the push tube remains extended after sample acquisition until sample delivery, while for the larger sample the auger is retracted after acquisition to contain the sample within the drill rod until delivery.

considering these factors will enable an appropriate level of volatile preservation and an improved science return from interpreting the obtained measurement data.

2.3 Technical interfaces

Table 1 provides a summary of key interface and functional aspects.

While the basic technical interfaces of the individual PROSPECT sub-units (ProSEED box, CEU, ProSPA AL and SIS) are well defined, the details of their accommodation on a lander depend on the selected platform. This will however not affect the basic performance of the PROSPECT package as long as the baseline accommodation requirements are met.

2.4 ProSEED

The ProSEED main subassemblies consists of Drill and Positioner (whose main task is the sample collection, transportation, and delivery of collected samples to ProSPA) and Control Electronics Unit (CEU) which houses the electronics controlling the whole PROSPECT package. In terms of instrumentation the key subassemblies are the ProSEED Imaging System IS (used to acquire images and videos during lunar surface operations) and the ProSEED permittivity sensor which provides both science and engineering data. Additional hardware includes the ProSEED Harness (connecting the CEU with the other units) and the ProSEED Multi-Layer Insulation (MLI) that serves as thermal insulator for the ProSEED package. The following paragraphs describe the main ProSEED subassemblies and the integrated instrumentation.

2.4.1 ProSEED CEU

The ProSEED CEU is the 'brain' of the overall PROSPECT package and provides the electrical (power, data) interfaces to the platform and to the ProSPA instrument. It controls the ProSEED drill mechanisms, acquires data from a range of sensors, and handles telecommands (TC) and telemetry (TM) for the ProSPA instrument. The CEU acts as the data buffer not only for ProSEED data sources (ProSEED housekeeping data, drill telemetry, ProSEED Imaging System science and housekeeping data, permittivity sensor data) but also for all ProSPA data. It supports generic lossless data compression (CCSDS 121) and lossy image compression (CCSDS 122) on PROSPECT science data and on parts of the housekeeping data, prevents failure propagation to the platform, and provides important FDIR functions. The CEU provides high levels of power for the drill and for ProSPA. Power and data interfaces are non-redundant in the baseline implementation, but a redundant option is supported by the hardware design. The PROSPECT CEU is closely based on a similar unit developed in ESA's ExoMars project (Vago et al., 2017) and is designed as a highly reliable system.

2.4.2 ProSEED drill and Positioner

The ProSEED drill consists of a drill box of considerable size (over 1.7 m in vertical height), and several mechanisms supporting the drill positioning and drilling functions. The drill box is a carbon fiber based construction which encloses the key drilling mechanisms, and which also interfaces externally to the rest of the Drill and Positioner unit (see Figure 3).

The bottom end of the drill box includes the mounting position for the ProSEED imaging system (see 2.4.3) and a set of brushes in contact with the drill rod for reducing dust ingress into the box.

The drill rod includes the sampling tool (shown in detail in Figure 4), a device developed by the PROSPECT prime contractor Leonardo, which is capable of collecting 2 dry or icy samples of different sizes and physical-mechanical properties in a single sampling operation. This has been successfully tested during PROSPECT Phase B+ via a dedicated test campaign with representative lunar regolith simulant in cryogenic conditions and with variable water content up to saturation.

The drill rod also includes the PROSPECT permittivity sensor which provides information on subsurface material dielectric constant and also supports the direct detection of medium to high quantities of water ice in the regolith.

There are critical requirements defining the relative positioning of the ProSEED drill and the ProSPA SIS, as the capability of the SIS to compensate for drill rod misalignment during sample transfer is limited and the relative positioning needs to meet the requirements after application of launch, landing, and deployment loads over an extended temperature range.

The sampling tool and permittivity sensor are accommodated at the end of the drill rod, which itself interfaces near the top of the drill box with the Mandrel. The Mandrel provides the rotational torque which is transmitted to the drill cutting face by the drill rod.

TABLE 1 Key interface and sample acquisition characteristics of the PROSPECT Package.

Mass (incl. margins)	PROSPECT 44.8 kg, consisting of
	ProSEED 31.8 kg CEU: 5.3 kg D&P: 23.4 kg Harness: 3.1 kg
	ProSPA 13 kg AP 10.35 kg SIS 2.65 kg
Dimensions (static envelopes) X x Y x Z w/o harness and connectors, *Z*-axis being vertical in landed position; mounting interface in X-Z plane (except CEU)	Drill box 257 × 228 × 1721 mm (w/o PRJ and HDRM) 497 × 290 × 1721 mm (with PRJ and HDRM)
	ProSEED CEU 226.5 × 198 × 200 mm
	ProSPA AP 277 × 135 × 374 mm
	ProSPA SIS 256 × 301.2 × 150 mm
Power interface	28 V, 2 power lines (feeders)
Power limits	max 50 W (line 1)
	max 200 W (line 2)
Data interface	RS422 serial link, optionally redundant
CEU I/F temp	−50 to +50 °C (operational) −50 to +60 °C (non-operational)
ProSPA AL I/F temp	−50 to +50 °C (operational) −50 to +65 °C (non-operational)
SIS interface temp	−60 to +0°C (operational) −80 to +80°C (non-operational)
Drill box interface temp	−50 to +50 °C (during transfer/flight) −150 to +50 °C (surface operational) −150 to +80 °C (surface non-operational)
Lifetime	1 lunar day (default)
	1 terrestrial year with platform-provided survival heating
Data volume	Typ. 120 MB per operational cycle
Sampling depth	surface to 1,000 mm (surface level assumed 200 mm under SIS X-Y interface)
Drill working area	287.2 mm along a 134° arc with radius 245.6 mm (nominal; actual size of the arc depends on SIS location)
Sample volume #1	45 mm^3 (push tube)
Sample volume #2	5,000 mm^3 (internal auger)
Temperature measurement requirements	Drill tip sensor ± 0.1K
	Other sensors ± 1K

Working alongside the Mandrel is the Drill Translation Joint (DTJ), consisting of a geared mechanism in the base of the box which rotates a lead screw coupled with an interface nut on the Mandrel, and which provides the vertical thrust for advancing the drill cutting face down into the lunar surface. The DTJ is also used for overall translation of the drill rod, e.g., in retrieving the sample from the subsurface, and in positioning the sampling tool for sample transfer to the ProSPA SIS.

Supporting the drill rod within the drill box is an Internal Hold Down Mechanism (IHDM) which, together with other preloads and launch constraints, ensure the drill rod and its mechanisms can sustain the launch vibration.

A Positioner Rotation Joint (PRJ) is attached externally to the drill box and connects it, via a Positioner Base Tower, to the lander platform. The PRJ provides a rotational 'horizontal' degree of freedom, for choosing and accessing different drilling sites along

10.3389/frspt.2024.1331828

TABLE 2 Key characteristics of the drill-integrated instrumentation.

ProSEED imaging system	
Sensor resolution	4 Mpixel
Resolution @ FOV center (@ working distance 6.2cm/20cm/50cm) Resolution @ FOV corner (@ working distance 6.2cm/20cm/50cm) Best focus distance	0.13mm/0.20mm/0.39mm 0.70mm/0.62mm/1.27mm 25 cm
Data Interface	SpaceWire
Power supply	+10 V
Heater supply voltage/power	+32 V max/15 W max
Power consumption (w/o heating power)	1.75 W (standby)
	2.9 W max (imaging w/o illumination)
	13 W max (imaging + illumination)
Illumination	6 spectral bands, VIS + NIR
Operational temp range	−40 to +50 °C
Non-operational temp range	−90 to +85 °C
Interface temp range (qualification)	−100 to +95 °C
FFOV size	54 × 54°
Mass (BEE) incl. mounting materials, baffle and dampers, without MLI	649 g
LED channels (# LEDs/beam angle)	451 nm (4/±40°)
	597 nm (4/±45°)
	730 nm (4/±40°)
	860 nm (4/±25°)
	910 nm (4/±23°)
	970 nm (8/±24°)
ProSEED Permittivity Sensor	
Frequency band	1.5 Hz–200 Hz
Relative permittivity range	1 to 20
Target accuracy	10%
Operational temp range	electronics −40 to +65 °C
	electrode assembly −150 to +80 °C
Non-operational temp range	electronics −110 to +65 °C
	electrode assembly −150 to +80 °C
Measurement duration	1.5 s –16 s, default of 5 s
Power consumption (w/o heaters)	<300 mW
Emitting electrode diameter	10.8 mm
Drill rod protrusion diameter	15 mm
Mass incl. electronics	<50 g
Data volume per measurement (default duration)	20 kB (time series, uncompressed)
	≤10 kB (compressed)

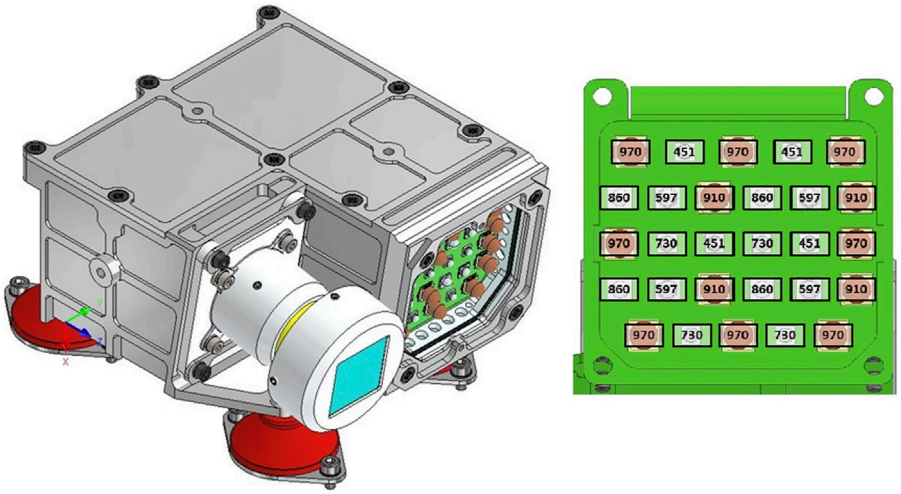

FIGURE 5
ProSEED Imaging System (IS) design (left) and LED spectral channel arrangement (right). The IS is mounted to the drill box via a set of dampers (depicted in red) for reducing mechanical loads during launch, EHDR release, and drilling.

an arc of approximately 90°, and for positioning the drill above the ProSPA SIS for sample delivery.

Before surface commissioning, the Drill box is also attached to the lander platform with two dedicated External Hold Down Mechanisms (EHDMs) which ensure the overall Drill and Positioner can sustain the launch environment. These EHDMs are then released during the surface commissioning phase, from which time the PRJ can rotate the drill box along the working area arc.

2.4.3 ProSEED imaging system

The ProSEED Imaging System (IS) will provide high resolution and multispectral images before, during and after the drilling activities. It can acquire 10 fps video in support of capturing the drill-regolith interaction and for monitoring purposes. In terms of science, the imaging system allows to investigate the mineralogy of surface and subsurface materials by means of multispectral imaging in a spectral range from 451 to 970 nm. It also supports PROSPECT operations verification and Public Relations objectives by provision of images and video. It allows witnessing the delivery of samples and an assessment of the positioning accuracy of drill tip vs. SIS inlet.

For multispectral imaging, an Artificial Illumination Unit (AIU) provides illumination in six spectral bands based on high power Light Emitting Diodes (LEDs), see Table 2. The LEDs are arranged in a Bayer-type pattern shown in Figure 5, and their beam angles are selected such that the decrease of the quantum efficiency of the IS detector towards higher wavelengths is partially compensated in order to achieve a sufficient signal-to-noise ratio at the FOV center for all wavelengths.

Due to power limitations, the optical power output of the AIU is not sufficient to perform high S/N multispectral imaging in the presence of direct sunlight. It is therefore important to ensure that relevant parts of the scenes of interest (such as parts of the cuttings cone) are in shadow when the imaging system is employed for this science investigation. This can be enabled by sunshields provided by the lander, and by selecting the drilling location according to the local time and the shadows cast by the lander, drill rod, and cuttings cone.

A color calibration target is also provided; its accommodation is foreseen at the base of the SIS where it can be imaged periodically when witnessing sample deliveries.

2.4.4 ProSEED permittivity sensor

The ProSEED permittivity sensor (Trautner et al., 2021a) is accommodated in the rod of the ProSEED drill as illustrated in Figure 6. It allows to sense the dielectric properties of the surrounding materials via the emission of an extremely low Frequency (ELF) alternating current (AC) signal through a small electrode. Apart from the capability to detect water ice, it measures regolith density and porosity of the subsurface and the drill cuttings that are transported upwards along the auger. This supports the estimation of sample mass from the sample volume measurements performed by ProSPA's SamCam (see 2.5.1). Measurements can be taken either at distinct drilling depths and drill rod angular positions, or in the context of a horizontal scan where multiple measurements are taken at a specific depth, with the drill rod being rotated by a small angle between subsequent measurements.

Performing multiple horizontal scans at equidistant depths allows the compilation of an electrical subsurface image, which provides information about permittivity trends with depth, the distribution of rocks embedded in the subsurface in proximity to the drill rod, and about the presence of subsurface ice within the sensor's detection limits. The sensor also allows to assess the size of the gap between drill rod and borehole wall, and provide inputs to the assessment of operational risks. A prototype of the permittivity sensor has been tested successfully in cryogenic conditions, demonstrating the capability to detect water ice at temperatures around −130 °C (Trautner et al., 2021a). Further optimizations of electrode design and data processing techniques implemented for the flight model design are expected to lead to a

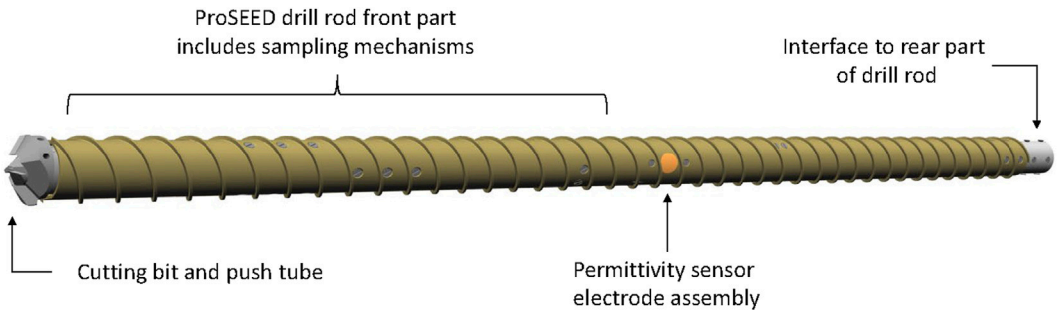

FIGURE 6
ProSEED drill rod (front part) and permittivity sensor accommodation.

detection limit for ice concentrations of < 1wt% at regolith temperatures around 125 K. Some key characteristics of the sensor are summarized in Table 2.

2.5 ProSPA

ProSPA comprises two physical units–the Solids Inlet System (SIS) that contains a number of single-use sample ovens on a rotary carousel together with a sample imager (SamCam) and an oven sealing mechanism, and a miniaturized Analytical Package (AP) incorporating elements for volatile processing, two mass spectrometers, and associated ancillary and control systems. Both units are connected by a harness and by the gas transfer pipe which is heated during operation. The SIS requires a mounting position that provides alignment of the ProSEED drill tip with the SIS sample inlet for enabling the transfer of acquired samples. The separate arrangement of SIS and AP allows provision of a separate thermal interface for the SIS to operate at low temperature and therefore minimize the loss of volatiles during sample handling, whereas the AP unit and its embedded electronics operate at more conventional (warmer) hardware temperatures. The AP can be mounted at some distance to the SIS, but with constraints for the maximum gas transfer pipe length, resulting harness mass, and SIS radiator field of view clearance. The functions of both AP and SIS are managed by software running on the processor of the Local Electronics System (LES) that is embedded in the AP. ProSPA is controlled by telecommands routed to the LES by the ProSEED CEU. All data generated by ProSPA is initially buffered in the LES and forwarded to the ProSEED CEU for further processing, data compression and storage. The overall architecture of ProSPA is depicted in Figure 7. The following chapters describe the instrument's SIS and AP subunits.

2.5.1 Solids inlet system

The Solids Inlet System (SIS) provides the necessary functions for receiving a sample from the ProSEED drill, measuring the sample volume, sealing the sample in one of its ovens, and performing controlled release of volatiles from the sample via heating of the sealed oven. Additional functions include the optical characterization of the samples in the spatial and spectral domains, cooling of the ovens for minimizing sample volatile loss, and temperature measurements for controlling the volatile release and for aiding volatile loss modeling. Figure 8 illustrates the SIS design.

Samples obtained from the lunar surface or subsurface by ProSEED are delivered to the SIS via a sequence of steps. First, the drill rod is positioned above the SIS delivery position. The drill tip is lowered slowly, allowing the alignment collet (a funnel-like device that has a rotational degree of freedom (DOF) at an angle to the ProSEED rotational joint DOF) to adjust to the drill tip position. ProSEED is continually adjusting the drill rod position using information from a lateral force sensor while moving downwards. The SIS collet assembly is connected to a position sensor; position information is fed back to ProSPA to align the oven position with the collet position. Once drill, collet and oven are aligned the push tube which contains the sample is retracted while the drill rod is moving downwards, and the sample is discharged into the target oven. The carousel assembly in the SIS allows accommodation of up to 25 ovens; an option to replace one oven by a SamCam calibration target may be chosen for missions where utilization of all ovens is considered unlikely due to mission constraints. After sample delivery, the carousel is rotated to place the sample-containing oven under the SamCam imager (Murray et al., 2020) to confirm the presence of a sample, determine its reflectance spectrum in a range from 450 to 970 nm, and enable an estimation of the sample volume via plenoptic imaging (see example image in Figure 9). Then the target oven is rotated to the Tapping Station (TS) position where an actuator is used to seal the oven to a pipe that runs to the AL. The quality of the seal is an important factor for volatile preservation; the chosen material (polytetrafluoroethylene) allows reliable sealing also in the presence of lunar dust and up to temperatures of 322 °C reached at the seal interface. To achieve the required thermal gradient between the heated zone inside the oven (up to 950 °C) and the seal at the top of the oven, various detail design features are incorporated to minimize heat transfer through conduction and radiation.

As the SIS is radiatively cooled, a cool-down phase is required after each sample analysis to allow the thermal energy released in the SIS during sample heating to dissipate and radiate away, so the SIS and specifically the ovens are cold enough once the next sample is delivered. Depending on lander accommodation constraints, this cooldown phase may take between 2 and 16 h. Good shadowing of the SIS unit from solar illumination and a low SIS interface temperature will allow to minimize the cool-down time.

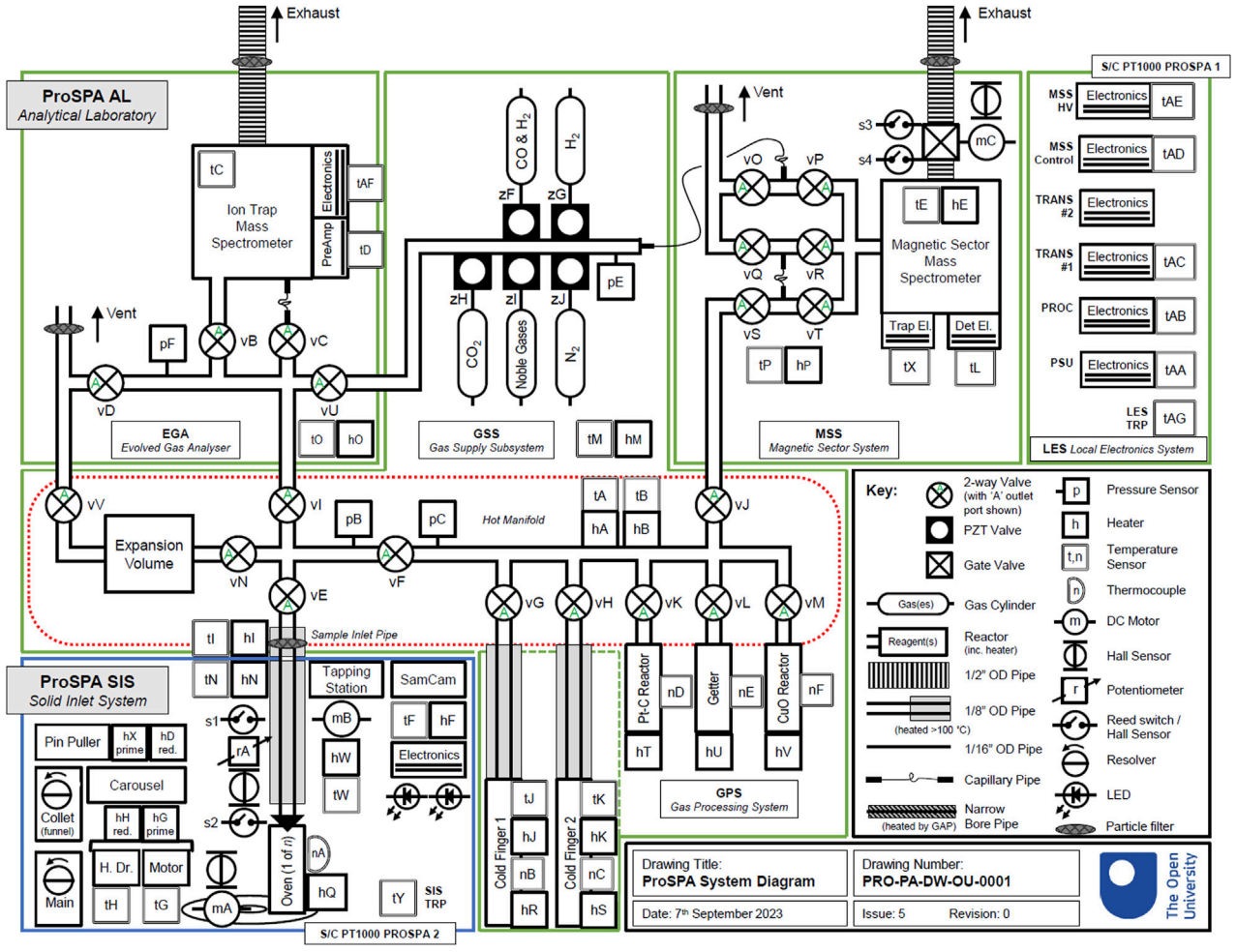

FIGURE 7
ProSPA functional diagram showing internal subunits: SIS (bottom left, blue box) and AP elements (green boxes): Gas Processing System (center), EGA/ITMS (top left), MSS (top right), and LES as well as legenda (black box, right side).

2.5.2 Analytical package

The purpose of the AP is the comprehensive characterization and analysis of volatiles and other gases released from the samples in terms of quantity and molecular and isotopic composition. Additional functions allow the demonstration of ISRU processes by reduction of the sample (mainly the $FeTiO_3$ and FeO content) in the presence of hydrogen.

In support of these functionalities the AP provides a range of hardware elements illustrated in Figure 10 which are controlled by ProSPA's Local Electronics System (LES) that provides the power and data interface to the ProSEED CEU.

The AP is connected to the SIS via a heated gas transfer pipe which leads to a hot manifold interconnecting various AP subassemblies. During operations, the temperature of hardware elements exposed to released volatiles is kept at ~100°C–120 °C to prevent condensation. The hot manifold is part of the Gas Processing System (GPS) that is equipped with temperature and pressure sensors and is connected to 2 cold fingers (radiatively coupled to space to support accumulation of volatile species under temperature control, and used for removal or separation of volatiles via cryogenic methods), temperature-controlled Platinum-Carbon and Copper Oxide reactors, and a Getter vessel. Together, they support the physical and chemical processing of volatiles into species suitable for isotopic analysis. The manifold is also connected to an expansion volume, the Evolved Gas Analyzer (EGA, including an Ion Trap Mass Spectrometer), and a Magnetic Sector System (MSS, that includes a Magnetic Sector Mass Spectrometer). Both the EGA and MSS are connected to a Gas Supply System (GSS) that provides reactants and calibration gases in pressure vessels with a volume of 2 mL under pressures of up to 50 bar. They are connected via pulse controlled low throughput Piezo Valves (patented by the OU). Available consumables include CO_2, a mixture of noble gases, N_2, H_2, and a CO/H_2 mixture; these gases are used for calibration purposes, for supporting the gas analysis, and–in the case of H_2–for the ISRU demonstration. The expansion volume and the spectrometers are connected to space via vent/exhaust openings that allow to purge these systems and allow analyzed volatiles to escape to space during or after spectrometer measurements.

After delivery of the sample to the SIS, sealing of the oven by the Tapping Station, establishing readiness of the AP for operation and conditioning of the hot manifold and gas

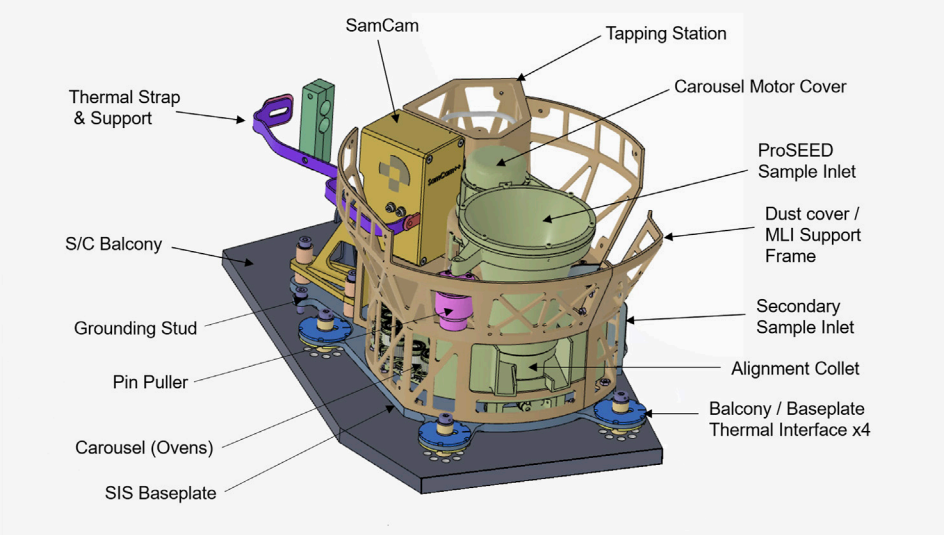

FIGURE 8
ProSPA Solids Inlet System design (MLI cover and connections to AP not shown).

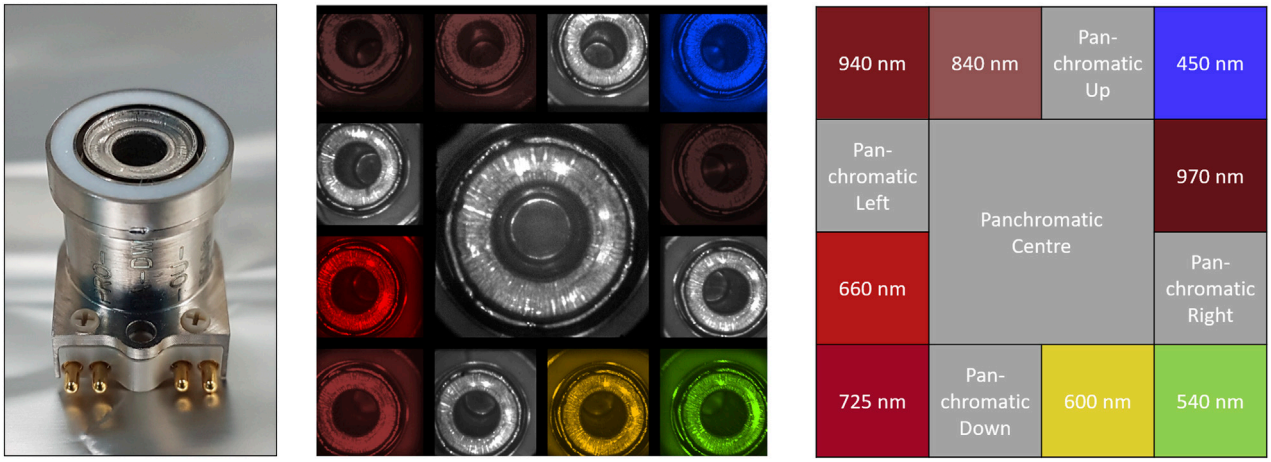

FIGURE 9
ProSPA SIS oven (left), SamCam image of oven (center), and SamCam optical filter characteristics (right).

transfer pipe to operational temperature, volatiles are extracted from the sample through heating the sealed oven in specific modes to accomplish a variety of analyses. In case of high amounts of volatiles in the sample, the expansion volume in the hot manifold can be used to sub-divide the quantity of released volatiles by the volume ratio of manifold and expansion volume. Depending on the intended investigation, the sample or sample gas can be processed using cold fingers, reactors, or a getter vessel, before the resulting gas is routed to the spectrometers. After analysis, the gases leave the spectrometers into the vacuum of space through the exhausts.

The main analysis techniques supported by ProSPA are Evolved Gas Analysis (EGA) and Stepped Pyrolysis or Combustion. For EGA, the sample temperature is increased steadily at a constant rate of ca. 6 K/min. Volatile molecules enter the EGA manifold and are routed to the ITMS sensor compartment directly or via a capillary depending on the gas pressure. In the ITMS sensor neutral species may be ionized through interaction with a beam of electrons released by thermionic emission from a resistively heated wire filament. Ions are trapped within the specifically configured electric field and are ejected towards an electron multiplier detector in order of increasing mass-to-charge (m/z) ratio. The output of the detector as a function of time constitutes a mass spectrum and is reported as part of science telemetry. In addition to analysis of inorganic species, the ITMS also provides operational modes which support the analysis of organic compounds via their molecular fragments.

For stepped pyrolysis/combustion, volatiles are released from the sample in a sequence of fixed temperature steps in vacuum or in presence of supplied oxygen. Data on released gases is collected for a

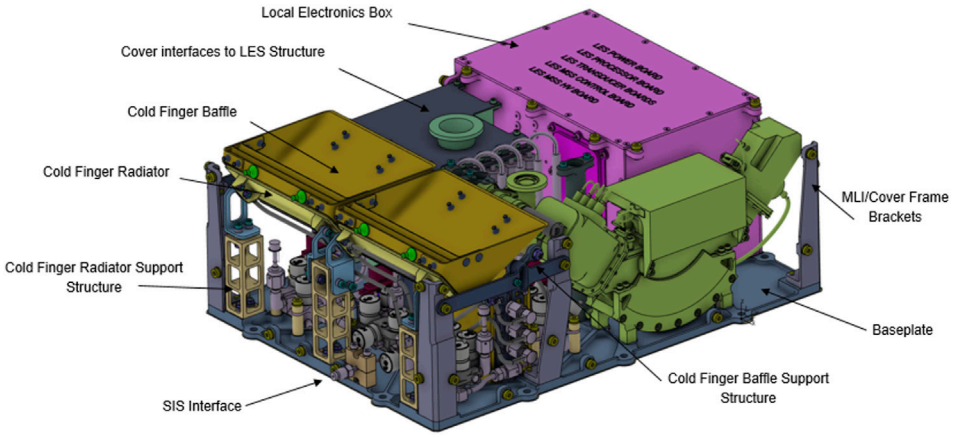

FIGURE 10
ProSPA Analytical Package Design (cover panels and MLI not shown). The spectrometers and their frontend electronics are accommodated close to the LES (pink) and are depicted in green (MSS) and dark grey (EGA/ITMS). GSS and GPS elements are accommodated between the two spectrometers and under the cold finger baffles.

typical duration of 30 min at each step. The resulting sample gas can then be routed to the Magnetic Sector System. The core sub-system of the MSS is the Magnetic Sector Mass Spectrometer which allows measurements of isotope ratios. In order to achieve good isotopic measurements over a range of sample sizes the instrument can operate in two modes: dynamic and static. In dynamic mode the mass spectrometer's exhaust is open to space (via the associated gate valve). Sample and reference gases from the GPS enter a change-over valve through capillary leaks which switches one of the gases into the mass spectrometer whilst the other leaks into vacuum. Switching the change-over valve switches the gases which are entering the mass spectrometer and vacuum, thus allowing rapid comparison between the sample and reference gases. This measurement approach allows good isotopic precision (~0.1‰) but requires µmol quantities of sample gas. In static mode, the mass spectrometer is sealed by closing the gate valve and the entire sample enters the mass spectrometer for analysis. Following analysis, the mass spectrometer is evacuated, and the procedure repeated for the reference gas. Since practically the entire sample gas enters the mass spectrometer and is available to be ionized and analyzed for a long period of time, static analysis gives the greatest sensitivity (~nmol quantities of sample gas). However, this comes at the cost of reduced isotope precision (~1‰) as the gas pressure reduces during the analysis and it is not possible to make a contemporaneous comparison with the reference gas. Furthermore, static analysis is only suitable for gases which are not modified (destroyed or chemically changed) by being in contact with the hot electron emitter filament. Therefore, only species such as noble gases, CO2, CO, N2 and CH4 are suitable for static analysis.

The choice of using either dynamic or static analysis method depends on the type of gas sample, the available quantity of sample gas, and the desired accuracy and sensitivity for the intended investigation.

Table 3 shows the basic characteristics of the ProSPA AP mass spectrometers and the measurement requirements applicable for these instruments.

The demonstration of *in-situ* Resource Utilization (ISRU) assumes the presence of oxygen-bearing minerals such as Ilmenite ($FeTiO_3$) in the sample and has been successfully demonstrated in the laboratory (Sargeant et al., 2020). The sample is reduced by exposing it to a suitable reactant, and heated to temperatures of ~900°C–1,000 °C. In ProSPA, the supplied reactant is H_2 which is stored in the GPS. For the ISRU demonstration, a suitable quantity is supplied to the hot manifold and sample gas pipe to expose the sample. The oven is then heated close to maximum temperature (950 °C) for several hours, and the resulting water vapor is trapped via a cold finger. Once the reaction phase is complete, the trapped gas is analyzed via the EGA subsystem.

The ISRU demonstration can be performed on a sample that has already been analyzed before, so it does not require use of a precious pristine sample. In fact, a completely outgassed sample is desired for performing the ISRU demonstration, as volatiles and mineral decomposition products could negatively impact the reduction process (limited water extraction yield) or complicate the interpretation of the gas products. Depending on the mission lifetime and available resources, the demonstration may only be performed on a small number of samples due to the time and energy required.

2.6 PROSPECT experimental concept validation

The general design concept of the PROSPECT package has been tested and validated ahead of the PROSPECT CDR via a series of experimental test campaigns that encompassed all key subassemblies.

For ProSEED, a Demonstration Model (DM) has been built and tested successfully in representative materials in a cryogenic environment. Gas concrete, brick layers, and mixtures of NU-LHT-2M lunar regolith simulant, small rocky inclusions and water (up to a water ice content of ~10 wt%) have been drilled successfully up to a depth of 1 m at temperatures down to < -150°C, followed by cryogenic sample acquisition and sample

delivery to representative hardware. All robotic elements (PRJ, DTJ, mandrel, sampling mechanisms) have been experimentally proven in that setup. HDRM prototypes have been tested separately. A flight-like ProSEED imaging system model has been built and demonstrated multispectral imaging and video capability on targets including rock samples. It also successfully passed a thermal test campaign that included exposure to temperatures as low as −100 °C. Testing of the permittivity sensor has been explained in section 2.4.4. and (Trautner et al., 2021b).

For ProSPA, a Bench Development Model (BDM) has been assembled and used to execute the key sample processing and analysis steps foreseen to be performed by ProSPA. Oven models, valve prototypes, reactor vessel and other key hardware have been tested in this setup and also separately for proofing their key performances. Development models of the ITMS and magnetic sector spectrometers have been assembled and tested with prototype electronics in support of finalizing the flight designs. An ITMS sensor and related flight electronics that are closely resembling the ProSPA design have been developed for the EMS spectrometer (Trautner et al., 2021b) and successfully tested in space during the Astrobotic M1 lunar mission. For the SIS, lower-level prototypes and a flight-like Engineering Model (EM) have been assembled and tested for proofing the concepts and for supporting the development of the final flight design. Figure 11 shows a number of PROSPECT hardware elements that were utilized for the experimental concept validation.

Once the PROSPECT qualification hardware is assembled, it will be used to execute flight-like operations in representative environments and for proving the compliance to all PROSPECT performance requirements. The data acquired during these test campaigns will enable further publications on the detailed performances of the robotic and scientific performances of the PROSPECT flight design and its subassemblies. The present paper is intended to serve as an anchor point for future publications on test results and on the results of the actual PROSPECT mission as part of the CP-22 lander payload.

3 PROSPECT operations planning

The operations planning for the PROSPECT package is highly dependent on the constraints posed by the target mission. For missions that support lunar night survival a very flexible operations approach that fully exploits all capabilities of the various instruments can be employed, and a cautious operations plan that retires operational risks step by step can be supported. For short-lived missions that span only a single lunar day, a highly automated approach using a more modest number of pre-validated operations sequences is advisable. This allows to maximize the number of samples that can be acquired and processed within the short mission lifetime but reduces operational flexibility and implies acceptance of higher operational risk. In the following chapters we present our baseline approach for the more challenging short-lived mission type. This should be understood as a baseline concept that needs to be adapted to an actual set of mission constraints.

3.1 Mission constraints

The baseline assumptions for a lunar polar landing site without lander night survival include the availability of a 10 Earth-day long window for spacecraft surface operations between landing and nightfall. This timeframe typically includes vehicle post-landing checks, propulsion system passivation, initial battery charging, payload commissioning and operations, as well as system safeing and lander passivation before lunar night. Payload operations are therefore expected to face significant constraints in terms of available resources. In addition to limitations on time, power and energy available to payloads, the spacecraft also imposes constraints on data rates and data volumes for commanding and telemetry downlink. An efficient planning of coordinated payload operations and resource utilization is therefore paramount for optimizing mission success and for maximizing the scientific return. The following paragraphs summarize the key PROSPECT operations phases and their specific requirements; the related resource requirements are provided in Table 4.

3.2 Checkout and commissioning activities

The possibilities for checkouts of payload systems during cruise are usually constrained; typically, limited functional checks will be conducted during transfer and/or in lunar orbit. Among the desirable checkout activities for PROSPECT are thorough functional checks of the electronics systems (CEU and LES) and operations of the ProSEED sensors and instrumentation, as well as activation of the ProSPA spectrometers. The goal is to confirm nominal function of all systems that do not depend on electromechanical or deployment systems to confirm their nominal condition after launch, and – for ProSPA - to obtain a first assessment of instrument signal background and spacecraft outgassing levels, which are important factors for subsequent science data analysis.

After landing, the successful commissioning of the PROSPECT package is a necessary pre-requisite for executing the science mission. Commissioning will include the same functional checks performed during cruise; however, in addition all deployment means (internal and external HDMs) will be activated and all mechanisms will be moved through their kinematic envelope as far as feasible without active drilling. During the execution of these functional checks, sensors and instrumentation will be employed as needed for acquiring data that supports the selection of the most suitable command sequences for initial operations. For ProSEED, this will include acquisition of multispectral images of the drill working area, images of the IS calibration target, images supporting the verification of post-landing drill-SIS alignment, calibration/noise level measurements for the permittivity sensor, and acquisition of environmental data including level of straylight and subsystem temperatures. The imagery will also allow to assess the level of dust deposition during the landing event. This data will be used for assessing the general situation and geology of the landing site, selecting the first drilling location, adjusting the IS exposure time, adjusting durations of mechanism warmup periods, and for selection of permittivity sensor measurement duration. For

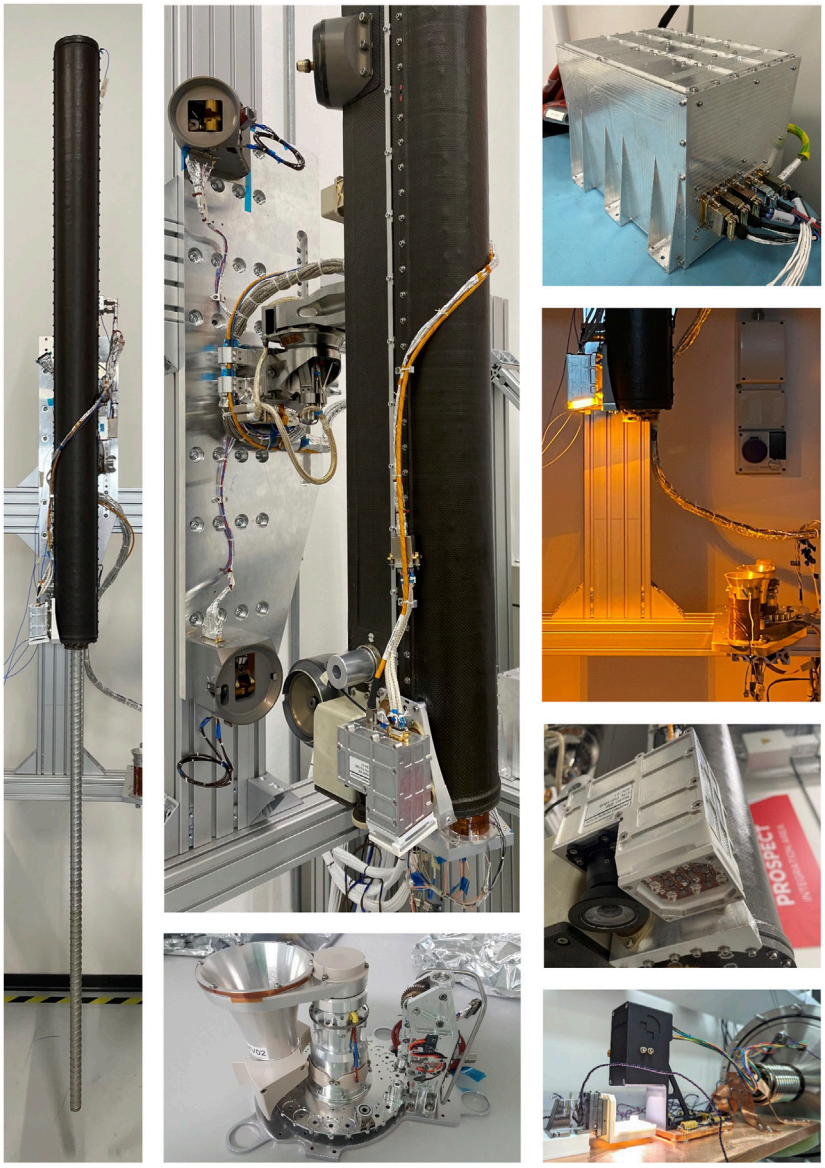

FIGURE 11
PROSPECT Engineering Model (EM) hardware. Left: ProSEED drill box with fully extended drill rod. Center top: ProSEED drill box including Imaging System, mechanical interface elements (PRJ, EHDMs) and harness in fully functional configuration. Center bottom: SIS EM during assembly, showing alignment collet, Tapping Station, and carousel with first oven installed. Right bottom: SIS SamCam during a calibration campaign. Right top: ProSEED CEU. Right center (2 images): ProSEED Imaging System; the 630 nm LEDs are activated in the upper image.

ProSPA, repeating the ProSPA spectrometer checkouts performed in orbit will provide information on the evolution of spacecraft outgassing after the cruise checkout, and on contamination from landing phase combustion products and from vented fuel. A bakeout of the AP, performed with activated spectrometers, will gradually reduce the background level caused by the presence of contaminants within the laboratory manifolds and allow to characterize the residual background. The SIS will be commissioned by releasing the carousel launch lock, actuation of the carousel and TS mechanisms, and taking images of the SamCam calibration target. Once bakeout is completed, resources permitting, an empty oven (called a “blank”) may be imaged, rotated to the TS and sealed. The blank is then processed using a default analysis sequence in support of system calibration and further background characterization. Commissioning of PROSPECT is complete as soon as the nominal function of all systems, sensors, instruments, and mechanisms has been confirmed, and all data necessary for selecting and adjusting the command sequences for initial nominal operations has been obtained.

3.3 Nominal PROSPECT operations

After successful commissioning, nominal operations can commence. While the basic sequence of activities for PROSPECT is well established, the lander platform and mission design including related constraints (power and energy availability, communication

TABLE 3 ProSPA mass spectrometer characteristics and measurement performance requirements.

Ion Trap Mass Spectrometer	
m/z range	10–150 amu
Mass resolution m/Δm	1
Operational modes	Multiple scan functions for covering m/z range
Operating pressure	max ~10^{-5} mbar
Measurement time per spectrum	~1 to 10/min, incl. averaging for S/N build-up
Magnetic Sector Mass Spectrometer	
m/z range	2–150 amu
Mass resolution m/Δm	65
Operational modes	Static + dynamic
Operating pressure	~10^{-6} mbar (static), ~10^{-7} mbar (dynamic)
Measurement time	~30 s

ProSPA measurement performance requirements				
Species	Minimum measurable concentrations (ug/g)	Mass in 50 mg of regolith assuming minimum measurable concentrations (ug)	Required isotopic ratios	Maximum permitted uncertainty on isotopic measurements
H_2O	414	20.7	N/A	See H and O rows
H	46	2.3	δ^2H	100‰ (δD)
^4He	14	0.7	-	-
^{20}Ne	0.5	0.025	-	-
^{21}Ne	0.002	0.0001	-	-
^{22}Ne	0.04	0.002	-	-
^{36}Ar	0.6	0.03	-	-
^{38}Ar	0.1	0.005	-	-
^{40}Ar	0.9	0.045	-	-
^{84}Kr	0.0005	0.000025	-	-
^{132}Xe	0.00015	0.0000075	-	-
C	124	6.2	$\delta^{13}C$	1‰ ($\delta^{13}C$)*
N_2	81	4.05	$\delta^{15}N$	10‰ ($\delta^{15}N$)
F	70	3.5	N/A	N/A
Cl	30	1.5	N/A	N/A
O	N/A	N/A	$\delta^{18}O$, $\delta^{17}O$	1‰ ($\delta^{18}O$), 22‰ ($\delta^{17}O$)
S	715	35.75	N/A	N/A

architecture and uplink/downlink windows, link latency and bandwidth, illumination and thermal conditions at the landing site and specifically in the drill working area) have a significant impact on the sequencing and timing of PROSPECT operations. For these reasons the operations concept presented here must be seen as a template that needs to be adapted to a specific mission environment.

After power is applied to PROSPECT, first housekeeping data and a boot report are generated and transmitted to the lander as part of essential telemetry. After loading the application software, PROSPECT is ready for executing *ad hoc* or pre-validated operations sequences. Initial activities typically include the warmup of mechanisms and other subsystems (IS) to bring them

TABLE 4 PROSPECT operations resource requirements.

Note: numbers include planning margins	In-flight checkout	Surface commissioning	Nominal operations cycle (resource requirements per sample)
Operations duration	8 h	12.5 h	~16 h ± 8 h[a]
Average power	21.5 W	78 W	85.6 W
Peak power	80 W	150 W	200 W
Data volume	20 Mbytes	40 Mbytes	120 Mbytes
TC mode	Manual commanding	Manual commanding	Manual commanding (initially)/automated timeline (subsequent)
TM mode/latency needs	Real time/low latency	Real time/low latency	Real time/low latency (initially)/store and forward (subsequent)

[a]The operations duration is strongly affected by drilling depth and regolith properties, selected type of ProSPA analysis, and interleaved secondary instrument operations. In case of a rapid succession of PROSPECT operations cycles, the required oven cooldown time may extend the operations cycle duration.

above minimal operational temperature and allow their engagement without delay via nominal operations command sequences. At least during initial operations, operator checkpoints are maintained for checking the boot report, for confirming the successful completion of the warmup phase, and for other points where operational risks need to be assessed. The first drilling location is pre-selected based on images acquired during the commissioning phase, and drilling is initiated in either power-limited, force limited, or constant speed mode. During drilling, depending on available resources, the drill may be stopped periodically (typically every few cm drilling depth) to allow the IS to acquire multispectral images of the drill cuttings. At depths beyond 40cm, the permittivity sensor is engaged after the IS before resuming the drilling activity. The depth for acquisition of the first sample depends on the scientific context of the landing site but is generally expected to be from a shallow depth that is deep enough to avoid the surface contaminants deposited by the spacecraft and landing process (combustion products, vented fuel, outgassing products). Subsequent samples are then expected to be acquired from multiple depths down to the maximum depth of 100 cm (ref. Table 1), adding up to a complete vertical survey. Before a sample is acquired, the drilling activity is stopped in order to allow the sampling tool to cool down for a typical period of 10–20 min. This allows to reduce the volatile loss during sample acquisition.

The ProSPA package is initialized at a suitable time after ProSEED power-up and before sample acquisition by ProSEED. As for ProSEED, boot software and application software are loaded, automatic checks are performed, and their results are reported in essential telemetry. SIS systems and mechanisms are warmed up, the selected oven is placed below the sample delivery position, and the system awaits the start of the sample transfer procedure.

For sample acquisition, ProSEED first implements a partial (few mm) retraction of the drill rod within the borehole and then extends the sampling tool's push tube and proceeds to drill to a depth that ensures the push tube is filled to an adequate level. The sample is not actively retained in the push tube but is held in place by adhesion and friction forces. After acquisition, the sample is extracted from the drill hole, rotated over to the SIS, and the sample transfer procedure commences. The drill (via the PRJ) and the SIS (via the DOF of the alignment device) have degrees of freedom that are approximately orthogonal at the sample delivery position, and a software-controlled alignment procedure ensures the correct position of the ProSEED drill and simultaneous position of the target oven at the sample delivery position in the SIS. The sample is transferred via simultaneous downward movement of the drill rod and retraction of the push tube, leading to the discharge of the sample (which may be in solid or fractured form) into the oven.

After sample transfer, the target oven is first rotated under the SamCam, where multispectral and 3D images are acquired before the oven is positioned under the TS and the oven is sealed.

The ProSEED drill is then retracted to clear the alignment device and rotated back to the drill's default position. On some occasions, the movement may be stopped after clearing the SIS for taking multispectral images of the IS calibration target that is accommodated at the base of the SIS. The drill is then stowed, outside the FOV of the SIS radiator, until the next sample acquisition is initiated.

After the sample is sealed in the ProSPA oven, volatile extraction and analysis can commence, a process expected to take several hours depending on the chosen analysis method. During this process, the carousel and SIS temperatures increase because of the energy spent heating the oven. As the conductive coupling of the SIS to the environment is minimized by design to allow nominal operation also in a warm interface environment, cooling of the SIS after an extraction process happens almost exclusively via radiative cooling. This results in an important operational constraint and highlights the importance of the thermal interface design aspects for enabling efficient operations.

The bulk of the data volume generated by PROSPECT consists of science data. After generation by the instruments and compression by the ProSEED CEU this data can be released for transmission by telecommand. Data processing, compression and the bulk of the data transmission is typically performed while ProSPA is processing the acquired sample. This allows to power down the PROSPECT package soon after completion of the sample analysis by ProSPA.

4 Summary and conclusion

PROSPECT is a comprehensive payload package for subsurface sample acquisition and analysis of volatiles and other gases in lunar environments including polar areas. It

includes the ProSEED drill, capable of acquiring samples from up to 1 m depth, and the ProSPA instrument which is dedicated to the extraction and analysis of volatiles from acquired samples. ProSEED also includes a multispectral imager, a subsurface permittivity sensor, and a set of additional sensors for acquisition of engineering and auxiliary data. ProSPA includes an analytical laboratory and two mass spectrometers, as well as a multispectral sample imager. PROSPECT supports vertical surveys at multiple drilling locations within its working area. The ProSPA instrument is capable of extracting volatiles from samples via heating and supports volatile analysis with respect to molecular species and isotopic composition. The built-in capabilities of the analytical laboratory for volatile storage, separation and processing further enhance the package's capabilities. ProSPA is also capable to demonstrate the thermal-chemical reduction of a sample with hydrogen to produce water/oxygen as a first *in-situ* small-scale proof of concept for ISRU processes. The PROSPECT package provides some flexibility for accommodation of its subunits on different types of landers and is compatible with mission durations of 1 lunar day or more. PROSPECT has been selected as a key payload for the CP-22 mission of NASA's Commercial Lunar Payload Services program and is expected to significantly enhance the understanding of the distribution, origin and behaviour of volatiles in lunar polar areas.

Data availability statement

The datasets presented in this article are not readily available because underlying designs and data are the Intellectual Property of ESA and ESA's industrial and academic contractors. Requests to access the datasets should be directed to Roland.Trautner@esa.int.

Author contributions

RT: Investigation, Supervision, Writing–original draft, Conceptualization, Project administration, Visualization, Funding acquisition, Methodology. SB: Conceptualization, Investigation, Project administration, Writing–review and editing, Supervision, Methodology, Visualization, Formal Analysis. RF: Conceptualization, Project administration, Supervision, Writing–review and editing, Funding acquisition, Methodology. DH: Investigation, Methodology, Supervision, Writing–review and editing, Validation. BH: Project administration, Resources, Supervision, Writing–review and editing, Funding acquisition. CH: Conceptualization, Project administration, Software, Supervision, Writing–review and editing, Methodology. SI: Supervision, Validation, Writing–review and editing. ML: Conceptualization, Investigation, Methodology, Project administration, Supervision, Writing–review and editing, Visualization. AMa: Conceptualization, Project administration, Visualization, Writing–review and editing. GM: Project administration, Supervision, Writing–review and editing. NM: Conceptualization, Investigation, Methodology, Project administration, Visualization, Writing–review and editing. CP: Conceptualization, Project administration, Visualization, Writing–review and editing, Supervision. PR: Conceptualization, Investigation, Methodology, Validation, Writing–review and editing. AR: Conceptualization, Project administration, Supervision, Writing–review and editing. FA: Formal Analysis, Investigation, Methodology, Validation, Writing–review and editing. NC: Project administration, Writing–review and editing. HC: Methodology, Validation, Writing–review and editing. CG: Conceptualization, Formal Analysis, Methodology, Writing–review and editing. PL: Investigation, Methodology, Writing–review and editing. RL: Methodology, Project administration, Supervision, Writing–review and editing. AMo: Conceptualization, Investigation, Methodology, Validation, Writing–review and editing. JM: Investigation, Methodology, Validation, Writing–review and editing. LN: Software, Supervision, Writing–review and editing. PP: Conceptualization, Methodology, Writing–review and editing. SS: Conceptualization, Investigation, Methodology, Validation, Writing–review and editing. AV: Investigation, Methodology, Validation, Writing–review and editing.

Funding

The author(s) declare financial support was received for the research, authorship, and/or publication of this article. The development of PROSPECT is funded by the European Space Agency ESA.

Acknowledgments

The authors would like to acknowledge significant project contributions from the following entities and individuals: European Space Agency—S. Boazman (landing site analysis), J. Carpenter (phase A/B studies), C. Delepaut and T. Szewcyzc (electronics), E. Koekkoek (structures), K. Lundmark and G. Corocher (EEE components and electronics assembly), P. Hager (thermal design), M. Poizat (radiation environment), C. Paul and L. Gaillard (mechanisms), R. Kroll (harness), C. Mooney (cleanliness and contamination), E. Sefton-Nash (science), J. F. Salgado, H. Stier and F. Frost (software), L. Santos (FPGAs), J. Wolf (EMC), and other ESA TEC support team members; Leonardo S.p.A.—A. Ampolo Rella and P. Bologna (software), M. Fani (thermo-mechanical analysis), S. Feraboli (structural analysis), A. Scudiero (electronics system engineering), S. Campadelli (electronics), M. Peruzzotti (thermo-mechanical design), G. Scarcia (system engineering), E. Tella (thermo-mechanical design), G. Zocchi (thermo-mechanical engineering), A. Zamboni (phase A/B project management); Kayser Italia—R. Nartallo (system engineering), H. Nasimi (electronics), S. Pellari (structures), M. Verna (product assurance); The Open University external experts—D. Yau (mechanical design), J. Sykes (MSS design), J. J. Cooper (ovens and specialist manufacturing); Max Planck Institute for Solar System Research - R. Gerhardy, F. Goesmann, S. J. Knierim, O. Roders, J. Zelmer (all TS design and development); Airbus Defense and Space–A. Briggs (system engineering), A. Kiley (thermal design), S. Morgan (thermal design); DIAL–Anthony Evagora (SamCam engineering); RAL Space/STFC—E. M. Butroid (electronics), S. Hall, A. Hellstenius, C. Kellett and J. Mayers (software), T. Morse (electronics and systems engineering), S. Woodward (FPGA design); TUM—L. Grill (volatile preservation and extraction);

Beyond Gravity—A. Schiaffini (project management), F. Urbinati (system engineering); Maxon–N. Steinert (project management); Sener—J. C. Bahillo (system engineering), F. del Campo (project management). Furthermore, the authors would like to thank the members of the PROSPECT science team and all those individuals not listed individually but who have supported the project in technical, administrative, managerial, and other domains.

Conflict of interest

Authors AMa and PP were employed by Kayser Italia S.r.L. Authors GM, CP, and AR were employed by Leonardo S.p.A. Author NM was employed by Dynamic Imaging Analytics Ltd.

The remaining authors declare that the research was conducted in the absence of any commercial or financial relationships that could be construed as a potential conflict of interest.

Publisher's note

All claims expressed in this article are solely those of the authors and do not necessarily represent those of their affiliated organizations, or those of the publisher, the editors and the reviewers. Any product that may be evaluated in this article, or claim that may be made by its manufacturer, is not guaranteed or endorsed by the publisher.

References

Barber, S. J., Wright, I. P., Abernethy, F., Anand, M., Dewar, K. R., Hodges, M., et al. (2018). "ProSPA: analysis of lunar polar volatiles and ISRU demonstration on the moon," in Lunar and Planetary Science Conference, Abs. 2172, The Woodlands, TX 77380, United States, March, 2018.

Colaprete, A., Schultz, P., Heldmann, J., Wooden, D., Shirley, M., Ennico, K., et al. (2010). Detection of water in the LCROSS ejecta plume. *Science* 330 (6003), 463–468. doi:10.1126/science.1186986

King, O., Warren, T., Bowles, N., Sefton-Nash, E., Fisackerly, R., and Trautner, R. (2020). The Oxford 3D thermophysical model with application to PROSPECT/Luna 27 study landing sites. *Science* 182, 104790. 104790. doi:10.1016/j.pss.2019.104790

Mortimer, J., Lécuyer, C., Fourel, F., and Carpenter, J. (2018). D/H fractionation during sublimation of water ice at low temperatures into a vacuum. *Planet. Space Sci.* 158, 25–33. ISSN 0032-0633. doi:10.1016/j.pss.2018.05.010

Murray, N. J., Evagora, A. M., Murray, S. Y., Barber, S. J., Mortimer, J. I., and Martin, D. J. P. (2020). "SamCam for the ESA PROSPECT lunar volatiles prospecting package; and a new family of miniature 3D multispectral cameras for space exploration," in Lunar and Planetary Science Conference, Abs. 1918, The Woodlands, TX 77380, United States, March, 2020.

Paige, D., Siegler, M. A., Zhang, J. A., Hayne, P. O., Foote, E. J., Bennett, K. A., et al. (2010). Diviner lunar radiometer observations of cold traps in the moon's south polar region. *Science* 330 (6003), 479–482. doi:10.1126/science.1187726

Pieters, C., Goswami, J. N., Clark, R. N., Annadurai, M., Boardman, J., Buratti, B., et al. (2009). Character and spatial distribution of OH/H_2O on the surface of the moon seen by M^3 on chandrayaan-1. *Science* 326 (5952), 568–572. doi:10.1126/science.1178658

Sargeant, H. M., Abernethy, F., Barber, S., Wright, I., Anand, M., Sheridan, S., et al. (2020). Hydrogen reduction of ilmenite: towards an *in situ* resource utilization demonstration on the surface of the moon. *Planet. Space Sci.* 180, 104751. doi:10.1016/j.pss.2019.104751

Trautner, R., Barber, S. J., Carpenter, J., Fisackerly, R., Houdou, B., Leese, M., et al. (2018). "Prospect: a novel package for subsurface sample acquisition and analysis of lunar volatiles," in Proceedings of the International Astronautical Congress, IAC-18, Bremen, Germany, October, 2018.

Trautner, R., Barber, S., Leese, M., Howe, C., Morse, T., Cohen, B. A., et al. (2021b). "EMS: fast track development of a miniaturized mass spectrometer for lunar applications," in Proceedings of the International Astronautical Congress, IAC-21,A3,2A,x62020, Dubai, United Arab Emirates, October, 2021.

Trautner, R., Reiss, P., and Kargl, G. (2021a). A drill-integrated miniaturized device for detecting ice in lunar regolith: the PROSPECT permittivity sensor. *Meas. Sci. Technol.* 32, 125117. doi:10.1088/1361-6501/ac261a

Vago, J., Westall, F., Pasteur Instrument Teams, Landing S, Coates, A. J., Jaumann, R., Korablev, O., et al. (2017). Habitability on early mars and the search for biosignatures with the ExoMars rover. *Astrobiology* 17, 471–510. doi:10.1089/ast.2016.1533

frontiers | Frontiers in Space Technologies

TYPE Original Research
PUBLISHED 12 April 2024
DOI 10.3389/frspt.2024.1366591

OPEN ACCESS

EDITED BY
Antonio Mattia Grande,
Polytechnic University of Milan, Italy

REVIEWED BY
Philipp Zanon,
Swinburne University of Technology, Australia
Aaron Noell,
NASA Jet Propulsion Laboratory (JPL), United States
Akos Kereszturi,
Hungarian Academy of Sciences (MTA), Hungary

*CORRESPONDENCE
Rieke Freer,
freerrieke@gmail.com

RECEIVED 06 January 2024
ACCEPTED 22 March 2024
PUBLISHED 12 April 2024

CITATION
Freer R, Pesch V and Zabel P (2024), Experimental study to characterize water contaminated by lunar dust.
Front. Space Technol. 5:1366591.
doi: 10.3389/frspt.2024.1366591

Experimental study to characterize water contaminated by lunar dust

Rieke Freer*, Victoria Pesch and Paul Zabel

Synergetic Material Utilization, Department of System Analysis Space Segment, Institute of Space Systems, German Aerospace Center, Bremen, Germany

The establishment of a permanent lunar base is the goal of several space missions, such as NASA's Artemis program. The feasibility of a lunar base is highly dependent on the supply of clean water, which can be recycled within the life support system or extracted in-situ on the Moon. Contamination of the water by lunar dust is an unavoidable problem due to the fact that lunar dust covers the entire surface and has adhesive properties as well as a very fine particle size. It is therefore important to study and characterise water contaminated by lunar dust in order to develop a safe water supply system. We combined existing studies on the dissolution behaviour of lunar regolith in aqueous solutions and performed dissolution experiments ourselves. We conducted dissolution experiments using the Lunar Highland Dust simulant from Exolith Lab (Orlando, United States), which resembles the Apollo 16 regolith and thus the terrain of the suspected Artemis landing sites. Our dissolution experiments investigate the effects of the dust to solution ratio, the aqueous solution used (ultrapure water and 5.5 buffer), the short exposure time (2 min up to 72 h), the dissolved oxygen in the solutions and the particle size of the simulant. As a result, this study provides a characterisation of lunar dust contaminated water and compares the results with the World Health Organization (WHO) and NASA requirements for drinking water. For all test batches, the lunar dust contaminated water exceeds the requirements for pH, turbidity and Al concentration.

KEYWORDS

lunar dust, lunar dust solubility, lunar dust dissolution experiments, lunar raw water, ISRU water treatment

1 Introduction

In future lunar habitats, the contact between lunar dust and water in its liquid form will be unavoidable, as described in the In-Situ Resource Utilization (ISRU) Gap Assessment Report (ISRU Gap Assessment Team, 2021) and the Dust Mitigation Gap Assessment Report (Dust Mitigation Gap Assessment Team, 2016). On the one hand, lunar dust with its adhesive properties and very fine particle sizes [about 20 wt% of the bulk regolith is < 20 µm (Liu and Taylor, 2008)] covers the entire surface of the Moon (Crotts, 2011). On the other hand, water is the most important resource for astronauts as well as for propellant production. Water can be brought from Earth or extracted in-situ, as water deposits on the Moon have been identified by space exploration missions such as Chandrayaan-1, Lunar Crater Observation and Sensing Satellite (LCROSS) and Lunar Reconnaissance Orbiter. Possible contamination pathways described in the In-Situ Resource Utilization (ISRU) Gap Assessment Report (ISRU Gap Assessment Team, 2021) and the Dust Mitigation Gap Assessment Report (Dust Mitigation Gap Assessment Team, 2016) include lunar dust

entering in-situ extracted water hardware operating on the dusty lunar surface, as the dust could reduce the effectiveness of seals. This can also be applied to all other water-bearing systems. Another way in which dust can enter water systems is during the cleaning process of dust-contaminated spacesuits. The problems caused by lunar dust in future lunar habitats are also described in the Gap Assessment Reports. For example, lunar dust can clog instruments, pipes and valves in the water recovery subsystem and have a negative impact on active chemical and biological water recovery components. If water is contaminated by lunar dust it cannot be used as feed water for proton exchange membrane (PEM) electrolysers to produce oxygen and hydrogen, as deionised water is required. Dissolved ions from lunar dust are not only a problem for hardware, but also for drinking water, which must meet high quality standards to avoid adverse effects on human health. For these reasons, it is important to study and characterise water contaminated by lunar dust to enable a safe water supply system within a lunar base.

Keller and Huang (1971) studied the ion release of an Apollo 12 (mare area) sample into deionised water, carbon dioxide CO_2-charged water, 0.01 M acetic acid and 0.01 M salicylic acid. These different solutions were used to determine the reaction of lunar material with solutions related to weathering processes on Earth. In parallel, experiments were carried out with powdered basalt and tektite (of approximately the same grain size as the Apollo 12 sample) to compare the results with the Apollo 12 dissolution experiments. The pH, as well as Si, Al, Fe, Mg, Ca, Na, K, Mn, Ti, Cr, Zn, Cu, Sr, and Ba, were analysed over a period of up to 81 days. Rapid ion release was observed within the first 3 days, and after 81 days the dissolution of the Apollo samples, basalt and tektite all approached equilibrium (except for tektite in CO_2-charged water, acetic and salicylic acid, and Si from basalt dissolving in acetic acid). All dissolution experiments show a parabolic curve for dissolved ions over time. The ion release from the lunar dust was much higher in organic acids than in deionised water, with the following order of major dissolved elements Si > Al > Mg > Fe > Ca > Na > K. In this study, the dissolution behaviour is depending on the aqueous solutions and solid material composition.

Eick et al. (1996a) investigated the effects of pH (3, 5, and 7) and citric and oxalic acids on the dissolution kinetics of a synthetic lunar basaltic glass. In addition, Eick et al. (1996b) conducted similar dissolution experiments by using a lunar Mare simulant MLS-1 (Minnesota Lunar Simulant, similar to Apollo 11 Mare soil) and demonstrated the influence of the mineral composition on the ion release. The dissolution of Si, Al, Fe, Mn, Ca, Mg, Ti, and Cr ions was studied over a period of up to 365 days for the glass simulant and 172 days for MLS-1. Both the glass simulant and MLS-1 showed an increase in ion release with decreasing pH. The order of ions released from the glass simulant at pH 3 and 5 was Al > Ca > Mg > Fe. At pH 7 the release of Ca and Mg was similar and Al and Fe were below the detection limit of the Inductively Coupled Plasma (ICP) emission spectrometry. Dissolution of MLS-1 resulted in a released ion order of Fe ≈ Mg > Si > Al > Ca. Comparing the results of the citrate and oxalate acids, ion release is higher in the citrate solution and increases with increasing organic acid concentration for both simulants used.

Cooper et al. (2011) tested the effect of fluid on lunar regolith by conducting experiments using Apollo 14 (highland area) samples and water, isopropanol and pH 4 buffer. The mixtures were analysed for dissolved Si, Ca, Al, Mg, Fe, S, Ti and it was found that of all the ions analysed, Ca was released the most in all solutions. The dissolution experiments showed that the major elements of plagioclase particles were the most affected by dissolution in water, and only negligibly dissolved by isopropanol. In water, the order of elements released from the Apollo 14 sample is Ca > Mg > Si > S > Fe > Al > Ti.

TABLE 1 Chemical composition of LHS-1D and LHS-1 simulant.

Oxide	wt%
SiO_2	48.1
Al_3O_3	25.8
CaO	18.4
Fe_2O_3	3.7
TiO_2	1.1
P_2O_5	1.0
K_2O	0.7
Cl	0.4
MgO	0.3
SO_3	0.3
MnO	0.1
SrO	0.1

The experiments described show that ion release depends on the simulant/Apollo sample composition and on the aqueous solutions. On the one hand, the order of ion release in the studies was dominated by the bulk composition of the samples, i.e., the solubility of the mineral components, and on the other hand, the concentration of the released ions was influenced by the aqueous solutions used (e.g., pH, organic acids). The complexity of the dissolution processes does not allow a general statement about the ion concentration present in regolith-contaminated water. For this reason, we conducted dissolution experiments with the Lunar Highland Dust simulant from Exolith Lab (Orlando, United States), which is similar to the Apollo 16 regolith. The Apollo 16 terrain is described as similar to that considered for the Artemis landing sites, a feldspathic highland terrain, and thus a possible region for future lunar habitats (Kumari et al., 2022). For the treatment of water contaminated with lunar dust in lunar habitats, even short contact times are relevant. Our experiments therefore focused on short contamination times ranging from 2 min to 72 h. For the aqueous solution, we used ultrapure water, because in ultrapure water the influence of other ions present in the solution can be excluded, and a buffer solution of pH 5.5 to compare experiments without considering the effect of pH. We also investigated the effect of dissolved oxygen in the solution, which is unavoidable in terrestrial conditions. Therefore, experiments were run in a nitrogen glove box with O_2 outgassed solutions. As contamination by very fine particles is expected, the effect of the particle size of the simulant used was also investigated. In summary, we investigate the effect of exposure time, the aqueous solution used (ultrapure water vs. buffer solution), the simulant to solution ratio, dissolved oxygen in the solutions, and the particle size of the lunar

TABLE 2 Mineral composition of LHS-1D and LHS-1 simulant.

Component	wt%
Anorthosite	74.4
Glass-rich basalt	24.7
Ilmenite	0.4
Olivine	0.3
Pyroxene	0.2

simulant on the dissolution behaviour. Additionally, this work combines the results of existing studies on the dissolution behaviour of lunar regolith in aqueous solutions with our own dissolution experiments. We compare our results with those of Cooper et al. (2011) using a real Apollo lunar highland sample. The study concludes with a characterisation of lunar dust-contaminated water in terms of possible water purification steps.

2 Material and methods

2.1 Solid materials

In this study we used the Lunar Highland Dust Simulant (LHS-1D) and the Lunar Highlands Simulant (LHS-1) from Exolith Lab (Orlando, United States) because of their similarity to the main chemical components of the average Apollo 16 regolith (Stockstill-Cahill et al., 2021). Tables 1, 2 show the composition of the LHS-1D and LHS-1 simulants. They have the same chemical and mineral composition as reported in the January 2021 Exolith Lab datasheets.

The LHS-1D simulant has a mean particle size of 7 µm with a range of < 0.04 µm–35 µm. The LHS-1 simulant has larger particles with a mean particle size of 60 µm and a range of < 0.04 µm–400 µm.

2.2 Aqueous solutions

The experiments were conducted with two different aqueous solutions, ultrapure water and a buffer solution. We used ultrapure water with a resistivity of 18 MΩcm (ROTISOLV HPLC Gradient Grade). The initial pH of the ultrapure water after contact with the laboratory atmosphere was 5.5–5.7 due to the dissolved CO_2 from the air, which forms carbonic acid. The buffer solution with a pH of 5.5 ± 0.1 was prepared by separately dissolving 2.86 µL of acetic acid ($C_2H_4O_2$, 100% Suprapur, Millipore) and 26.978 g of ammonium acetate (NH_4CH_3COO, reagent-grade, Honeywell) in 1 L of ultrapure water and finally mixed to produce 2 L of pH 5.5 ± 0.1 buffer solution.

2.3 Experimental procedure

First, 250 mL of the aqueous solution were filled into high-density Polyethylene (HDPE) wide-mouth bottles. The regolith simulant was then weighed, added to the aqueous solution and placed directly on an overhead shaker. Simultaneously, the time measurement and the overhead shaker were started, by mixing at 20 RPM. After specific times, 2 min, 15 min, 30 min, 1 h, 12 h, 24 h, and 72 h, the over-head shaker was stopped and approximately 10 mL sample was taken with a graduated pipette and centrifuged at 6000 RPM for 10 min. A sub-sample was taken for pH measurements before the sample was filtered with a polytetrafluorethylene 0.45 µm syringe filter to prepare for the elemental concentration analysis. In a final step, the elemental concentrations of the following nine elements were measured by inductively coupled plasma optical emission spectrometry: Al, Ca, Fe, K, Mg, Mn, S, Si, and Ti. Table 3 summarises the different parameters of the test batches. In addition to the use of two different simulants and aqueous solutions, two ratios of simulant dry weight in grams to solution volume in millilitres were tested (1:100 and 1:500). All test batches with LHS-1D were conducted firstly under 20°C and Earth atmosphere and secondly in a nitrogen glove box with oxygen degassed solutions to mimic the lack of an oxygen-containing atmosphere on the Moon. For quality assurance, all test batches were run in duplicate and a blank of each solution was analysed. The experimental procedure is based on the guidelines of Kerschmann et al. (2020) and Stewart et al. (2013).

2.4 ICP-OES and ICP-MS analysis

The elemental concentrations of the following elements were determined by inductively coupled plasma optical emission spectrometer (ICP-OES, Perkin Elmer, Optima 8300 DV): Al (analytical wavelength: 396.153 nm), Ca (317.933 nm), Fe (238.204 nm), K (766.490 nm), Mg (285.213 nm), Mn (257.610 nm), S (181.975 nm), Si (251.611 nm), and Ti (334.940 nm). Each sample was measured three times to check the reproducibility of the analysis. The ion concentrations of Fe, Mn, and Ti of test batches 2.1, 2.2, 3.1, 3.2, 4.1, and 4.2 were also determined using inductively coupled plasma mass spectrometry (ICP-MS, Perkin Elmer, NexION 300 D) due to its low concentration. For both techniques, concentrations were determined via external calibration against standards with known concentrations and checked for accuracy by quality control standards with known certified concentrations. The ICP-OES and ICP-MS analysis were performed by the Central Laboratory TUHH, Hamburg, Germany. Test batches 1.1 and 1.2 were measured by ICP-OES in the laboratory of the Geochemistry and Hydrogeology Group, Faculty of Geosciences, University of Bremen.

2.5 Turbidity measurements

Turbidity, a measure of relative liquid clarity, of test batches 1.1, 1.2, 5.1, and 5.2 was measured after 72 h mixing time using a TB 211IR turbidimeter (Tintometer). The turbidimeter measures the extent to which light is either absorbed or scattered by suspended particles in the solution. For each turbidity measurement 11 mL was taken directly from the 250 mL wide-mouth bottles. If the turbidity was above the measuring range, a 1:11 dilution was made. The measuring range of the turbidimeter is 0.01–1100 NTU.

10.3389/frspt.2024.1366591

TABLE 3 Test batch parameters of lunar regolith dissolution experiments.

Test batch	Simulant	Ratio/g mL^{-1}	Aqueous solution	Initial pH	Initial dissoveld oxygen
1.1	LHS-1D	1:100	ultrapure H_2O	5.5	8 mg L^{-1}
1.2	LHS-1D	1:500	ultrapure H_2O	5.6	8 mg L^{-1}
2.1	LHS-1D	1:100	buffer solution	5.5	8 mg L^{-1}
2.2	LHS-1D	1:500	buffer solution	5.5	8 mg L^{-1}
3.1	LHS-1D	1:100	ultrapure H_2O	4.5	< 1 mg L^{-1}
3.2	LHS-1D	1:500	ultrapure H_2O	4.4	< 1 mg L^{-1}
4.1	LHS-1D	1:100	buffer solution	5.4	< 1 mg L^{-1}
4.2	LHS-1D	1:500	buffer solution	5.4	< 1 mg L^{-1}
5.1	LHS-1	1:100	buffer solution	5.6	8 mg L^{-1}
5.2	LHS-1	1:500	buffer solution	5.6	8 mg L^{-1}

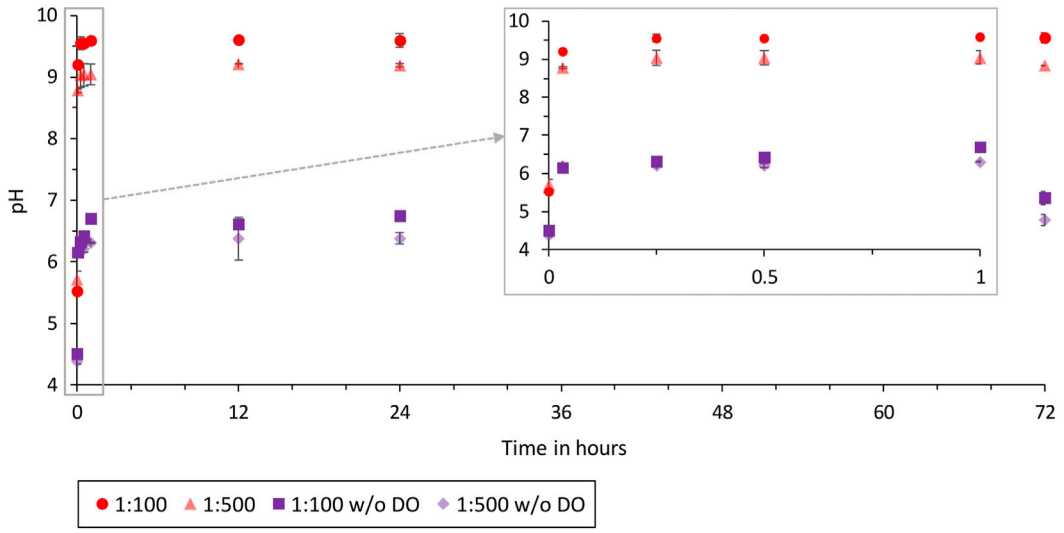

FIGURE 1
pH over time for the ratios 1:500 and 1:100 LHS-1D in ultrapure water with and without dissolved oxygen (test batches 1.1, 1.2, 3.1, and 3.2).

3 Results

3.1 Ion concentration

The measured ion concentrations in mg L^{-1} and the pH for each test batch are given in tabular and graphical form in the Supplementary Material.

All experiments dissolving the LHS-1D simulant showed a parabolic release of Si, Al, Ca, Mg, and K within 12 h. After 12 h, the release of ions decreased and approach constant values. Using a buffer solution, the release of Fe and Mn also showed a parabolic behaviour within 12 h. For all test batches, no statement can be made about the release of Ti ions, as more than 50% of the samples are below the detection limit of 10 µg L^{-1}. The same applies to the dissolved Fe ions in ultrapure water with a detection limit of 20 µg L^{-1}. The results of the experiments performed in the nitrogen glove box and in ultrapure water differ from those performed under terrestrial atmosphere. No Al was detected in test batches 3.1 and 3.2, because the samples were not acidified and stored for more than 4 weeks before being analysed by ICP-OES, causing Al to precipitate in the solution. In addition, the parabolic release described above was also observed for Mn in test batches 3.1 and 3.2, which was additionally analysed by ICP-MS, which has a lower detection limit. In the case of a measurable release of S (test batches 1.1, 3.1, and 4.1), the values remained approximately constant.

For the dissolution of LHS-1D in buffer solution, the order of ions in the solution is Ca > Si > Al > K > Mg > Fe > Mn. The order in ultrapure water is similar, but with a change in the order of Al and Si (test batch 1.1) and of K and Mg (test batch 3.1).

Using the LHS-1 simulant, the released Ca ions showed a parabolic behaviour within 12 h and then a constant value. In

TABLE 4 Turbidity of LHS-1D and LHS-1 in ultrapure water.

Test batch	Simulant	Ratio/ g mL^{-1}	Turbidity in NTU
1.1	LHS-1D	1:100	9,862
1.2	LHS-1D	1:500	1,070
5.1	LHS-1	1:100	1,015
5.2	LHS-1	1:500	240

test batch 5.1 the released Al ions also showed a parabolic behaviour, but over 72 h without reaching a constant value. The order of ion concentrations in the solution is Ca > Al. No statement can be made about the Si, Fe, Ti, Mg, S, Mn, K, and Al (test batch 5.2) ions released because the ICP-OES detection limits were not reached.

3.2 pH of solution

The rapid release of ions during the first 2 minutes to 1 hour is also shown by the increase in the pH of the solution (Figure 1). The comparison of the pH values of the two different ratios shows that the pH value of the 1:100 ratio is on average 0.5 higher than the pH value of the 1:500 ratio, due to the higher ion concentration at a ratio of 1:100. The initial pH of the O_2 degassed ultrapure water is 4.4 and 4.5, rising to 6.2 after 2 min. The pH after 72 h is 7.0 (1:100) and 6.7 (1:500).

3.3 Turbidity of the solution

The turbidity caused by LHS-1D (test batch 1.1 and 1.2) is higher than by LHS-1 (test batch 5.1 and 5.2) in ultrapure water. The ratio, 1:100 results in a higher turbidity than 1:500. The turbidity in NTU of LHS-1D and LHS-1 are given in Table 4.

Photographs of the turbidity samples in the cuvettes of the turbidimeter are shown in Figure 2. The samples are arranged from left to right in order of decreasing turbidity.

4 Discussion

4.1 Interpretation of results

The detected ion concentrations in milligrams per litre (mg L^{-1}) were converted to the release of ions from the simulant into the solution per gram of solid material/simulant (mg g$^{-1}_{solid}$). This conversion allows the comparison of test batches with different simulant to solution ratios. The elements for which 50% of the measured concentrations are below the detection limit are not included in the graphs. For clarity, the ion release of the elements is split into two plots so that the points of released ions do not overlap and a zoom to the first hour is also provided within the graphs.

4.1.1 Comparison of 1:100 and 1:500 simulant weight to solution volume ratios

The following plots (Figures 3, 4), compare the 1:500 and 1:100 ion release from the LHS-1D simulant into ultrapure water and buffer solution.

For all elements detected, the release of ions into ultrapure water (Figure 3) was higher at the 1:500 ratio. As no statement can be made about the release of S for the 1:500 ratio, a comparison of the two ratios is not possible.

The release of ions in the buffer solution (Figure 4) of the two ratios can be considered equal, except for the elements Al and Si. The experiment with the 1:500 ratio shows after 72 h a release of Al and Si ions of 0.7 mg g$^{-1}_{solid}$ higher than for the 1:100 ratio.

In all four test batches, the most released ions from the simulant are Ca, Al, and Si. These are also the elements that are present in anorthosite and glass-rich basalt, the main components of the simulant. Also the experiments of Cooper et al. (2011), using a sample from Apollo 14, showed that the ion that is released the most from the sample is Ca. A noticeable difference between the ratios can only be observed in ultrapure water. The more solution is used per simulant, the more ions are dissolved per gram of simulant. These can be attributed to saturation effects of the solution inhibiting dissolution reactions on the grains. When the pH is kept constant by using a buffer solution, this difference is not observed (except

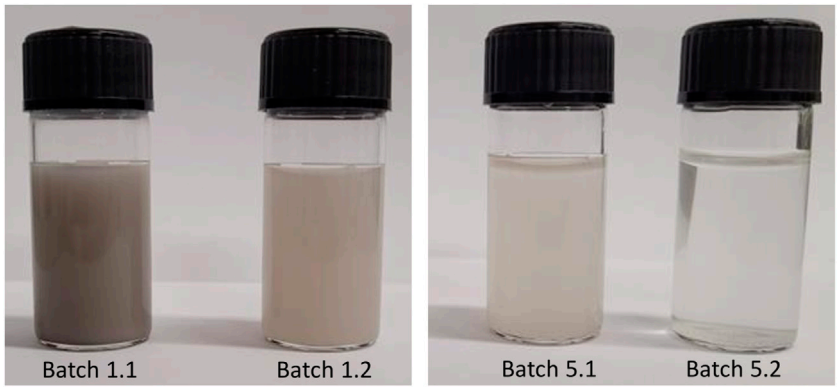

FIGURE 2
Turbidity samples, from left to right: LHS-1D 1:100, LHS-1D 1:500, LHS-1 1:100, and LHS-1 1:500.

10.3389/frspt.2024.1366591

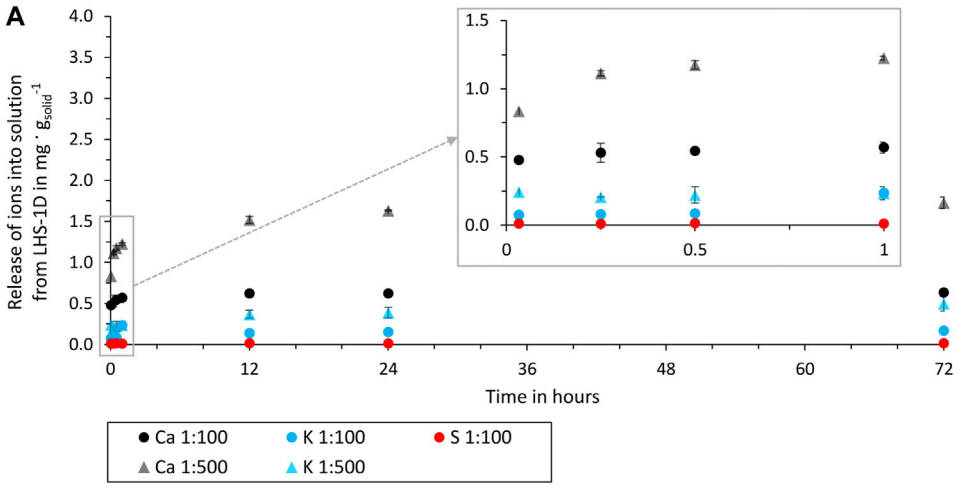

Ca, K, and S ion release from LHS-1D into ultrapure water over time for 1:500 and 1:100 ratios.

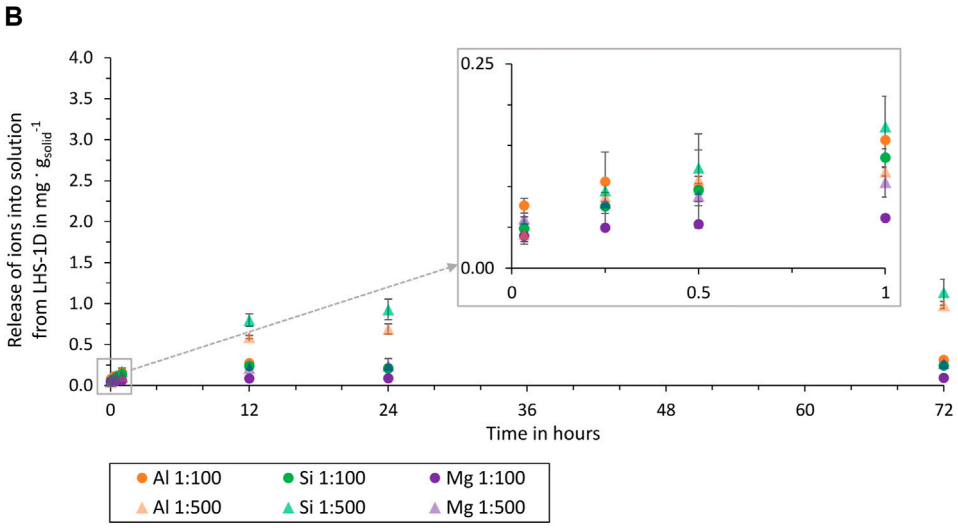

Al, Si, and Mg ion release from LHS-1D into ultrapure water over time for 1:500 and 1:100 ratios.

FIGURE 3
Release of ions from LHS-1D into ultrapure water over time for 1:500 and 1:100 ratios (test batch 1.1 and 1.2). **(A)** Release of Ca, K, and S ions. **(B)** Release of Al, Si, and Mg ions.

for Al and Si). This suggests that the release of Al and Si ions is more dependent on the other ions already dissolved in the solution. The experiments in buffer solution show that in an acidic solution (pH = 5.5) the ion release of the individual elements is higher than in the ultrapure water, which is also the result of Eick et al. (1996a,b) and Cooper et al. (2011). The order of the dissolved elements is not changed by the use of the buffer solution, but Fe and Mn ions are dissolved, which could not be detected in ultrapure water.

4.1.2 Effect of dissolved oxygen

Only the comparison between the O_2 degassed and non-degassed buffer solution is shown in Figures 5, 6, as the use of the buffer solution negates the effect of the different initial pH of the solutions. Figure 1 shows the different initial and final pH values of O_2 degassed and non-degassed ultrapure water. The solutions have been degassed with CO_2 and therefore more carbonic acid is formed in the degassed solution, reducing the pH.

The comparison between the test batches shows that a O_2 degassed buffer solution effects the release of Ca and Fe ions. After 72 h the released Ca ions into the degassed buffer solution are 0.14 mg g$^{-1}_{solid}$ (1:100) and 0.23 mg g$^{-1}_{solid}$ (1:500) higher than into a non-degassed buffer solution and the released Fe ions are 0.11 mg g$^{-1}_{solid}$ (1:100) and 0.37 mg g$^{-1}_{solid}$ (1:500) higher. The differences between the other ions released are negligible, as can be seen in Figures 5A, B. At this stage, these observations cannot be attributed to a specific dissolution mechanism, as no other studies are available. Due to the higher release of Fe and Ca

10.3389/frspt.2024.1366591

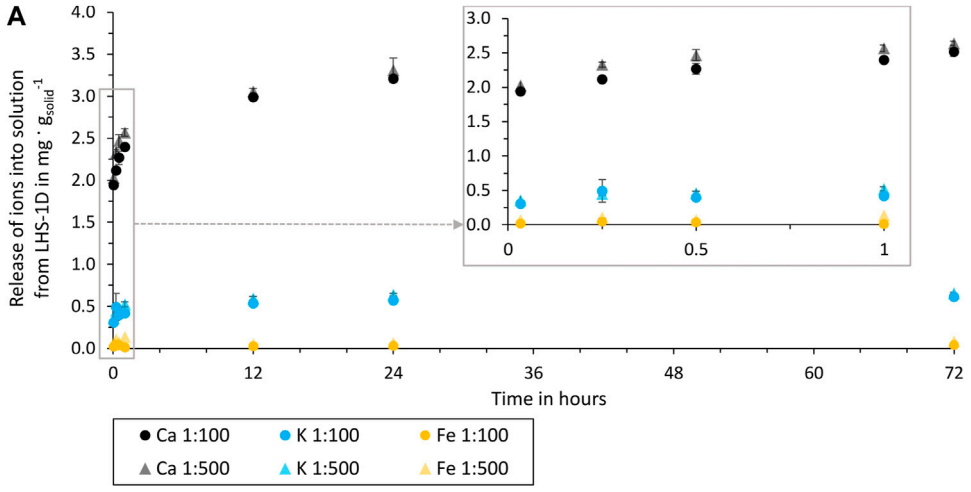

Ca, K and Fe ion release from LHS-1D into buffer solution over time for 1:500 and 1:100 ratios.

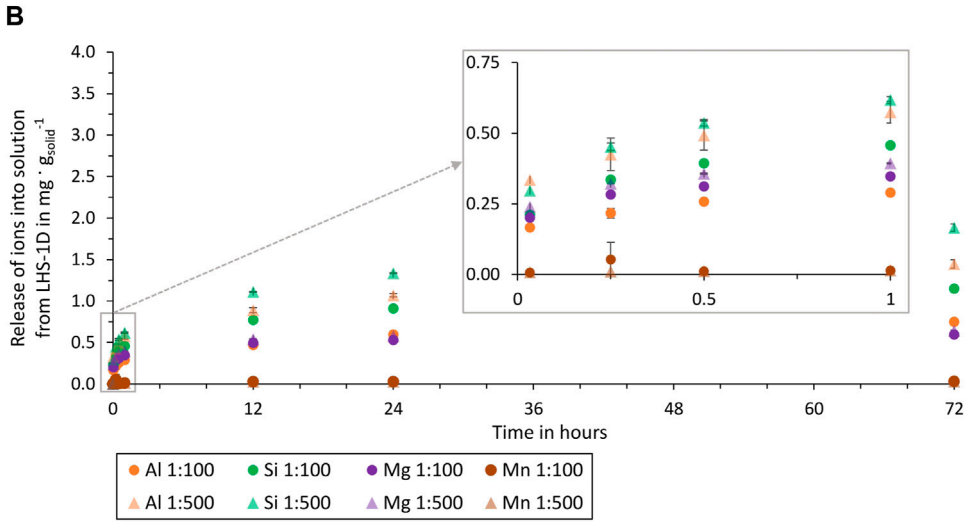

Al, Si, Mg, and Mn ion release from LHS-1D into buffer solution over time for 1:500 and 1:100 ratios.

FIGURE 4
Release of ions from LHS-1D into buffer solution over time for 1:500 and 1:100 ratios (test batch 2.1 and 2.2). **(A)** Release of Ca, K and Fe ions. **(B)** Release of Al, Si, Mg, and Mn ions.

in O_2 degassed water, these concentrations must be critically questioned in experiments conducted under terrestrial conditions. Especially, if the results are used for water purification tests within the ISRU process chain. In-situ extracted water will not contain dissolved oxygen as in the Earth's atmosphere. For life support systems, these results can be neglected if the water treatment will take place in an oxygenated lunar habitat atmosphere.

4.1.3 Effect of particle size

Figure 7 compares the release of ions from the LHS-1D and the LHS-1 simulant into the buffer solution. For comparison the results of the 1:100 ratio and buffer solution is used, as for this ratio the most elements where detectable and the effect of a changing pH can be neglected.

LHS-1 and LHS-1D have the same bulk composition but a different mean particle size. By comparing ion release in buffer solution and the same ratio, the only changing parameter is the particle size. Using LHS-1 in buffer solution results in no dissolved Fe, K, Mg, Mn, S, Si, and Ti ions, while using LHS-1D these elements are present in the buffer solution from the first extraction time. Figure 7 shows that the use of LHS-1D results in a higher release of Ca and Al ions with an increasing difference over time. The percentage difference after 72 h of LHS-1D and LHS-1 Ca release is 79% and Al release is 193%. This proves that particle size and ion release are related. As smaller particle sizes expose more surface area to the aqueous solution, more ions are released from the lunar regolith particles into the aqueous solution over time.

10.3389/frspt.2024.1366591

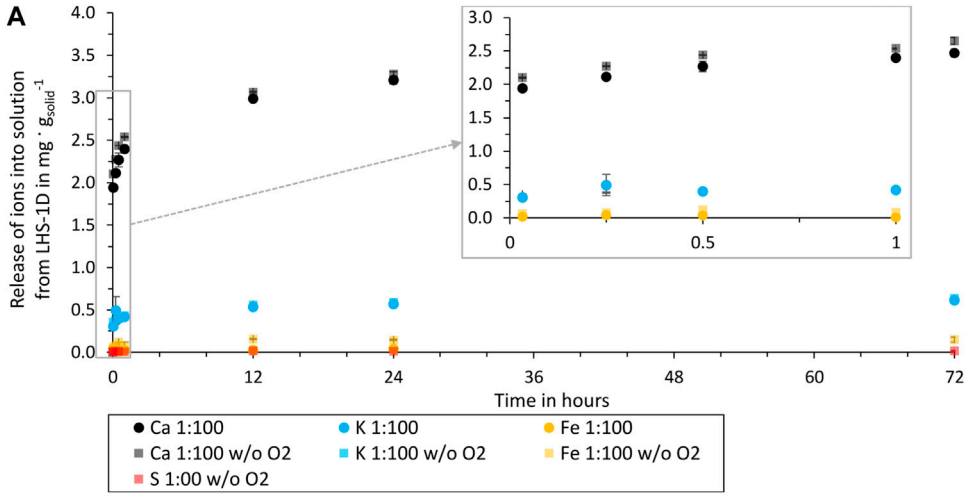

Ca, K, Fe, and S ion release from LHS-1D into O_2 degassed and non-degassed buffer solution over time for 1:100 ratio.

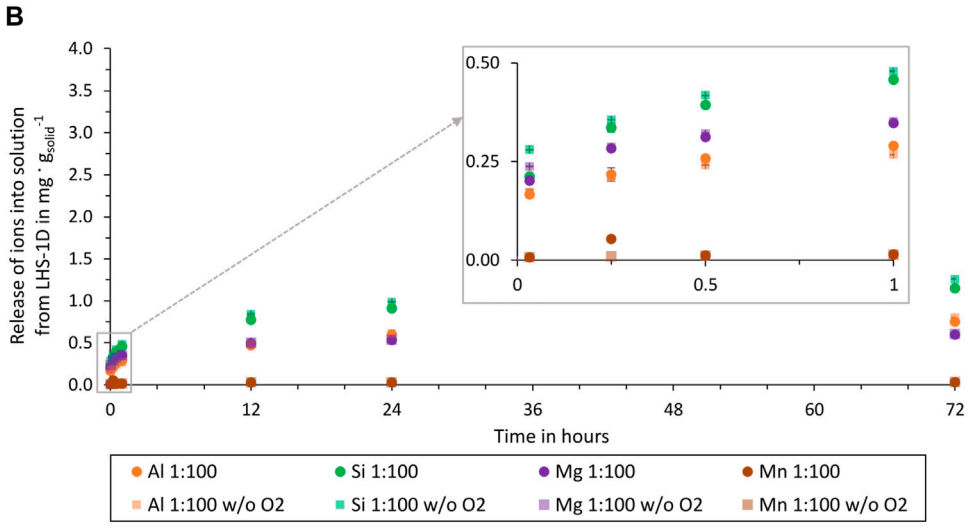

Al, Si, Mg, and Mn ion release from LHS-1D into O_2 degassed and non-degassed buffer solution over time for 1:100 ratio.

FIGURE 5
Release of ions from LHS-1D into O_2 degassed and non-degassed buffer solution over time for 1:100 ratio (test batch 2.1 and 4.1). **(A)** Release of Ca, K, Fe, and S ions. **(B)** Release of Al, Si, Mg, and Mn ions.

These results are consistent with the findings of Eick et al. (1996a), where rapid ion release is also explained by the "higher free energy" of fine grains, i.e., a high surface area. All our test batches showed the fastest release of ions within the first hour, which can also be explained by the fact that the fine grains of the simulant dissolve first, before the dissolution decreases, and can be described as more linear, typical of a surface controlled reaction.

4.2 Experiment-based assumptions for water purification

Water in future space habitats is more likely to be contaminated by fine regolith particles than by larger particles. In addition, the comparison between the LHS-1D and LHS-1 simulants showed that more ions are released at finer particle sizes, making the LHS-1D experiments the worst case. For this reason, only the LHS-1D simulant experiments are discussed below. When comparing the ion concentrations in mg L^{-1} after 72 h, test batch 1.2 (1:500, ultrapure water) represents the best case, i.e., low ion concentration in the solution, and test batch 2.2 (1:100, buffer solution) the worst case. These two cases are compared in Table 5 with the limits given in the World Health Organization (WHO) Guideline for Drinking Water Quality (World Health Organization, 2018), the NASA Human Integration Design Handbook (HIDH) (NASA, 2014), and the NASA Advanced Life Support Requirements Document (NASA, 2003).

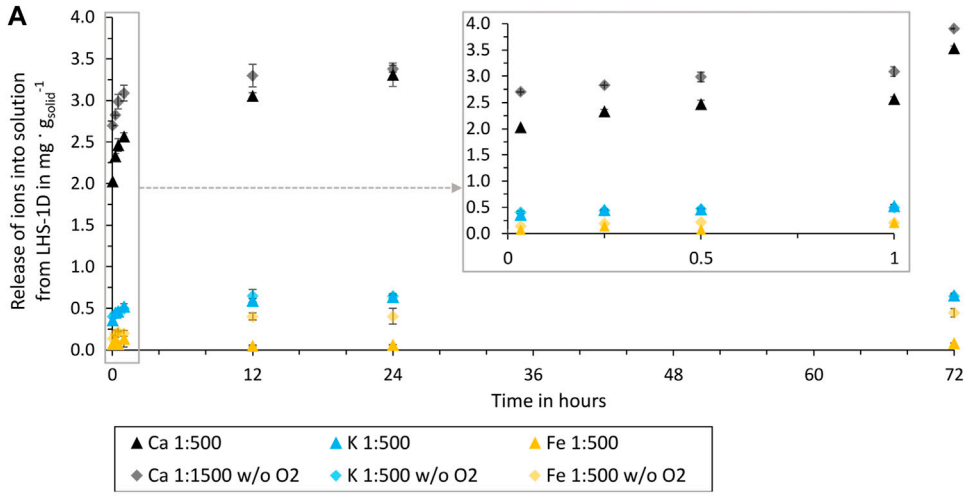

Ca, K, and Fe ion release from LHS-1D into O_2 degassed and non-degassed buffer solution over time for 1:500 ratio.

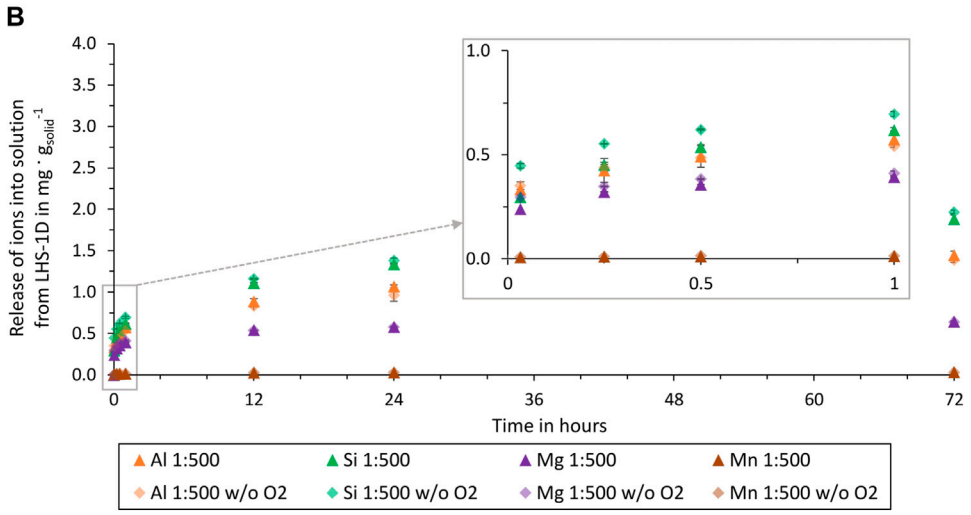

Al, Si, Mg, and Mn ion release from LHS-1D into O_2 degassed and non-degassed buffer solution over time for 1:500 ratio.

FIGURE 6
Release of ions from LHS-1D into O_2 degassed and non-degassed buffer solution over time for 1:500 ratio (test batch 2.2 and 4.2). **(A)** Ca, K, and Fe ion release. **(B)** Al, Si, Mg, and Mn ion release.

Test batch 1.2, the best case, does not meet the requirements for Al concentration, pH, and turbidity. In the worst case batch 2.1, Ca, Fe and Mn are also exceeded. For batch 2.1 it can also be assumed that turbidity will be above 1,000 NTU, even if not measured in buffer solution (cf. batch 1.1 with 9,862 NTU). It is not possible to say whether the limits for sulphur have been exceeded as the total S concentration was measured by ICP-OES and not the specific compounds. Both the best and worst cases exceed WHO and/or NASA requirements and will need to be treated. The first step is to remove the particles to meet the turbidity limits. Possible methods include filtration and sedimentation/flotation. Then, in both cases, the Al concentration needs to be reduced. That the release of Al from lunar regolith into water causes problems, is also shown by Paul et al. (2022). In their experiment, they grew plants in Apollo lunar regolith and showed that the plants expressed genes related to aluminium toxicity. The worst case test batch 2.1 showed that Ca, Fe and Mn also need to be removed. In conclusion, treatment steps are necessary to remove ions, e.g., distillation, reverse osmosis or ion exchange.

Another use of water in a space habitat is to split it into O_2 and H_2 by electrolysis. The feed water for electrolysers is usually Type I or Type II water according to the American Society for Testing and Materials (ASTM) ASTM (2017). The conductivity

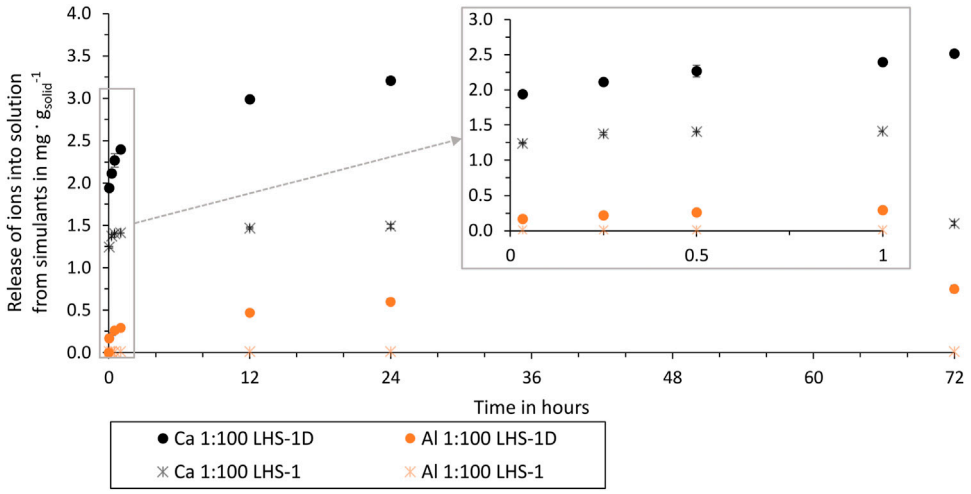

FIGURE 7
Al and Ca release from LHS-1D (mean particle size = 7 µm) and LHS-1 (mean particle size = 60 µm) in ultrapure water over time of test batch 2.1 and 5.1.

TABLE 5 Comparison of released ion concentration, pH, and turbidity with WHO and NASA requirements for potable water.

Component	Concentration in mg L^{-1}			
	Best case	Worst case	World Health Organization (2018)	NASA (2003)[a]
	Test batch 1.2	Test batch 2.1		NASA (2014)[b]
Si	2.28	11.49	-	-
Al	1.96	7.49	0.20	-
Ca	3.46	35.27	150–300	30
Fe	< 0.02	0.40	0.3	0.3
Ti	< 0.005	< 0.005	-	-
Mg	0.54	5.69	-	50
S	< 0.067	0.09	SO_4^{2-}: 250	S^{2-}: 0.05; SO_4^{2-}: 250
Mn	< 0.005	0.30	0.05–0.4	0.3[b]/0.05[a]
K	0.99	6.13	-	340
pH	9.2	5.5	6.6–8.5	4.5–9.0
Turbidity	1070 NTU	-	-	1.5 NTU

of Type I is defined as $< 0.056\ \mu S\ cm^{-1}$ and Type II as $< 1\ \mu S\ cm^{-1}$. This means that almost all ions have to be removed from the water, which is a more complex treatment than meeting WHO and NASA standards.

In summary, the experiments showed that water contaminated with lunar dust contains dissolved ions from the LHS-1D simulant within a few minutes, that the pH of ultrapure water increases immediately, and that turbidity increases up to 1000 NTU. Even at a ratio of 1:500, the limits of WHO and NASA guidelines are exceeded. It is also difficult to predict the concentration of the released ions in the water, as this is highly dependent on the water matrix, the pH, the particle size, and the amount of lunar dust dissolved in the water. Since the simulant used in these experiments resembles the terrain of possible future lunar habitats, the results can be used as a basis for development and testing of water purification processes for ISRU and life support applications, as well as experiments on plant growth and habitat construction.

4.3 Outlook

For a better characterisation of lunar dust contaminated water extracted in-situ on the Moon, the volatiles measured by the LCROSS mission (Colaprete et al., 2010) should be taken into account. Volatiles present in the aqueous solution will alter the pH and therefore the dissolution behaviour of the lunar regolith. In addition to improving the dissolution experiments, the simulant used can also be refined by adding nanophase (3–33 nm) Fe^0 particles. These nanophase Fe^0 are embedded in a thin rim of SiO_2-rich glass (Loftus et al., 2010) and can alter the dissolution behaviour. An indication of this is provided by the study of Wallace et al. (2010), which shows an increasing production of hydroxyl radicals in correlation with the presence of nanophase Fe^0 in the solution. For analysis of the dissolution experiments, the water samples should be tested for a wider range of ions and also for compounds. It is recommended to determine the concentration of S^{2-} compounds, which is specified in the NASA Advanced Life Support Requirements Document as 0.05 mg L^{-1}, and to analyse Cl, SiO_2 and Na, as these are requirements for electrolysis feed water set by ASTM.

Data availability statement

The original contributions presented in the study are included in the article and Supplementary Material, further inquiries can be directed to the corresponding author.

Author contributions

RF: Writing–original draft, Writing–review and editing. VP: Writing–original draft. PZ: Funding acquisition, Supervision, Writing–review and editing.

Funding

The author(s) declare financial support was received for the research, authorship, and/or publication of this article. The laboratory equipment for performing the lunar dust dissolution experiments and all related expenses were funded by the DLR internal funding sources.

Acknowledgments

I am very grateful to Kristina Beblo-Vranesevic from the Institute of Aerospace Medicine, DLR Cologne, for enabling and supporting the nitrogen glove box experiments. I am also thankful for the entire Radiation Biology Department of that institute for providing the nitrogen glove box with all the necessary equipment and for their expertise. Many thanks to Bo-Magnus Elfers of the TUHH Central Laboratory, Hamburg for the inspiring discussions on the interpretation of the results and the best choice of analytical methods. I also thank the laboratory of the Geochemistry and Hydrogeology Group, Faculty of Geosciences, University Bremen for their support at the beginning of the experiments and for providing detailed insights into the ICP-OES measurement method.

Conflict of interest

The authors declare that the research was conducted in the absence of any commercial or financial relationships that could be construed as a potential conflict of interest.

Publisher's note

Supplementary material

The Supplementary Material for this article can be found online at: https://www.frontiersin.org/articles/10.3389/frspt.2024.1366591/full#supplementary-material

References

ASTM (2017). *Standard specification for reagent water*, 11. American Society for Testing and Materials, 01. doi:10.1520/D1193-99E01

Colaprete, A., Schultz, P., Heldmann, J., Wooden, D., Shirley, M., Ennico, K., et al. (2010). Detection of water in the LCROSS ejecta plume. *Science* 330, 463–468. doi:10.1126/science.1186986

Cooper, B., McKay, D., Wallace, W., and Gonzalez, C. (2011). Fluids and their effect on measurements of lunar soil particle size distribution. Tech. rep., NASA.

Crotts, A. (2011). Water on the Moon, I. Historical overview. *Astron. Rev.* 6, 4–20. doi:10.1080/21672857.2011.11519687

Dust Mitigation Gap Assessment Team (2016). *Dust mitigation Gap assessment Report*. International Agency Working Group. Available at: https://www.globalspaceexploration.org/wordpress/docs/Dust%20Mitigation%20Gap%20Assessment%20Report.pdf (Tech. rep).

Eick, M., Grossl, P., Golden, D., Sparks, D., and Ming, D. (1996a). Dissolution kinetics of a lunar glass simulant at 25 °C: the effect of pH and organic acids. *Geochimica Cosmochimica Acta* 60, 157–170. doi:10.1016/0016-7037(95)00377-0

Eick, M., Grossl, P., Golden, D., Sparks, D., and Ming, D. (1996b). Dissolution of a lunar basalt simulant as affected by pH and organic anions. *Geoderma* 74, 139–160. doi:10.1016/s0016-7061(96)00055-9

ISRU Gap Assessment Team (2021). In-situ *resource utilization Gap assessment Report*. International Space Exploration Coordination Group. Available at: https://www.globalspaceexploration.org/wordpress/wp-content/uploads/2021/04/ISECG-ISRU-Technology-Gap-Assessment-Report-Apr-2021.pdf (Tech. rep).

Keller, W. D., and Huang, W. H. (1971). Response of Apollo 12 lunar dust to reagents simulative of those in the weathering environment of Earth. *Lunar Sci. Conf.* 1, 973–981.

Kerschmann, R., Winterhalter, D., Scheiderich, K., Damby, D. E., and Loftus, D. J. (2020). Profiling lunar dust dissolution in aqueous environments: the design concept. *Acta Astronaut.* 178, 308–313. doi:10.1016/j.actaastro.2020.08.032

Kumari, N., Bretzfelder, J. M., Ganesh, I., Lang, A., and Kring, D. A. (2022). Surface conditions and resource accessibility at potential Artemis landing sites 007 and 011. *Planet. Sci. J.* 3, 224. doi:10.3847/PSJ/ac88c2

Liu, Y., and Taylor, L. (2008). *Lunar dust: chemistry and physical properties and implications for toxicity*. Knoxville: LPI Contributions.

Loftus, D. J., Rask, J. C., McCrossin, C. G., and Tranfield, E. M. (2010). The chemical reactivity of lunar dust: from toxicity to astrobiology. *Earth, Moon, Planets* 107, 95–105. doi:10.1007/s11038-010-9376-x

NASA (2003). Advanced life support requirements document. Tech. rep., NASA.

NASA (2014). Human integration design Handbook. Tech. rep., NASA.

Paul, A.-L., Elardo, S. M., and Ferl, R. (2022). Plants grown in Apollo lunar regolith present stress-associated transcriptomes that inform prospects for lunar exploration. *Commun. Biol.* 5, 382. doi:10.1038/s42003-022-03334-8

Stewart, C., Horwell, C., Plumlee, G., Cronin, S., Delmelle, P., Baxter, P., et al. (2013). Protocol for analysis of volcanic ash samples for assessment of hazards from leachable elements. *Int. Volcanic Health Hazards Network Publ.*

Stockstill-Cahill, K., Blewett, D. T., Bussey, D. B. J., Cahill, J. T. S., Clyde, B., Denevi, B. W., et al. (2021). *JHU-APL lsii report: 2021 lunar simulant assessment*. Maryland: Johns Hopkins Applied Physics Laboratory. Tech. rep.

Wallace, W. T., Phillips, C. J., Jeevarajan, A. S., Chen, B., and Taylor, L. A. (2010). Nanophase iron-enhanced chemical reactivity of ground lunar soil. *Earth Planet. Sci. Lett.* 295, 571–577. doi:10.1016/j.epsl.2010.04.042

World Health Organization (2018). A global overview of national regulations and standards for drinking-water quality (WHO).

frontiers | Frontiers in Space Technologies

TYPE Original Research
PUBLISHED 29 May 2024
DOI 10.3389/frspt.2024.1352213

OPEN ACCESS

EDITED BY
Yue Wang,
Beihang University, China

REVIEWED BY
Shuhao Cui,
Beihang University, China
Luiz S. Martins-Filho,
Federal University of ABC, Brazil

*CORRESPONDENCE
Sven J. Steinert,
sven.julius.steinert@outlook.com

RECEIVED 07 December 2023
ACCEPTED 19 February 2024
PUBLISHED 29 May 2024

CITATION
Steinert SJ, Zabel P and Quantius D (2024), Location-dependent flight cost difference from the lunar surface to an orbital fuel depot and its influence on *in situ* resource utilisation location selection.
Front. Space Technol. 5:1352213.
doi: 10.3389/frspt.2024.1352213

Location-dependent flight cost difference from the lunar surface to an orbital fuel depot and its influence on *in situ* resource utilisation location selection

Sven J. Steinert[1,2]*, Paul Zabel[2] and Dominik Quantius[2]

[1]School of Engineering and Design, Technical University of Munich (TUM), Munich, Germany, [2]Institute of Space Systems, Systemanalyse Raumsegment, German Aerospace Center (DLR), Bremen, Germany

Given the increasing relevance of lunar activities, the location selection for *in situ* resource utilisation (ISRU) facilities is necessary for identifying the most suitable configuration during mission planning. To gather information about the dominant location dependencies, a scenario is established wherein an ISRU product is exported to an orbital depot and its mass costs are used for classification. In the selected scenario, oxygen is produced in an ilmenite reduction plant and subsequently exported to the lunar gateway via an oxygen–hydrogen fuelled launcher operated in a round-trip to refuel oxygen at the lunar surface and hydrogen at the lunar gateway. This showed that the transport cost variations could be avoided entirely or have a recessive influence on the mission's total costs over an extended period of time, such as 20 years. The identification of the top-10 most optimal locations for various resolutions was altered only slightly upon consideration of flight costs as compared to considering only the ISRU factors; this indicates the insignificance of flight cost dependencies for the analysed case.

KEYWORDS

***in situ* resource utilisation, orbital fuel depot, delta-v map, lunar outpost, location selection, ilmenite reduction, lunar gateway, near-rectilinear halo orbit**

1 Introduction

The Moon and its currently unused resources hold great potential in terms of economics and development for the human presence. A large collaborative field study by Kornuta et al. (2019) showed that an undertaking of this magnitude is technologically feasible, which was presented in a commercial architecture. In contrast to Kornuta et al. (2019), who focus on the water ice in the permanently shadowed regions near the poles as the sources of hydrogen and oxygen via electrolysis, oxygen may also be obtained through extraction from regolith. This involves downsides as oxygen is only one component of the propellant and requires large machinery for regolith handling; however, the opportunities are vast as oxygen is abundantly available in regolith, with a combined weight percent of up to 45% as measured from the Apollo return samples (Papike et al., 1982). This oxygen is bonded to various elements, which is where an extraction method such as hydrogen reduction of ilmenite that focuses on a single specific bond is an effective procedure for processing. Therefore, propellant production need not be restricted to the polar regions, especially when a fully robotic *in situ* resource utilisation (ISRU) plant is feasible on the lunar surface without the

requirement of life support systems and their water resources. Optimisation can therefore be based on the process factors to pick the most optimal location globally. Accordingly, the goal of this study was to identify the significance of two types of process factors, namely ISRU efficiency and transport efficiency. In the case where one of these influences is deemed insignificant, prioritisation is provided for future mission analyses for similar scenarios.

2 Materials and methods

The influences are determined using an example scenario in which both the ISRU hardware costs and flight costs can be combined within a joint model, through which comparisons may be drawn using the mass costs as the central unit. The example scenario comprises an ISRU oxygen plant on the lunar surface and an orbital fuel depot to which a comparable launcher delivers and consumes the produced oxygen, while the consumed hydrogen is supplied externally.

2.1 ISRU efficiency

When the optimal location is chosen on the basis of the highest ISRU efficiency, the entire production line has to be inspected first for location-dependent factors. These factors include raw material concentration, solar irradiance, temperature, flat surface conditions, and further scenic requirements. Here, the production method is decisively sensitive to the location-dependent factors. One of the prominent extraction methods used is the hydrogen reduction of ilmenite, as already been demonstrated by Sargeant et al. (2020). In this process, the chemical bonds of $FeTiO_3$ are broken down by hydrogen, as shown in Eq. (1); the resulting water is then electrolysed, from which the hydrogen is fed back so that the net reaction leaves pure oxygen.

$$FeTiO_3 + H_2 \rightarrow Fe + TiO_2 + H_2O \tag{1}$$

Hydrogen reduction of ilmenite is chosen as the production method for analysis, which is expected to have high dependency on the raw material concentration; therefore, there is strong location dependency owing to the inhomogeneity of ilmenite distribution. An alternative extraction method would be molten regolith electrolysis as regolith distribution is mostly invariant over the lunar surface; this is why all results presented here are applicable only to the chosen production method.

2.1.1 Model

To reduce complexity, the model includes only the raw material concentration factor as the argument, i.e., the ilmenite weight ratio w_{ilmenite}. While this does not cover all influences, the raw material concentration accounts for a major part of the location dependency and therefore serves as an approximation to a full location-dependent model of the hydrogen reduction of ilmenite. The hardware mass that has to be moved to the lunar surface for ISRU operation serves as the criterion to be minimised. In a previous work by Guerrero-Gonzalez and Zabel (2023), this hardware mass $m_{hardware}$ dependent on ilmenite concentration was determined for a combined plant producing low-carbon steel and oxygen. This production plant was sized for an annual output of 23.9 t of oxygen and 25 t of low-carbon steel. The model comprises several subsystems, as defined in Eq. (2) (Guerrero-Gonzalez and Zabel, 2023). These subsystems entail all the processing steps of the infrastructure required to extract metals as well as oxygen from lunar regolith. The power law equations are then the fitted results of sensitivity analysis, so that the size of a given subsystem can be estimated to be explicitly dependent on the input parameter w_{ilmenite}, i.e., weight percent (wt%) of ilmenite concentration.

$$\begin{aligned}
y_0(x) &= 4036 \cdot x^{-1.064} - 9.59 && \text{Excavation}\\
y_1(x) &= 17580 \cdot x^{-1.003} - 390.8 && \text{Handling}\\
y_2(x) &= 19240 \cdot x^{-1.003} - 421.9 && \text{Beneficiation}\\
y_3(x) &= 21780 \cdot x^{-1.198} + 120.3 && \text{O2 Extraction}\\
y_4(x) &= 17910 \cdot x^{-1.265} + 1370 && \text{O2 Purification}\\
y_5(x) &= 29650 \cdot x^{-0.7005} - 602.5 && \text{Metal Processing}\\
y_6(x) &= 2541 \cdot x^{-0.7434} + 286.8 && \text{Gas Liquefaction \& Storage}\\
y_7(x) &= 32440 \cdot x^{-0.8312} + 125.2 && \text{Thermal Control}\\
y_8(x) &= 12000 \cdot x^{-0.9657} + 63.99 && \text{Power}
\end{aligned}$$

$$\mathrm{m}_{\text{hardware}}(x = w_{\text{ilmenite}}\ [wt\%]) = \sum_{i=0}^{8} y_i(x)\ [kg]. \tag{2}$$

In the proposed scenario, only oxygen production is relevant, and the additional subsystems for metal processing are scaled similar to the rest of the system such that the spread between the low and high values of w_{ilmenite} is not distorted significantly (88.69% spread to the maximum value vs. 89.97% spread without metal processing, for $1\ wt\% \leq w_{\text{ilmenite}} \leq 11\ wt\%$). Furthermore, this combined production plant may still be a viable choice for the synergistic effects of shared infrastructure. This is the reason for choosing the present model as the reference production plant in its entirety rather than trimming the subsystems. Therefore, the proposed model is expressed using Eq. (2) as well.

2.1.2 Data processing

To determine the cost for each location on the Moon, a global lunar map of ilmenite weight ratio is required. In a previous work, Sato et al. (2017) created an almost global TiO_2 abundance map, where the values of the wt% for TiO_2 are used as equivalents for ilmenite. The resulting map has an applied mask leaving out only the lunar Mare regions, with limited latitude coverage from −70° to 70°. The coverage limit originates from the orbiter sensor data and its limitations when measuring at increasingly steep sunlight irradiation angles towards the poles. The initial data were obtained using the Lunar Reconnaissance Orbiter Camera (LROC) wide-angle camera (WAC), which is the starting point for recreating a similar dataset as that used by Sato et al. (2017) but on a global scale. The original WAC data segments are joined together as shown in Figure 1.

2.1.2.1 Cleanup and estimation

The first problem with the acquired data is the unusually high measurements towards the poles that are considered as incremental noise scattered over the entire longitudinal axis. The second problem is incomplete coverage along the latitude and hence the poles themselves. To estimate the missing information along the latitudinal region, the following strategy is applied. If ilmenite

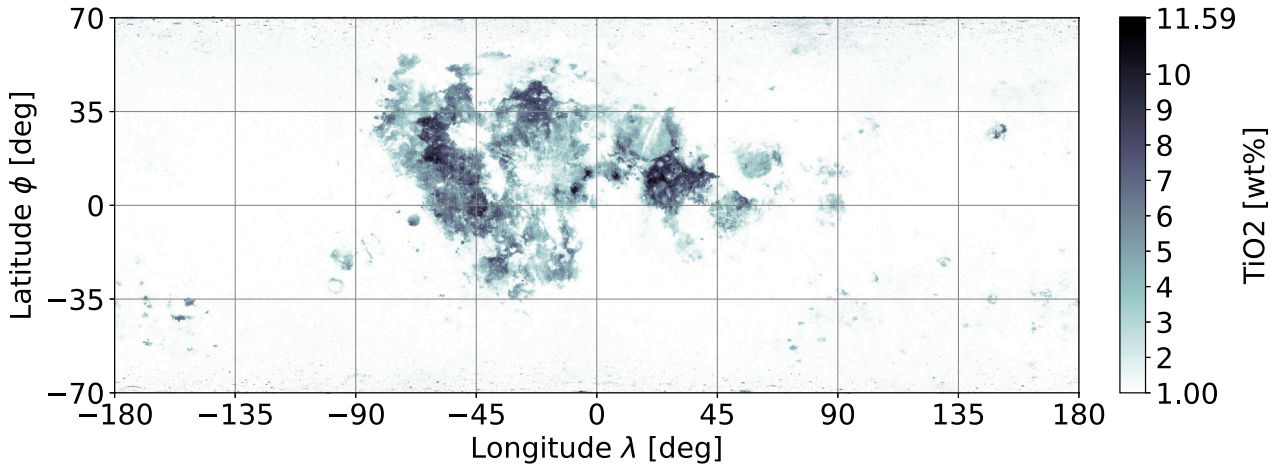

FIGURE 1
Combined original TiO_2 data on the wide-access camera (WAC) (Sato et al., 2017).

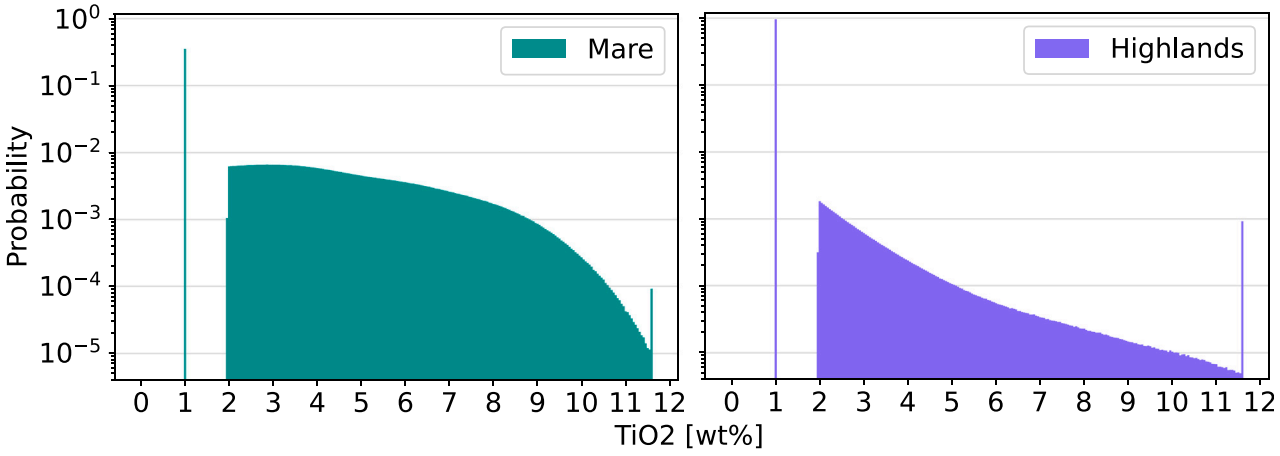

FIGURE 2
Distribution of ilmenite content clustered into the Mare and highland regions (equirectangular corrected) for the combined WAC data with Mare boundaries from Nelson et al. (2014).

abundance is correlated with the classification of the highlands/Mare regions and if the pole region geology features highland characteristics, then the expected values of the known highland regions serve as estimates of the ilmenite content at the poles.

As shown in Figure 2, the distribution characteristics of these two regions deviate considerably, where the average abundances also vary from 3.38 wt% in Mare to 1.1 wt% in the highland regions. Therefore, the ilmenite content correlation is given, and the estimates over the missing latitudinal areas of the highlands are set to 1 wt%; this matches with the original assumption of the WAC for values under the detection ratio. To remove the incremental noise at the extreme latitudes, a mask is created from the Mare boundaries as per the method of Nelson et al. (2014) and merged with a constant separation at $\phi = \pm 56^{\circ}$. The replacement values for the mask are set equally to 1 wt%. After applying both estimates, a low-noise global ilmenite map is obtained as shown in Figure 3.

2.1.2.2 ISRU mass cost map

The global ilmenite abundance map of Figure 3 is now used as the input to Eq. (2), which results in the location-dependent ISRU hardware mass shown in Figure 4.

2.2 Transport efficiency

2.2.1 Mission planning

The mission was designed to be carried out by a single-stage launcher that loops between the lunar surface and target orbit destination. The oxygen fuel component and oxygen payload are refilled on the lunar ground at the ISRU production plant. However, the hydrogen fuel component is refilled at the fuel depot to which the oxygen payload is delivered additionally. This hydrogen is supplied from a different process, where Earth is the assumed origin for the associated equivalent mass costs later on. This effectively results in

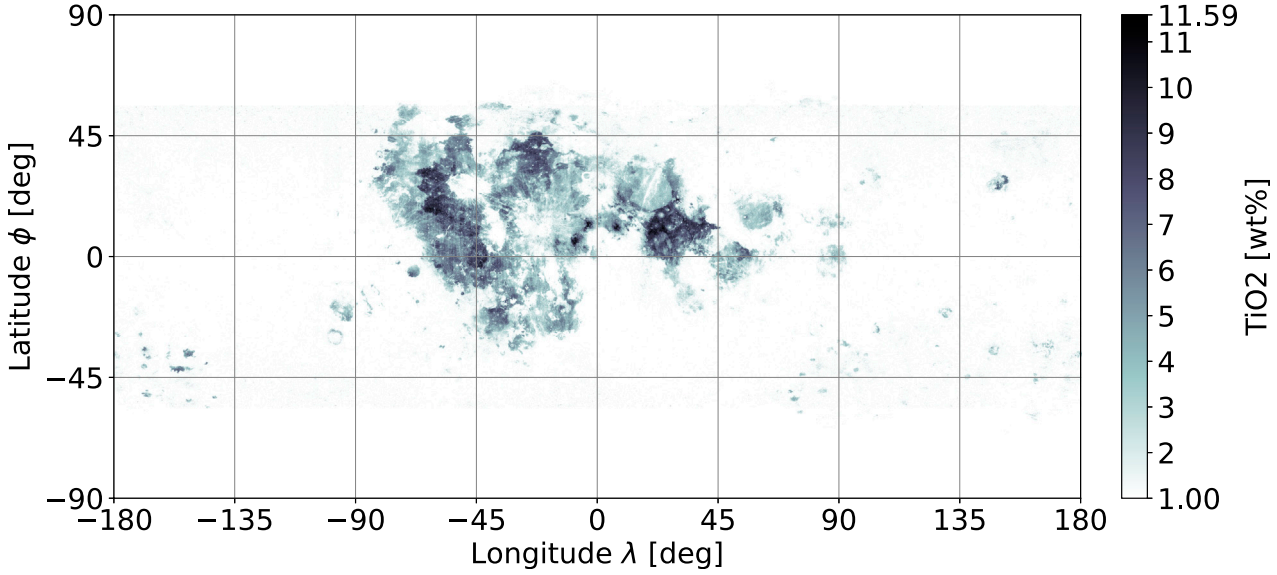

FIGURE 3
Global lunar ilmenite map in weight percent through TiO_2 based on WAC data and estimates.

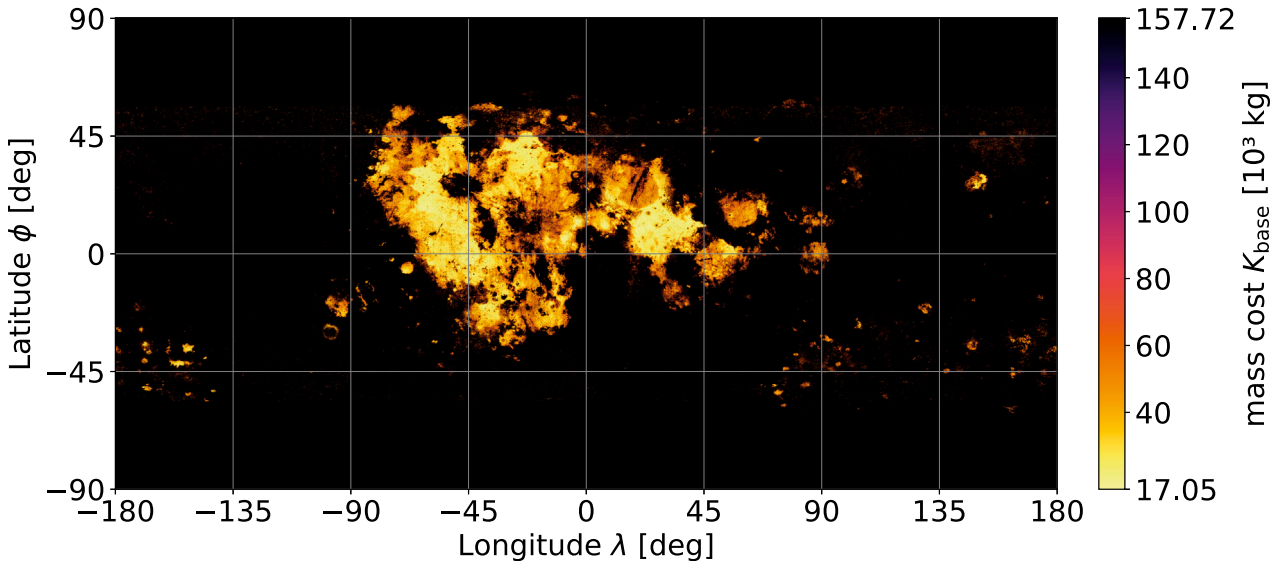

FIGURE 4
Location-dependent ISRU hardware mass cost K_{base} in its base configuration of 23.9 t of oxygen annually.

exchange of the delivered oxygen to the deducted hydrogen from the station. A multi-stage launcher or a shuttle exchange system was neglected in this analysis but would potentially help increase the transport efficiency.

2.2.2 Orbital fuel depot location

The primary requirement for the fuel depot location is accessibility from both the supplying and consuming units. For an interplanetary or cis-lunar logistic hub near Earth, the liberation points are especially suitable, as considered in a previous study by Perrin and Casler (2016). Similar to the liberation points, their corresponding halo orbits also offer the benefit of accessibility. In the case of an interplanetary logistic hub near Earth, which is supplied by the lunar surface, the currently planned lunar gateway on its near-rectilinear halo orbit (NRHO) is a suitable fit as a theoretical test bed. An NRHO fuel depot was also considered in the commercial lunar propellant export study by Kornuta et al. (2019); this is why the lunar gateway orbit is chosen for analysis as the export destination and considered a fuel depot.

2.2.3 Target orbit

For the selected fuel depot location at the lunar gateway, the target orbit is a specific NRHO that is in a 9:2 lunar synodic

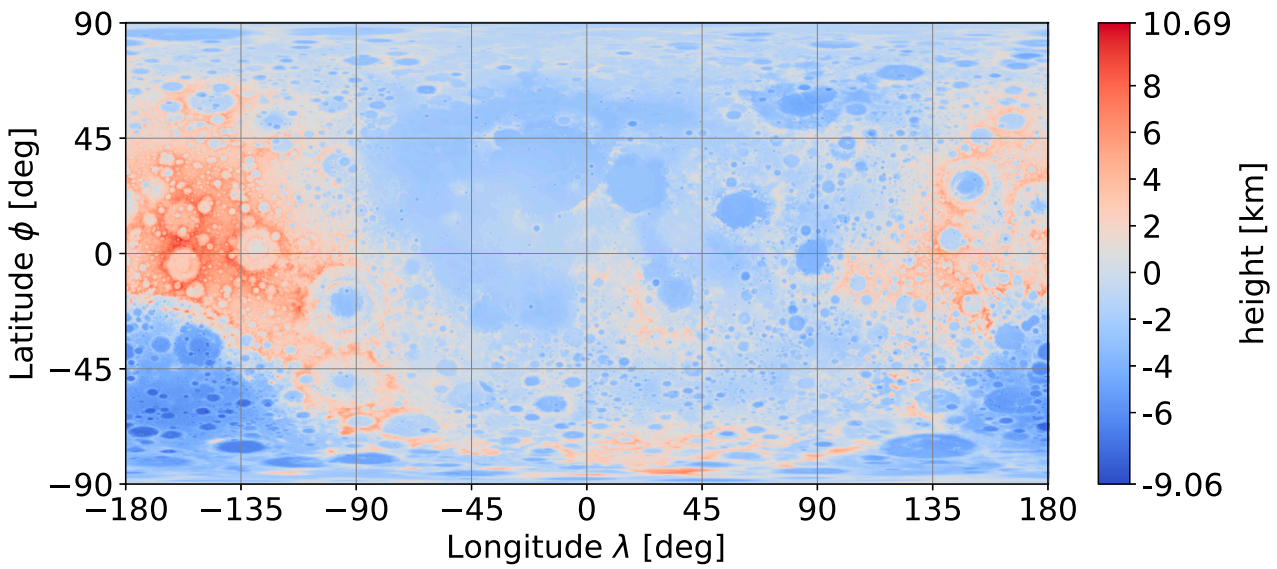

FIGURE 5
Lunar displacement map for reference radius (r_{ref} = 1737.4 *km*). Data from NASA CGI Kit (Wright and Petro, 2019) based on Smith (2015).

resonance with an average perilune of h_{peri} = 3557 *km* and average orbital period of T = 6.562 *days* (Lee, 2019). It is worth mentioning that this orbit has a variable polar crossing as well as other time-dependent changes in its trajectory that are often simplified to more static conditions during analyses (Whitley et al., 2018).

2.2.4 Delta-v estimation

First, regardless of the mission or the trajectory, the planetary conditions such as ground elevation and surface velocity influence the required Δv. These influences are briefly assessed for the Moon to determine their relevance.

2.2.4.1 Celestial influences

The initial radial distance to the Moon's centre of mass $r(\phi, \lambda)$ influences the ideal Δv demand directly, as shown in Eq. (3), for ascent into a circular orbit at r_{orbit} with standard gravity g_0 and standard gravitational parameter μ.

$$\begin{aligned}\Delta v_{ideal}(\phi,\lambda) &= \sqrt{v_{orbit}^2 + v_{ascent}^2} \\ &= \sqrt{\left(\frac{\mu}{r_{orbit}}\right) + \left(2 \cdot g_0 \cdot \left[r(\phi,\lambda) - \frac{r(\phi,\lambda)^2}{r_{orbit}}\right]\right)}\end{aligned} \tag{3}$$

The global ground elevation data are now used in the form of a displacement map (Wright and Petro, 2019), which originates from the Lunar Orbiter Laser Altimeter (LOLA) measurements (Smith, 2015). The elevation ranges from −9.115 km to 10.757 km with regard to the reference radius r_{ref} of 1737.4 km and therefore defines $r(\phi, \lambda)$ globally. The displacement map is shown in Figure 5.

Evaluating the extreme values on a low lunar orbit (LLO) at 100 km altitude (r_{orbit} = 1837.4 *km*) using Eq. (3) yields

$$\Delta v_{min} = \Delta v_{ideal}(\max\{r(\phi,\lambda)\}) = 1725.187 \ \frac{m}{s}$$
$$\Delta v_{max} = \Delta v_{ideal}(\min\{r(\phi,\lambda)\}) = 1725.204 \ \frac{m}{s}.$$

The influence of ground elevation on Δv is therefore of the order of 0.001%, which is extremely low.

The second celestial influence, namely, the initial surface velocity v_0, is either an additional Δv demand or a Δv reduction depending on the shared velocity components in the launch direction. Together with the sidereal rotation period and assumption of a spherical lunar surface of r_{ref}, the surface velocity can be derived as a function of the latitude ϕ, as displayed in Eq. (4).

$$v_0(\phi) = \frac{2\pi}{27.322 \text{ days}} \cdot \cos(\phi) \cdot r_{\text{ref}} \tag{4}$$

Evaluating the extreme points of the polar and equatorial locations on Eq. (4) yields

$$\Delta v_{min} = \Delta v_0(\phi = \pm 90°) = 0.000 \ \frac{m}{s}$$
$$\Delta v_{max} = \Delta v_0(\phi = 0°) = \pm 4.624 \ \frac{m}{s}.$$

Comparing this range $|\Delta v_{\max}| - \Delta v_{\min}$ with the ascent from the reference radius to a circular LLO of 100 km as $\Delta v_{ideal}(r_{ref})$ = 1725.196 $\frac{m}{s}$ gives the Δv influence of the surface velocity to be of the order of 0.27%, which is significantly more than the influence of elevation but still considerably low.

2.2.4.2 Transfer options

Explicit transfer from any lunar geodetic point to an NRHO and *vice versa* entail a high-fidelity problem that is usually solved non-analytically, as in Trofimov et al. (2020). Additionally, there are multiple transfer strategies that can be deployed for different optimisation goals. Between optimisation of the required Δv and transfer time, two transfer options were analysed for the chosen scenario.

First, a long-duration transfer that features a very low required Δv of only 664.9 $\frac{m}{s}$ to an LLO at an altitude of 100 km, which is very

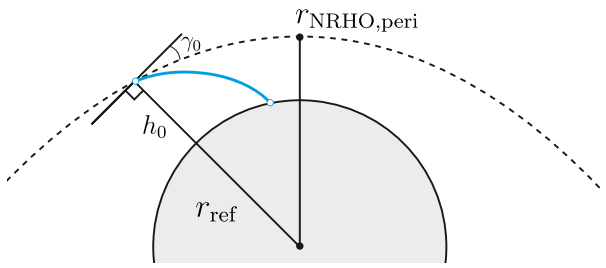

FIGURE 6
Direct descent trajectory scheme according to Trofimov et al. (2020).

close to the theoretical limit of 654.8 $\frac{m}{s}$, requires minimum energy change (Whitley et al., 2018). Moreover, it features an almost complete independency with the surface location that is achieved by something similar to a three-impulse transfer, where the lunar sphere of influence is left to circle once around the Earth before reinsertion. This allows removal of any inclination restrictions but at a cost of a long transfer time of 100.1 days. If this transfer option is chosen, the influence of the transfer efficiency is extremely low and marginal to the ISRU dependencies derived earlier. In this case, the transfer dependencies can be neglected and location selection can be simplified based on only ISRU efficiency.

Oftentimes, a transfer time of 100 days is simply too long for certain applications as it may, for example, induce general system lag times and therefore poor dynamics in propellant delivery adjustments for the target missions. For this reason, a second transfer option is analysed as a direct transfer trajectory between the NRHO and surface as per Trofimov et al. (2020), featuring the shortest transfer time of only hours but at the cost of a higher Δv and greater location dependency. The direct transfer, illustrated in Figure 6, is the subject of the analyses hereafter and serves as a worst-case scenario for an NRHO transfer in terms of the location dependency.

2.2.4.3 Data processing

In the previous work by Trofimov et al. (2020), a set of possible direct descent trajectories and their associated landing points and Δv demand were identified. The resulting map of scatter points for the southern 9:2 NRHO was taken as the starting point to derive a global Δv map. As this result does not contain the solutions of the cheapest trajectory for each location but rather all the solutions for direct descent, the data points can have both low- and high-cost solutions for the same location. Since the lowest cost option of a location is chosen during mission planning, a minimum estimation is performed by splitting the map into 20° square tiles, where constancy is assumed and the lowest value is set for the entire tile. This tiling on an equirectangular projected map gives higher resolutions towards the poles causing the problem; accordingly, the solution coverage is so low in the southern polar region that only high-cost solutions are present in a tile even if the neighbouring tiles may feature low-cost solutions. To mitigate this, the data were removed from particular high-cost trajectories of $\Delta v > 2985.65$ $\frac{m}{s}$, leaving a few non-defined tiles on the southern pole. If such data removal is not performed, up to 3300 $\frac{m}{s}$ transfer options would be carried over to the final map, which are clearly high-cost solutions, and would not be considered in a real mission. This process is visualised in Figure 7.

The non-defined tiles are estimated from their longitudinal neighbouring tiles via linear interpolation, which is only necessary in tiles at the southern polar region where there is already a higher geodetic resolution. This results in the final Δv map depicted in Figure 8.

2.2.4.4 Delta-v map

Even though the data in Figure 8 are computed for the descent only, they also serve as estimates for the ascent, which is biased because these problems are not entirely symmetric. Additionally, it should be mentioned that even though a 2414 $\frac{m}{s}$ transfer is very viable, a transfer of around 2900 $\frac{m}{s}$ may be used in a real-world scenario based on a different transfer strategy through an LLO with a waiting time to reduce Δv. However, in the present analysis, $\Delta v(\phi, \lambda)$ is globally defined in Figure 8 with $\Delta v_{min} = 2414.35$ $\frac{m}{s}$ and $\Delta v_{max} = 2985.65$ $\frac{m}{s}$.

2.2.5 Transport carrier

2.2.5.1 Reference launcher

To derive the associated transport mass costs, the previously determined Δv has to be applied to a specific launcher. The Argonaut, formerly known as the European Large Logistics Lander (EL3), is chosen as a starting point for this scenario. Its initial configuration is based on the published information from the European Space Agency (2023) of wet mass of 10,000 kg, dry mass of 1,600 kg, and payload of 2,100 kg as of the time of writing this article. Additionally, a hydrogen and oxygen propulsion system with an oxidiser fuel ratio of 6 and a specific impulse of 400 s is assumed. When this original configuration is applied the proposed mission with Δv_{max}, the fuel is depleted before the round-trip can be completed. Therefore, the launcher configuration has to be altered according to the needs of the scenario.

2.2.5.2 Launcher upscaling

Launcher upscaling is performed by maintaining the dry mass constant at 1,600 kg but adding fuel until the mission can be completed. The minimal viable system features an empty H_2 tank upon arrival at the gateway and an empty O_2 tank at the lunar surface. The iteration scheme for upscaling is visualised in Figure 9, which can converge to a minimal viable launcher for any given payload. The iteration commences with an undersized launcher starting from the moon with "initial H_2" as the amount of hydrogen in the tank at the lunar surface, "wet mass" that together with a constant dry mass indirectly represents the amount of oxygen in the tank on the lunar surface, and "refill H_2" as the amount of hydrogen refuelled upon arrival at the lunar gateway. When Δv is applied to this simulated round-trip, the undersized launcher experiences one of the defined failure cases, which indicates a particular missing propellant at some point of the mission. "O_2 empty" and "H_2 empty" describe the depletion of the oxygen and hydrogen tanks during flight, which results in an increase of the desired propellant for the next iteration, at which point "O_2 leftover" and "H_2 leftover" trigger the analogue opposite. "H_2 insufficient" is a less obvious failure case in which the launcher returns to the lunar surface but does not have

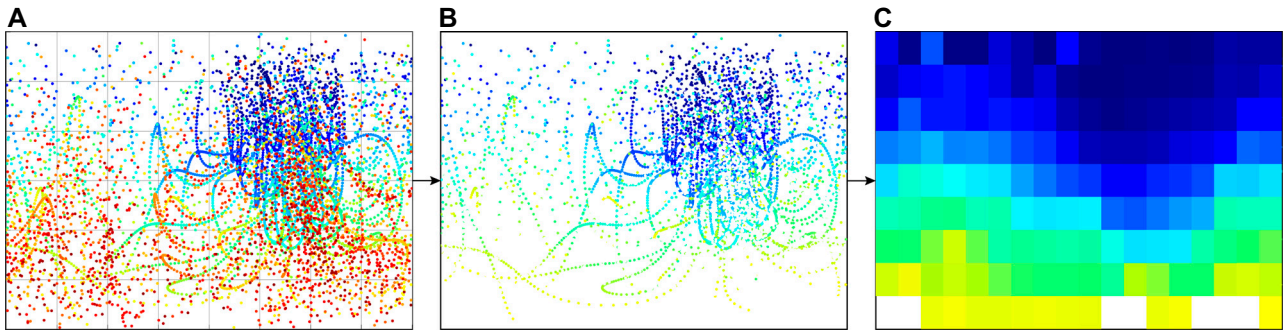

FIGURE 7
Processing of results from Trofimov et al. (2020) **(A)** to reduce data **(B)** into a minimum of 20° square tiles **(C)**.

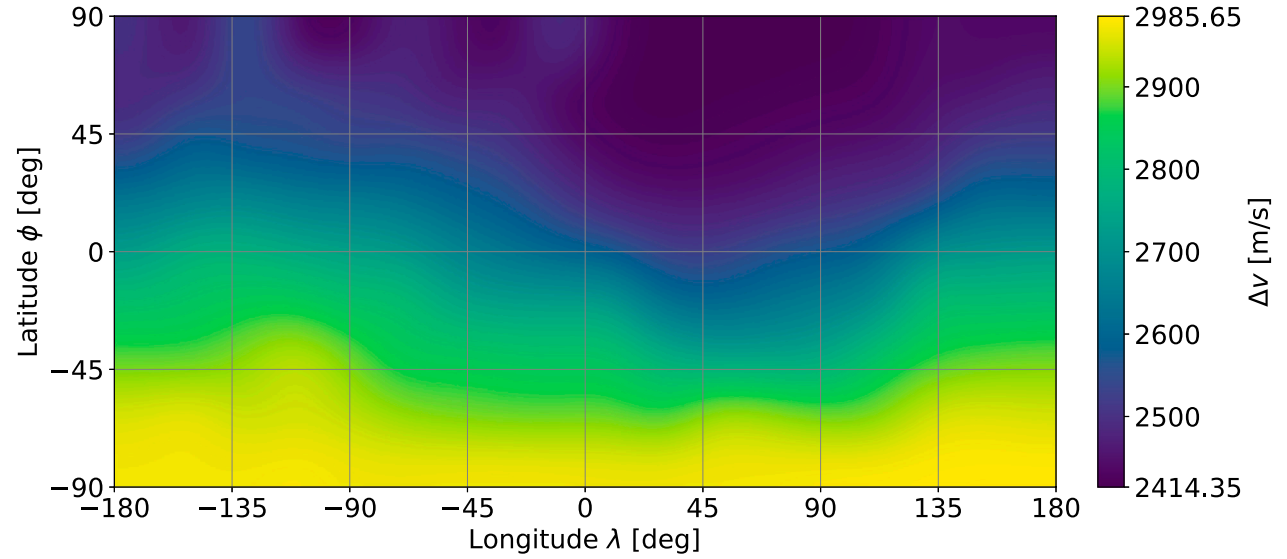

FIGURE 8
Required Δv for direct descent from the southern 9:2 near-rectilinear halo orbit (NRHO) to the lunar surface (bicubic interpolation).

enough hydrogen to perform the next round-trip run as it can only be refuelled at the lunar gateway and not on the ground. Owing to the fact that the launcher used in the iteration is undersized, the value of "refill H_2" may be considered unidirectionally while still reaching convergence with a small enough increment of the propellant.

Since this method of upscaling effectively increases the mass ratio ($r_m = \frac{m_{\text{wet}}}{m_{\text{dry}}}$) of the launcher, this assumption becomes increasingly unrealistic. Additionally, from the perspective of the fuel depot, oxygen is delivered but hydrogen is also removed, thereby effectively trading their masses according to the exchange ratio ($r_{ex} = \frac{m_{\text{payload}}}{m_{\text{H2,refill}}}$). To decide upon the range of launchers that must be compared to derive the cost differences, Figure 10 presents the parameter space between the exchange ratio r_{ex} and mass ratio of the launcher r_m.

Here, two sections are greyed out, where $r_{ex} < 1$ for economic reasonableness and $r_m > 10$ as the soft border of the mass ratio for a realistic single-stage launcher. The chosen launcher frames were selected through a sequence of movements in the parameter space, starting with economically reasonable exchange ratios of 1.5 and 2.0 (solid black lines, also called milestones) that are then projected to their required mass ratios (dashed black lines). This currently holds a set of constant exchange ratios over the Δv range; however, to obtain comparable results, the mass ratio r_m has to be constant over one set as it represents the efficiency of the launcher. Therefore, the maximum value of the mass ratio (at $\Delta v_{\max}$) is maintained constant over the Δv range to yield the chosen frame for the mass ratio (solid yellow line). When this set is then back-projected onto the exchange ratio (yellow dashed line), a span of exchange ratios can be achieved over the Δv range.

This determines the two chosen frames (yellow lines) as

$$\begin{aligned} r_m &= 8.555 \quad \text{with} \quad 1.5 \le r_{ex} \le 3.303 \\ r_m &= 10.688 \quad \text{with} \quad 2.0 \le r_{ex} \le 3.889 \end{aligned}.$$

Analysing the problem on two frames with different mass ratios provides insights into the sensitivity towards more efficient launchers in general and their influences on location selection.

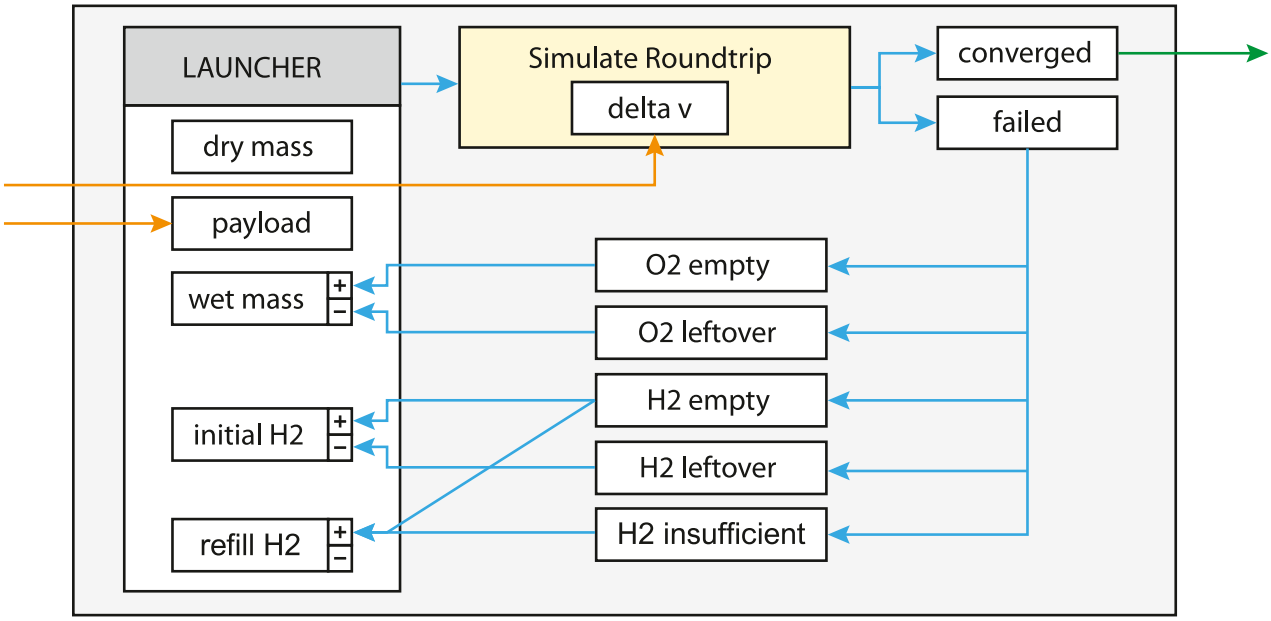

FIGURE 9
Launcher iteration scheme to converge a round-trip for a given payload and Δv.

2.2.5.3 Spent fuel

Using another iteration scheme targeting the chosen mass ratio r_m, a launcher can be converged for any Δv. The expended fuel is directly drawn from the simulated round-trip and normalised by the payload size, which can be combined into a direct mapping from the required Δv to spent fuel k_{Flight} in kg per kg of the payload. This dependency can be seen in Figure 11 for both mass ratios $r_m = 8.6$ and $r_m = 10.7$. In this comparison, the higher mass ratio $r_m = 10.7$ features a smaller absolute and relative growth, indicating that the differences in the spent fuel decrease with increasing launcher efficiencies.

2.3 Joint model

2.3.1 Total cost modelling

When both the efficiency influences are combined, the comparable mass costs have to be drawn from the mission scenario. Rather than assuming all the expended fuel as the transport cost, the fuel components may be separated with the reason that oxygen is not shipped from the Earth but rather fully supplied by the ISRU facility.

2.3.1.1 Fix costs

To meet the additional demand for oxygen that the launcher requires for transport every year, the ISRU facility is upscaled linearly by its ISRU costs per kilogram oxygen k_{ISRU} for each location and corresponding fuel requirements. The scaling factor originates from the base configuration cost in Figure 4 and the annual base production of $m_{base} = 23.9\,t$, which gives $k_{ISRU}(\phi,\lambda) = \frac{K_{base}(\phi,\lambda)}{m_{base}}$. The additional oxygen demand every year is derived from the yearly payload of $m_{pl,y} = 8\,t$ that is set to minimise scaling on the base configuration, oxidiser–fuel ratio of r_{of}, and spent fuel k_{Flight} depending on the two selected mass ratios $r_m \in \{8.6, 10.7\}$. Therefore, the fix costs representing the mass supplied from Earth towards the construction of the ISRU facility are determined through Eq. 5

$$K_{Fix}(\phi,\lambda,r_m) = K_{base}(\phi,\lambda) + k_{ISRU}(\phi,\lambda) \left(\left[m_{pl,y} \cdot k_{Flight}(\phi,\lambda,r_m) \cdot \frac{r_{of}}{r_{of}+1} \right] + m_{year} - m_{base} \right). \quad (5)$$

2.3.1.2 Dynamic costs

The expended hydrogen is fully considered as a mass cost since it is retrieved from the lunar gateway depot and assumed to be delivered from Earth. Here, the cost levels of the lunar gateway and lunar surface are simplified to be equal to those from the Earth for comparability, which rather overestimates the cost of hydrogen compared to costs on the lunar surface when supplied from Earth. Therefore, the dynamic costs representing the mass of hydrogen supplied from the Earth to the lunar gateway every year t are determined through Eq. 6

$$K_{Dynamic}(\phi,\lambda,t,r_m) = t \cdot m_{pl,y} \cdot k_{Flight}(\phi,\lambda,r_m) \cdot \frac{1}{r_{of}+1}. \quad (6)$$

2.3.1.3 Total costs

Combining both K_{Fix} and $K_{Dynamic}$, the final total costs of the mission over the location and time are

$$K_{Total}(\phi,\lambda,t,r_m) = K_{Fix}(\phi,\lambda,r_m) + K_{Dynamic}(\phi,\lambda,t,r_m). \quad (7)$$

Applying Eq. (7) to the earlier location-dependent results gives the total cost maps for the mission time of 20 years for $r_m = 8.6$ (Figure 12) and $r_m = 10.7$ (Figure 13). In a direct comparison between Figures 12 and 13, the flight cost influence is visibly less pronounced for the higher mass ratio. Moreover, a reduced variation in the total mission cost is observed.

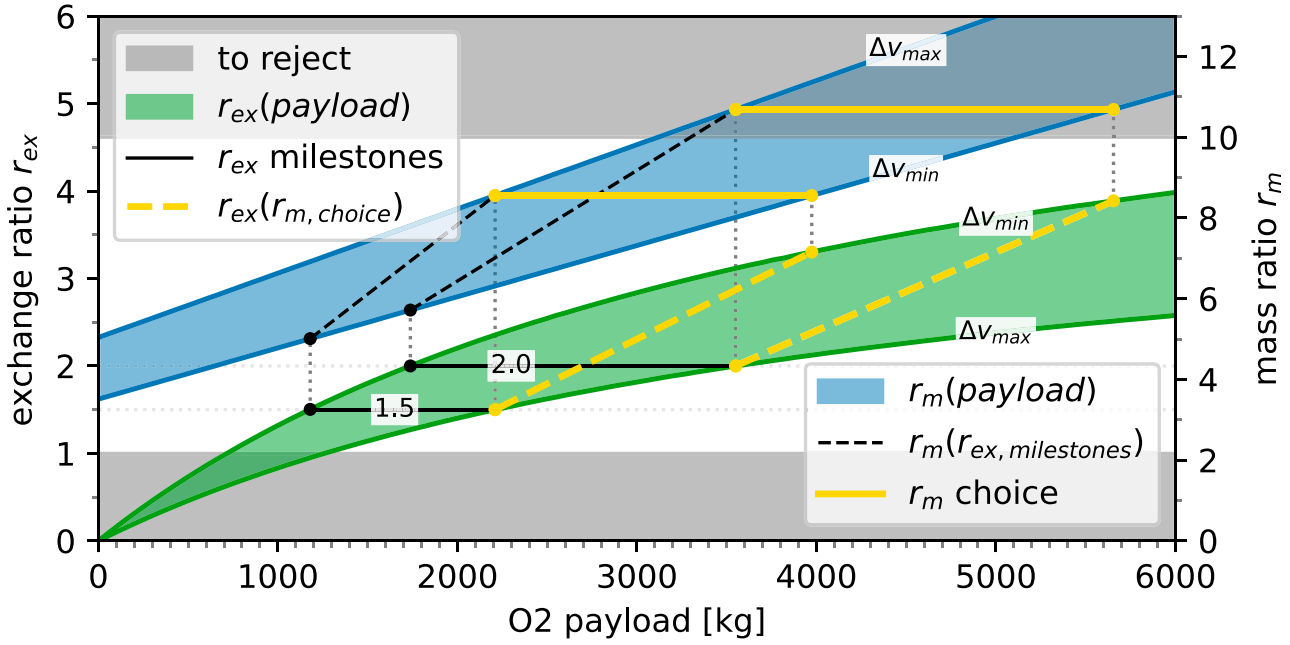

FIGURE 10
Exchange ratio r_{ex} and mass ratio r_m depending on the payload size of the launcher over the Δv range.

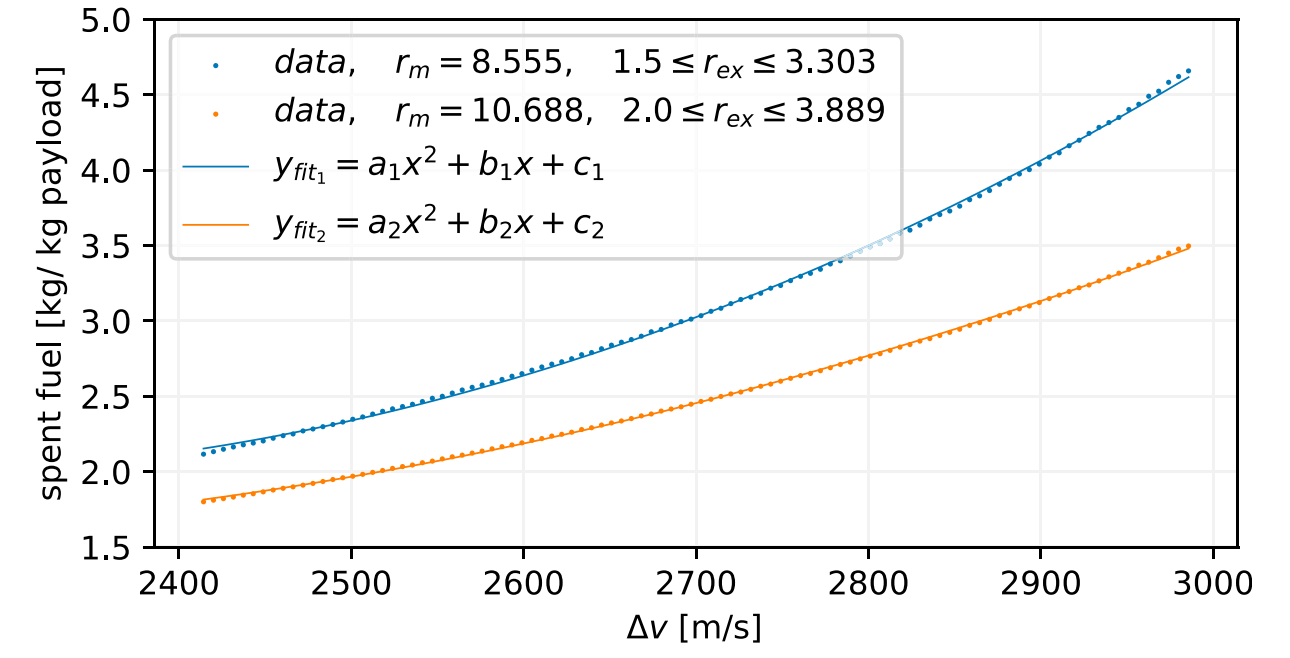

FIGURE 11
Relationship between required Δv and spent fuel k_{Flight} for two mass ratios.

3 Results

3.1 Flight cost influences

In the case of availability of long-duration transfer (Section 2.2.4.2) for which location dependencies can be diminished almost completely as well as insignificant celestial influences (Section 2.2.4.1), the effects on mission location selection are eliminated by an assumable uniform Δv requirement.

Under only the short-duration transfer strategy of a direct descent, the location-dependent Δv requirements are prominent (Section 2.2.4.4), translating to a significant difference in the spent

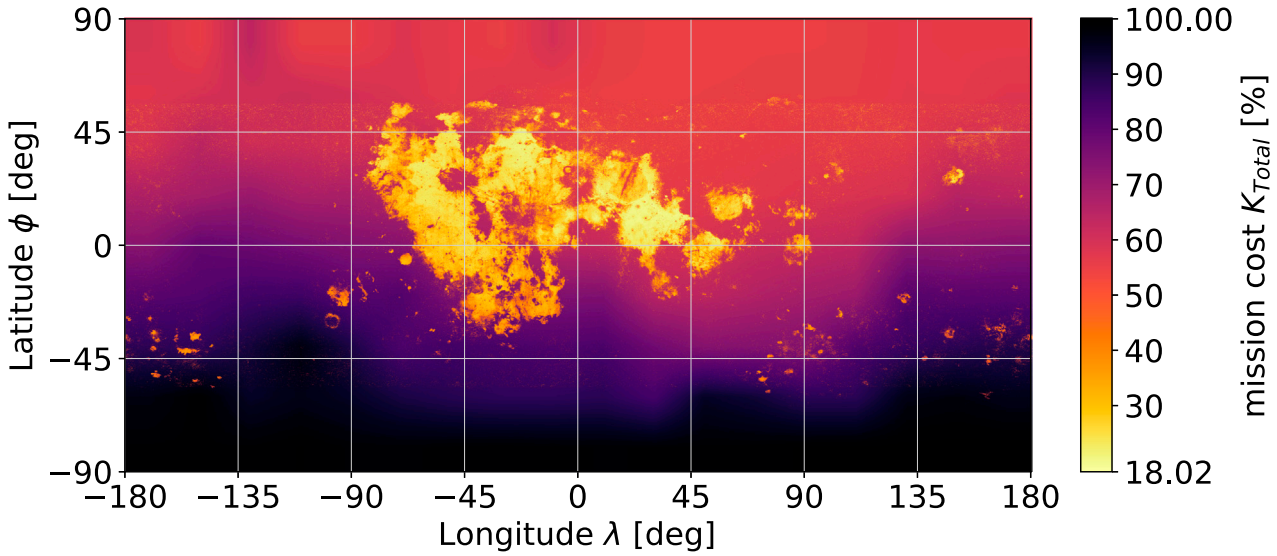

FIGURE 12
Location-dependent total mission cost K_{Total} in % for t = 20 years and r_m = 8.6.

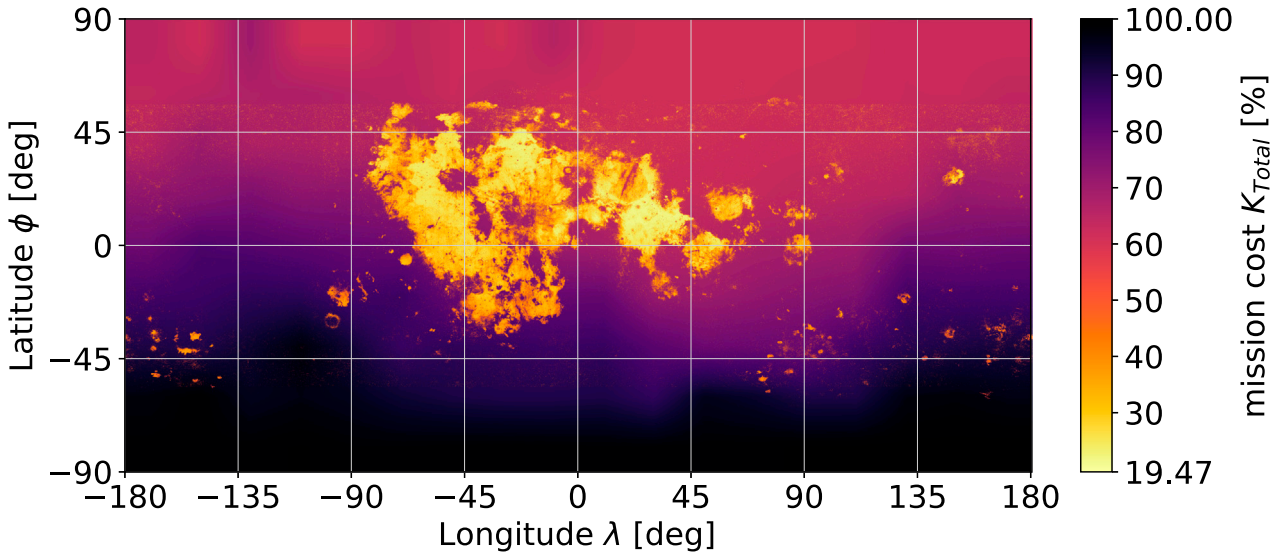

FIGURE 13
Location-dependent total mission cost K_{Total} in % for t = 20 years and r_m = 10.7.

fuel (Section 2.2.5.3). However, under ISRU influence, ilmenite reduction introduces vast location dependencies (Section 2.1.2.2) that overshadow the differences in the spent fuel, resulting in a total cost dominated by ISRU features when both influences are combined (Section 2.3.1.3).

3.2 Flight cost insignificance

To provide insights into the errors induced when the flight costs are neglected completely, the best locations from the ISRU model (Section 2.1) are compared with the best locations from the joint model (Section 2.3). To limit the possible locations, the location-dependent results of both models are reduced to geodetic square tiles of 15°, 5°, and 1° (ϕ, λ) to compare the behaviours at multiple resolutions; the tiles $T_{\phi\ index,\lambda\ index}$ were created by considering the pixel-area relation to yield index resolutions of 12 × 24, 36 × 72, and 180 × 360. From these tiles, the top-10 choices were ranked and compared for the models. The top-10 choices constitute the top 3.47% for the 15° tiles, top 0.39% for the 5° tiles, and top 0.015% for the 1° tiles. Table 1 shows these tiles that are colourised by the ranking of the ISRU model, with green being the most optimal to orange being the less optimal location, to provide a baseline for comparisons of the ordered and featured tiles. The joint model is

TABLE 1 Top-10 best mission locations compared between the ISRU and joint (J.) models after t years in pixel-area-relation-resized square tiles ($T_{\phi\ index,\lambda\ index}$), with resolutions ϕ, λ of 15° (top), 5° (middle), and 1° (bottom).

15° tiles	#1	#2	#3	#4	#5	#6	#7	#8	#9	#10
ISRU	$T_{5,8}$	$T_{5,13}$	$T_{3,10}$	$T_{4,7}$	$T_{6,9}$	$T_{3,8}$	$T_{5,14}$	$T_{4,13}$	$T_{6,8}$	$T_{4,10}$
J. t = 0	$T_{5,8}$	$T_{5,13}$	$T_{3,10}$	$T_{4,7}$	$T_{3,8}$	$T_{4,13}$	$T_{5,14}$	$T_{6,9}$	$T_{4,10}$	$T_{5,11}$
J. t = 10	$T_{5,13}$	$T_{3,10}$	$T_{5,8}$	$T_{4,13}$	$T_{4,7}$	$T_{3,8}$	$T_{5,14}$	$T_{6,9}$	$T_{4,10}$	$T_{5,11}$
J. t = 20	$T_{5,13}$	$T_{3,10}$	$T_{5,8}$	$T_{4,13}$	$T_{5,14}$	$T_{3,8}$	$T_{4,7}$	$T_{4,10}$	$T_{4,12}$	$T_{5,11}$
5° tiles	#1	#2	#3	#4	#5	#6	#7	#8	#9	#10
ISRU	$T_{15,40}$	$T_{14,24}$	$T_{16,41}$	$T_{14,23}$	$T_{16,40}$	$T_{12,23}$	$T_{10,31}$	$T_{13,24}$	$T_{15,25}$	$T_{15,42}$
J. t = 0	$T_{15,40}$	$T_{16,41}$	$T_{16,40}$	$T_{14,24}$	$T_{10,31}$	$T_{15,42}$	$T_{15,43}$	$T_{14,23}$	$T_{15,41}$	$T_{16,42}$
J. t = 10	$T_{15,40}$	$T_{16,41}$	$T_{16,40}$	$T_{15,42}$	$T_{10,31}$	$T_{15,43}$	$T_{15,41}$	$T_{16,42}$	$T_{17,40}$	$T_{11,31}$
J. t = 20	$T_{15,40}$	$T_{16,41}$	$T_{15,42}$	$T_{15,43}$	$T_{16,40}$	$T_{10,31}$	$T_{15,41}$	$T_{16,42}$	$T_{11,31}$	$T_{14,41}$
1° tiles	#1	#2	#3	#4	#5	#6	#7	#8	#9	#10
ISRU	$T_{79,204}$	$T_{81,201}$	$T_{80,200}$	$T_{72,118}$	$T_{80,201}$	$T_{84,171}$	$T_{72,117}$	$T_{81,199}$	$T_{72,116}$	$T_{80,204}$
J. t = 0	$T_{79,204}$	$T_{81,201}$	$T_{80,200}$	$T_{80,201}$	$T_{80,204}$	$T_{81,199}$	$T_{80,203}$	$T_{79,203}$	$T_{80,199}$	$T_{81,200}$
J. t = 10	$T_{79,204}$	$T_{80,200}$	$T_{80,201}$	$T_{81,201}$	$T_{80,204}$	$T_{79,203}$	$T_{80,203}$	$T_{76,201}$	$T_{78,218}$	$T_{78,204}$
J. t = 20	$T_{79,204}$	$T_{71,206}$	$T_{78,218}$	$T_{76,201}$	$T_{75,206}$	$T_{77,212}$	$T_{76,206}$	$T_{80,204}$	$T_{80,201}$	$T_{79,203}$

Indices start at zero on (90°ϕ, −180°λ) with −180° to 180° longitude range. Data for mass ratio r_m = 8.6.

also shown in the table in tree time steps of 0, 10, and 20 years, providing a sense of the temporal evolutions of the featured tiles.

The induced errors of the flight cost neglect increases over the mission time; nevertheless, even for a long time span of 20 years, the top-10 choices of the joint model feature many tiles that are also in the top-10 choices based on ISRU ranking. The greater conservation of the highest ranked tiles can be explained by the coincidental overlap between low flight costs and low ISRU costs. At higher resolutions, fewer tiles are shared but the top-10 choices constitute the entire set given the differences in percentage, so the shared tiles remain substantial. Therefore, from Table 1, it is concluded that the induced errors during location selection are small enough that a simplification of considering only the ISRU effects may be valid even with larger differences in Δv, as in the analysed case.

4 Discussion

Identifying the features of secondary relevance and even neglecting the flight costs in the selected mission scenario cannot be generalised directly without considering the requirements because other ISRU production methods may be influenced by the target orbits, trajectories, or mass ratios, which may differ greatly from those in the present analysis.

However, given the case of ilmenite reduction and transport properties that are comparable to or weaker than those of the analysed case, the flight cost differences can be assumed to be insignificant. In particular, the major influence that can be verified by a quick assessment of a general case involves estimating the difference in Δv requirements, which should be less than that of the analysed case, i.e., ≈ 20%. Lower mass ratios of the launchers can amplify the differences in Δv when transferred to spent fuel and thereby the fuel costs. Furthermore, it should be noted that this analysis features a scenario involving propellant refilling by own entities that can reduce the fuel costs in general; this needs to be reconsidered when a different cost modelling is present. The flight frequency can scale up flight costs linearly and can compress the shift over time for the most optimal location, for which the delivered payload of 8 t per year can be considered a rough reference value from the present analysis.

Although the significant difference in the accessibility of the southern hemisphere is a result of the direct descent trajectory, it must be noted that this does not imply worse accessibility from the NRHO to the southern hemisphere in general. In the chosen set of trajectories, no options were considered for intermediate parking orbits that could reduce the differences between the northern and southern hemispheres, as seen from the 1-day transfer reported by May et al. (2020) that shows entirely different characteristics.

As global lunar data are increasingly available, problems as these can be analysed and optimised close to their entirety over the entire lunar surface. In particular, when infrastructure is yet to be deployed on the lunar surface at this point in time, location selection can be performed by optimisation instead of dependencies on prior infrastructure.

To avoid a prior infrastructure restriction, the plan for mankind's presence, economics, and even sustainability on the Moon should be expanded and considered from the perspective of greater scope as much as possible. As an oxygen propellant facility is just one entity in an economics network, its most optimal location may move away completely from its presently analysed location under a larger context. Such a large-scale technical investigation would also make for a compelling future study.

Data availability statement

The original contributions presented in the study are included in the article/supplementary material; further inquiries can be directed to the corresponding author.

Author contributions

SS: data curation, formal analysis, investigation, methodology, resources, software, visualization, and writing–original draft. PZ: conceptualization, funding acquisition, supervision, and writing–review and editing. DQ: writing–review and editing.

Funding

The authors declare that financial support was received for the research, authorship, and/or publication of this article. The publication fees are covered by the publication fund of the German Aerospace Center (DLR) in support of open access publishing.

Conflict of interest

The authors declare that the research was conducted in the absence of any commercial or financial relationships that could be construed as a potential conflict of interest.

Publisher's note

References

European Space Agency (2023). Argonaut - technical details. Available at: https://www.esa.int/Science_Exploration/Human_and_Robotic_Exploration/Exploration/Argonaut.

Guerrero-Gonzalez, F. J., and Zabel, P. (2023). System analysis of an ISRU production plant: extraction of metals and oxygen from lunar regolith. *Acta Astronaut.* 203, 187–201. doi:10.1016/j.actaastro.2022.11.050

Kornuta, D., Abbud-Madrid, A., Atkinson, J., Barr, J., Barnhard, G., Bienhoff, D., et al. (2019). Commercial lunar propellant architecture: a collaborative study of lunar propellant production. *REACH* 13, 100026. doi:10.1016/j.reach.2019.100026

Lee, D. E. (2019). White paper: Gateway destination orbit model: a continuous 15 year nrho reference trajectory (National Aeronautics and Space Administration (NASA)). *Tech. Rep. Doc. ID 20190030294.*

May, Z. D., Qu, M., and Merrill, R. (2020). "Enabling global lunar access for human landing systems staged at earth-moon l2 southern near rectilinear halo and butterfly orbits," in *AIAA scitech 2020 forum* (America: American Institute of Aeronautics and Astronautics). doi:10.2514/6.2020-0962

Nelson, D. M., Koeber, S. D., Daud, K., Robinson, M. S., Watters, T. R., Banks, M. E., et al. (2014). Mapping lunar maria extents and lobate scarps using lroc image products. *Lunar Planet. Sci.* 45, 2861.

Papike, J. J., Simon, S. B., and Laul, J. C. (1982). The lunar regolith: chemistry, mineralogy, and petrology. *Rev. Geophys.* 20, 761–826. doi:10.1029/RG020i004p00761

Perrin, T. M., and Casler, J. G. (2016). "Architecture study for a fuel depot supplied from lunar resources," in *Aiaa space 2016* (America: American Institute of Aeronautics and Astronautics). doi:10.2514/6.2016-5306

Sargeant, H., Abernethy, F., Barber, S., Wright, I., Anand, M., Sheridan, S., et al. (2020). Hydrogen reduction of ilmenite: towards an *in situ* resource utilization demonstration on the surface of the moon. *Planet. Space Sci.* 180, 104751. doi:10.1016/j.pss.2019.104751

Sato, H., Robinson, M. S., Lawrence, S. J., Denevi, B. W., Hapke, B., Jolliff, B. L., et al. (2017). Lunar mare tio 2 abundances estimated from uv/vis reflectance. *Icarus* 296, 216–238. doi:10.1016/j.icarus.2017.06.013

Smith, D. E. (2015). 2009 lunar orbiter laser altimeter radiometry data set, lro-l-lola-3-radr-v1.0. doi:10.17189/1520639

Trofimov, S., Shirobokov, M., Tselousova, A., and Ovchinnikov, M. (2020). Transfers from near-rectilinear halo orbits to low-perilune orbits and the moon's surface. *Acta Astronaut.* 167, 260–271. doi:10.1016/j.actaastro.2019.10.049

Whitley, R., Davis, D., Burke, L., McCarthy, B., Power, R., McGuire, M., et al. (2018). Earth-moon near rectilinear halo and butterfly orbits for lunar surface exploration

Wright, E., and Petro, N. (2019). SVS: CGI moon Kit — svs. Available at: https://svs.gsfc.nasa.gov/4720.

frontiers | Frontiers in Space Technologies

TYPE Original Research
PUBLISHED 06 June 2024
DOI 10.3389/frspt.2024.1345337

OPEN ACCESS

EDITED BY
Joseph N. Pelton,
International Space University, United States

REVIEWED BY
Madhu Thangavelu,
University of Southern California, United States
Scott Madry,
University of North Carolina at Chapel Hill, United States

*CORRESPONDENCE
Jonas Walther,
jm.walther@hotmail.com

RECEIVED 27 November 2023
ACCEPTED 02 April 2024
PUBLISHED 06 June 2024

CITATION
Walther J, Johns RL, Kolvenbach H, Bickel VT and Hutter M (2024), Autonomous construction of lunar infrastructure with in-situ boulders. *Front. Space Technol.* 5:1345337. doi: 10.3389/frspt.2024.1345337

Autonomous construction of lunar infrastructure with in-situ boulders

Jonas Walther[1]*, Ryan Luke Johns[1], Hendrik Kolvenbach[1], Valentin Tertius Bickel[2] and Marco Hutter[1]

[1]Robotic Systems Lab, Institute of Robotics and Intelligent Systems, D-MAVT, ETH Zürich, Zürich, Switzerland, [2]Center for Space and Habitability (CSH), University of Bern, Bern, Switzerland

Significant infrastructure is required to establish a long-term presence of humans on the lunar surface. *In-situ* resource utilization (ISRU) is a fundamental approach to ensure the viability of such construction. Here, we investigate the feasibility of constructing blast shields as one example of lunar infrastructure using unprocessed lunar boulders and an autonomous robotic excavator. First, we estimate the volume of unprocessed material required for the construction of blast shield segments. Secondly, we quantify the amount of available boulders in two exploration zones (located at the Shackleton-Henson Connecting Ridge and the Aristarchus Plateau pyroclastic deposit) using LRO NAC images and boulder size-frequency distribution laws. In addition, we showcase an alternative approach that relies on Diviner rock abundance data. Thirdly, we use a path planning algorithm to derive the distance, energy, and time required to collect local material and construct blast shield elements. Our results show that our construction method requires two orders of magnitudes less energy than alternative ISRU construction methods, while maintaining realistic mission time and payload capacity margins.

KEYWORDS

Moon, ISRU, construction, boulder, dry stone wall, infrastructure, excavator, autonomous

1 Introduction

Permanent lunar infrastructure will be required to establish a sustainable human presence on the Moon, and as a first step in the preparation for the first human mission to Mars (NASA, 2023a). As part of programs such as Artemis (NASA, 2020), frequent landings and launches of spacecraft will continuously eject dust and small particles which cause a significant threat to such infrastructure, as well as to the lunar environment (Mueller et al., 2009; Qiao et al., 2023). The significant detrimental character of blast-debris has first been observed during the Apollo era, after the Apollo 12 astronauts returned parts of the Surveyor III lander to Earth, which was affected by debris blasted off by the Apollo 12 module during touchdown (Immer et al., 2011). The SpaceX HLS (Human Landing System)—selected for the first crewed missions to the Moon (NASA, 2021a)—is expected to physically affect the environment hundreds or even thousands of meters away from the landing site (Qiao et al., 2023), which is one of the reasons why past studies have called for landing pads and blast shields to mitigate blast damage (Mueller et al., 2009; Susante and Metzger, 2016).

Such infrastructure projects require significant building materials—yet the transport of mass from Earth to the Moon is extremely expensive, with current prices of around 1.2 mln

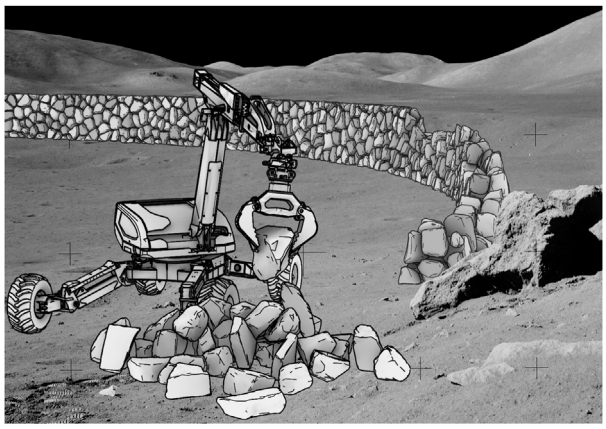

FIGURE 1
Illustration of the construction of a blast shield with our proposed construction method. Background: photo credit to NASA, processing/scanning credit to Kipp Teague and NASA Johnson (image AS17-141–21610), edited.

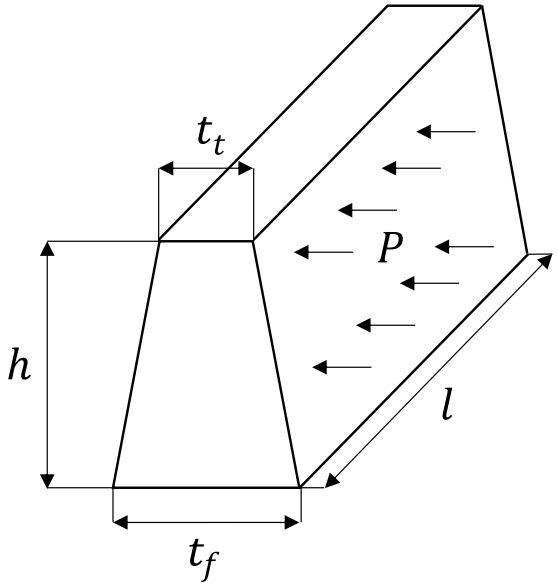

FIGURE 2
Blast shield segment.

USD per kilogram (Astrobotic, 2018). Literature suggests *in-situ* resource utilization (ISRU) for the construction of infrastructure, which can reduce the need of mass transport from Earth, while in return more energy is required (Moses and Mueller, 2021). Methods and materials based on *in-situ* resources proposed for construction purposes include, for example, microwave heating (Lim et al., 2021), cast regolith (Benaroya et al., 2012), waterless/sulfur concrete (Susante, 2012; Susante and Metzger, 2016; Khoshnevis et al., 2017), 3D-printing (Cesaretti et al., 2014; Yashar et al., 2021) and dry packing of processed rocks (Thangavelu and Adhikari, 2017).

This paper proposes a novel way of constructing vital infrastructure using boulders that are abundant on the lunar surface, using autonomous construction machines. Such work has been recently demonstrated on Earth, where a robotic hydraulic excavator platform has demonstrated the construction of dry stone walls using irregular boulders and debris (Johns et al., 2020). The advantage of this particular construction method is that *in-situ* boulders can be used without the need of preprocessing, making it remarkably energy efficient (Johns et al., 2020).

In this work, we assess the viability of deploying such a method toward the construction of key infrastructure on the Moon, using found boulders. First, we calculate in section 2 the amount of *in-situ* material required for the construction of a blast shield. Next, in section 3, we quantify the amount of physically-available *in-situ* material (boulders) in two sites of increased exploration interest. Based on those maps, we derive the cost of retrieving the material (i.e., the distance, time, and energy) in section 4. We conclude with a general discussion of the approach and results in section 5. Figure 1 visualizes how the construction of a blast shield with our proposed construction method might look like.

2 Blast shield construction

Previously-proposed construction methods for blast shields include regolith berms (Mueller et al., 2009; Morris, 2012; Moses and Mueller, 2021), cast regolith (Benaroya et al., 2012) and microwave heating (Lim et al., 2021). The landing pad for Artemis-class missions is expected to have a diameter of 200 m (with possible reduction to 100 m) (Gelino et al., 2023). A possible ratio of blast shield height to radius (resulting in the shielding angle) was given by Morris (2012). Figure 2 shows how the blast shield is geometrically parameterized. Note that the blast shield is shown as a straight wall for simplicity, while it would be wrapped around a round landing pad in practice.

Table 1 shows assumptions on the main dimensions of the considered blast shield and thereafter the required parameters, as well as the results of further calculations. Note that for the friction angle of regolith, the smallest angle in the range mentioned by Benaroya and Bernold (2008) was taken, as this will lead to conservative results.

A first approximation of the pressure P on the wall induced by the engine blast is done with help of the value of Morris (2012). Morris (2012) found out that for a blast shield with height 1.5 m at radius $r = 15$ m, the average pressure on the shield is 11.4 Pa and is proportional to $r^{-2.463}$, when the height is kept constant. In our problem the height however changes, but the ratio of height and radius stays the same, which is why the pressure rather should be proportional to r^{-2} (Roberts, 1966; Morris, 2012). So, at $r = 50$ m, the average pressure induced by that rocket should be approximately 1.03 Pa. The pressure thereby consists of the pressure from the exhaust gasses, as well as of the blasted regolith particles that are impacting the blast shield. The named pressure seems to be calculated for an engine thrust of about 13.3 kN (Morris, 2012). The first lander for Artemis is anticipated to be SpaceX's Starship (NASA, 2021a). The Starship currently is rated to have 1500 tf ≈ 14715 kN of thrust[1]. Note that the thrust during the lunar landing

1 https://www.spacex.com/vehicles/starship/ accessed: 23.08.2023.

TABLE 1 Parameters of the blast shield.

Parameter	Value	Source
radius r	50 m	based on Gelino et al. (2023)
height h	$\frac{10}{3}$ m ≈ 3.33 m	based on Morris (2012)
perimeter l	$\pi \cdot 100$ m ≈ 314 m	calculated
boulder volume fraction ϵ	0.67	(SIA, 2012)
gravitational constant of the Moon g_M	1.64 m/s^2	Susante and Metzger, (2016)
bulk density of the boulders ρ_b	2650 kg/m^3	Susante and Metzger, (2016)
bearing capacity of the soil $q_s(t_f)$	~ 6000 kPa $\cdot \frac{t_f}{1\text{m}}$	based on Heiken et al. (1991)
friction angle of regolith φ_r	$30° \cdot \frac{\pi}{180°}$	Benaroya and Bernold, (2008)
pressure induced by the engine blast P	1135 Pa	described in section 2
wall thickness on the floor t_f	1.79 m	described in section 2
wall thickness on the top t_t	1.12 m	described in section 2
required boulder volume $V_{b,req}$	~ 1020m^3	calculated

might be different. The pressure on the blast shield now is linearly scaled by the thrust. The resulting pressure then is $P = 1135$ Pa. Note that this is a very rough approximation. For a more reliable estimate, the work of Morris (2012) would need to be redone with the characteristics of the engines of the Starship, which however is out of the scope of this paper.

By using assumptions on the relation between t_f and t_t (Stiftung Umwelt-Einsatz Schweiz, 2014) and applying safety factors on sliding, overturning and the bearing capacity of the soil (McCombie et al., 2015), the values for t_f and t_t can be obtained and are as well shown in Table 1. Given the thickness of the blast shield, the required boulder volume is calculated and also shown in Table 1. Due to the large size we suggest not to construct the full ring, but only a ring segment in the direction where the shielding really is needed. In the remaining part of this paper, only a quarter ring segment instead of a full ring is considered.

3 Boulder availability

According to the Wentworth scale, boulders are stones that are larger than 256 mm (Wentworth, 1922), which is also the size range that is reasonable for the construction method of Johns et al. (2020). Clusters with lots of lunar boulders are typically found within and near recent impact craters, along potentially tectonically active wrinkle ridges, or at the bottom of topographic depressions (Bickel et al., 2020; Valantinas and Schultz, 2020; NASA, 2021b; Ruesch and Bickel, 2023).

The candidate regions for the Artemis program are all located near the lunar south pole (NASA, 2022c). The region which is closest to the south pole is called Connecting Ridge (NASA, 2022c). This region is of very high interest, as it offers proximity to permanently shadowed and sunlit regions, i.e., access to volatiles and energy (Swiney and Hernandez, 2022).

Additionally, a non-polar region is considered. During the "foundational exploration" of NASA's "Moon-to-Mars architecture", possible missions also consider non-polar regions (NASA, 2023a). The HLS is anticipated to be able to land at non-polar sites in future missions (see HLS-S-R-0357 of NASA (2022a)). A top-tier exploration site is the Aristarchus Plateau (NASA, 2022a), a geologically very interesting region (Zisk et al., 1977) containing the deepest and widest sinuous rille of the Moon, which is called Vallis Schröteri (Hurwitz et al., 2013). We focus on a section of the Aristarchus pyroclastic deposit adjacent to Vallis Schröteri, ranging from longitude −51.85° to −51.3° and from latitude 26.21° to 26.71°. The region is approximately 15 km by 15 km, which resembles the approximate size of the Artemis candidate regions (NASA, 2022c). The region contains a small part of Vallis Schröteri and was selected considering resource availability, rock abundance, and topographic slope.

3.1 Manual boulder mapping

We used images taken by the Lunar Reconnaissance Orbiter (LRO) Narrow Angle Camera (NAC) (Robinson, 2010; Robinson et al., 2010; Speyerer et al., 2012; Humm et al., 2016; Mahanti et al., 2016) to quantify the availability of boulders at the two sites of interest. The NAC images were obtained as EDR (Experimental Data Record) and processed using ISIS3 (Laura et al., 2023) to derive georeferenced images, following Bickel et al. (2021). The mapping of the boulders then was done using QGIS[2] version 2.18.28. Some minor processing steps of the resulting shapefiles were done with Python and GDAL (GDAL/OGR contributors, 2020).

The two NACs have a nominal resolution of 0.5 $^{\text{m}}/_{\text{pixel}}$ at an altitude of 50 km, enabling the detection of "blocks" with horizontal sizes of about 1 m (Robinson et al., 2010). The size of most boulders in the images is only a few pixels. Similar as done by Boazman et al. (2022), only boulders which are at least two pixels wide were

2 https://qgis.org/de/site/

mapped. Boulders can be identified by their bright appearance followed by a shadow, while the order of bright and dark pixels is opposite to how it is the case for craters (Gawronska et al., 2020; Boazman et al., 2022).

For Connecting Ridge, we utilized shapefiles provided by Boazman et al. (2022) featuring the location of boulders in this region. With the help of this data, we generated boulder shapefiles, which additionally have information on the size of the boulders. A list of the NAC images used by Boazman et al. (2022) is given at the end of their paper. Our augmented boulder shapefiles are available online (Walther et al., 2023).

For the chosen region at the Aristarchus Plateau, no files with mapped boulders were available. Therefore, the whole mapping process was done for this region, starting with the selection of NAC images that were used. The NAC images were chosen with help of the QuickMap[3], with the goal of getting the best visibility for boulders, e.g., using images with high resolution and intermediate solar incidence angle. Regions that were covered by multiple images were mapped with the image with highest resolution. We note that there is a high variation in the resolution of the available images, which affects the size of the smallest identified boulders. The southern part of the chosen region contains parts of the Vallis Schröteri. Here, we consider a traverse of the rille's slopes ($> 25^{\circ}$) to be infeasible, which is why the area was excluded from boulder mapping.

3.2 Boulder size-frequency distribution laws

We combine our mapping results with boulder size-frequency distribution laws to estimate the fraction of boulders smaller than ~2 m. Li et al. (2017) used a power law $\alpha \cdot d^{\beta}$ to derive the cumulative number of lunar boulders of a certain size d or larger. They compared the data with surface and NAC images in a log-log plot and found out that, except for two of the seven considered landing sites, the data points resulting from the two different imaging methods had the same slope. Based on that they claim that the size-frequency distribution (SFD) of the boulders on the Moon can be modeled using a power law. The SLS-SPEC-159 Cross-Program Design Specification for Natural Environments (DSNE) (NASA, 2021b) also assumes that a power law would be valid for rocks smaller than 2 m (see section 3.4.1.4 in the mentioned document). Baloga et al. (2012) on the other hand stated that a power law leads to unreasonable extrapolations for lunar boulders with size 10 cm, while an exponential law $\alpha \cdot \exp(\beta d)$ does not have this issue. Rüsch et al. (2022) find that the size-frequency distribution of lunar boulders depends on the age of the considered location. They state that the size-frequency distribution of regions younger than approximately 50 Ma is a power law, while for older regions, it is an exponential law.

Due to different views in literature and as the age of the considered regions are not exactly known and also are assumed to vary within the regions, both the power law (Li et al., 2017) and the exponential law (Rüsch et al., 2022) will be considered in the following. We note that the exponential law is more conservative with respect to the estimated amount of small boulders. This will further be discussed in section 5.3.2.

The size-frequency distribution laws are fitted using the data of the boulders that were mapped as described in section 3.1. For the size d in the size-frequency distribution laws, the longest visible axis of the boulders was used. For the power law, the power index β is region-dependent (Krishna and Kumar, 2016; Rüsch et al., 2022). It therefore should not be assumed to be constant over the whole region. Based on that, it can also be assumed that the size-frequency distribution can be regionally dependent, when the exponential law is used instead.

The fit of the exponential law is derived by applying the natural logarithm and then solving the linear system of equations for $\ln \alpha$ and for β. For the power law, a maximum likelihood approach was used, which was proposed by DeSouza et al. (2015) for size-frequency distributions in the context of celestial bodies, which in turn was based on Clauset et al. (2009) and therefore also on Muniruzzaman (1957). A threshold $d_{threshold}$ for the minimum size of the boulders used for the fit was set. This was done for both mentioned size-frequency distribution laws. The used value was 2 m and motivated by Powell et al. (2023). Fits of the power law and the exponential law for the mapped boulders in Connecting Ridge and the chosen Aristarchus Plateau region will later be shown in the discussion in section 5.3.2.

3.3 Boulder volume estimation

The precise volume of the mapped boulders is unknown, and thus an approximation based on the longest diameter is performed. We introduce a factor, which relates the cube of the longest diameter d_{long} to the estimated volume of the boulder V_b. The volume estimate is done by assuming the boulder to be an ellipsoid, as applied by Bickel et al. (2021). It can be assumed, that the height of the boulder corresponds to the smallest of the three axes (Demidov and Basilevsky, 2014). Using a ratio between the height and the visible diameter in surface made images, which was mentioned to be 0.6 by Demidov and Basilevsky (2014), together with an approach mentioned by them to relate this visible diameter with the longest and medium axis length, and by using a ratio between the longest and medium axis length of 2, which is the most conservative value mentioned by Krishna and Kumar (2016), the following relation can be obtained (used for this study)

$$V_b \approx 0.1 \cdot d_{long}^3 \tag{1}$$

Our standard assumption is that the useable boulders for the construction are those with the longest axis d_{long} being in the interval [0.5 m, 1.5 m]. Given a map with large boulders mapped using LRO NAC images, the number of small boulders in a certain area can be estimated based on a size-frequency distribution law from section 3.2. While the map with large boulders contains the location of the boulders, the exact location of the expected smaller boulders of course is unknown. Therefore, a map with smaller boulders should rather be a grid, in which for every grid cell, a separate size-frequency distribution is fitted, which allows to get the number of small boulders. The standard value for the grid spacing was

3 https://quickmap.lroc.asu.edu/

10.3389/frspt.2024.1345337

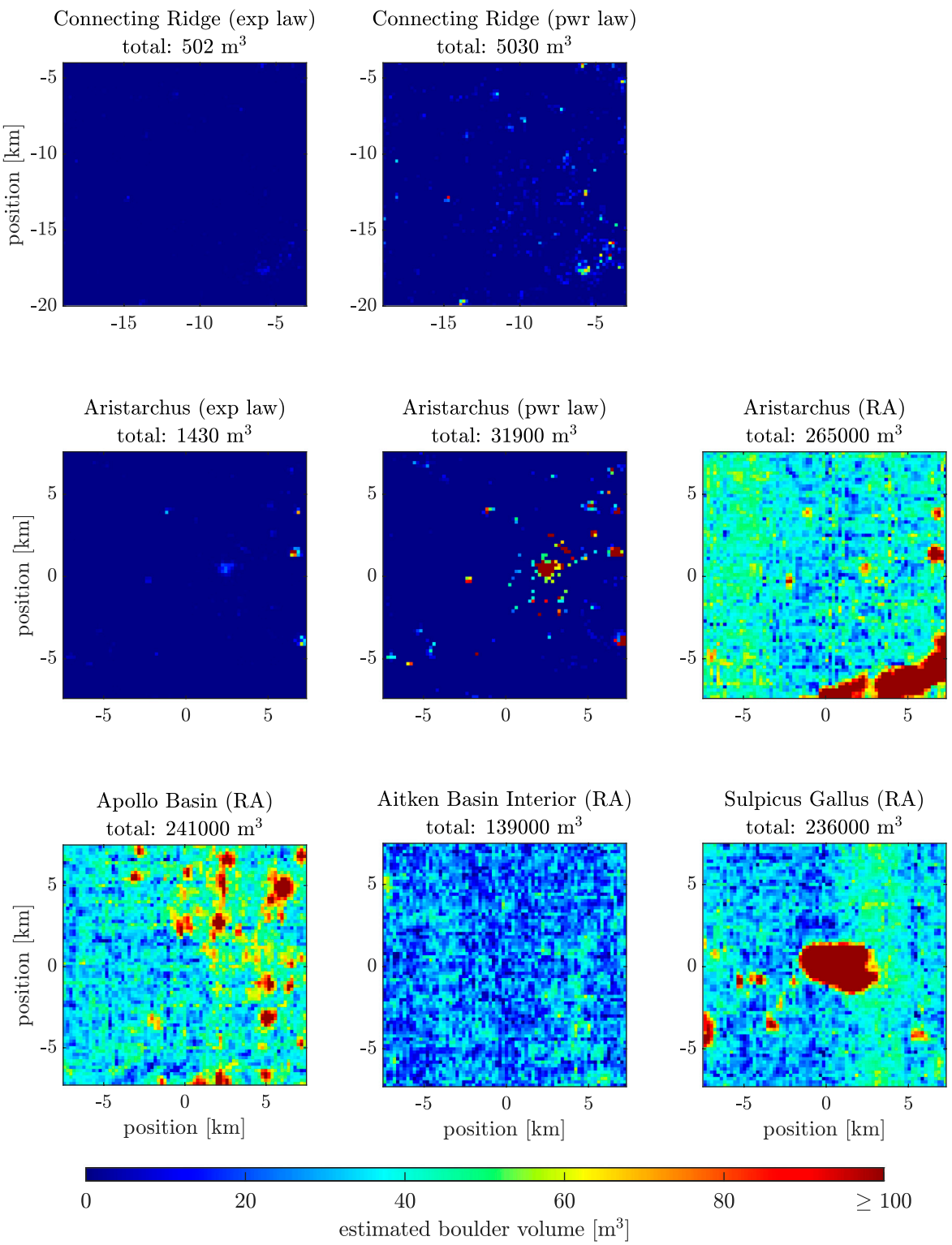

FIGURE 3
Comparison of the boulder volume maps of different regions with different size-frequency distribution laws (exp law: exponential law; pwr law: power law; RA: rock abundance dependent exponential law by Li and Wu (2018)).

chosen to be 200 m. Choosing it much smaller would not make sense due to the uncertainty of the position of the NAC images, which leads to an uncertainty of the position of the mapped boulders.

As mentioned in section 3.2, the size-frequency distribution is region-dependent (Krishna and Kumar, 2016; Rüsch et al., 2022). Both parameters, so not only the scaling α, but also β, which stands

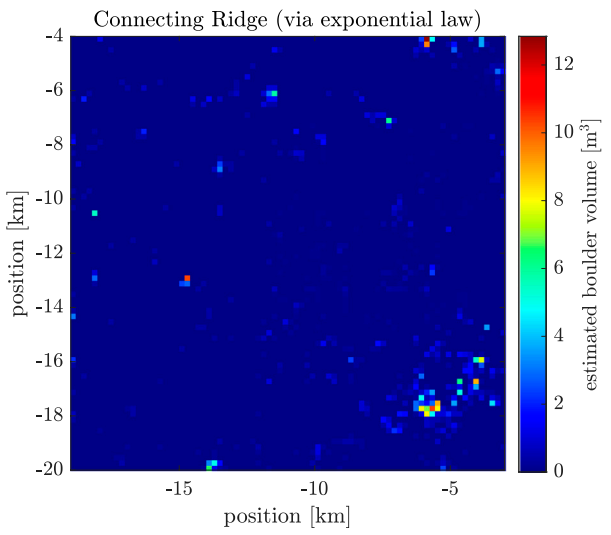

FIGURE 4
Boulder volume map of Connecting Ridge by using an exponential law for the SFD.

for the ratio between large and small boulders, therefore should be estimated for all grid cells individually. For the fit of β, a minimum number of 400 close-by boulders was used in order to get a good sense of the ratio between large and small boulders. Given the size-frequency distribution of a grid cell, not only the number of smaller boulders can be estimated, but also the volume of boulders with d_{long} in the interval [0.5 m, 1.5 m]. For this, the relation between longest axis and the boulder volume as shown in Eq. 1 is used. The exact formulas are also shown in the Supplementary Material.

3.4 Boulder volume estimation using Diviner rock abundance data

Manual boulder mapping is a time-consuming process. As an alternative, we propose using rock abundance data (Powell, 2022) derived by Powell et al. (2023) using LRO's Diviner instrument in combination with a description of the fractional area $F(d)$ of boulders of size d or larger (Li and Wu, 2018) to calculate the locally available boulder volume. Note that the mentioned rock abundance data is only available between the latitudes 70 S and 70 N. The Diviner instrument is able to sense rocks larger than 1–2 m (Bandfield et al., 2011; Powell et al., 2023). The rock abundance data $k_{diviner}$ needs to be converted to the total rock abundance k before it is used. This can be done by requiring F (1 m) to be equal to $k_{diviner}$ and solving it for k. Using the value 1 m instead of 2 m is more conservative with respect to the expected amount of available boulders, as it estimates a lower total rock abundance k.

The volume of boulders with d_{long} in the interval [0.5 m, 1.5 m] then can be calculated (Li and Wu, 2018) (section 3.3). The exact formulas are shown in the Supplementary Material. Note that boulder volume maps first are generated with the grid given by the rock abundance data of Powell (2022), and afterwards interpolated to a 200 m by 200 m grid, as a 200 m spaced grid is also used in the method based on mapped boulders.

3.5 Boulder volume maps

Figure 3 compares the expected available boulder volume of boulders with longest axis between 0.5 m and 1.5 m in Connecting Ridge, the chosen Aristarchus Plateau region and three of the Constellation Program regions of interest. The different size-frequency distribution laws mentioned in section 3.2 were used, including the exponential law and power law together with mapped boulders and the rock abundance dependent exponential law by Li and Wu (2018). The Connecting Ridge site (exponential law) is shown separately in Figure 4 in large.

4 Construction effort determination

This section describes the determination of the distance the excavator has to travel to collect the required boulders for construction, as well as how long the whole construction process takes and how much energy is needed.

4.1 Path planning problem statement

In the following, the problem statement of the path planning for the collection of the boulders is described. The goal of the path planning was to minimize the overall boulder collection distance. This size is linear to the required time and furthermore also has an influence on the total energy consumption, as will be described in section 4.4 and section 4.5.

4.1.1 Payload capacity

One of the constraints is the limited payload capacity of the vehicle used for the collection of boulders. It was mentioned by Johns et al. (2023) that the payload in their case usually was about 7 m^3. The standard value considered in this study will be 10 m^3 of boulders. The influence of the payload capacity on the results will be discussed in section 5.2.3.

4.1.2 Terrain slope

Another considered constraint is the allowable slope of the terrain, such that it still is traversable by the vehicle. The LRV (Lunar Roving Vehicle) of the Apollo missions, for example, according to the "Lunar Sourcebook" by Heiken et al. (1991) was able to climb slopes of up to 19°–23°. Another source even mentions that the LRV is capable of climbing 25° steep slopes, while the steepest slopes it actually did climb during the missions were about 10°–15° (Jones and Nola, 1971). For the LTV (Lunar Terrain Vehicle), which will enable to transport crew during Artemis missions (O'Shea, 2023), a draft of a document mentions that the road used to test the vehicle has phases with 20° uphill, downhill, as well as sideways (NASA, 2023b). Based on this, we decided to consider a direction independent slope constraint of 20°.

4.1.3 Excavator landing site

In the following, two constraints on the excavator landing site are discussed. The term excavator landing site thereby stands for where the excavator will be landed, which does not necessarily

need to be at the same location as the base camp site, because the excavator is able to move from its landing location to the base camp site. The HDL (Human-class Delivery Lander), who is considered here as a reference lander for the transport of the excavator, is required to be capable of landing on slopes of at least 10° (requirement HDL-S-R-0041) (NASA, 2022b).

The second constraint concerns hazardous boulders in the landing region and is motivated by Grant et al. (2018). The size of the regions checked for hazardous boulders is chosen to be 100 m by 100 m, which is based on the required 50 m landing precision of the HDL (requirement HDL-S-R-0040) (NASA, 2022b). This constraint will be formulated differently for when the boulder volume map was generated with mapped boulders or rock abundance data as in section 3.4. In the case, where rock abundance data is used, this is done based on a probability to encounter a hazardous rock, which was used by Grant et al. (2018) for Curiosity and Perseverance, as well as on additional information about lunar landers[4] (Astrobotic, 2018). In the case, where mapped boulders are used, the possible excavator landing sites are required to be free of any boulders mapped in the NAC images.

4.1.4 Further constraints

For Connecting Ridge, an additional constraint is to not enter permanently shadowed regions. Those regions are scientifically uniquely interesting and should not be traversed or contaminated (Swiney and Hernandez, 2022).

4.2 Path planning pipeline

The path planning pipeline consists of multiple modules. It uses a greedy score, motivated by Walther et al. (2022), which is used to select the next target location for the boulder collection. A global planner then searches for the shortest path to the target using the A* algorithm introduced by Hart et al. (1968). The A* algorithm is an adjusted version of the Dijkstra algorithm (Dijkstra, 1959), which, for example, was used by Pena-Asensio et al. (2023) for the path planning of lunar EVA's. The distance to collect the boulders at the target site itself then is estimated using a formula proposed by Few (1955). The global path planner additionally ensures the payload capacity constraint of the vehicle by sending it back to the base camp location to unload the boulders, when the payload capacity is about to be reached.

A further module of the path planning pipeline is a local planner, which ensures the slope constraints of the vehicle and keeps it out of permanently shadowed regions. For the slope constraint, the elevation data of Barker et al. (2021) is used for Connecting Ridge and the SLDEM2015 data of Barker et al. (2016) otherwise. Regions are considered to be permanently shadowed if the 60 m spaced Sun visibility data of Mazarico et al. (2011) is equal to zero at the corresponding location. For more details about the implementation of the path planning pipeline, the interested reader is referred to the Supplementary Material.

4 https://www.spacex.com/vehicles/starship/accessed: 23.08.2023.

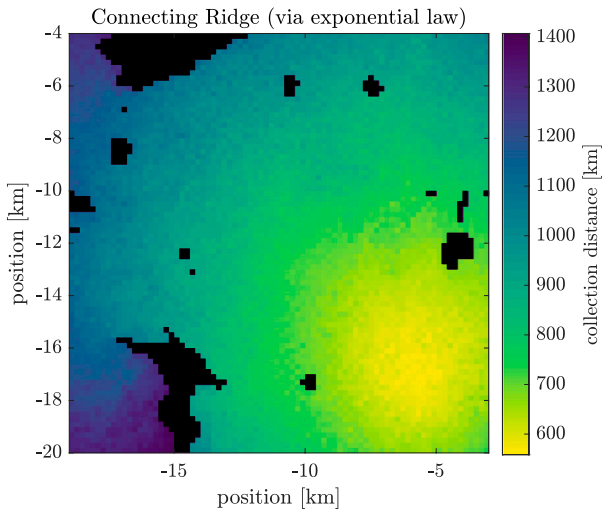

FIGURE 5
Distance map of Connecting Ridge by using an exponential law for the SFD.

4.3 Distance maps

This section presents the results of the boulder collection distances using the path planning pipeline described in the previous sections. The considered task thereby is to collect 250 m^3 of boulders, which is about enough for a quarter ring segment of a blast shield as mentioned in section 2. The results are shown in the form of distance maps, where the color of a pixel indicates the collection distance required to build a quarter ring segment at that particular location. Black pixels denote sites without access to a sufficient amount of boulders, as otherwise the slope constraints of the vehicle would be violated or permanently shadowed regions would be entered.

Figure 5 shows the distance map of Connecting Ridge by using an exponential law for the SFD. Note that the x- and y-axis are the position in [km] in the polar-stereographic coordinate system. Figure 6 compares the collection distance maps with different regions and with different size-frequency distribution laws for the boulders. For Connecting Ridge, the x- and y-axes are the polar-stereographic x- and y-coordinates. For the other regions, the x- and y-axes are x- and y-coordinates of a flattened coordinate system with origin in the center of the respective region.

4.4 Required construction time

The overall time for the construction, assuming the boulder collection and the construction itself take part sequentially, is composed as:

$$t_{total} = t_{collect,driving} + t_{construct,driving} + t_{handling}, \quad (2)$$

where $t_{collect,\ driving}$ is the needed time for driving to collect the required boulders, $t_{construct,\ driving}$ the time for driving during the construction and $t_{handling}$ the time to scan and place the boulders.

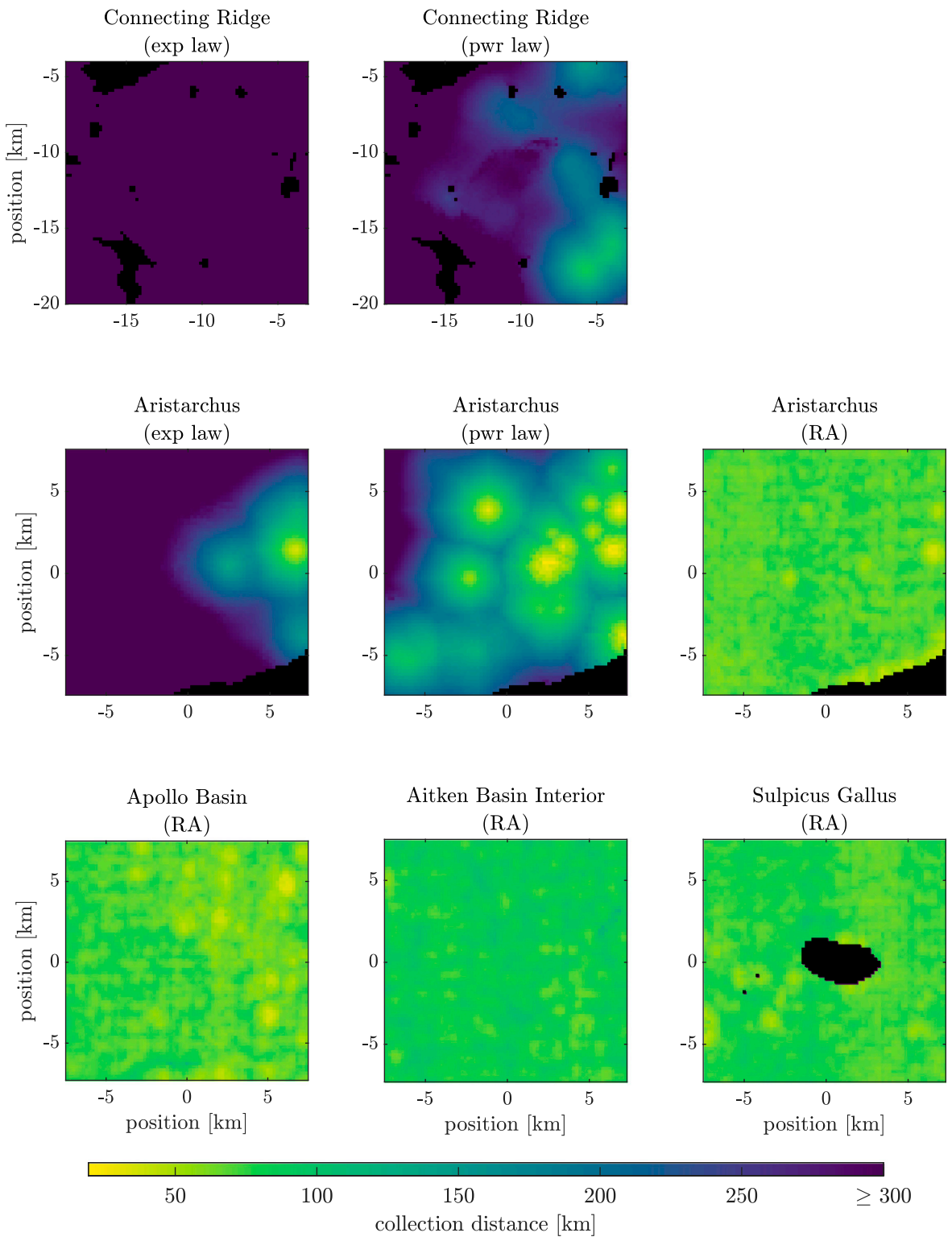

FIGURE 6
Comparison of the collection distance maps of different regions with different size-frequency distribution laws (exp law: exponential law; pwr law: power law; RA: rock abundance dependent exponential law by Li and Wu (2018)).

For the calculation of the driving times, the velocity of the LRV of the Apollo missions is taken as a reference. For the Apollo 15 mission, the average velocity was 9.2 $^{km}/_{h}$ according to Jones and Nola (1971). The calculation of the handling time is based on the value 21 $^{min}/_{stone}$ by Johns et al. (2023). The exact formulas are shown in the Supplementary Material.

Note that the time calculated as in Eq. 2 is the operational time and neglects charging times and furthermore also the lunar nights, during which operation might not be feasible. The actual time therefore might be about twice as long.

4.5 Energy consumption

The overall energy for the construction is

$$E_{total} = E_{collect} + E_{construct}, \quad (3)$$

where $E_{collect}$ is the needed energy to collect the required boulders and $E_{construct}$ the energy for the construction itself.

$E_{collect}$ and $E_{construct}$ furthermore are composed of the work against the driving resistance and the work related to the potential energy change during the collection:

$$E_{collect} = W_{collect,driving} + W_{collect,pot} \quad (4)$$

$$E_{construct} = W_{construct,driving} + W_{construct,pot} \quad (5)$$

The calculation of the individual parts is shown in the Supplementary Material. Some of the calculations require the gravitational constant of the Moon g_M and the density of the boulders ρ_b. For this, the values $g_M = 1.64\ \mathrm{m/s^2}$ and $\rho_b = 2650\ \mathrm{kg/m^3}$ provided by Susante and Metzger (2016) are used. Note that $W_{collect,pot}$ also can be negative. We use the elevation data by Barker et al. (2021) for the Connecting Ridge site and the SLDEM2015 data by Barker et al. (2016) for the Aristarchus site.

We assume the driving work to scale linearly with distance and mass, which accords with a formula by Sripad and Viswanathan (2017). The energy per distance and mass is estimated based on data of the LRV of the Apollo missions, which was mentioned by Jones and Nola (1971) and results in 0.334 J/m kg.

The vehicle mass $m_{vehicle}$ is also approximated using data of the LRV given by Jones and Nola (1971), which is scaled according to the payload capacity. For the mass of the incorporated excavator, a rough estimate was done based on a data sheet[5] of Menzi Muck. For the full formula of the vehicle mass, the interested reader is referred to the Supplementary Material.

4.6 Results for the construction of a blast shield segment

We use some of the parameters of Table 1 to compute the median values of the boulder collection distance and different energy and time components of all base camp sites in Connecting Ridge for a quarter segment of a blast shield (Table 2). An exponential law (boulder size frequency distribution) was assumed when generating those results.

Furthermore, we present the results of a specifically chosen base camp site in the middle of Connecting Ridge. This base camp site was selected based on the local slope (motivated based on the HLS requirement HLS-S-R-0022 (NASA, 2022a)), in direct proximity of the ridge's topographic summit, maximizing illumination and direct-to-Earth communication (NASA, 2022c). For this, we used elevation data of Barker et al. (2021) and Sun and Earth visibility data of Mazarico et al. (2011). We again consider a quarter segment of a blast shield, use parameters of Table 1 and assume an exponential law (boulder size-frequency distribution). The resulting boulder collection distance, as well as the energy and time components for this selected base camp site are summarized in Table 3. The driving work turns out to be larger than the energy related to the potential energy change of the collected boulders. The latter one, however, is also not negligible, which is due to the fact that the chosen base camp site is located in a topographic high, as can be seen in elevation data of Barker et al. (2021). The required energy for construction turns out to be much lower than the required energy for the collection of the boulders.

TABLE 2 Median boulder collection distance, duration and required energy in Connecting Ridge for a quarter segment of a blast shield at a radius of 50 m and by assuming an exponential law.

Value	Result
median $d_{collect}$	880 km
median $W_{collect,\ driving}$	10.1 GJ
median $W_{collect,pot}$	159 MJ
$W_{construct,\ driving}$	11.6 MJ
$W_{construct,pot}$	1.71 MJ
median E_{total}	10.3 GJ
median $t_{collect,\ driving}$	624 h
$t_{construct,\ driving}$	0.697 h
median $t_{handling}$	893 h
median t_{total}	1520 h

TABLE 3 Distance, total duration and required energy at the selected base camp site for a quarter segment of a blast shield at a radius of 50 m and by assuming an exponential law.

Value	Result
$d_{collect}$	776 km
$W_{collect,\ driving}$	9.04 GJ
$W_{collect,pot}$	954 MJ
$W_{construct,\ driving}$	11.6 MJ
$W_{construct,pot}$	1.71 MJ
E_{total}	10 GJ
$t_{collect,\ driving}$	551 h
$t_{construct,\ driving}$	0.697 h
$t_{handling}$	893 h
t_{total}	1440 h

5 https://www.menzimuck.com/fileadmin/menzimuck.com/public/03-produktgruppen/38-Menzi-Baumaschinen-Zubehoer/Prospekt/zubehoer-0318-de.pdf accessed: 12.09.2023.

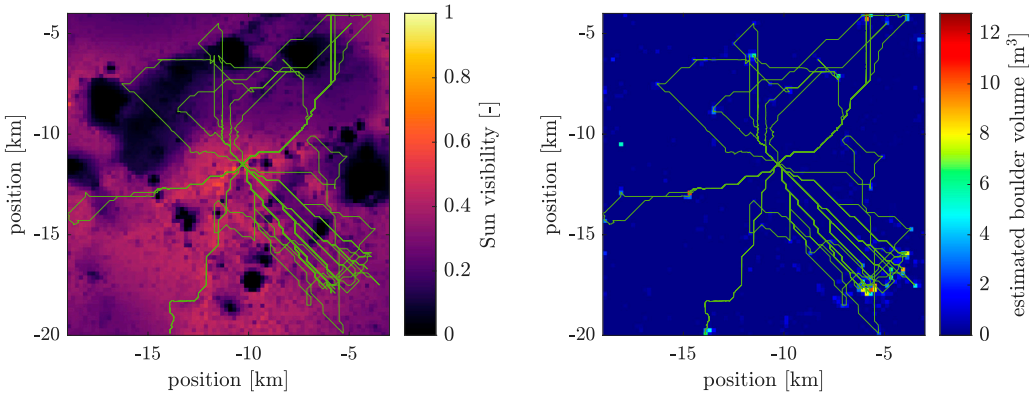

FIGURE 7
Path for the boulder collection (left background: Sun visibility data of Mazarico et al. (2011) interpolated to the 200 m by 200 m grid; right background: estimated boulder volume; white square with black edge: base camp site and excavator landing site).

The resulting path to collect the boulders is visualized in Figure 7. The white square with black edge in Figure 7 shows where the base camp site and the landing site of the excavator are located. As the base camp site fulfils the excavator landing site requirements mentioned in section 4.1.3, the two sites are identical. The right map in the figure indicates sites with available boulders. The vehicle has to traverse a significant portion of the area to collect the boulders, focusing on target locations with high boulder abundance.

5 Discussion

5.1 Available amount of boulders

In Figure 3, the boulder volume maps of different regions and via different assumptions on the size-frequency distribution law were compared. Boulder volume maps based on manually mapped boulders tend to be sparser than maps based on rock abundance data, which rarely feature locations without boulders. There is also a difference between the resulting expected boulder volume as derived with a power law and an exponential law (both with manually mapped boulder data), which will further be discussed in section 5.3.2.

We note that in case the available boulder volume is insufficient, the region where boulders are collected could simply be enlarged. Furthermore, the Moon is known to have subsurface rocks (Thompson et al., 1970; Elder et al., 2019). As an alternative, those subsurface rocks could be dug out and used for construction. Potential disadvantages include dust ejection and an increased energy consumption (Taylor et al., 2005; Lim et al., 2017).

5.2 Trade-offs

This section shows multiple trade-offs between design parameters and their implications on the proposed construction method.

5.2.1 Uncertainty on required boulder volume

The required boulder volume to construct a blast shield as described in section 2 mainly depends on the geometrical dimensions of it. The amount of required boulders increases with the radius of the blast shield ring. This is because of a) the increased perimeter and b) the increased height of the blast shield. Our results indicate that the decrease of the gas/dust pressure for larger blast shield radii does not compensate these effects. Further, the landing accuracy of incoming spacecraft has a large influence on the required boulder volume. In all previous examples it was assumed that incoming landers perform pinpoint landings. The requirements of the sustained HLS and HDL however mention a landing accuracy of 50 m (see requirement HLS-S-R-0021 (NASA, 2022a), respectively HDL-S-R-0040 (NASA, 2022b)). The lack of pinpoint landing capabilities would significantly increase the required amount of boulders, marking a clear trade-off between landing accuracy and the amount of required construction material.

5.2.2 Influence of the boulder size on the construction process

The size range of the considered boulders for the construction is a crucial design parameter. It is limited by the dimensions of the gripper of the excavator and the thickness of the walls that will be constructed. Our results indicate that extending the size range to larger boulders not only increases the amount of available boulders, but also decreases the collection distance and the time to scan and place the boulders. If however only large boulders are used, the time to scan and place the boulders further gets reduced significantly. This is due to the fact that the average volume per boulder is larger, when larger boulders are used, and therefore fewer boulders need to be scanned and placed. It remains unclear how homogeneous/heterogeneous a dry-stone blast shield can be without compromising its ability to retain engine-ejected dust and pebbles.

5.2.3 Payload capacity trade-off

An important design parameter of the vehicle that collects the boulders is its payload capacity. A larger payload capacity will make the vehicle both larger and heavier, which in turn increases the transportation costs to ship it from Earth to the Moon. In addition,

the larger empty mass of the vehicle will lead to a larger energy consumption during traverses without any payload. A larger payload capacity however also decreases the driving distance and therefore the duration of the collection process. The number of empty drives also gets decreased with a larger payload capacity, which then reduces the required energy to move the overhead mass of the gripper across the region.

The standard value for the payload capacity was chosen to be 10 m^3. It was found out that the time and energy for driving during the boulder collection are already quite low for a payload capacity of about 5 m^3. When increasing it to 10 m^3, it will get slightly faster, but the required energy starts to slightly increase due to the larger empty mass. We note that the driving time could also be linearly decreased by increasing the number of vehicles that collect the boulders. The required energy thereby would remain as it is. The drives from the base camp site to the boulder collection sites and back would be split up between the vehicles. The downside of this however is the additional mass that has to be transported from Earth to the Moon, as all vehicles would have their own excavator gripper.

A method to reduce the required energy and, in case of multiple vehicles also the transportation cost to the Moon, would be to separate the excavator and the truck. This would be particularly useful for boulder clusters located far away from the construction site.

5.3 Sensitivity analysis

This section shows the influence of uncertainties on the results. Note that the trade-offs in section 5.2 in contrast were showing the influence of design parameters on the results.

5.3.1 Uncertainty of the pressure induced on the blast shield

The assumptions regarding the engine-driven pressure on the blast shield, as described in section 2, are relatively broad. The used scaling of the pressure was done based on the maximum thrust of the Starship from SpaceX. The actual applied thrust during a lunar landing is probably much lower, especially also due to the low lunar gravity. Furthermore, there is also some uncertainty on how well the laws, which are used to scale the pressure by the landing pad radius and the mentioned actual thrust, are. While the used pressure probably should lead to conservative results, more research will be required in the future in order to get a better understanding of the actual pressure induced on the blast shield by a specific lander.

5.3.2 Uncertainty of the boulder size-frequency distribution law

A large uncertainty lies in the estimated amount of boulders based on the extrapolation with the size-frequency distribution law. As already mentioned in section 3.2, Rüsch et al. (2022) find that the applicable law depends on the age of the region. We note that the exact absolute geologic age of the two considered regions is poorly constrained and is subject to local variations. Throughout this work we fall back to using the exponential law as it provides conservative estimates of the amount of available boulders. Figure 8 shows the longest axis length *versus* the cumulative number of boulders of this size or larger, together with the exponential law and power law fits. Note that the fits only use the data points with $d_{long} \geq d_{threshold}$ as described in section 3.2, where $d_{threshold}$ was set to 2 m in this study. Note that the SFD-law fits here are made for the whole regions and not locally as done for the boulder volume maps described in section 3.3. In contrast to the power law, the exponential law has a drop off for small sizes and thus predicts lower boulder volume amounts, making it a more conservative approach.

The available boulder volume, as well as the median distances, median total energies and median total times of all base camp locations are also shown in Table 4 for the case with exponential law and power law. The table shows that the available amount of boulders with the power law is one order of magnitude higher than with the exponential law. Thus, the distances also are much shorter. This then also results in lower total energy consumption.

The handling times however are shorter when the exponential boulder size-frequency distribution is assumed, as the ratio of small to large boulders is lower with the exponential law than with the power law, which then results in assuming less boulders for the same volume. When less boulders have to be scanned and placed, the handling time is shorter. The shorter distance and thus shorter collection time in the case with the power law cannot fully compensate the larger handling time, which is why the total time will be larger with the power law, unless the collection is biased towards large boulders.

Ultimately, the exponential law is conservative with respect to the estimated amount of available small boulders, the distance and the energy consumption. In turn, it might lead to an underestimation of the construction duration.

5.3.3 Accuracy of manual boulder count *versus* rock abundance data

It stands out in Figure 6 that the distances using the rock abundance dependent exponential law by Li and Wu (2018) are much shorter than when mapped boulders are used. Further, the boulder volume maps using the mentioned rock abundance based method in Figure 3 are much denser than the maps created based on manually mapped boulders. Golombek et al. (2008) observed the phenomena that less small (Martian) boulders are found in orbiter images than in surface made images or predicted by models. Li and Wu (2018) also assume that multiple small boulders sometimes appear as one large boulder in NAC images, which is why too many large and too few small boulders are expected when mapping boulders in images with limited spatial resolution. Bandfield et al. (2011) state that the mapped amount of boulders smaller than 3 m might always be too low. Further, Bandfield et al. (2011) notice that the fractional area of mapped boulders was much lower than the one obtained using the Diviner data. Note that in section 3.4 the new rock abundance data of Powell et al. (2023) is used and not the one created by Bandfield et al. (2011), but the mentioned statements still indicate that the mapped boulders could be incomplete.

In conclusion, this shows that there also is an uncertainty on the completeness of the mapped boulders, and not only on the SFD-law used for the extrapolation. The accuracy of the estimated amount of available boulders could be improved, if there was a lunar orbiter equipped with a camera with a higher resolution than the LRO NAC.

5.3.4 Uncertainty of the shape of the boulders

The relation between the longest boulder axis and the volume, which was shown in section 3.3 and depends on the shape of the

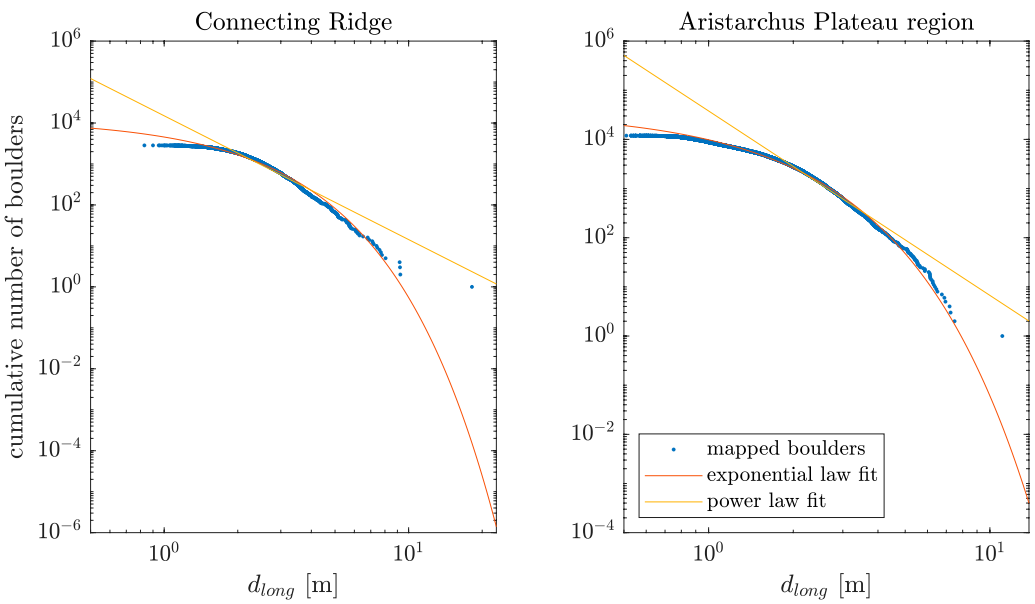

FIGURE 8
Longest axis length *versus* cumulative number over the whole Connecting Ridge and chosen Aristarchus Plateau regions.

TABLE 4 Comparison of the totally available boulder volume and the median distances, median total energies and median total times of all base camp locations using different size-frequency distribution laws and for 250 m^3 of boulders. CR: Connecting Ridge, A: chosen Aristarchus Plateau region, exp law: exponential law, pwr law: power law.

Region	SFD	$V_{b,total}$	Median $d_{collect}$	Median E_{total}	Median t_{total}
CR	exp law	502 m^3	880 km	10.4 GJ	1520 h
CR	pwr law	5030 m^3	275 km	3.29 GJ	2300 h
A	exp law	1430 m^3	366 km	4.25 GJ	1260 h
A	pwr law	31900 m^3	149 km	1.75 GJ	2620 h

boulders, is not known exactly. By only using the information about the axis length relations that were mentioned by Demidov and Basilevsky (2014), the factor between longest boulder axis and the volume would approximately be 0.23, while with values of Krishna and Kumar (2016), it can also be down to 0.1 (considered as the standard case in this paper) or 0.025. We note that with the last mentioned value, there would not be enough boulder volume available in Connecting Ridge, when assuming the exponential law, to build a quarter ring segment of a blast shield, while with the value 0.23, the collection distances are significantly shorter than with the standard value of 0.1.

5.4 Challenges of the proposed construction method

The proposed construction method is facing a series of challenges, some of which require further consideration. A dry stone wall constructed using irregular, unprocessed boulders will contain small gaps. It needs to be examined, whether those gaps are an issue when the wall is used as a blast shield. This will require simulations and experiments under lunar conditions. In case the regolith blasts could pass through the gaps, it would be necessary to seal them, e.g., by using small boulders or loose regolith.

A further challenge is the travel distance and time required to collect the material and construct a blast shield. As shown in Figure 5, the distance to collect the boulders can be around 1000 km. Table 2 on the other hand showed, that the median operation time is about 1500 h, which corresponds to 63 full Earth days. This does not include charging times or hibernation during the lunar night, which is why the actual mission time will be at least twice as long. As a reference, the Lunokhod 1 rover was operative for 321 Earth days and travelled ~10 km (Karachevtseva et al., 2013). This indicates, that the mission duration is achievable. The LRV of the Apollo 17 mission on the other hand drove approximately 35 km in about 4.5 h driving time Smith et al. (1973), which shows, that much farther distances than the mentioned one of Lunokhod 1 are possible—assuming the rover can reach a human level of navigation autonomy. A remaining

challenge will be the recharging process. The robotic excavator thereby might either harvest energy by itself, rely on a few recharging stations, or could be powered by RTGs (radioisotope thermoelectric generators).

5.5 Comparison to other construction methods

In the following, the energy consumption of two alternative blast shield construction methods are calculated and compared to the energy consumption of the proposed method. We note that the creation of un-cast regolith berms, as proposed by Mueller et al. (2009) and Moses and Mueller (2021), is not discussed here. This method probably would need less energy than the other construction methods, but comes with other disadvantages: the impacting stream of spacecraft exhaust and pebbles/dust could erode a regolith berm over time (Morris, 2012). In addition, the excavation and dumping of large amounts of regolith can lead to serious issues with the resulting dust (Taylor et al., 2005; Lim et al., 2017).

5.5.1 Cast regolith

Cast regolith has a very high compressive strength and is proposed to be used as a building material on the Moon, including blast shields (Benaroya et al., 2012). Benaroya et al. (2012) state that the creation of cast regolith takes 360 $^{kWh}/_{t}$, while the density of cast regolith is 3 $^{g}/_{cm^3}$. This leads to a needed energy per volume of 3888 $^{MJ}/_{m^3}$.

The required amount of cast regolith is calculated similarly as it was done in section 2 for our proposed construction method and by also using some of the parameters mentioned in Table 1. The required energy to produce the cast regolith then is 1250 GJ for a quarter ring segment of the blast shield.

5.5.2 Microwave heating

Microwave heating of lunar regolith leads to melting or sintering of the material (Lim et al., 2021). Lim et al. (2021) showed in experiments with regolith simulant JSC-1A that 50 g could be hardened with 1000 W and an applied energy of 900 kJ. They state that the true density of the regolith simulant is 2904 $^{kg}/_{m^3}$ and that the resulting material after the microwave treatment had a true density of 3020 $^{kg}/_{m^3}$ (Lim et al., 2021). The required energy per volume then is 54.4 $^{GJ}/_{m^3}$.

The calculation of the needed volume of construction material for a blast shield with radius r = 50 m is done similarly as in section 5.5.1 and also by using some of the parameters mentioned in Table 1. The result is about 1290 m^3, respectively only about 322 m^3, when only a quarter ring segment is built. The needed energy then is 17500 GJ for the quarter ring segment. Note that the used value for the density given by Lim et al. (2021) is the true density and not the bulk density, which unfortunately is not provided and therefore unknown. Lim et al. (2021) mention that the void ratio in the regolith simulant prior to microwave heating was 47%. By assuming the bulk density to be half of the true density, which probably is too low as melting or sintering takes place according to Lim et al. (2021), the required energy still is 6440 GJ for the quarter ring segment.

5.5.3 Comparison

In Table 5, the required energy of the three construction methods are compared. Our proposed method requires about two to three orders of magnitudes less energy than the other construction methods. By assuming equal construction time, this would mean that solar arrays used for charging would need about 100–1000 times less surface area. The very low energy consumption is one of the main advantages of the proposed construction method.

5.6 Sustainability and conservation considerations

Figure 7 suggests that the collection of boulders can be quite invasive, as boulders are systematically moved across the surface, negatively impacting future scientific studies. The sustainable utilization of lunar resources—including boulders—is subject to an ongoing debate (Pirtle et al., 2023). We note that the systematic collection of boulders might in fact aid scientific analyses, if properly conducted: all boulders remain unprocessed and can be accessed in the blast shield wall (Johns et al., 2020). Context data collected before and during the collection of boulders (location, orientation, composition, etc.) could be used to create a digital twin of the area of interest, opening up new research venues, such as related to the regional study of impact ejecta composition.

5.7 Applicability of the method for Mars

In future missions to Mars, ISRU will become even more important, as the transportation costs from Earth to Mars are much higher than from Earth to the Moon, due to the larger distance, motivating a basic comparison of the median available boulder volume on the Moon and on Mars. For the Moon, the rock abundance dependent exponential law by Li and Wu (2018) and the rock abundance data of Powell (2022) and Powell et al. (2023) was used. For Mars, the rock abundance dependent exponential law and boulder axis length ratio by Golombek and Rapp (1997) and information about the rock abundance of Christensen (1986) was used. For the lunar case, the median area that contains 250 m^3 of boulders is slightly larger than 0.2 km^2, while the median area on Mars that contains 250 m^3 of boulders is about 0.06 km^2. This shows, that the proposed construction method would work even better on Mars than on the Moon. We note that the regional geologic context can significantly influence the availability of boulders, particularly on an atmospheric planet like Mars.

5.8 Outlook

This section gives an overview of what work remains open for future research. As mentioned, the estimate of the available amount of boulders has some uncertainties. High resolution images of landers at the regions of interest will allow to get a better understanding of how many small boulders are available. Furthermore, the usage of the proposed construction method could be expanded to also build arch vaults, which could be used as habitats and shelters. The capability of autonomously constructing arches with irregular boulders will need to be demonstrated in experiments. Finally, an excavator capable of operating in the lunar environment needs to be developed and the exact dimensions of the infrastructure need to be set.

TABLE 5 Comparison of the energy consumption to build a quarter ring segment of a blast shield with different construction methods.

Method	Required energy
Dry stone wall (our method) (median E_{total})	10.3 GJ
Cast regolith Benaroya et al. (2012)	1250 GJ
Microwave heating Lim et al. (2021)	17500 GJ
Microwave heating (assuming half the density) Lim et al. (2021)	6440 GJ

6 Conclusion

In this work we propose an autonomous excavator that is able to collect boulders across the lunar surface and use them to construct dry-stone blast shields. We calculate that a total of about 1000 m^3 and 250 m^3 is required for a full and a quarter ring blast shield segment. We determine the number and sizes of boulders physically present across two sites of interest, the Shackleton-Henson Connecting Ridge and a section of the Aristarchus pyroclastic deposit, using LRO NAC images. We use size-frequency distribution laws to estimate the fraction of boulders smaller than the NAC spatial resolution. In addition, we explore an alternative approach that exclusively relies on LRO Diviner rock abundance data to estimate the abundance of appropriate construction material. We use a path planning pipeline to calculate the distance an excavator needs to transverse to collect the required amount of boulders and perform energy and time calculations of the overall construction process. We find that the required energy is two to three orders of magnitudes lower than with other construction methods proposed in the literature.

We show that the landing pad radius and the lander precision have a large influence on the boulder volume required for a blast shield. Utilization of large boulders reduces the overall construction time, while utilizing boulders with a wide size range reduces the overall driving distance. Our results indicate that a large vehicle payload capacity does not provide any significant energy consumption and construction time benefits. The results presented here rely on a number of conservative estimates and assumptions, such as the boulder size-frequency distribution law used for the extrapolation of the number of boulders towards small sizes. Finally, we demonstrate the applicability of our overall method on planet Mars using rock abundance data.

This work showcases the strategic importance of innovative *in-situ* resource utilization and construction strategies for the sustainable exploration of the Moon and beyond.

Data availability statement

The datasets presented in this study can be found in online repositories. The names of the repository/repositories and accession number(s) can be found below: Our boulder shapefiles, some geotiff files of the boulder volume maps and the distance maps, as well as the code of the path planning pipeline are available online (Walther et al., 2023). The used data, which is publicly available, is listed in the following, including the source where it can be found:

- NAC images (Robinson et al., 2010; Humm et al., 2016; Mahanti et al., 2016; Speyerer et al., 2012; Robinson, 2010): e.g., via https://wms.lroc.asu.edu/lroc/search or https://pds.lroc.asu.edu/data/LRO-L-LROC-2-EDR-V1.0/
- Artemis candidate regions geojson file: https://files.actgate.com/lunar/A3_Named_regions.geojson
- Constellation Program regions of interest shapefile by Lucey et al. (2009): https://wms.lroc.asu.edu/lroc/view_rdr/SHAPEFILE_CX_TARGETS
- Earth visibility and Sun visibility data of Mazarico et al. (2011): http://imbrium.mit.edu/EXTRAS/ILLUMINATION/JP2/
- Rock abundance data by Powell (2022): https://doi.org/10.25346/S6/LFAVXU
- SLDEM2015 elevation data by Barker et al. (2016): http://imbrium.mit.edu/DATA/SLDEM2015/TILES/JP2/
- SLDEM2015 slope data by Barker et al. (2016): http://imbrium.mit.edu/DATA/SLDEM2015_SLOPE/TILES/JP2/
- SLDEM2015 azimuth data by Barker et al. (2016): http://imbrium.mit.edu/DATA/SLDEM2015_AZIMUTH/TILES/JP2/
- South pole elevation data by Barker et al. (2021): https://pgda.gsfc.nasa.gov/products/78

Author contributions

JW: Conceptualization, Methodology, Software, Validation, Formal analysis, Investigation, Data curation, Visualization, Writing–original draft, Writing–review and editing. RJ: Conceptualization, Methodology, Supervision, Funding acquisition, Visualization, Writing–review and editing, Writing–original draft. HK: Conceptualization, Methodology, Supervision, Funding acquisition, Writing–review and editing, Writing–original draft. VB: Conceptualization, Methodology, Supervision, Funding acquisition, Software, Data curation, Writing–review and editing, Writing–original draft. MH: Conceptualization, Funding acquisition, Supervision, Writing–review and editing, Writing–original draft.

Funding

The author(s) declare financial support was received for the research, authorship, and/or publication of this article. This work has been conducted as part of ESA contract No. 4000134584/21/NL/GLC/my. Open access funding by ETH Zurich.

Acknowledgments

We want to thank Ottaviano Rüsch for his advice concerning the fit of boulder size-frequency distribution laws. Furthermore, we want to thank Boazman et al. (2022) for providing us with the boulder shapefiles of Connecting Ridge. We also acknowledge the use of QGIS[6], as well as GDAL (GDAL/OGR contributors, 2020) to handle georeferenced data.

6 https://qgis.org/de/site/

Conflict of interest

The authors declare that the research was conducted in the absence of any commercial or financial relationships that could be construed as a potential conflict of interest.

Publisher's note

All claims expressed in this article are solely those of the authors and do not necessarily represent those of their affiliated organizations, or those of the publisher, the editors and the reviewers. Any product that may be evaluated in this article, or claim that may be made by its manufacturer, is not guaranteed or endorsed by the publisher.

Supplementary material

The Supplementary Material for this article can be found online at: https://www.frontiersin.org/articles/10.3389/frspt.2024.1345337/full#supplementary-material

References

Astrobotic (2018). *Peregrine lunar lander, payload user's guide*. version 3.0.

Baloga, S. M., Glaze, L. S., and Spudis, P. D. (2012). Inferred lunar boulder distributions at decimeter scales

Bandfield, J. L., Ghent, R. R., Vasavada, A. R., Paige, D. A., Lawrence, S. J., and Robinson, M. S. (2011). Lunar surface rock abundance and regolith fines temperatures derived from LRO Diviner Radiometer data. *J. Geophys. Res. Planets* 116, E00H02. 0–02. doi:10.1029/2011JE003866

Barker, M. K., Mazarico, E., Neumann, G. A., Smith, D. E., Zuber, M. T., and Head, J. W. (2021). Improved LOLA elevation maps for south pole landing sites: error estimates and their impact on illumination conditions. *Planet. Space Sci.* 203, 105119. doi:10.1016/J.PSS.2020.105119

Barker, M. K., Mazarico, E., Neumann, G. A., Zuber, M. T., Haruyama, J., and Smith, D. E. (2016). A new lunar digital elevation model from the lunar orbiter laser altimeter and SELENE terrain camera. *Icarus* 273, 346–355. doi:10.1016/J.ICARUS.2015.07.039

Benaroya, H., and Bernold, L. (2008). Engineering of lunar bases. *Acta Astronaut.* 62, 277–299. doi:10.1016/J.ACTAASTRO.2007.05.001

Benaroya, H., Indyk, S., and Mottaghi, S. (2012). Advanced systems concept for autonomous construction and self-repair of lunar surface isru structures. *Moon Prospect. Energy Material Resour.* 9783642279690, 641–660. doi:10.1007/978-3-642-27969-0_27/COVER

Bickel, V. T., Aaron, J., Manconi, A., and Loew, S. (2021). Global drivers and transport mechanisms of lunar rockfalls. *J. Geophys. Res. Planets* 126. doi:10.1029/2021JE006824

Bickel, V. T., Aaron, J., Manconi, A., Loew, S., and Mall, U. (2020). Impacts drive lunar rockfalls over billions of years. *Nat. Commun.* 11 (1 11), 2862–2867. doi:10.1038/s41467-020-16653-3

Boazman, S. J., Shah, J., Gawronska, A. J., Halim, S. H., Satyakumar, A. V., Gilmour, C. M., et al. (2022). The distribution and accessibility of geologic targets near the lunar south pole and candidate Artemis landing sites. *Planet. Sci. J.* 3, 275. doi:10.3847/PSJ/ACA590

Cesaretti, G., Dini, E., Kestelier, X. D., Colla, V., and Pambaguian, L. (2014). Building components for an outpost on the lunar soil by means of a novel 3d printing technology. *Acta Astronaut.* 93, 430–450. doi:10.1016/J.ACTAASTRO.2013.07.034

Christensen, P. R. (1986). The spatial distribution of rocks on mars. *Icarus* 68, 217–238. doi:10.1016/0019-1035(86)90020-5

Clauset, A., Shalizi, C. R., and Newman, M. E. (2009). Power-law distributions in empirical data. *SIAM Rev.* 51, 661–703. doi:10.1137/070710111

Demidov, N. E., and Basilevsky, A. T. (2014). Height-to-diameter ratios of moon rocks from analysis of Lunokhod-1 and -2 and Apollo 11–17 panoramas and LROC NAC images. *Sol. Syst. Res.* 48, 324–329. doi:10.1134/s0038094614050013

DeSouza, I., Daly, M. G., Barnouin, O. S., Ernst, C. M., and Bierhaus, E. B. (2015). Improved techniques for size–frequency distribution analysis in the planetary sciences: application to blocks on 25143 itokawa. *Icarus* 247, 77–80. doi:10.1016/J.ICARUS.2014.10.009

Dijkstra, E. W. (1959). A note on two problems in connexion with graphs. *Numer. Math.* 1, 269–271. doi:10.1007/bf01386390

Elder, C. M., Douglass, B., Ghent, R. R., Hayne, P. O., Williams, J.-P., Bandfield, J. L., et al. (2019). The subsurface coherent rock content of the Moon as revealed by cold-spot craters. doi:10.1029/2019JE006128

Few, L. (1955). The shortest path and the shortest road through n points. *Mathematika* 2, 141–144. doi:10.1112/S0025579300000784

Gawronska, A. J., Barrett, N., Boazman, S. J., Gilmour, C. M., Halim, S. H., Harish, , et al. (2020). Geologic context and potential EVA targets at the lunar south pole. *Adv. Space Res.* 66, 1247–1264. doi:10.1016/J.ASR.2020.05.035

GDAL/OGR contributors (2020). GDAL/OGR geospatial data abstraction software library. *Open Source Geospatial Found.* Available at: http://gdal.org.

Gelino, N. J., Mueller, R. P., Sibille, L., Dixon, K. L., Gleeson, J., and Buckles, B. (2023). *In-situ* lunar launch and landing pad construction with regolith-thermoset polymer composite materials. American Society of Civil Engineers (ASCE). Earth and Space 2022: Space Exploration, Utilization, Engineering, and Construction in Extreme Environments - Selected Papers from the 18th Biennial International Conference on Engineering, Science, Construction, and Operations in Challenging Environments , 789–803. doi:10.1061/9780784484470.067

Golombek, M., and Rapp, D. (1997). Size-frequency distributions of rocks on mars and earth analog sites: implications for future landed missions. *J. Geophys. Res. Planets* 102, 4117–4129. doi:10.1029/96JE03319

Golombek, M. P., Huertas, A., Marlow, J., McGrane, B., Klein, C., Martinez, M., et al. (2008). Size-frequency distributions of rocks on the northern plains of Mars with special reference to Phoenix landing surfaces. *J. Geophys. Res. Planets* 113, 0–09. doi:10.1029/2007JE003065

Grant, J. A., Golombek, M. P., Wilson, S. A., Farley, K. A., Williford, K. H., and Chen, A. (2018). The science process for selecting the landing site for the 2020 Mars rover. *Planet. Space Sci.* 164, 106–126. doi:10.1016/J.PSS.2018.07.001

Hart, P. E., Nilsson, N. J., and Raphael, B. (1968). A formal basis for the heuristic determination of minimum cost paths. *IEEE Trans. Syst. Sci. Cybern.* 4, 100–107. doi:10.1109/TSSC.1968.300136

Heiken, G. H., Vaniman, D. T., and French, B. M. (1991). Lunar sourcebook: a user's guide to the moon

Humm, D. C., Tschimmel, M., Brylow, S. M., Mahanti, P., Tran, T. N., Braden, S. E., et al. (2016). Flight calibration of the LROC Narrow angle camera. *Space Sci. Rev.* 200, 431–473. doi:10.1007/s11214-015-0201-8

Hurwitz, D. M., Head, J. W., and Hiesinger, H. (2013). Lunar sinuous rilles: distribution, characteristics, and implications for their origin. *Planet. Space Sci.* 79-80, 1–38. doi:10.1016/J.PSS.2012.10.019

Immer, C., Metzger, P., Hintze, P. E., Nick, A., and Horan, R. (2011). Apollo 12 lunar module exhaust plume impingement on Lunar Surveyor III. *Icarus* 211, 1089–1102. doi:10.1016/J.ICARUS.2010.11.013

Johns, R. L., Wermelinger, M., Mascaro, R., Jud, D., Gramazio, F., Kohler, M., et al. (2020). Autonomous dry stone. *Constr. Robot.* 4, 127–140. doi:10.1007/S41693-020-00037-6

Johns, R. L., Wermelinger, M., Mascaro, R., Jud, D., Hurkxkens, I., Vasey, L., et al. (2023). A framework for robotic excavation and dry stone construction using on-site materials. *Sci. Robotics* 8, eabp9758. doi:10.1126/scirobotics.abp9758

Jones, C. S., and Nola, F. J. (1971). Mobility systems activity for lunar rovers at MSFC

Karachevtseva, I., Oberst, J., Scholten, F., Konopikhin, A., Shingareva, K., Cherepanova, E., et al. (2013). Cartography of the lunokhod-1 landing site and traverse from lro image and stereo-topographic data. *Planet. Space Sci.* 85, 175–187. doi:10.1016/J.PSS.2013.06.002

Khoshnevis, B., Carlson, A., and Thangavelu, M. (2017). ISRU-based robotic construction technologies for lunar and martian infrastructures

Krishna, N., and Kumar, P. S. (2016). Impact spallation processes on the moon: a case study from the size and shape analysis of ejecta boulders and secondary craters of censorinus crater. *Icarus* 264, 274–299. doi:10.1016/J.ICARUS.2015.09.033

Laura, J., Acosta, A., Addair, T., Adoram-Kershner, L., Alexander, J., Alexandrov, O., et al. (2023). Integrated software for imagers and spectrometers. doi:10.5281/ZENODO.7644616

Li, B., Ling, Z., Zhang, J., and Chen, J. (2017). Rock size-frequency distributions analysis at lunar landing sites based on remote sensing and *in-situ* imagery. *Planet. Space Sci.* 146, 30–39. doi:10.1016/J.PSS.2017.08.008

Li, Y., and Wu, B. (2018). Analysis of rock abundance on lunar surface from orbital and descent images using automatic rock detection. *J. Geophys. Res. Planets* 123, 1061–1088. doi:10.1029/2017JE005496

Lim, S., Bowen, J., Degli-Alessandrini, G., Anand, M., Cowley, A., and Prabhu, V. L. (2021). Investigating the microwave heating behaviour of lunar soil simulant jsc-1a at different input powers. *Sci. Rep.* 11 (1 11), 2133–2216. doi:10.1038/s41598-021-81691-w

Lim, S., Prabhu, V. L., Anand, M., and Taylor, L. A. (2017). Extra-terrestrial construction processes – advancements, opportunities and challenges. *Adv. Space Res.* 60, 1413–1429. doi:10.1016/J.ASR.2017.06.038

Lucey, P. G., Gillis-Davis, J. T., Hawke, B. R., Taylor, L. A., Duke, M. B., Brady, T., et al. (2009). Leag review of constellation program regions of interest for human exploration of the moon. *LPICo* 1483, 73–74.

Mahanti, P., Humm, D. C., Robinson, M. S., Boyd, A. K., Stelling, R., Sato, H., et al. (2016). Inflight calibration of the lunar reconnaissance orbiter camera wide angle camera. *Space Sci. Rev.* 200, 393–430. doi:10.1007/s11214-015-0197-0

Mazarico, E., Neumann, G. A., Smith, D. E., Zuber, M. T., and Torrence, M. H. (2011). Illumination conditions of the lunar polar regions using LOLA topography. *Icarus* 211, 1066–1081. doi:10.1016/J.ICARUS.2010.10.030

McCombie, P. F., Morel, J. C., and Garnier, D. (2015). *Drystone retaining walls: design, construction and assessment*. Boca Raton: CRC Press. doi:10.1201/B19095

Morris, A. B. (2012). Simulation of rocket plume impingement and dust dispersal on the lunar surface. MS dissertation. Available at: https://repositories.lib.utexas.edu/handle/2152/ETD-UT-2012-12-6718.

Moses, R. W., and Mueller, R. P. (2021). Requirements development framework for lunar *in situ* surface construction of infrastructure. American Society of Civil Engineers. Earth and Space 2021: Space Exploration, Utilization, Engineering, and Construction in Extreme Environments - Selected Papers from the 17th Biennial International Conference on Engineering, Science, Construction, and Operations in Challenging Environments , 1141–1155. doi:10.1061/9780784483374.106

Mueller, R., Wilkinson, R. A., Gallo, C. A., Nick, A. J., Schuler, J. M., and King, R. H. (2009). "Lightweight bulldozer attachment for construction and excavation on the lunar surface," in AIAA 2009 Space Conference and Exposition, Pasadena. Available at: https://ntrs.nasa.gov/citations/20130012987.

Muniruzzaman, A. N. M. (1957). On measures of location and dispersion and tests of hypotheses in a pare to population. *Calcutta Stat. Assoc. Bull.*, 115–123. Secondary reference via [Clauset et al., "Power-law distributions in empirical data," 2009]. doi:10.1177/0008068319570303

NASA (2020). NASA's lunar exploration program overview. Available at: https://www.nasa.gov/sites/default/files/atoms/files/artemis_plan-20200921.pdf (Accessed August 10, 2023).

NASA (2021a). NASA picks SpaceX to land next americans on Moon. Available at: http://www.nasa.gov/press-release/as-artemis-moves-forward-nasa-picks-spacex-to-land-next-americans-on-moon (Accessed August 8, 2023).

NASA (2021b). SLS-SPEC-159 cross-program design specification for natural environments (DSNE), revision I. Available at: https://ntrs.nasa.gov/api/citations/20210024522/downloads/SLS-SPEC-159%20Cross-Program%20Design%20Specification%20for%20Natural%20Environments%20(DSNE)%20REVISION%20I.pdf (Accessed June 2, 2023).

NASA (2022a). HLS-RQMT-006 HLS program integrated lander requirements document – sustained phase, revision A + HLS-MD-001. Available at: https://sam.gov/opp/b1852a6dfa144607a517628bcb273e6a/view (Accessed June 2, 2023). 1.

NASA (2022b). HLS-RQMT-007 HLS program human-class delivery lander (HDL) requirements document – sustained phase, revision A. Available at: https://sam.gov/opp/b1852a6dfa144607a517628bcb273e6a/view (Accessed June 2, 2023).

NASA (2022c). NASA identifies candidate regions for landing next americans on moon. Available at: https://www.nasa.gov/press-release/nasa-identifies-candidate-regions-for-landing-next-americans-on-moon (Accessed August 24, 2023).

NASA (2023a). Exploration systems development mission directorate Moon-to-Mars architecture definition document (ESDMD-001). Available at: https://ntrs.nasa.gov/api/citations/20230002706/downloads/M2MADD_ESDMD-001(TP-20230002706).pdf (Accessed August 10, 2023).

NASA (2023b). Lunar Terrain Vehicle (LTV) standard road, draft. Available at: https://sam.gov/opp/17def9439fd348fc8d4dbc4feb9ee80d/view (Accessed June 2, 2023).

O'Shea, C. A. (2023). NASA pursues lunar terrain vehicle services for Artemis missions. Available at: https://www.nasa.gov/press-release/nasa-pursues-lunar-terrain-vehicle-services-for-artemis-missions (Accessed August 23, 2023).

Pena-Asensio, E., Sutherland, J., Tripathi, P., Mason, K., Goodwin, A., Bickel, V. T., et al. (2023). Automated astronaut traverses with minimum metabolic workload: accessing permanently shadowed regions near the lunar south pole. *Acta Astronaut.* 214, 324–342. doi:10.1016/J.ACTAASTRO.2023.10.010

Pirtle, Z., Mcbrayer, K., Beauchemin, A., Swiney, G., Lopez, L. D., Merrill, G., et al. (2023). in Artemis, ethics and society: Synthesis from a workshop.

Powell, T. (2022). Replication data for: high-resolution nighttime temperature and rock abundance mapping of the moon using the diviner lunar radiometer experiment with a model for topographic removal. doi:10.25346/S6/LFAVXU

Powell, T. M., Horvath, T., Robles, V. L., Williams, J. P., Hayne, P. O., Gallinger, C. L., et al. (2023). High-resolution nighttime temperature and rock abundance mapping of the moon using the diviner lunar radiometer experiment with a model for topographic removal. *J. Geophys. Res. Planets* 128, e2022JE007532. doi:10.1029/2022JE007532

Qiao, L., Hess, M., Xu, L., Wöhler, C., Head, J. W., Chen, J., et al. (2023). Extensive lunar surface disturbance at the Chang'e-5 mission landing site: implications for future lunar base design and construction. *J. Geophys. Res. Planets* 128. doi:10.1029/2022JE007730

Roberts, L. (1966). "The interaction of a rocket exhaust with the lunar surface *AGARD the Fluid Dyn. Aspects of Space Flight* 2. Secondary reference via," in *Simulation of rocket plume impingement and dust dispersal on the lunar surface*. Editor A. Morris, 2012.

Robinson, M. S. (2010). Lunar reconnaissance orbiter camera experimental data record, LRO-L-LROC-2-EDR-V1.0, NASA Planetary Data System.

Robinson, M. S., Brylow, S. M., Tschimmel, M., Humm, D., Lawrence, S. J., Thomas, P. C., et al. (2010). Lunar reconnaissance orbiter camera (LROC) instrument overview. *Space Sci. Rev.* 150, 81–124. doi:10.1007/s11214-010-9634-2

Ruesch, O., and Bickel, V. (2023). Global mapping of fragmented rocks on the moon with a neural network: implications for the failure mode of rocks on airless surfaces. *PSJ* 4, 126. doi:10.3847/psj/acd1ef

Rüsch, O., Marshal, R. M., Iqbal, W., Pasckert, J. H., van der Bogert, C. H., and Patzek, M. (2022). Catastrophic rupture of lunar rocks: implications for lunar rock size–frequency distributions. *Icarus* 387, 115200. doi:10.1016/J.ICARUS.2022.115200

SIA (2012). SIA 266/2:2012, Secondary reference via Stiftung Umwelt-Einsatz Schweiz, Trockenmauern: Grundlagen, Bauanleitung, Bedeutung. Haupt Verlag, 2014.

Smith, E. C., Mustin, W. C., and Marshall, G. C. (1973). Lunar roving vehicle navigation system performance review

Speyerer, E. J., Wagner, R. V., Robinson, M. S., Humm, D. C., Becker, K., Anderson, J., et al. (2012). In-flight geometric calibration of the lunar reconnaissance orbiter camera. *Int. Archives Photogrammetry, Remote Sens. Spatial Inf. Sci.* XXXIX-B4, 511–516. doi:10.5194/ISPRSARCHIVES-XXXIX-B4-511-2012

Sripad, S., and Viswanathan, V. (2017). Performance metrics required of next-generation batteries to make a practical electric semi truck. *ACS Energy Lett.* 2, 1669–1673. doi:10.1021/acsenergylett.7b00432

Stiftung Umwelt-Einsatz Schweiz (2014). *Trockenmauern: Grundlagen, Bauanleitung, Bedeutung* (Haupt Verlag).

Susante, P. J. V. (2012). Landing pad construction rover attachment development earth and Space 2012 - proceedings of the 13th ASCE aerospace division conference and the 5th NASA/ASCE workshop on granular materials in Space exploration , 165–174. doi:10.1061/9780784412190.019

Susante, P. J. V., and Metzger, P. T. (2016). "Design, test, and simulation of lunar and mars landing pad soil stabilization built with *in situ* rock utilization," in Earth and Space 2016: Engineering for Extreme Environments - Proceedings of the 15th Biennial International Conference on Engineering, Science, Construction, and Operations in Challenging Environments, 642–652. doi:10.1061/9780784479971.060

Swiney, G., and Hernandez, A. (2022). *Lunar landings and operations policy analysis*. Available at: https://www.nasa.gov/wp-content/uploads/2022/10/lunar_landing_and_operations_policy_analysis_final_report_24oct2022_tagged_0.pdf (Accessed September 30, 2022).

Taylor, L. A., Schmitt, H. H., Carrier, W. D., and Nakagawa, M. (2005). Lunar dust problem: from liability to asset. *A Collect. Tech. Pap. - 1st Space Explor. Conf. Continuing Voyage Discov.* 1, 71–78. doi:10.2514/6.2005-2510

Thangavelu, M., and Adhikari, P. (2017). *MPIT: minimally processed ISRU technology structures for rapid extraterrestrial settlement infrastructure development*, 5208. Orlando: AIAA SPACE and Astronautics Forum and Exposition.

Thompson, T. W., Pollack, J. B., Campbell, M. J., and O'leary, B. T. (1970). Radar maps of the Moon at 70-cm wavelength and their interpretation. *Radio Sci.* 5, 253–262. doi:10.1029/RS005i002p00253

Valantinas, A., and Schultz, P. H. (2020). The origin of neotectonics on the lunar nearside. *Geology* 48, 649–653. doi:10.1130/G47202.1

Walther, J., Johns, R. L., Kolvenbach, H., Bickel, V. T., and Hutter, M. (2023). Dataset for the paper: "autonomous construction of lunar infrastructure with *in-situ* boulders". Available at: http://hdl.handle.net/20.500.11850/643602. doi:10.3929/ethz-b-000643602

Walther, J., Lim, J., Lawrance, N., and Siegwart, R. (2022). *Topological path planning for information gathering in alpine environments*, ETH Zurich, Autonomous Systems Lab. doi:10.3929/ETHZ-B-000559560

Wentworth, C. K. (1922). A scale of grade and class terms for clastic sediments, *The Journal of Geology* 30, 377–392. doi:10.1086/62291030

Yashar, M., Netti, V., Rajkumar, A., Morris, M., Pailes-Friedman, R., Elshanshoury, W., et al. (2021). "Project olympus: off-world additive construction for lunar surface infrastructure," in 50th International Conference on Environmental Systems.

Zisk, S. H., Hodges, C. A., Moore, H. J., Shorthill, R. W., Thompson, T. W., Whitaker, E. A., et al. (1977). The Aristarchus-Harbinger region of the moon: surface geology and history from recent remote-sensing observations. *Moon* 17, 59–99. doi:10.1007/bf00566853

Frontiers in
Space Technologies

Explores innovation in space technology and its applications

An exciting journal which advances our understanding of space technologies and their commercialization - from weather forecasting to satellite navigation.

Discover the latest Research Topics

See more →

Frontiers

Avenue du Tribunal-Fédéral 34
1005 Lausanne, Switzerland
frontiersin.org

Contact us

+41 (0)21 510 17 00
frontiersin.org/about/contact